The search for high-energy gamma-ray emission from the close binary system AR Scorpii using *Fermi*-LAT data

Quinton Kaplan

Submitted in fulfilment of the requirements for the degree

Magister Scientiae

in the

Faculty of Natural and Agricultural Sciences,

Department of Physics,

University of the Free State,

South Africa

Submission date: 20 October 2021

Supervised by: Prof. P.J. Meintjes

Co-supervised by: Dr. H.J. van Heerden

Abstract

AR Scorpii (AR Sco) is an enigmatic close binary system which is observable across most of the electromagnetic spectrum. Multi-wavelength emission consists of both thermal and non-thermal components, where pulsed non-thermal emission has been observed from radio to X-ray. The apparent lack of accretion in the system also suggests that the highly magnetic white dwarf is primarily spin-powered, similar to pulsars, where particles can be accelerated to produce non-thermal emission. The multi-wavelength nature from radio to X-ray of AR Sco has been extensively studied and presented since 2016, showing a clear non-thermal synchrotron component from optical to X-ray. However, the parameters and processes towards the high-energy regime still need to be clearly verified and explored. Hence, a search for non-thermal γ-ray emission from AR Sco using archival *Fermi* data from the past decade has been performed. By using updated *Fermi*-LAT software and Pass 8 analysis methods, low-level upper-limit emission has been observed above 100 MeV, with a possible low-level pulsed signal at the spin period ($P_s = 117$ s) of the white dwarf. Given the results, the possibility of non-thermal emission at higher energies can not be excluded. An updated spectral energy distribution using *Fermi*-LAT data was also produced to serve as a template for future studies using more sensitive Cherenkov telescope detectors like e.g. the Cherenkov Telescope Array (CTA).

Key words: High-energy emission, Non-thermal emission, *Fermi* γ-ray space telescope, 4FGL, Pass 8, Likelihood analysis, Time-series analysis, Cataclysmic variable star, star - AR Sco.

Opsomming

AR Scorpii (AR Sco) is 'n raaiselagtige nabye binêre stelsel wat waarneembaar is oor die grootste deel van die elektromagnetiese spektrum. Multigolflengte uitstraling bestaan uit beide termiese en nie-termiese komponente, waar gepulseerde nie-termiese straling van radio tot X-straal waargeneem is. Die skynbare gebrek aan akkresie in die stelsel dui ook daarop dat die hoogs magnetiese witdwerg hoofsaaklik spin-gedrewe is, soortgelyk aan pulsare, waar deeltjies versnel word om nie-termiese straling te produseer. Die multigolflengte aard van radio tot X-strale van AR Sco is sedert 2016 uitvoerig bestudeer en aangebied, wat 'n duidelike nie-termiese synchrotron komponent van die optiese na X-straal band toon. Die parameters en prosesse in terme van die hoë γ-straal energie bly egter onbeproef en moet nog steeds duidelik geverifieer en ondersoek word. Daarom is 'n soektog na nie-termiese γ-straal emissie vanaf AR Sco met behulp van *Fermi*-data van die afgelope dekade uitgevoer. Deur opgedateerde *Fermi*-LAT sagteware en Pass 8 analise metodes te gebruik, is bo-grens-emissie bo 100 MeV op 'n lae vlak waargeneem, met 'n moontlike lae-vlak pulsasies by die spin periode van die witdwerg. Gegewe die resultate, kan die moontlikheid van nie-termiese emissie by hoër energieë nie uitgesluit word nie. 'n Opgedateerde spektrale energie-distribusie is ook geproduseer in terme van *Fermi*-LAT data om as templaat te dien vir toekomstige studies met gesofistikeerde atmosferiese cherenkov teleskope soos bv. die Cherenkov Telescope Array (CTA).

Sleutelwoorde: Hoë-energie emissie, Nie-termiese emissie, *Fermi* γ-straal ruimteteleskoop, 4FGL, Pass 8, Waarskynlikheidsanalise, Tydreeksanalise, Kataklismiese veranderlike ster, ster - AR Sco

Acknowledgements

The author wishes to acknowledge the following parties for their contributions towards the completion of this study:

- My supervisor, Prof. P.J. Meintjes, for his role as supervisor, and for all the motivation, guidance and patience that I have received from him during the completion of this study.
- My co-supervisor, Dr. H.J. van Heerden, for his role as co-supervisor and assistance in the analysis process.
- My parents, brother and friends for their love and support throughout all of my endeavours during the good and difficult times. Without them my studies would not be possible.
- My girlfriend, Cindy, for her endless love, constant support, motivation, patience and understanding during the good and frustrating times of this study.
- The UFS Department of Physics staff and students for their inspiration and assistance.
- The UFS High Performance Computing (HPC) team for their operation and maintenance, for without them, this project would not be possible.
- The UFS postgraduate school and SA Gamma for the financial support during this project.

Finally and most importantly to our Almighty God, for the privilege and talent to study the majesty that is His creation. As well as giving me the strength and guidance to see this project through, for without Him I would be lost.

Dedicated to my grandfather, Theo "Kappies" Kaplan,
Whose legacy will live on forever.

Contents

List of Abbreviations

3FGL	Third *Fermi* Gamma-ray LAT Catalogue
4FGL	Fourth *Fermi* Gamma-ray LAT Catalogue
ACD	anticoincidence detector
AGN	Active Galactic Nuclei
ATCA	Australia Telescope Compact Array
BPL	Broken Power-Law
CCD	Charged Coupled Device
COM	Centre of Mass
CRTS	Catalina Real Time Survey
CTA	Cherenkov Telescope Array
CV	Cataclysmic Variable
Dec	Declination
EGRET	Energetic Gamma-ray Experimental Telescope
EPIC	European Photon Imaging Camera

FFT	Fast Fourier Transform
FORS	FOcal Reducer and low dispersion Spectrograph
FoV	Field of View
FSSC	*Fermi* Science Support Center
GRBs	Gamma-ray Bursts
H.E.S.S	High Energy Stereoscopic System
HEASARC	High Energy Astrophysics Science Archive Research Center
HIPPO	HIgh speed Photo-POlarimeter
HPC	High Performance Computer
IC	Inverse-Compton
IP	Intermediate Polar
IR	Infrared
L1	Langrangian Point 1
LAT	Large Area Telescope
LBA	Long Baseline Array
LP	Log Parabola
MCV	Magnetic Cataclysmic Variable
MHD	Magnetohydrodynamics
MJD	Modified Julian Date
NS	Neutron Star

OM	Optical/UV Monitor
pdf	Probabilty Distribution Function
PL	Power-Law
PSF	Point Spread Function
RA	Right Ascension
ROI	Region of Interest
SAAO	South African Astronomical Observatory
SED	Spectral Energy Distribution
SNR	Supernovae Remnants
TS	Test Statistic
UFS	University of the Free State
UV	Ultraviolet
VLA	Very Long Array
VLBI	Very Long Baseline Interferomiter
VLT	Very Large Telscope
XMM-Newton	X-ray Multi-Mirror Mission Newton

Chapter 1

Introduction

High-energy astrophysics has been a very productive research field over the past few decades, where studies are conducted in the pursuit of unravelling the secrets of the high-energy Universe. A vast number of ground and space-based telescopes have been designed and built to study the high-energy Universe, among others, the *Fermi Gamma-ray Space Telescope* (henceforth *Fermi*). Since its commissioning, the primary instrument aboard the telescope, i.e. the Large Area Telescope (LAT), has detected an immense number of Galactic and extragalactic γ-ray sources.

The recently published Fourth *Fermi* Gamma-ray LAT Catalogue (4FGL), (Abdollahi et al., 2020), lists a staggering 5064 high-energy sources between 100 MeV and 1 TeV,[1] of which 358 (7.1%) are considered identified and classified based on the correlation of their emission properties with observations in other parts of the electromagnetic spectrum. The catalogue also includes 3370 (66.5%) counterparts at lower energies, with the remaining 1336 sources (26.4%) which are classified as un-associated[2] (see Fig. 1.1).

As in previous *Fermi* catalogs, sources are included based on a statistical significance of their detection considered over the entire period of observation. For this

[1] MeV = 10^6 eV; TeV = 10^{12} eV

[2] For more information regarding the catalogue see the 4FGL paper published by Abdollahi et al. (2020).

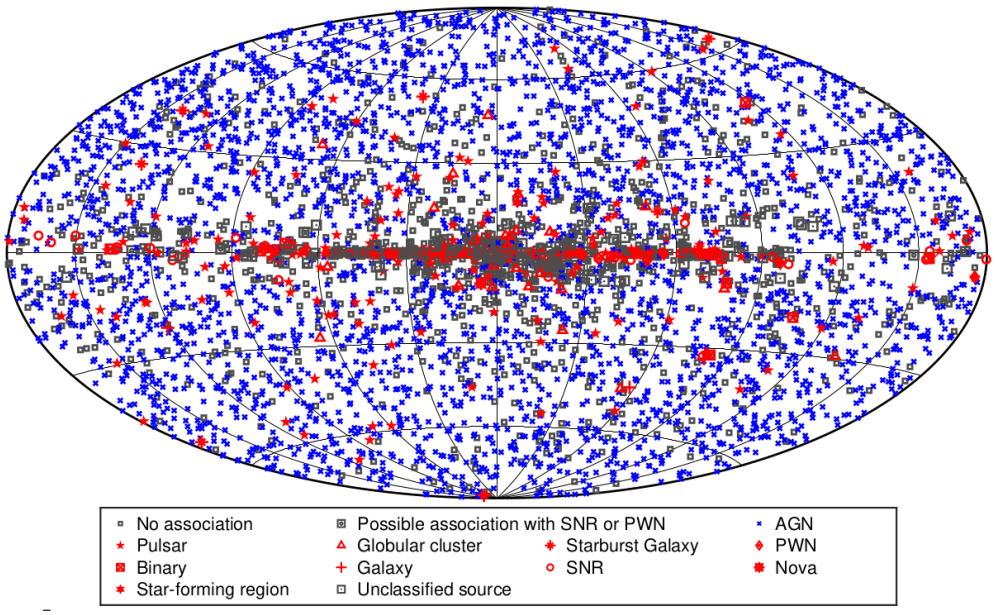

Figure 1.1: *Fermi* full sky map of all sources listed in the 4FGL catalog. All Active Galactic Nuclei (AGN) classes are plotted with a blue symbol for simplicity, where other associations to a well-defined class are plotted in red. Unassociated sources and sources associated with counterparts of unknown nature are plotted in grey. Adopted from Abdollahi et al. (2020).

reason the 4FGL catalog may not contain some transient γ-ray sources which are only detectable over short periods during outburst, including Gamma-ray Bursts (GRBs) and most novae, (e.g., Abdollahi et al., 2020; Ackermann et al., 2014; Ajello et al., 2019).

Fermi-LAT has detected γ-ray emission from six Galactic novae since the start of its mission in 2008, (Ackermann et al. 2014; Cheung et al. 2016). Recently, long-term optical observations led to the identification of a peculiar close binary system called AR Scorpii (henceforth AR Sco), which shares several characteristics with that of nova-like Cataclysmic Variable (CV) stars and displays fascinating multi-wavelength emission properties from radio to X-ray wavelengths, (e.g., Marsh et al., 2016; Takata et al., 2018). This system consists of a highly magnetic white dwarf primary star and a red dwarf secondary orbiting around their common Centre of Mass (COM). (Not sure if to include?)

Detailed multi-wavelength studies of AR Sco reveal strong brightness variations across most of the (electromagnetic/electro-magnetic?) spectrum, showing transient-like pulsed thermal and possibly non-thermal emission from radio to X-ray energies, (e.g., Marsh et al., 2016), where pulsations are observed at the spin ($P_s = 117$ s) and beat ($P_b = 118.2$ s) period of the white dwarf in AR Sco.. This implies that AR Sco may be a source where particles are accelerated to relativistic energies, perhaps in the magnetosphere of the white dwarf with associated pulsed pulsar-like emission through, among other, synchrotron radiation. An emphatic theoretical framework was provided by Buckley et al. (2017), in an attempt to explain the multi-frequency emission from AR Sco from radio frequencies to X-ray energies. These authors also reported significant ($\leq 40\%$) linear polarization of the optical light, which perhaps signifies a significant synchrotron component in the radio to X-ray part of the Spectral Energy Distribution (SED) of AR Sco.

Buckley et al. (2017) further showed that the SED between Infrared (IR) and X-ray wavelengths (see Fig. 1.2) can be explained satisfactorily by a pulsar-like particle acceleration process in the magnetosphere of the white dwarf, showing some similarity to the nova-like CV AE Aquarii (henceforth AE Aqr), (Oruru & Meintjes, 2012). In order to explain the pulsed hard X-ray emission ($\epsilon \sim 10$ keV) from AE Aqr, as reported using *Suzaku* observations (Terada et al., 2007), these authors proposed pulsar-like particle acceleration of electrons to relativistic energies ($\gamma \sim 10^6$) and the associated synchrotron emission linked to the spin period of the white dwarf in AE Aqr. Among other alternative models that may be able to explain emission from AR Sco, is a magnetized striped wind (Coroniti, 1990) outside the light cylinder of the white dwarf, a process that is currently being investigated to explain the pulsed pulsar-like emission, (Ramamonjisoa et al., in progress).

Based on pure energetic perspectives, the white dwarf in AR Sco can accelerate charged particles like electrons and protons to energies of the order of $\gamma \sim 10^5 - 10^6$ within the light cylinder of the rotating white dwarf, (e.g., Buckley et al., 2017;

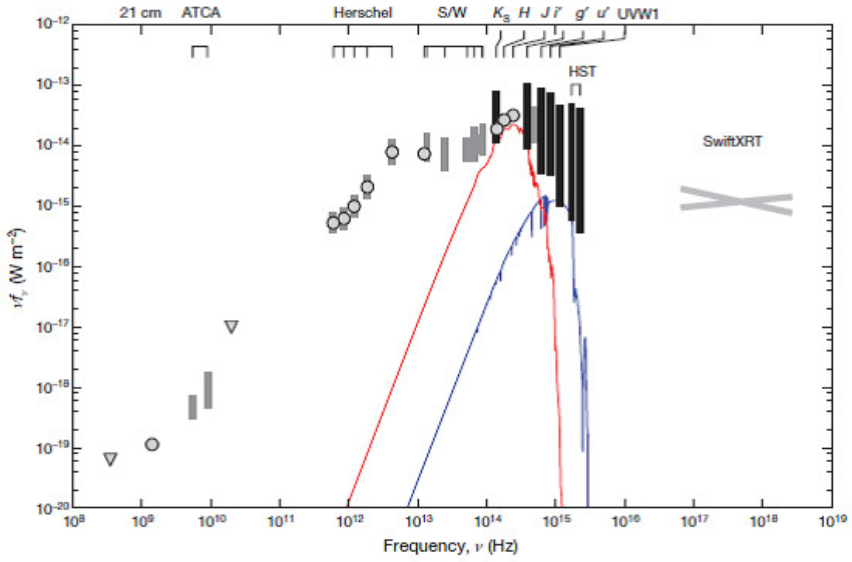

Figure 1.2: The multi-frequency Spectral Energy Distribution (SED) of AR Sco from radio to X-ray frequencies. The blue and red curves represent model atmospheres of a white dwarf (T = 9750 K) and red M5 secondary dwarf star (T = 3100 K) respectively. Adopted from Marsh et al. (2016)

Takata et al., 2017). This provides a possible mechanism to produce γ-rays with energies of the order $\sim$ 1 TeV through Inverse-Compton (IC) scattering between the relativistic electrons and the photons from the secondary star, or alternatively through hadronic interactions and associated π°-decay. The presence of a particle accelerator and the huge reservoir of target photons or hadronic material for γ-ray production through both leptonic and hadronic channels makes AR Sco an ideal candidate to search for possible detectable pulsed γ-ray emission, given its proximity of $d \approx 120$pc.

Hence, the aim of this study is to do a complete γ-ray analysis using the total *Fermi*-LAT dataset of the past decade (2008-2019). By doing *Fermi*-LAT likelihood tests, utilizing the upgraded *Fermi*-LAT Pass 8 dataset and analysis pipeline, a search for pulsed or continuum γ-ray excess from AR Sco can be performed above 100 MeV. With the upgraded Pass 8 data pipeline, better constraints can be placed on the level of emission above the diffuse Galactic γ-ray background compared to previous pipelines.

With a possible detection, or determining upper-limits on the γ-ray flux, important constraints can be placed on the γ-ray spectrum above 100 MeV. This may prove important and decisive for a possible future search for γ-ray emission from AR Sco utilising the superior sensitivity and resolution of the Cherenkov Telescope Array (CTA). The discovery of γ-ray emission from AR Sco will certainly be an enormous contribution to the field of γ-ray astronomy, since it will add fast rotating highly magnetized white dwarfs to the list of Galactic γ-ray source classes and help to enhance the understanding of non-thermal radiative mechanisms in these systems.

This study is structured as follows: Chapter 2 outlines an overview of AR Sco focusing on its unique multi-wavelength emission properties reported in various studies.; Chapter 3 will focus on the theoretical frameworks explaining how non-thermal emission can be produced and where within the system it originates; in Chapter 4 the complete *Fermi*-LAT analyses methodology to search for any γ-ray excess using a 10-year *Fermi*-LAT data set, utilising the updated *Fermi* software, is discussed; finally the conclusions of this study is summarized in Chapter 5.

Appendix A presents a discussion of the different particle acceleration and γ-ray production mechanisms that may be present in AR Sco. Appendix B includes periodograms at the spin and beat period of AR Sco using an alternative ephemeris. A periodogram control test at locations in a different direction from the location centred at AR Sco's coordinates is presented in Appendix C. Appendix D lists Rayleigh periodograms at noise level. Included in Appendix E are peer-reviewed conference proceedings where *Fermi*-LAT and *Fermipy* results are presented in part. Conference proceedings articles include: *SAIP2018*, *HEASA2018*, *HEASA2019*, *ICRC2019* and *HEASA2021*. Also included in the appendix is the peer-reviewed Astroparticle Physics journal paper where the multi-wavelength SED modelling of AR Sco is presented, (Singh et al., 2020).

Chapter 2

AR Sco - An Overview

2.1 Introduction

Before this discussion focuses on AR Sco and its enigmatic multi-wavelength emission properties, a general review of the basic properties of close binary systems focusing especially on CV systems, which share some similarities with AR Sco, will be presented.

The brightness variation of AR Sco observed from radio to X-ray establishes the source as a variable star. By definition, a variable star is any star that varies in brightness or colour over a defined period (e.g., Sterken & Jaschek, 2005). These variations can be caused by different mechanisms which make it necessary to classify variable stars into groups or categories. The variability associated with these stars or systems can be the result of different processes, namely mechanical reasons due to rotation or eclipses, i.e., *extrinsic variables*, or due to physical changes in the star's properties leading to a change in luminosity within the star, i.e., *intrinsic variables*. Variable stars can for example then be further classified into subgroups (e.g., Joshi, 2019) by the nature of their light curves, periodicity and evolutionary stage. Some examples include:

Eclipsing variables are binary stellar systems with an orbital plane oriented (roughly?) in the line-of-sight of the observer. The components of the system periodically eclipse each other, causing a decrease in the apparent brightness of the system from the vantage point of the observer.

Rotating variables are stars where the variability changes with the star's rotation. This can be due to brighter regions on the star's surface that can change its apparent brightness as the star rotates about its axis, or fast rotating stars that deform to an ellipsoidal shape.

Pulsating variables are stars that show periodic expansion and contraction of the surface layers as part of their natural evolutionary processes. Pulsations may be radial, where the star remains spherical in shape, or non-radial where the geometry deviates from spherical symmetry.

Eruptive variables are stars varying in brightness because of violent processes and flares occurring in their outer shell. The brightness changes are usually accompanied by shell events or mass outflow in the form of stellar winds of variable intensity and/or by interaction with the surrounding interstellar medium.

Cataclysmic variables (CV), in particular, stand out as being very interesting when it comes to variability. Per definition, they are close binary systems consisting of a white dwarf primary that accretes matter from a late-type main sequence companion/secondary star, with the system having occasional violent outbursts that result in dramatic changes in their brightness. These brightness variations are generally believed to be associated with the accretion process of matter onto the surface of the white dwarf. For a more in depth review of CVs, see e.g. Hellier (2001); Warner (2003).

Because CVs and AR Sco (as inferred by observations) are binary systems, the structure and interaction processes in binaries are important to define and describe. Binary systems consist of two components, which are bound by the gravitational force between them and rotate about their common COM. Binary

systems are classified by their light curves, how close the components are to each other and how they interact (e.g., mass transfer mechanisms). This means that there exist a number of different binary system classifications, among them are: detached, semi-detached and contact binaries[1]. See Fig. 2.1 for an illustration.

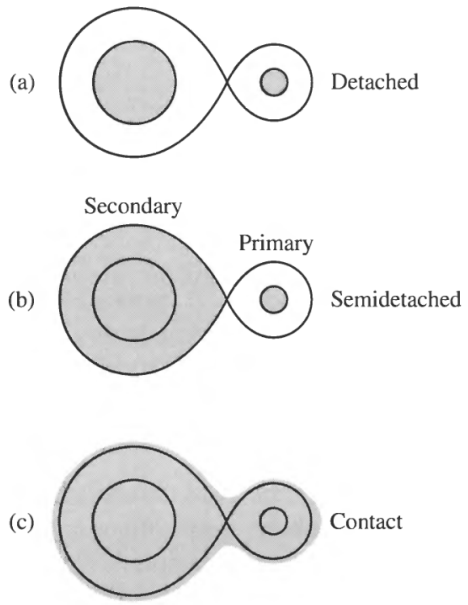

Figure 2.1: Classification of close binary star systems. Here (a) represents a detached system, (b) a semi-detached system in which the secondary star has expanded to fill its individual Roche lobe and (c) a contact binary. Adopted from Introduction to Modern Astrophysics, (Carroll & Ostlie, 2014, p. 723).

In compact/close binaries the separation distance between the two objects are normally comparable to the size of one of the stars. The two components of the system are surrounded by closed equipotential/gravitational surfaces, with the inner critical surface in the form of a figure-eight (or "dumbell" shape), (e.g., Carroll & Ostlie, 2014; van Heerden, 2015). The two halves are known as the Roche Lobes, with the material from each individual star belonging to its respective Roche lobe, i.e., material to the left is gravitationally bound to the star on the left and the material to the right is gravitationally bound to the star on the right, (see Fig. 2.2 for illustration). The point at which the respective Roche lobes connect is called the inner Langrangian Point (L1) where the effective gravity is zero.

[1]More general cases of binary system classifications exist (e.g., Carroll & Ostlie, 2014), but does

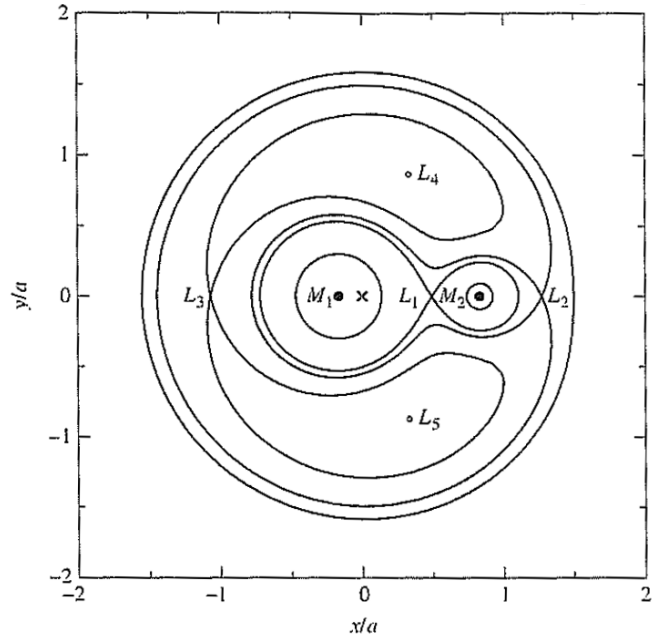

Figure 2.2: Equipotential surfaces around two stars, where M_1 is known as the primary star, and M_2 known as the secondary star. Material is transported from the secondary through the L_1 point to the primary. This is an example of a system where the masses of the primary and secondary stars are defined as $M_1 = 0.85\ M_\odot$ and $M_2 = 0.17\ M_\odot$ respectively, where the binary separation is defined as $a = 5 \times 10^8$ cm. Adopted from Introduction to Modern Astrophysics, (Carroll & Ostlie, 2014, p. 721).

A binary is classified as a *detached* system when the two components fit within their respective Roche lobes, without touching the equipotential surface. When the secondary star starts to fill and expand beyond its Roche lobe, the system evolves into a *semi-detached* binary where the Roche lobe of the secondary star is filled but not that of the primary. At this point mass transfer from one star to the other can occur. If both the secondary and the primary stars fill, or expand beyond their individual Roche lobes, they start to share a common envelope and the system is known as a *contact* binary[2].

CVs are close binary systems and are among the well studied stellar sources. Due to their short orbital time scales ($\sim$ 3 h), they serve as great space "laboratories" to study accretion physics in binary systems. The same physical processes

not fall under the scope of this discussion, which is more focused towards compact binaries.
[2]See (Carroll & Ostlie, 2014, Chapter 18) and Hilditch (2001) for a more detailed discussion on compact binary systems.

also manifest on a much grander scale in the heart of Active Galactic Nuclei (AGNs), where a supermassive black hole in the centre can accrete matter from a well developed accretion disc. CVs are thought to originate and evolve from binary systems containing two main sequence stars that orbit each other (e.g., Hellier, 2001).

The more massive star in the system will start to evolve into the giant branch, e.g., due to hydrogen depletion throughout the core (Hellier, 2001). The outer layers of the giant star will be pushed far from the core and are no longer strongly bound. The material from these outer layers are then pushed away by radiation pressure from below, out into space. What is left is the hot, dense core resulting in the star ending up as a white dwarf. As the two stars orbit within a common envelope the separation between the stars will start to decrease as a result of gravitational attraction between the two stars and friction. Once the common envelope starts to dissipate, it leads to the formation of a white dwarf (primary)/main-sequence (secondary) binary system that evolves without mass transfer (e.g., Szkody & Gaensicke, 2012). The binary continuously loses mass and angular momentum through a stellar wind from the secondary star, resulting in the binary inter-distance to shrink. This causes the secondary star to fill its Roche lobe at some point, from where mass transfer can start by Roche lobe overflow across the L1 region, consequently leading to a CV system (see Fig. 2.3 for illustration).

CVs normally contain a primary compact object orbiting a low-mass, cooler, secondary donor star (usually K-type) around their common COM. Most often, such as in the case of dwarf novae, these systems consist of a white dwarf primary ($M_{WD} \sim 1\ M_{\odot}$) orbiting a late type main sequence secondary star ($M_s \leq 1\ M_{\odot}$) accompanied by an associated accretion process (e.g., Giovannelli, 2008; Smak, 1985). Depending on the magnetic field strength of the white dwarf, the type of CV can be defined by the type of mass transfer mechanism between the secondary and primary components.

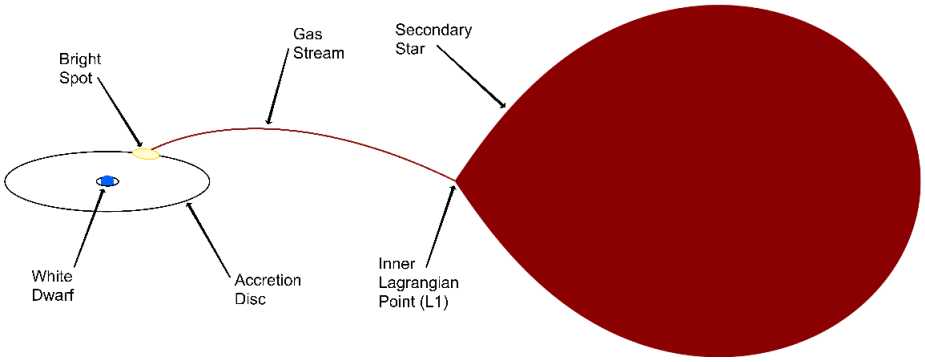

Figure 2.3: Example of a CV binary system where mass is transferred from the secondary star onto/to the white dwarf through the L_1 point, forming an accretion disc around the white dwarf. Adopted from Szkody & Gaensicke (2012).

In the case of non-magnetic CVs, where there is no detectable magnetic field (< 1 MG), the material slowly spirals inwards towards the compact primary, where the mass-flow rate depends on the viscosity of the material in the accretion disc. It is this viscosity that allows for the exchange of angular momentum (e.g., Wynn, 2000). For example, in low-mass-transfer systems, the material in the accretion disc has a low viscosity and is cool. As the disc gradually grows in mass it heats up, i.e., the temperature becomes sufficiently high to switch the disc into a hot, high viscosity state. The accumulated mass then rapidly starts to accrete onto the white dwarf (e.g., Hellier, 2001; Smith, 2007; Szkody & Gaensicke, 2012).

For a Magnetic Cataclysmic Variable (MCV), the mass transfer and resulting formation of the accretion disc will be influenced by the relative strength of the white dwarf's magnetic field. In MCVs there exist different scales for the magnetic field strength of the white dwarf, rotation period of the white dwarf and/or energy spectrum of the radiated emission, which leads to different classifications of MCVs, (e.g. Giovannelli 2008; Szkody & Gaensicke 2012). If the white dwarf has a very high magnetic field ($B_{\rm WD}>$ 10 MG) they are called Polars, because of optical observations revealing circular polarized light due to thermal plasma trapped in the magnetic field of the polar cap regions of the accreting white dwarf, (e.g., Hellier, 2001). If the magnetic field ranges between 1-10 MG, the system is known as an Intermediate Polar (IP).

In Polars the magnetic field of the white dwarf is so intense, the mass transfer stream is intercepted by the magnetic field and guided to the polar caps, preventing the formation of a thin accretion disc. The field locks the secondary star and the white dwarf spin in the same synchronised orbital timescale. Hence, the formation of an accretion disc will be prevented due to the synchronised rotation of the two stars (e.g., Cropper, 1990; Giovannelli, 2008). See Fig. 2.4 for an illustration of Polars.

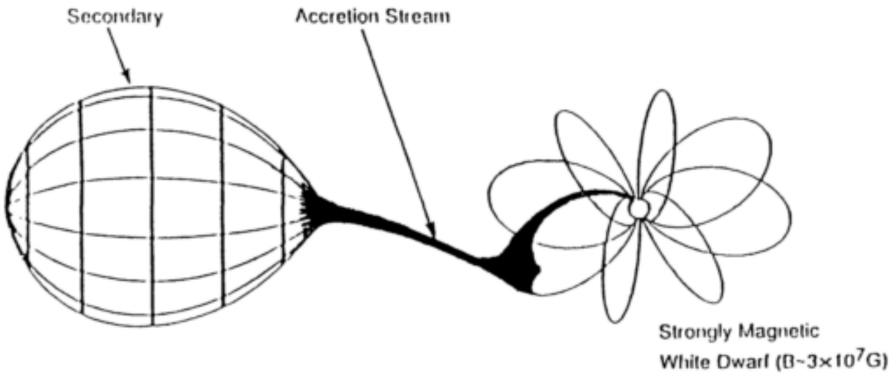

Figure 2.4: Illustrative sketch of Polar. Adopted from Cropper (1990).

Intermediate Polars (IP), as the name implies, has the characteristics of a non-magnetic CV and a Polar combined. In these systems the lower magnetic field intensity allows the formation of an accretion disc but prevents the disc to reach the surface of the white dwarf (e.g., Ferrario, 1996; Patterson, 1994; Szkody & Gaensicke, 2012). Instead, a truncated accretion disc is formed where the inner disc is disrupted by the magnetic field, leading the material to rain onto the white dwarf in broad accretion curtains (see Fig. 2.5 and (Hellier, 2001, p. 109)). The size of the accretion discs is dependent on the morphology and physical parameters of the system. For example, the inner region of the disc is dependent on the white dwarf's magnetic field strength whereas the size of the outer acretion region is determined by the Roche lobe of the white dwarf.

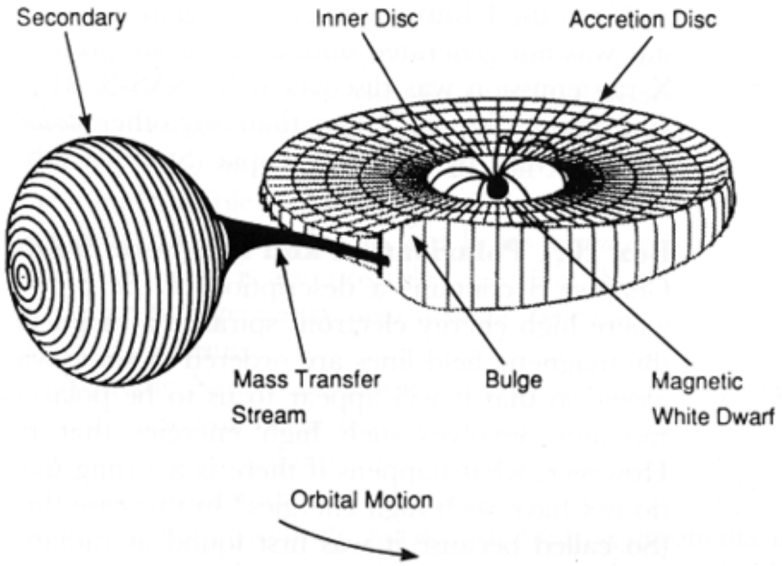

Figure 2.5: Illustrative sketch of Intermediate-Polar. Adopted from Giovannelli (2008).

The magnetic field of the secondary star also has an influence on the mass transfer process (Ritter, 1988). It has been shown by e.g., Meintjes (2004) and Meintjes & Jurua (2006) that the presence of a magnetic viscosity can have a significant effect on the mass flow from the secondary. It is argued that strong magnetic obstructions in the mass flow through the L1 funnel may provide magnetic viscosity that can lead to significant deceleration and compression, resulting in a clumpy/fragmented mass flow, which plays a fundamental role in the evolution of CVs. In extreme cases, strong magnetic prominences near the L1 region may prevent mass flow across the L1 point altogether, which may shut down mass transfer and accompanying accretion in the system (Meintjes & Jurua, 2006).

2.2 AR Sco's binary properties

AR Sco has been studied since its initial discovery in the 1970's, where at the time it was classified as a δ-Scuti star, which are regularly short period ($\sim$ 7 hours) pulsating variables stars (e.g., Satyvaldiev, 1971). The initial δ-Scuti classification was due to the regular and periodic variations in brightness over short/

observational timescales observed from AR Sco (∼ 3 hours). However, a few decades later, the system was revealed to be a close binary that contains a main sequence star orbiting a compact object around a common COM (Marsh et al., 2016). Observations revealed that the white dwarf is spinning about its own axis on a timescale of $P_s = 117$ s, with pulsed emission strongly modulated at the beat period ($P_b = 118.2$ s) with the orbital period of $P_o = 3.56$ h. Hence, interest was renewed in AR Sco.

The components if this compact binary system consists of a M5-type main sequence star, with a lower mass limit $M_1 >\sim 0.4\ M_\odot$ on the white dwarf primary, and the radius of the white dwarf estimated as $R_{\rm wd} \sim 7{\times}10^8$ cm. The mass range of each star was given as $0.81\ M_\odot < M_1 \leq 1.29\ M_\odot$ and $0.28\ M_\odot < M_2 \leq 0.45\ M_\odot$ respectively (with a mass ratio of $q = \frac{M_2}{M_1} > 0.375$)[3], where the mean distance estimation to the source is given as $d \sim 116 \pm 16$ pc, (Marsh et al., 2016).

With a binary separation of $a \sim 8 \times 10^{10}$ cm, the Roche lobe radius of the secondary star is estimated to be $R_{L,2} \sim 0.3a \sim 2.53 \times 10^{10}$ cm. In comparison to the L1 region from the primary, $b_1 \sim 0.6a \sim 5 \times 10^{10}$ cm, the light cylinder radius of the white dwarf is of the order of $r_{l-c} \sim 6 \times 10^{11}$ cm, implying that the binary system fits inside the white dwarf primary's light cylinder (Buckley et al., 2017). The light cylinder is where the magnetosphere of the primary co-rotates at the speed of light, $c = \omega_{\rm wd} r_{l-c}$, where $\omega_{\rm wd}$ is the angular velocity of the white dwarf.

Optical and Ultraviolet (UV) spectra of AR Sco show no evidence of broad and variable Doppler-broadened emission lines (Marsh et al., 2016). This implies an apparent lack of accretion in AR Sco, making this a very peculiar system compared to other compact binaries. AR Sco's X-ray luminosity ($L_{\rm X} \sim 5 \times 10^{30}$ erg s^{-1}) is also less than 1% of the X-ray luminosity of a typical IP, about two orders of magnitude less than a typical accreting magnetic white dwarf (e.g., Pretorius & Mukai, 2014), supporting the notion that little or no accretion is visible in the system.

[3] M_1 and M_2 are defined as the mass of the white dwarf and secondary star respectively.

The rotating white dwarf is currently spinning down on a timescale of $\tau = \frac{\nu}{\dot{\nu}} \sim 10^7$ yr ($\dot{P} = 3.92 \times 10^{-13}$ s s^{-1}), with a spin-down luminosity of $\simeq 3 \times 10^{33}$ erg s^{-1}, (Marsh et al., 2016). It is speculated that a previous high mass-accretion phase was instrumental in the spin-up of the white dwarf to a period of around 2 min, since white dwarfs are not born spinning rapidly (e.g., Charpinet et al., 2009). The absence of an accretion disc, and the fact that the spin-down luminosity is orders of magnitude larger than seen in electromagnetic radiation, suggest that AR Sco is primarily spin-powered (e.g., Katz, 2017; Marsh et al., 2016).

However, a re-evaluation of the spin-down ephemeris with higher timescale observations taken between 2016 and 2017 taken by Potter & Buckley (2018a) showed inconsistencies with the proposed spin-down rate of Marsh et al. (2016). Hence the exact spin-evolution of the white dwarf in AR Sco has not yet been confirmed and needs to be better constrained to understand its energetics and evolution. It has, however, been suggested that the source of AR Sco's observed luminosity comes from the spin-down power of the highly magnetic white dwarf, which provides more than enough energy to account for the system's radiative luminosity (e.g., Buckley et al., 2017; Stiller et al., 2018).

The white dwarf in AR Sco also appears to be highly magnetized. An upper-limit on the magnetic dipole strength of the white dwarf was derived assuming that the bulk of the spin-down power is radiated by the magneto-dipole radiation (Buckley et al., 2017). For a maximum dipole tilt angle to the spin axis of $\chi = 90°$ and taking $L_{m-d} = L_{\dot{\nu_s}}$, the upper-limit placed on the white dwarf magnetic field was estimated by these authors to be

$$B \approx 500 \left[\frac{L_{\dot{\nu_s}}}{1.5 \times 10^{33} \text{ erg s}^{-1}}\right]^{0.5} \left[\frac{P_s}{117 \text{ s}}\right] \left[\frac{R_{\text{wd}}}{5.5 \times 10^8 \text{ cm}}\right]^{-3} \text{MG}, \tag{2.1}$$

where $L_{\dot{\nu_s}}$ is the spin-down luminosity of the white dwarf and L_{m-d} is the luminosity from magnetic dipole radiation. This upper-limit value on the magnetic

field is still within the range of expected magnetic field values of white dwarfs, albeit on the high end (Ferrario et al., 2015; Wickramasinghe & Ferrario, 2000, 2005). Assuming that a fraction of the spin-down power is dissipated through a magnetic stand-off shock near the secondary, it gives an estimate of the surface magnetic field of the white dwarf to be $\sim$ 100 MG (Katz, 2017). It was also shown that for a $\sim$ 500 MG magnetic white dwarf, the field strength will be 160 G at the distance of the secondary star, namely $a \sim 8 \times 10^{10}$cm, (Buckley et al., 2017).

Although AR Sco share many similarities with MCVs, the apparent lack of mass transfer form the secondary star (e.g., Marsh et al., 2016) does not place it strictly speaking within the CV framework. It is, however, possible that AR Sco is currently in a phase of CV evolution where mass transfer is temporarily prevented by the secondary star slightly underfilling its Roche lobe due to a classical nova eruption in the past resulting in the secondary star to shrink and consequently restarting the mass transfer process, or by the magnetic field of the secondary star, e.g., a magnetic gating effect, where prominences near the L1 region prevents the flow of gas across the L1 region (e.g., Meintjes & Jurua, 2006)[4].

This, however, raises the question whether the developed models for AR Sco can be associated with those of CV's. Due to AR Sco's unique binary and emission properties it is still speculated by some authors that AR Sco may be an IP in a special evolutionary state (e.g., Lyutikov et al., 2020; Meintjes, 2017; Stanway et al., 2018) or that it may represent an entirely new astrophysical source class altogether. AR Sco is relatively new in the astrophysical community and more studies should be performed over the electromagnetic spectrum to constrain the source's emission properties and evolution. This may help to find similar sources of this nature, if any, and/or determine the class of binary sources to which AR Sco belongs. The above-mentioned parameters are just some of the properties of AR Sco and a more detailed discussion relative to multi-wavelength observations and the inferred system parameters will now be presented.

[4]See e.g., Jackson (1998); Meintjes & Breedt (2015) for a discussion related to magnetic viscosity.

2.3 Multi-wavelength observations

AR Sco emits across most of the electromagnetic spectrum, (e.g. Marsh et al. (2016); Buckley et al. (2017); Marcote et al. (2017); Takata et al. (2017)), making it necessary to evaluate the emission from selected regions of the electromagnetic spectrum. The emission and corresponding mechanisms can be confined to specific sections of the electromagnetic spectrum, with observed signatures and measured parameters defining the processes involved.

For example, in dick accreting CVs, accretion discs are observed to be dominated by UV radiation, especially during outbursts (e.g., Hellier, 2001; Szkody & Gaensicke, 2012). Historical radio observations suggest that radio emission in dwarf novae and MCVs probably originate from the magnetospheres of their secondaries, (Warner, 2003), but recent studies show radio emission originating from the accretion disc during outbursts coupled with possible synchrotron emission (Coppejans et al., 2016). Selected novae have also been observed to show γ-ray emission in some rare cases (e.g., Kamae et al., 2018; Schlegel et al., 1995), where MeV detections of V834 Cen and VV Pup have been claimed by Barrett et al. (1995), with more recent discoveries made with *Fermi*-LAT (Ackermann et al., 2014). Signals have also been detected and studied in AE Aqr, which has been observed in the TeV range (Meintjes et al., 1992, 1991), suggesting non-thermal emission due to particle acceleration.

This makes simultaneous multi-wavelength observations, coupled with detailed modelling over all energy regimes necessary to expand our understanding of the physical behaviour of CVs, including AR Sco. Following is a discussion of previous observations of AR Sco in selected electromagnetic spectral windows to give a clearer picture of the system, and the current physical parameters and proposed mechanisms involved.

2.3.1 Radio and IR observations

Radio emission from AR Sco was first discovered by Marsh et al. (2016), making it the first known radio pulsating white dwarf discovered so far. By doing hour-long observations using the Australia Telescope Compact Array (ATCA), it was reported that AR Sco shows pulsations at the spin period of $P_s = 117$ s, with an accompanying beat period of $P_b = 118.2$ s. These radio flux pulsations are unique among white dwarfs and white dwarf binaries, as isolated white dwarfs and white dwarf binaries are not expected to produce pulsed radio emission (e.g., Barrett et al., 2017; Wickramasinghe & Ferrario, 2000).

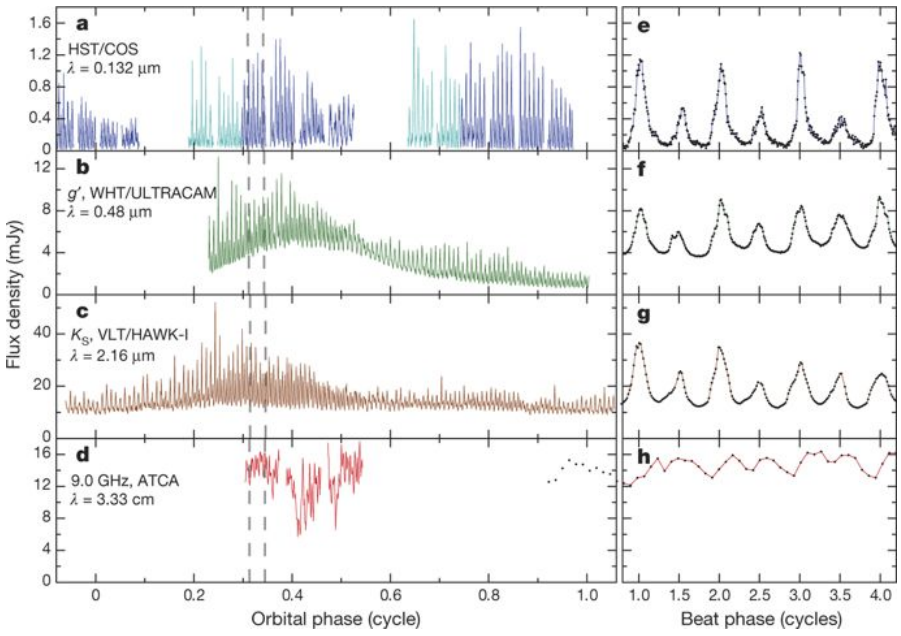

Figure 2.6: High-speed ultraviolet (a), optical (b), IR (c) and radio (d) flux measurements of AR Sco plotted against the orbital phase. An expanded view (e-h) of sections of similar orbital phases (grey dashed line markers in a–d), are plotted against the beat pulsation phase. Black dots represents individual measurements. None of the four sets of data were taken simultaneously in time. The different colours indicate that the data were taken in different orbital cycles. Adopted from Marsh et al. (2016).

Radio emission was detected at 9 GHz with flux densities ranging between 6-17 mJy (see Fig. 2.6). This is very similar to that of AE Aqr which at a similar frequency was observed to vary from 3-17 mJy (during a multi-wavelength

campaign by Mauche et al. 2012). AR Sco's IR and radio pulsations of the M-dwarf in particular are orders of magnitude brighter than the thermal Planck brightness spectra of its component star (see Fig. 1.2 in Chapter 1), where the SED between radio and IR represents a typical self-absorbed synchrotron spectrum ($\nu I_\nu \propto \nu^\alpha$), with a power-law slope of $\alpha \sim 1.3$. The ATCA data used in the discovery paper, however, were too short in duration to test whether the radio emission in AR Sco is also affected by the binary orbit.

Follow-up radio observations were made by Marcote et al. (2017) to confirm the nature of AR Sco's radio emission. It was speculated that most of the emission come from or near the M-dwarf, however it is not clear how the energy is transferred from the white dwarf to the M-dwarf. Very long baseline interferometric radio observations were made to investigate two competing scenarios by Marsh et al. (2016) for AR Sco (to explain its emission), i.e. collimated fast particle outflows, and/or direct interactions between the magnetospheres of the white dwarf and the M-dwarf in particular, e.g., heating and ionization of the inner face of the secondary star due to magnetic reconnection (Garnavich et al., 2019).

Observations were made at 8.4 GHz using the Australian Long Baseline Array (LBA) and AR Sco was found to be unresolved on milli-arcsecond scales at a flux density of 6.5 $\pm$ 0.7 mJy, (Marcote et al., 2017). AR Sco shows (Fig. 2.7) a compatible flux density of $\sim$ 6.5 mJy in both the ATCA and LBA data at a 2σ level, implying that there is no significant flux lost. These observations support the idea, suggested by Marsh et al. (2016), that most of the radio emission can be produced from a compact region near the white dwarf or close to the surface of the M-dwarf star. It is argued by Marcote et al. (2017) that if the energy transport between the white dwarf and the secondary M-dwarf is via collimated jets (Marsh et al., 2016), then either the jet does not contribute significantly to the generated flux from the system or alternatively there is no jet and the energy flow is supported through a magnetic interaction close to the M-dwarf. The latter

is suggested to be the most probable explanation due to there being no evidence of radio outflow observed within the LBA data.

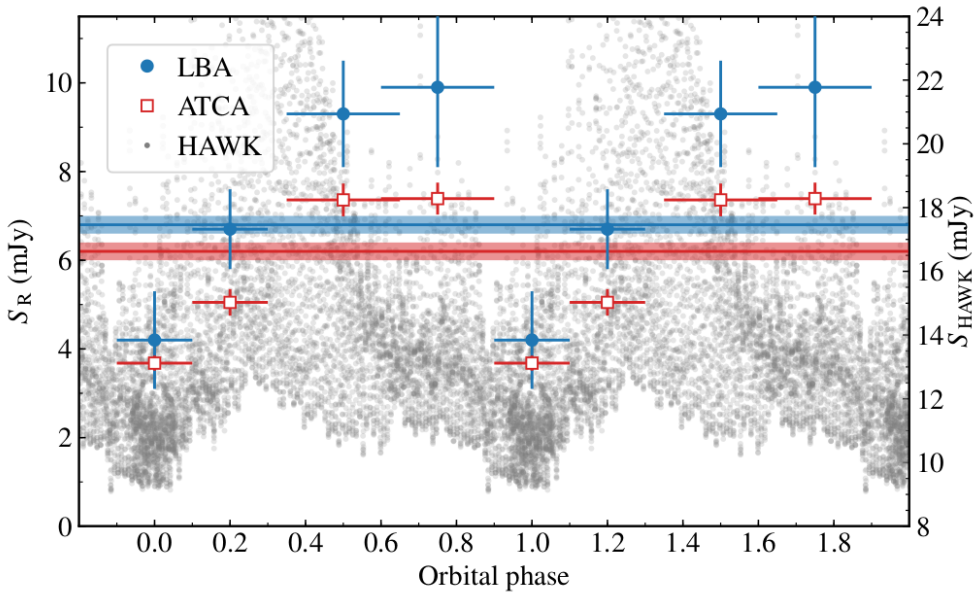

Figure 2.7: Radio light curves of AR Sco using the ATCA and LBA data at 8.5 GHz, along with VLT HAWK data. Average flux densities obtained from the full observation are illustrated by the blue (LBA) and red (ATCA) horizontal lines. Fluxes at specific orbital phases have been obtained by splitting the observation and combining different orbital cycles. Adopted from Marcote et al. (2017).

Even though the radio observations presented by Marsh et al. (2016) confirmed the unusual nature of the source, it was not possible to constrain the orbital modulation due to the limiting single-hour observation at a low spatial resolution. Similarly, Marcote et al. (2017) were able to produce an orbital variation light curve using the VLBI, but it had neither the frequency range nor the time resolution to fully explore the properties of this source in the radio regime. Hence, high time resolution radio observations were made by Stanway et al. (2018) using the Karl G. Jansky VLA over the full 3.56 hour orbital period. Radio data centred around frequencies of 1.5 GHz (L band for 6 hours), 5 GHz (C band for 4 hours) and 9 GHz (X band for 4 hours) over the full 3.56 hr orbital period revealed strong beat-phase pulsations at 9 GHz, decreasing in strength with decreasing frequency.

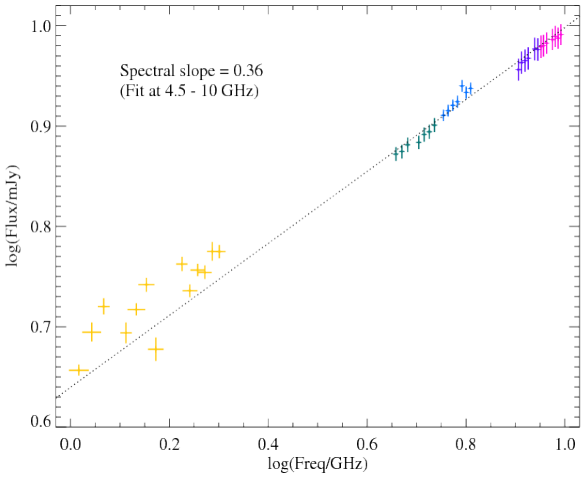

Figure 2.8: Radio SED of AR Sco, averaged over a full orbital period ($P_o = 3.56$ h). The dashed line indicates a spectral fit of the form $F_\nu \propto \nu^\alpha$, fitted to the data in the 5 GHz and 9 GHz bands, extrapolated to the 1.5 GHz band. The best fit is found at $\alpha = 0.358 \pm 0.015$. Adopted from Stanway et al. (2018).

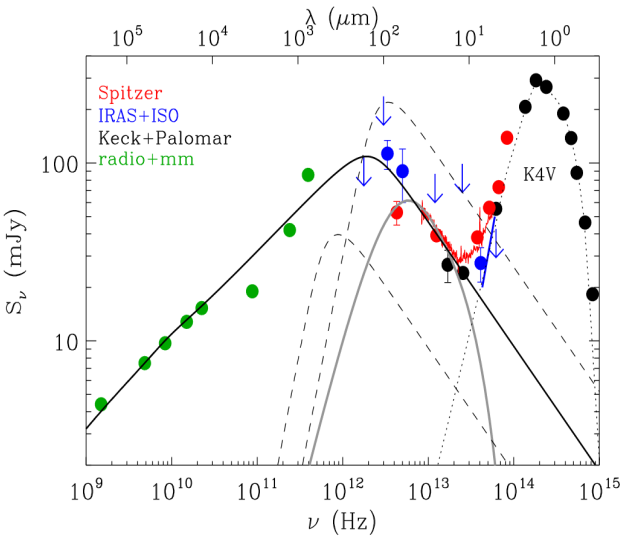

Figure 2.9: Overall spectral energy distribution of AE Aqr. Here, the green dots represents the observed radio spectrum. Adopted from Dubus et al. (2007).

A time-averaged SED (see Fig. 2.8), was generated over the full orbital period, where the data between 5 and 9 GHz are explained using a power-law SED ($F_\nu \propto \nu^\alpha$), with $\alpha = 0.358 \pm 0.015$. This time-average spectrum closely resembles the radio to IR spectrum in AE Aqr (see Fig. 2.9), which has been explained (e.g., Bastian et al., 1988; Dubus et al., 2007) as a superposition of synchrotron-emitting plasma blobs viewed in difference phases of their expansion as they evolve from being opaque to transparent as the plasma density decreases with increasing diameter. Due to the lower signal to noise in the 1.5 GHz band, these data were not used to constrain the power-law at higher frequencies. The 4-10 GHz power-law fit is similar in spectral slope to the observed flux variation extrapolated to both the 1.5 and 9 GHz bands. Radio observations also revealed a high non-relativistic circular polarization ($\sim 30\%$) component at lower frequencies, suggesting that the radio emission (1-10 GHz) arise close to the vicinity of the M-dwarf, as suggested by e.g., Garnavich et al. (2019); Marsh et al. (2016); Stanway et al. (2018).

2.3.2 Optical and UV observations

AR Sco's pulsating nature over its orbital period, was first explored in the optical part of the spectrum by Marsh et al. (2016). By using various telescopes, and 7 years of archival data from the Catalina Real Time Survey (CRTS), (Drake et al., 2009) to obtain data amplitude spectra, pulsed emission was observed showing the presence of two components of similar frequency as seen at radio frequencies, over the 3.56 h orbital period (see Fig. 2.10).

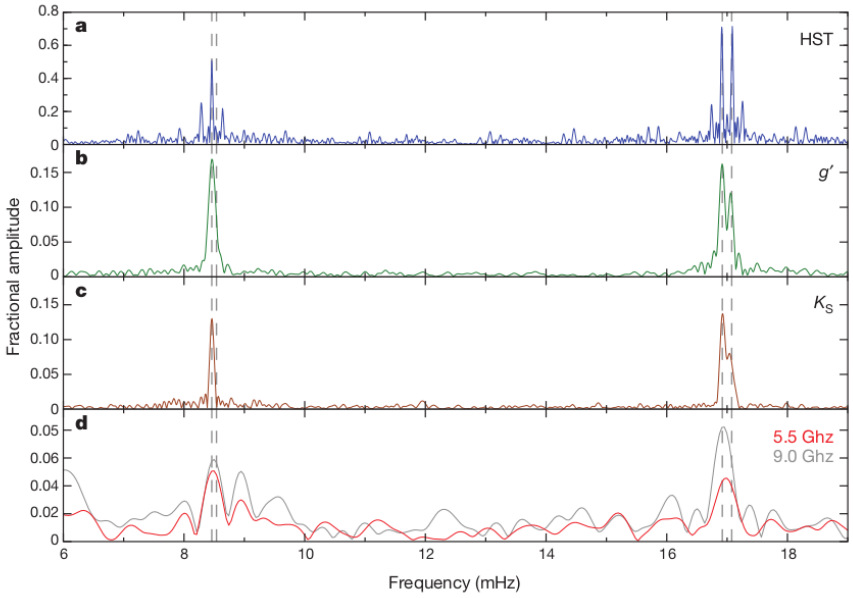

Figure 2.10: Periodograms obtained in ultraviolet (a), optical (b), IR (c) and radio fluxes (d), all revealing the strong double pulse beat period between the spin and orbital periods of the system. The beat (left-peak) and spin (right-peak) pulses are most prominent at the first harmonic, at approximately $\sim$ 17 mHz. UV data was obtained using HST. Optical data was obtained using WHT/ULTRACAM. IR was obtained using VLT/HAWK-I. Radio data was obtained using VLT. Adopted from Marsh et al. (2016).

The observed optical and radio bands show signals at both the spin period $P_s = 117$ s (higher frequency component) and its beat period $P_b = 118.2$ s (lower frequency component) with the orbital period of $\sim$ 3.5 hours. Repeatable spin, beat and orbital modulations were also reported by Potter & Buckley (2018a,b). The normalised phase separation between the two peaks are revealed to be $\sim$ 0.5 in the optical and UV bands, with a pulse fraction exceeding 95% in UV,

(Marsh et al., 2016). Littlefield et al. (2017) have also reported long-cadence optical photometry using archival Kepler data, showing aperiodic brightness fluctuations at the level of a few percent on a timescale of days, otherwise indicating that the overall brightness stays relatively stable.

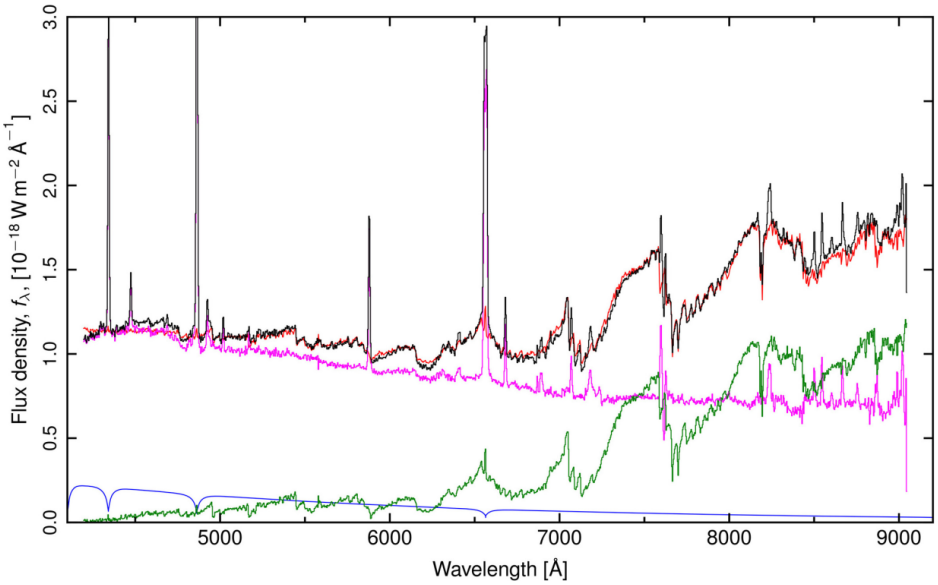

Figure 2.11: The optical spectrum of the M-dwarf companion star. A 10-min exposure of AR Sco wastaken with FORS on the Very Large Telscope (VLT) between orbital phases 0.848 and 0.895 (black). Other spectra include an optimally scaled template spectrum for the M5 companion (green), the sum of the template plus a fitted smooth spectrum (red) and AR Sco minus the template i.e. the extra light (magenta). Adopted from Marsh et al. (2016).

The optical and UV spectra (see Fig. 2.11) both show atomic emission lines that originate from the side of the M-dwarf's surface that faces the compact object (e.g. Garnavich et al. 2019; Marsh et al. 2016). The M-dwarf's radial velocity amplitude ($K_2 = 295 \pm 4$ km s^{-1}) sets a lower limit on the mass of its companion of $M_* >\sim 0.395 \pm 0.016\ M_\odot$. With a mass ratio of $q = \frac{M_2}{M_1} > 0.375$, (Marsh et al., 2016) the mass range placed on the two objects can be given as $0.81\ M_\odot < M_1 \leq 1.29\ M_\odot$ and $0.28\ M_\odot < M_2 \leq 0.45\ M_\odot$ (as mentioned before). AR Sco's optical magnitude varies by a factor of 20 in flux, ranging from 16.9 mag at its faintest to 13.6 mag at its maximum., with the combined luminosity of the stellar components estimated as $L_* \approx 4.4 \times 10^{31}$ erg s^{-1}.

Optical light curves over AR Sco's orbital period were obtained using data acquired at the University of the Free State (UFS)-Boyden Observatory outside of Bloemfontein, South Africa. The light curve (see Fig. 2.12) depicts the nature of the pulses as seen over the orbital period, possibly due to the interaction between the magnetosphere of the magnetic white dwarf and secondary companion star. The overall light curve shape is similar to that of Littlefield et al. (2017) and Stiller et al. (2018), where the light curve is asymmetric with a quick rise to a maximum brightness ($\phi \sim 0.4$) with an accompanying smaller peak ($\phi \sim 0.75$). See Fig. 2.13 of optical light curve from Stiller et al. (2018) for comparison.

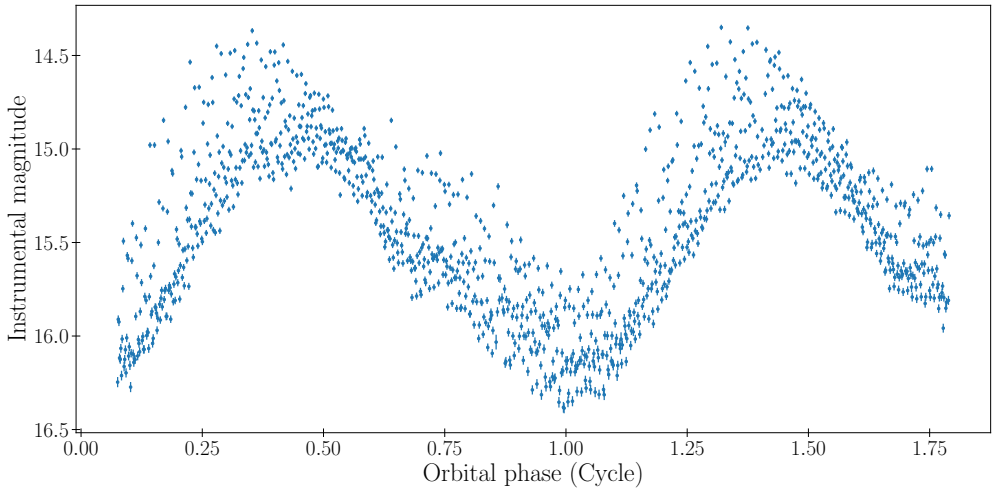

Figure 2.12: Ellipsoidal variation can be seen in this optical light curve over the 1.75 phase orbital period of AR Sco, using the UFS-Boyden 1.5 m telescope equipped with an Apogee U55 Charged Coupled Device (CCD) camera at the Boyden Observatory outside Bloemfontein, South Africa. Observation were made on the 24th of June 2016 using a Clear filter, courtesy of Ms. Helene Szegedi.

A smaller time interval light curve, focused on the spin period of the white dwarf (see Fig. 2.14), was also produced to investigate the pulsed nature of the spinning white dwarf. These pulsation suggest that the white dwarf is spinning around its own axis as seen from the line-of-sight to the observer. The double pulse profile may also be explained emission due to consequential pumping of material towards the secondary through either collimated jets from both polar caps

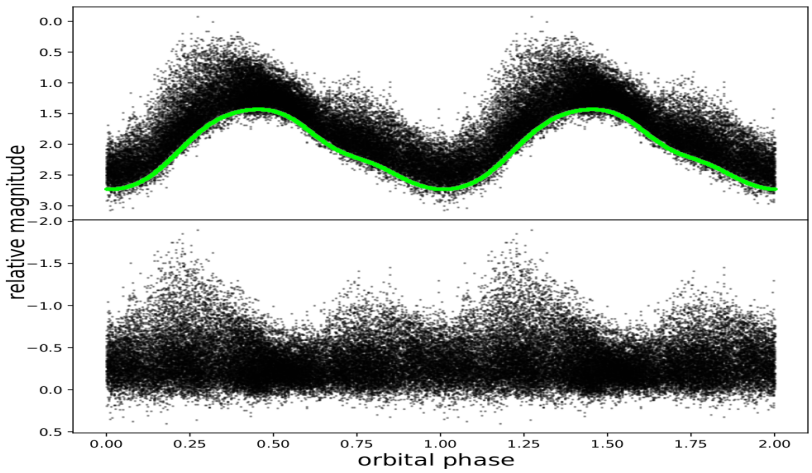

Figure 2.13: Optical light curve of AR Sco phased on the system's orbital period. The green line represents the orbital modulation in the absence of pulsations. Bottom: Residuals after subtraction of the orbital modulation. The amplitude of the pulsed variation peaks at orbital phases $\phi \sim 0.4$ and $\phi \sim 0.75$. Adopted from Stiller et al. (2018).

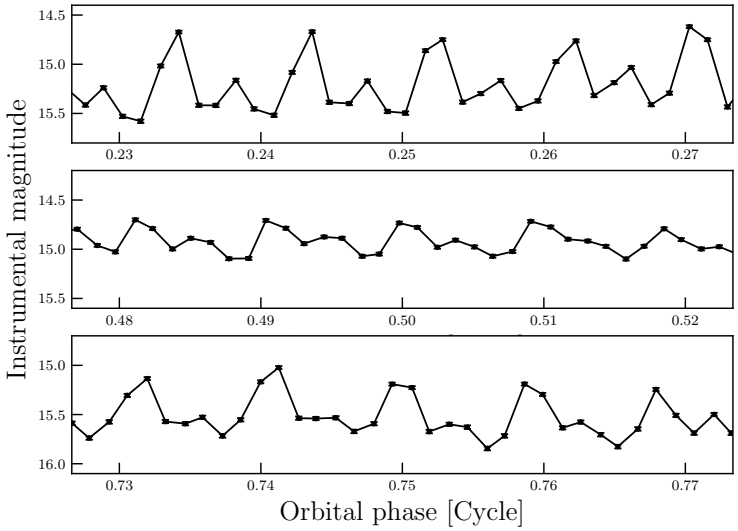

Figure 2.14: Low time resolution optical light curve obtained using an Apogee U55 CCD camera mounted on the UFS-Boyden 1.5 m telescope at the Boyden Observatory outside Bloemfontein, South Africa, showing a strong double-peaked pulsed emission profile close to the spin period of the white dwarf, suggesting that both polar caps of the magnetic white dwarf interact with the secondary or that both caps are visible to the observer. Data courtesy of Ms. Helene Szegedi.

of the spinning white dwarf as it sweeps past the secondary, or magnetospheric interactions between the M-dwarf and the primary white dwarf, as speculated by Geng et al. (2016); Marsh et al. (2016).

In the UV band similar features can be found in the pulse profile, which is also composed of a prominent first peak with a second smaller peak with a phase separation of ~ 0.5 in the beat phase (Takata et al., 2018), consistent with the results obtained by Marsh et al. (2016) in the optical/UV bands.

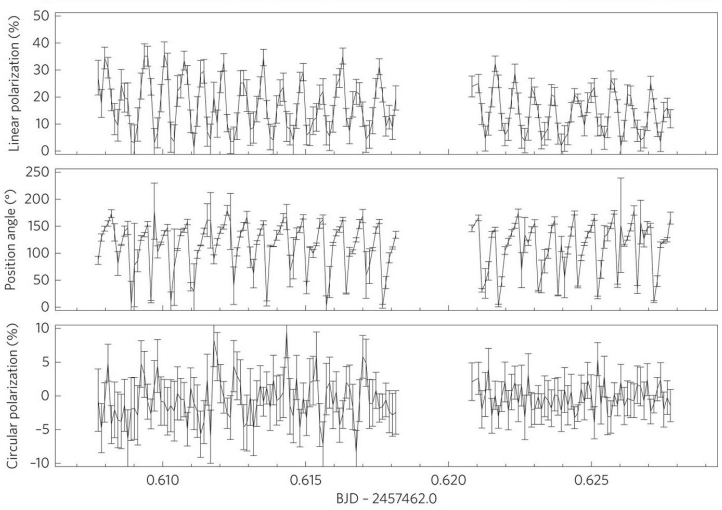

Figure 2.15: Time series polarimetry where the degree of linear polarization, position angle of linear polarization and degree of circular polarization (V/I) are respectively shown, all with 10 s bins. Adopted from Buckley et al. (2017).

Optical polarimetry studies performed by Buckley et al. (2017), by means of high speed all-Stokes optical polarimetry using the HIgh speed Photo-POlarimeter (HIPPO) polarimeter on the South African Astronomical Observatory (SAAO) 1.9 m telescope located at Sutherland, South Africa, revealed high levels of linearly polarized ($\sim 40\%$) emission and weakly circular polarized emission (up to a few percent), see Fig. 2.15. The degree of linear polarization shows pulse fractions of up to 90%, in contrast with the relatively low level of circular polarization (few percent).

The polarimetry data were also subjected to period analyses where power spectra (see Fig. 2.16) were produced for the Stokes U and Q parameters along with the total polarized intensity amplitude. These results show power from both the spin (ω) and beat ($\omega - \Omega$) frequencies, as well as strong modulation from the first harmonic of the spin period. This implies that polarized emission is seen

from both magnetic poles, suggesting that the bipolar outflow of charged particles confined by the magnetic field of the white dwarf emits strong linearly polarized synchrotron emission.

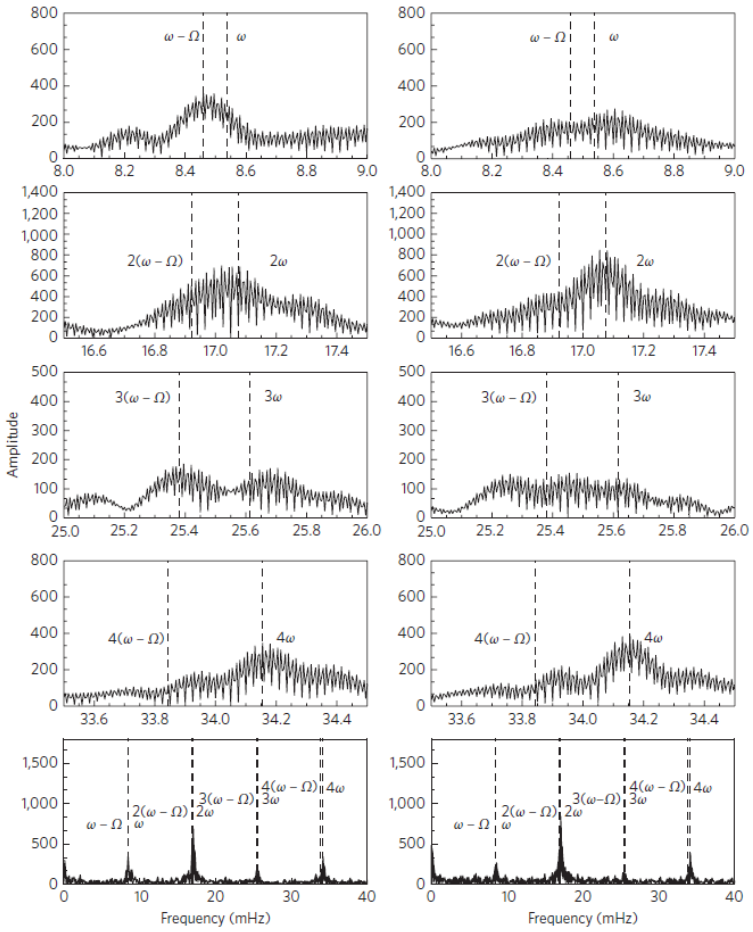

Figure 2.16: Polarization periodograms showing amplitude spectra of the Stokes U (left) and Q (right) parameters of HIPPO data. The dashed vertical lines denotes the beat and spin frequencies. Adopted from Buckley et al. (2017).

The high level of linear polarization compared to the lower level of circular polarization, is characteristic of synchrotron emission. AR Sco's linear polarization is also much higher than that previously detected in other IPs (e.g., Butters et al., 2009; Potter et al., 2012), where they are predominately circular polarized due to cyclotron emission from the accreting magnetic white dwarf.

The polarized emission also appears to be repeating over multiple orbits (Potter & Buckley, 2018b), specifically the amplitudes of the polarized spin and beat pulses modulated over the orbital period. These authors also presented a model in an attempt to explain the modulation of the polarized emission. In this model it is assumed that the observed polarized emission emanates from both magnetic poles of the spinning white dwarf (e.g., Buckley et al., 2017), where the spin pulses are modulated as a function of the relative angle between the magnetic poles and the secondary, resulting in larger spin pulses at certain orbital phases.

2.3.3 X-ray observations

Since the broadband spectrum from radio to optical appears to be non-thermal in nature (Buckley et al., 2017; Marsh et al., 2016), suggesting particle acceleration from relativistic electrons, further investigation to search for pulsed X-ray emission, in correlation with pulsed radio and optical emission, is thus very important. Marsh et al. (2016) estimated that AR Sco's X-ray luminosity, $L_{\rm X} \approx 4.9 \times 10^{23}$ W, is only 4% of the optical luminosity. This, along with the spectroscopic observations by Marsh et al. (2016), implies that there is little or no accretion in the system.

Thus, it is suggested that the white dwarf in AR Sco must have been spun-up by another process, or that an accretion disc was present at some stage in AR Sco's evolution (Meintjes, 2017). The ratio of X-ray luminosity to spin-down power for AR Sco is given as $L_{\rm X} \sim 10^{-3} L_{s-d}$, implying that most of the luminosity of the system is not produced by accretion of matter, but by spin-down energy loss, just as in spin-down powered pulsars (e.g., Buckley et al. (2017) and references therein).

The first in-depth observations in terms of non-thermal radiation at X-ray energies were done by Takata et al. (2018) to determine the origin of the X-ray emission using XMM-Newton data. These X-ray observations were taken over two orbits and revealed that the X-ray emission is significantly modulated over the orbital period (see Fig. 2.17), revealing that the emission region is comparable to

the size of the binary system.

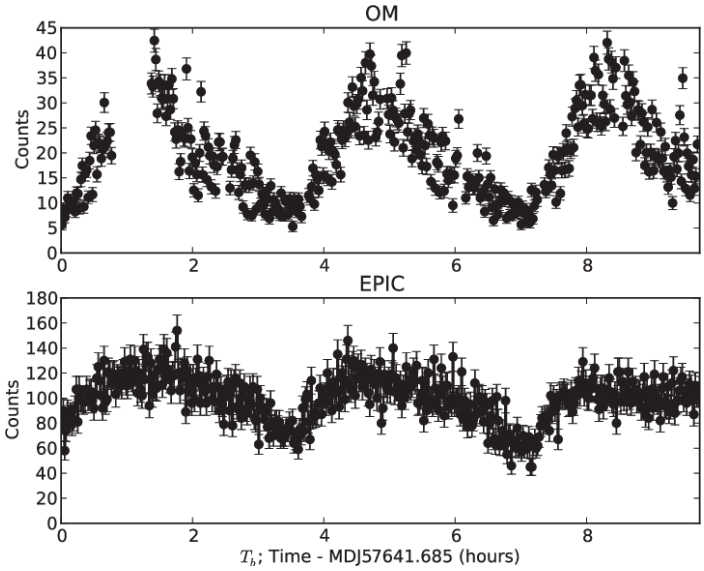

Figure 2.17: X-ray light curve of OM (top) and EPIC (bottom) data after background subtractions, showing an 80 second timing resolution. Here, similar ellipsoidal variation and orbital features can be seen as in radio and optical over AR Sco's orbital period. Adopted from Takata et al. (2018)

Takata et al. (2018) also showed a significant peak at the beat frequency in Lomb-Scargle periodograms (see Fig. 2.18) of data obtained from the Optical/UV Monitor (OM) and European Photon Imaging Camera (EPIC) based on the ephemeris of Marsh et al. (2016), suggesting significant detection of pulsed X-ray emission. A detailed phase-resolved analysis revealed that the pulse profile in the soft X-ray band (0.15-2 keV) is similar to that obtained in UV (Takata et al., 2018), suggesting that the pulsed emission in these two bands is probably non-thermal and produced by the same population of particles.

The broadband SED (see Fig. 2.19) shows a spectrum which resembles a power-law model with a photon index of $\Gamma = 2.3 \pm 0.5$ at an X-ray flux level of $F_{\rm X} = 3.7 \pm 0.65 \times 10^{-13}$ erg cm^{-2} s^{-1} in the 0.15-2 keV range[5]. It is speculated that most of the X-ray emission is produced by thermal plasma which is heated up to several keV, accelerating electron to relativistic speeds Takata et al. (2018).

[5]The flux value obtained is comparable to that estimated by Marsh et al. (2016).

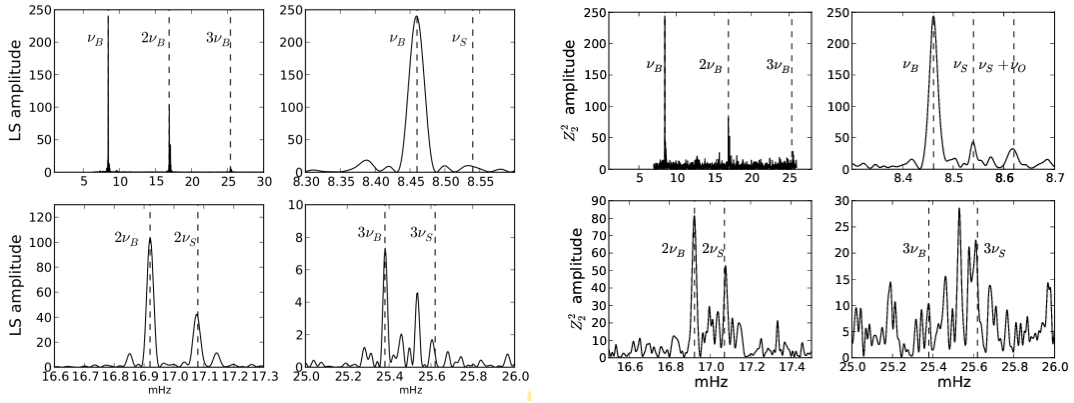

(a) OM data. (b) EPIC data.

Figure 2.18: Lomb Scargle periodograms of OM and EPIC data respectively with dashed vertical lines showing the beat frequency, spin frequency and their harmonics. Adopted from Takata et al. (2018).

Also, since there is no evidence of an accretion column, an alternative plausible process may be magnetic interaction between the white dwarf and M-dwarf, where a magnetic dissipation process heats up and accelerates the plasma on the M-dwarf surface, as suggested by Garnavich et al. (2019). When the white dwarf's magnetic field lines sweep past the M-dwarf, magnetic energy from the white dwarf will be actively used to accelerate electrons (e.g., Geng et al., 2016), which will be radiated away by synchrotron emission, peaking in the IR/optical band of the spectrum. Proposed theoretical non-thermal emission models will be discussed in more detail in Chapter 3.

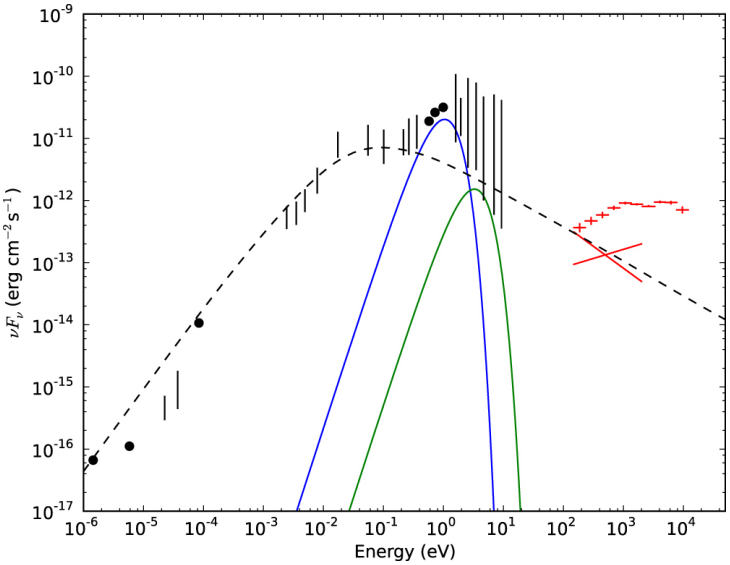

Figure 2.19: Broadband SED of AR Sco with the dashed line showing the model spectrum of the synchrotron emission by means of a power-law particle spectrum with an index of the injected electrons of $p = 3$. The red crosses and lines represent the spectrum of the time average and of the pulsed component respectively. Adopted from Takata et al. (2018).

Chapter 3

Non-Thermal Radiative Processes in AR Sco

3.1 Introduction

AR Sco's unique emission features complicate its classification. The fact that this low-mass binary system exhibits observational evidence of non-thermal-like emission over most of the electromagnetic spectrum implies that this system must be a source where particles can be accelerated to relativistic energies through various mechanisms, with strong evidence suggesting pulsar-like synchrotron emission, (e.g., Buckley et al., 2017; Singh et al., 2020; Takata et al., 2018). Other non-thermal emission mechanisms that may produce γ-rays within AR Sco, include inverse-Compton (IC) radiation, interactions between particle pairs and/or decay of radioactive material in the form of π°-decay. These mechanisms, along with no clear evidence of accretion (e.g., Marsh et al., 2016) distinguishes AR Sco from classical accretion-driven close binary CVs. Thus, by exploring these mechanisms combined with AR Sco's observed features, theoretical models for AR Sco can be developed in an attempt to explain the system's enigmatic emission features and expand its broadband spectrum predictions to higher energies.

In this chapter a discussion will follow on theoretical models presented to explain AR Sco's multi-wavelength non-thermal radiation, primarily focusing on the models of Geng et al. (2016); Takata et al. (2017) and Bednarek (2018). The discussion will include the investigation of acceleration processes that can produce relativistic particles and pulsar-like scenarios from the highly magnetic white dwarf in AR Sco. A general theoretical discussion of relativistic kinematics and non-thermal radiation is presented in Appendix A. In the following section a brief overview will be presented of models that were proposed to explore the enigmatic multi-wavelength properties of AR Sco.

3.2 Non-thermal models

3.2.1 Perpendicular rotator (bow shock)

The first non-thermal model of AR Sco was proposed by Geng et al. (2016) who theorise that the white dwarf in AR Sco is a nearly perpendicular rotator (the angle between the spin and magnetic axes is $\theta \sim 90°$), where both open and closed field lines of the white dwarf periodically sweep past the secondary M-dwarf's stellar wind. The interaction between the particle beam streaming out from the white dwarf's open field line regions and the M-dwarf wind will result in the formation of a "bow shock" which propagates into the M-dwarf's stellar wind, accelerating electrons to relativistic energies. See Fig. 3.1 for an illustration of the geometry of the proposed model.

Here, the accelerated electrons that are trapped within the magnetosphere of the white dwarf can give rise to synchrotron radiation in the magnetosphere. The open field lines of the white dwarf will then be forced out/open by the ram pressure of the stellar wind at the moment when they sweep past the M-dwarf wind. As the polar cap of the white dwarf faces the centre of the M-dwarf, the opening angle of the open field lines reaches a maximum value, consequently resulting in peak

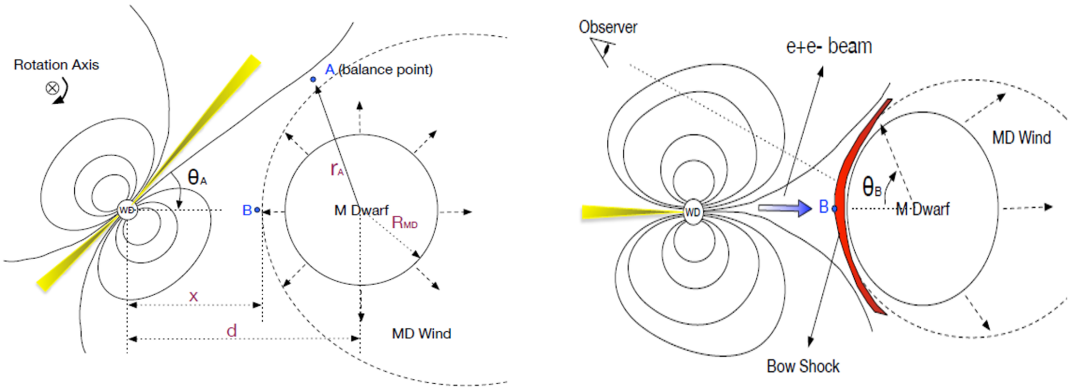

Figure 3.1: Schematic illustrations of the white dwarf/M-dwarf binary in AR Sco. The left panel shows a scenario where emission begins to rise as the open field lines start to sweep past the M-dwarf wind. The right panel shows a scenario when the emission reaches peak emission. In this illustration, the rotation axis of the white dwarf points into the plane of the page, while the orbital plane and the line of sight are on/in the page plane. Adapted from Geng et al. (2016).

luminosity value (see position B in Fig. 3.1). During this period the magnetic field strength will also change, reaching a maximum magnetic field strength of $B \simeq 1860$G at the maximum orientation at point B, with an average magnetic field strength between points A and B estimated to be $(B_{\rm A} + B_{\rm B})/2 \approx 1200$ G.

It is speculated that the resulting synchrotron emitting electrons come from the M-dwarf wind and not the white dwarf itself (Geng et al., 2016). The reason being that the estimated electron density at the observed peak flux density (Continue with sentence. Not sure what is meant with this?), $F_{\nu,\rm peak}$, i.e.

$$n_e \simeq 3.5 \times 10^8 \left(\frac{F_{\nu,\rm peak}}{1.6 \times 10^{-24}\ \rm erg\ cm^{-2}\ s^{-1}\ Hz^{-1}} \right) \rm cm^{-3}, \tag{3.1}$$

is significantly larger than the electron number density of the white dwarf wind at position B that can sustain a (co-rotating magnetosphere/vacuum) necessary for a pulsar-like acceleration process, (Goldreich & Julian, 1969), which is defined as

$$n_{\rm GJ} = \frac{\Omega \cdot B_{\rm B}}{2\pi q_e c} = 1.1 \text{ cm}^{-3} \left(\frac{\Omega_{\rm WD}}{117 \text{ s}}\right)^{-1} \left(\frac{B_{\rm B}}{1860 \text{ G}}\right), \tag{3.2}$$

where $B_{\rm B}$ is the magnetic field at position B. It is however assumed that the possibility exist that the emitting electrons come from the stellar wind of the MD. In order to interpret the observed SED, the required electron number density is too high for a WD wind. Rather electrons are accelerated by a "bow shock" into the MD wind and can produce the right amount of electrons to interpret both the shape and the normalization of the SED, as well as to produce the non-thermal emission. Hence, Geng et al. (2016) suggest that their model accounts for almost all of the observational properties detected by Marsh et al. (2016), in which AR Sco needs to be a nearly perpendicular rotator for electrons to be accelerated by the "bow shock" into the M-dwarf wind.

3.2.2 Magnetic mirror effect

In contrast to the model developed by Geng et al. (2016), the non-thermal theoretical model developed by Takata et al. (2017) suggests the possibility of relativistic electrons that are trapped in the closed magnetic field lines of the white dwarf by means of the magnetic mirror effect[1] (e.g., Parker, 1976; Spitzer, 1956). Observations show that the white dwarf's magnetic field lines sweep past the companion star periodically, where the magnetic field strength of the white dwarf at the M-dwarf's surface is estimated to be of the order $B_{\rm WD} \sim 195$ G, (Takata et al., 2017). Modulations of the optical emission at the orbital period suggest that the spinning of the M-dwarf is synchronised with the orbital motion. It has been shown that rapidly spinning M-dwarfs can generate magnetic fields through a stellar dynamo process, which can generate a polar magnetic field of several kG (e.g., Meintjes & Jurua, 2006).

[1]See Appendix A.2 for a more detailed discussion on the magnetic mirror effect.

Since the light cylinder of the white dwarf is larger than the binary separation of the system (Marsh et al., 2016), the M-dwarf's magnetosphere will interact with the closed magnetic field lines of the white dwarf. The magnetic interaction between the white dwarf and the M-dwarf will then cause magnetic reconnection, where the dissipated magnetic energy will cause the M-dwarf surface to heat up, accelerating electrons and producing an outflow from the M-star. The magnetic dissipation will have an estimated power of:

$$\begin{aligned} L_B &= \frac{\eta B^2}{8\pi}(4\pi R_2^3 \delta)\Omega_{\rm WD} \\ &\approx 2.8 \times 10^{32}\,{\rm erg\,s^{-1}} \left(\frac{P_{\rm WD}}{117\ {\rm s}}\right)^{-1} \left(\frac{R_2}{3\times 10^{10}\ {\rm cm}}\right), \end{aligned} \tag{3.3}$$

where $\Omega_{\rm WD} = 2\pi/P_{\rm WD}$, and R_2 is the radius of the M-dwarf.

The magnetic interaction on the companion star surface may eventually cause matter to be stripped from the M-star's surface, which can also accelerate electrons to relativistic energies. This ablation of the companion star by the magnetic field of the white dwarf can only occur if the binary separation is small enough so that an electromagnetic energy deposition in the envelope of the stellar surface is high. This phenomenon is a common process in Neutron Star (NS) pulsars and low-mass companion star binaries (Roberts, 2013). It has been observed in these NS systems that most of this deposited energy in the stellar surface is converted into the heating of the companion star's surface or resulting non-thermal radiation (e.g., Cheng, 1989; van den Heuvel & van Paradijs, 1988).

Takata et al. (2017) makes the assumption that most of the dissipated magnetic energy can be used to accelerate electrons and/or the heating of the companion star. This leads to an estimated Lorentz factor of the accelerated electrons of

$$\gamma_0 = \frac{m_p v_{esc}^2}{2\chi m_e c^2} \sim 50 \left(\frac{\chi}{5\times 10^{-5}}\right)^{-1} \left(\frac{v_{esc}}{5\times 10^7 {\rm cm/s}}\right), \tag{3.4}$$

where χ is the efficiency factor for converting the dissipated energy into kinetic energy and $v_{esc} = \sqrt{2GM_2/R_2}$ is the escape velocity of the particles, with $M_2 \sim 0.3\ M_\odot$ being the mass of the companion star[2]. Here $\chi = 5 \times 10^{-5}$ is chosen to fit the observed luminosity of the SED in AR Sco. Since AR Sco emits in the X-ray band as well, it indicates that the dissipated electrons from the M-dwarf with Lorentz factor larger than $\gamma_0 \sim 50$ exist in the magnetosphere of the white dwarf. It is assumed that the accelerated electrons follow a power-law distribution, i.e.

$$\frac{dN(E)}{dE} = N_0 \gamma^{-p}, \quad \gamma_0 \leq \gamma \leq \gamma_{\max} \tag{3.5}$$

over several decades of energy, yielding a maximum Lorentz factor of $\gamma_{\max} \sim 8 \times 10^6$, (Takata et al., 2017). To explain the X-ray emission, the authors assume a process related to the magnetic dissipation on the M-dwarf's surface which accelerates the electrons to relativistic velocities to form the power-law distribution.

After sweeping past the M-dwarf's surface, the white dwarf magnetic field lines will remain closed, trapping injected electrons in the closed magnetic field lines by means of the magnetic mirror effect, where the electrons move along the magnetic field lines (similar to the Van Allen radiation belts of the Earth). Electrons are injected towards the white dwarf's surface from the M-dwarf with an almost constant Lorentz factor Takata et al. (2017). Since the electrons travel in the closed magnetic field lines, they eventually moves towards the white dwarfs surface at the other hemisphere. These electrons are then reflected back by the magnetic mirror effect. In this model, at least, it is speculated that most of the energy from the electrons are radiated away at the first magnetic mirror point through synchrotron emission, and that the emission from the first magnetic mirror point mainly contributes to the observed pulsed emission and formation of the double-peaked structure in the light curves, assuming that the white dwarf is an inclined rotator with the dipole magnetic field.

[2]See Takata et al. (2017) for a more detailed discussion.

3.2.3 Hadronic scenarios

Another approach in explaining the non-thermal emission for AR Sco considering different scenarios of hadronic interactions have also been developed by Bednarek (2018). As discussed previously, Geng et al. (2016) postulates that most of the emission can be explained by means of a synchrotron process from relativistic electrons during the interaction with the white dwarf's magnetosphere and wind from the companion star, where the white dwarf injects a magnetised plasma towards the M-dwarf producing a "bow shock". Alternatively, Katz (2017) suggests that the spin-down power is dissipated by the direct interaction of the white dwarf's magnetic field with dense matter from the M-dwarf's atmosphere. This can cause particles to be accelerated in a turbulent collision region either by the magnetic reconnection and/or a Fermi acceleration mechanism.

In the model presented by Bednarek (2018), it is hypothesised that electrons and hadrons can be accelerated to multi-TeV energies in the strongly magnetised, turbulent regions formed at the point where the rotating white dwarf magnetosphere interact strongly with the dense atmosphere of the M-dwarf close to the stellar surface, as suggested by the above-mentioned authors (Geng et al., 2016; Katz, 2017). In this scenario the possibility is high for relativistic protons to find enough target material for efficient interaction. As a result of proton-proton interactions the production of secondary $e^{\pm}$ (electron-positron) pairs, neutrino pairs (ν_e, ν_μ) and high-energy γ-rays from decay of neutral pions (π^0) becomes a distinct possibility[3].

It is assumed that in these turbulent magnetized regions, electrons and hadrons can be accelerated by Fermi acceleration mechanisms and possibly by magnetic reconnection at the collision region between the white dwarf and M-dwarf. However, it is not yet clear if the accelerated electrons are secondary products from other processes or whether they are accelerated directly into the turbulent collision re-

[3]See Appendix A.6 for a discussion on $\pi^0 -$ decay.

gion between the M-dwarf atmosphere and white dwarf's magnetosphere. Hence, Bednarek (2018) suggests that the observed non-thermal X-ray emission detected by Takata et al. (2018) and possible γ-ray production can thus be explained by one of three scenarios:

In the first instance it is speculated that a hybrid (lepto-hadronic) scenario exists where both electrons and protons are accelerated. In this scenario the observed non-thermal X-ray emission can be explained by the synchrotron emission from the primary electrons in the strong magnetic field of the turbulent region[4], whereas the γ-rays originate from the decay of neutral pions, that are in turn produced by the protons during a single interaction with matter from the stellar atmosphere. See Fig. 3.2a for proposed synchrotron emission spectrum.

In the second scenario, the X-ray emission can be explained by the synchrotron emission of the primary electrons (and/or secondary $e^{\pm}$ pairs). But, the relativistic protons can also be accelerated in the turbulent region and subsequently transported to the dense region of the M-dwarf's atmosphere suffering complete cooling in the hadronic collisions. Hence they interact with the matter of the companion star's atmosphere to produce $e^{\pm}$ pairs and γ-rays from neutral pion decay. The synchrotron emission curves for these scenarios can be calculated (see in Fig. 3.2) from the proton-proton collision by-products, i.e., the secondary $e^{\pm}$ pairs, assuming that particles are produced in the pion decay that originated in a single interaction of protons (Fig. 3.2a) and in a complete cooling of protons in the hadronic collision (Fig. 3.2b), where the γ-ray fluxes are larger.

In the third scenario the assumption is made that only protons are efficiently accelerated. The non-thermal X-ray emission can then be explained by the synchrotron radiation from the secondary $e^{\pm}$ pairs, i.e., primary electrons are not accelerated to large energies in the turbulent region. The emission might also additionally be influenced by the absorption of γ-rays in the matter. In this scenario the γ-ray emission is shown in Fig. 3.2c, where it is expected to be well above the

[4]See Bednarek (2018) for a more detailed discussion.

Fermi-LAT and High Energy Stereoscopic System (H.E.S.S) sensitivity curves.

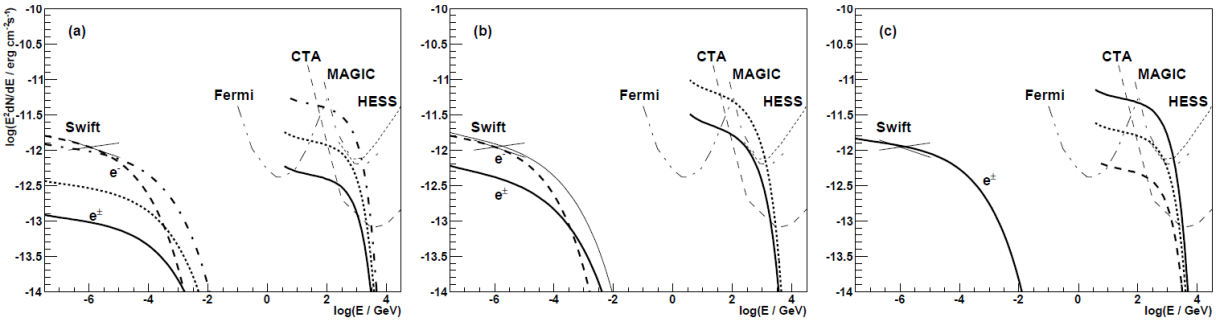

Figure 3.2: Proposed leptonic and hadronic scenarios for non-thermal emission in AR Sco (a) AR Sco's non-thermal X-ray spectrum (Marsh et al. (2016), thin solid lines) compared to the proposed synchrotron emission from primary electrons (e^-, dashed curves) and the synchrotron emission of the secondary $e^{\pm}$ pairs ($e^{\pm}$, solid curve). (b) same as in figure (a) but for the case of a complete cooling of relativistic protons in the interaction with matter. (c) A scenario where only protons are accelerated. It is proposed that the X-ray emission observed using *Swift* can be explained by the synchrotron emission from the secondary $e^{\pm}$ pairs from the decay of charged pions. In all three scenarios, the γ-ray emission is also compared to the sensitivity curves of *Fermi*-LAT (10 yrs, see dot-dot-dashed curve), the H.E.S.S. array (25 hrs, thin dotted curve) the MAGIC array (50 hrs, thin dot-dashed curve) and the future CTA array (50 hrs, thin dashed curve). Adopted form Bednarek (2018).

3.3 AR Sco as a pulsar-like emitter

Observational results from AR Sco suggest that it exhibits pulsed pulsar-like features. Pulsars are rapidly rotating, highly magnetised compact objects that are the remnants of supernovae explosions. Pulsars were first discovered by J. Bell and A. Hewish as rapidly "pulsating" radio sources, (Hewish et al., 1968). It was later pointed out by Gold (1968) that these pulsating radio sources were powered by an NS, and he proposed that what were originally thought to be periodic pulsations were in fact due to rapid rotations combined with a lighthouse effect. These observed "pulsations" are caused by the radio emission from the poles of the NS, where the emission is observed as short-period pulsations, which are detected when beams of radiation from the polar caps rotate through the line-of-sight of the observer.

These compact objects are normally associated with particle acceleration, where particles can be accelerated to relativistic velocities within the magnetosphere of the NS. This can produce pulsed emission from the polar caps (or higher up), mostly through the synchrotron process, where emission can be observed at different wavelengths. The most well-known pulsar is the Crab pulsar, which is an isolated young NS that emits electromagnetic radiation from radio to TeV energy bands (e.g., Kuiper et al., 2001). Gold (1968) also postulated the notion of a co-rotating magnetosphere in these systems and suggested that these sources are primarily spin-powered, spinning down due to its rotational energy being radiated away by relativistic particles.

It is hypothesised that AR Sco displays emission features similar to those of a pulsar. The double-peak structure of the pulse profile and the morphology of the linear polarization (Q and U variations) at optical wavelengths are similar to that of the Crab pulsar (Buckley et al., 2017). The observations made by these authors also support the notion that the pulsed luminosity of AR Sco is powered by the spin-down of the highly magnetic ($\leq$ 500 MG), rotating white dwarf similar to that of NS pulsars. Also, the modulation at the orbital period in the optical band, which reflects the heating of the dayside of the companion star by the interaction of the radiation from the white dwarf, is similar to that found in millisecond pulsar binaries (e.g., Fruchter et al., 1988).

The presence of the highly magnetic white dwarf in AR Sco provides an ideal environment for particle acceleration[5] within the magnetic field lines to produce the observed non-thermal emission, possibly through synchrotron radiation. The synchrotron power to spin-down power ration of AR Sco is estimated to be $P_{sync} \sim 0.06\ P_{sd}$, which is similar to the ratio of synchrotron-produced γ-ray emission to spin-down power as reported for a sample study of spun-up γ-ray emitting millisecond radio pulsars, (Abdo et al., 2010).

[5]See appendix A.2 for a discussion on particle acceleration.

The observed ratios of X-ray to spin-power luminosities for AR Sco and AE Aqr are very similar to those of spin-powered NS pulsars (Becker & Trumper, 1997). Assuming a 0.8 $M_{\odot}$ white dwarf primary, the spin-down luminosity in AR Sco is of the order $L_{\dot{\nu}_s} = 1.5 \times 10^{33}$ erg s^{-1}. With an X-ray luminosity of $L_{\rm X} = 4.9 \times 10^{30}$ erg s^{-1}, this implies a ratio of $\alpha = (L_{\rm X}/L_{\dot{\nu}_s}) = 3.27 \times 10^{-3}$ (e.g., Buckley et al. 2017; Marsh et al. 2016). This is very similar to ratios found in spin-powered pulsars, as well as the white dwarf in AE Aqr (Oruru & Meintjes, 2012), which has a similar ratio of $\alpha \sim 10^{-3}$. This places both these white dwarfs in the same class as spin-powered pulsars (see Fig. 3.3). This implies that the multi-frequency emission in both these systems are likely driven by the spin-down of the white dwarf and not by mass accretion from the secondary companion, making both of them analogous to spun-up radio pulsars.

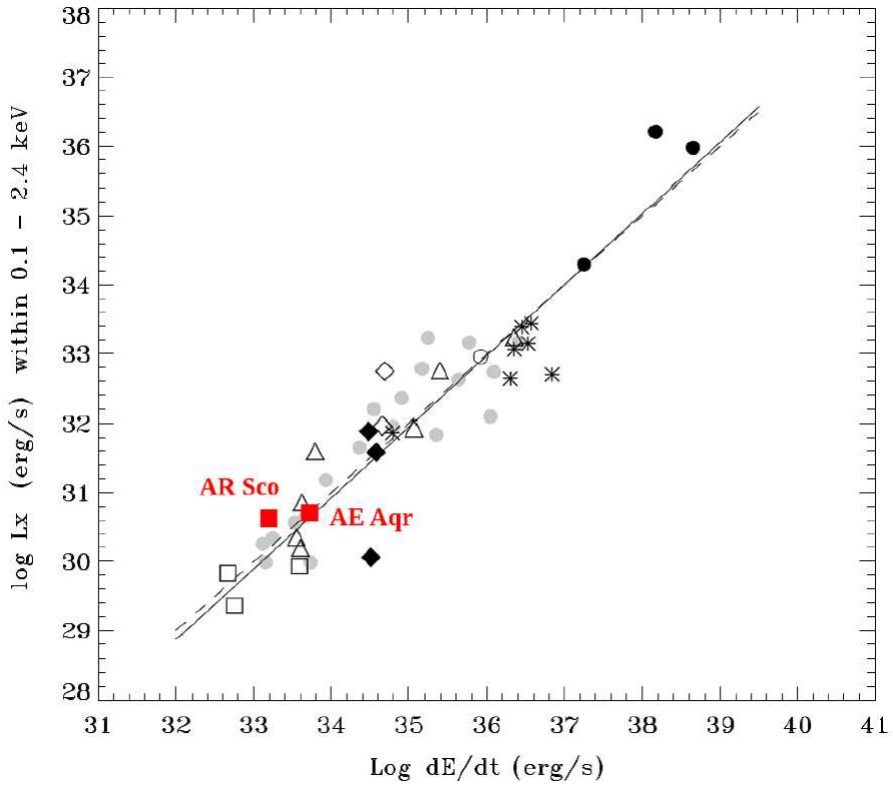

Figure 3.3: X-ray luminosity vs spin-down power of spin-powered NSs, compared to the white dwarfs in AR Sco and AE Aqr. Figure adapted by Meintjes (2018) from Becker & Trumper (1997).

The absence of accretion and consequently a conducting plasma allows for an estimated electrical potential of the order

$$\Delta V \sim 10^{12} \left(\frac{P_{\rm wd}}{117\ {\rm s}}\right)^{-5/2} \left(\frac{\mu}{8\times10^{34}\ {\rm G\ cm^3}}\right) \left(\frac{R_{\rm wd}}{5.5\times10^{8}\ {\rm cm}}\right)\ {\rm V} \tag{3.6}$$

to be induced between the white dwarf and the light cylinder (Buckley et al., 2017). In the above equation $P_{\rm wd}$ and $R_{\rm wd}$ represent the spin period and radius of the white dwarf respectively, with the magnetic moment defined by μ ($\mu = BR^3$ or $0.5BR^3$?). Since the electric field is several orders of magnitude stronger than the force of gravitation, charged particles such as electrons (and ions) can be pulled from the white dwarf's surface and accelerated to relativistic energies, of the order of $\gamma_e \approx 10^6$ (Buckley et al., 2017), resulting synchrotron emission frequencies of the order

$$\nu_{\rm sync} \leq 10^{18} \left(\frac{B_{l-c}}{0.4\ {\rm G}}\right) \left(\frac{\gamma_e}{10^6}\right)^2 {\rm Hz} \tag{3.7}$$

in the vicinity of the light cylinder, with peak emission at $\nu \approx 0.3\nu_{\rm sync} \approx 3\times10^{17}$ Hz in the soft X-ray regime of the spectrum (e.g., Buckley et al., 2017). Additionally, if the white dwarf is an oblique rotator, with the magnetic dipole tilted relative to the spin axis, the rotating magnetosphere is expected to produce a wavy relativistic outflowing Magnetohydrodynamic (MHD) wind outside the light cylinder, known as a "striped" wind (Coroniti, 1990; Meintjes, 2018), with alternating regions of opposite polarity resulting in additional particle acceleration through magnetic reconnection and associated pulsed polarised synchrotron emission. This process is currently being investigated in AR Sco (Ramamonjisoa et. al (in progress)). However, the non-thermal emission geometry have been investigated using a rotating vector model, where the model supports the scenario that the synchrotron emission originates close to the polar caps of the white dwarf

"pulsar" (e.g., du Plessis et al., 2022; Du Plessis et al., 2018)

Interaction between the fast rotating magnetosphere of the white dwarf and coronal fields of the magnetised secondary star can also generate field-aligned potentials to accelerate charged particles to high energies, (e.g., Haerendel, 1994). It can be shown, (Buckley et al., 2017), that the compression of the secondary star's coronal fields by the white dwarf field sweeping periodically across it can generate potentials of the order of

$$\Phi_{\parallel} \sim 200 \left(\frac{\Delta B_{\perp}}{700\ \mathrm{G}}\right)^{3} \left(\frac{n_e}{10^{10}\ \mathrm{cm}^{-3}}\right)^{-3/2} \left(\frac{T}{10^{4}\mathrm{K}}\right)^{-1/2} \mathrm{MV}. \tag{3.8}$$

Potentials of this magnitude can then accelerate charged particles like electrons to energies $\gamma_e \rightarrow 400$, which can result in synchrotron emission in average coronal fields of ~ 100 G to frequencies up to

$$\nu_{sync} \sim \gamma_e^2 e\ B/(2\pi m_e c) \leq 4 \times 10^{13} \left(\frac{\gamma_e}{400}\right) \left(\frac{B}{100\ \mathrm{G}}\right) \mathrm{Hz}, \tag{3.9}$$

which is in the IR regime where the observed spectrum peaks, $\nu S_{\nu} \propto \nu^{\alpha}$ ($\alpha \approx 0.3$; Buckley et al. (2017); Meintjes (2018)). The continuous pumping of the coronal loops may result in the generation of relativistic electron clouds trapped in the coronal fields, that may result in a superposition of synchrotron flares from these expanding clouds, similar to the radio flares seen in the nova-like variable AE Aqr (e.g., Bastian et al., 1988).

Takata et al. (2017) have also shown that by using a simple outer gap model (e.g., Cheng et al., 1986), particles can be accelerated to relativistic energies. The outer gap model assumes particle acceleration around the light cylinder and has been considered as the origin of observed GeV γ-ray emission from NS pulsars, (Abdo et al., 2013). In the outer gap model accelerated particles lose their energy through curvature radiation and the IC process[6].

[6]See Takata et al. (2017) for a more detailed discussion regarding the outer gap scenario applied to the white dwarf in AR Sco.

The models proposed by the above-mentioned authors all serve as viable scenarios where particles can be accelerated to relativistic energies to produce the observed non-thermal emission from AR Sco. Hence, exploring the γ-ray regime of AR Sco is essential to constrain possible mechanisms for the observed non-thermal emission of AR Sco at higher energies.

Chapter 4

High-energy *Fermi*-LAT Analyses

4.1 Introduction

The detected pulsed non-thermal emission from radio to X-ray characteristic of synchrotron radiation implying relativistic particle acceleration (e.g., Marsh et al. 2016; Takata et al. 2018), combined with the theories postulating high-energy γ-ray production within AR Sco (e.g., Bednarek 2018; Geng et al. 2016; Takata et al. 2017), generated interest to search for similar features above 100 MeV utilising publicly available archival data from *Fermi*-LAT.

By using recently upgraded *Fermi* software (Pass 8), along with updated Galactic diffuse and isotropic background models[1], a search for pulsed or continuum emission over a 10-year period could be conducted in an attempt to resolve and understand AR Sco's non-thermal emission features at higher energies. In this chapter a discussion will follow on the primary analyses methods used and results obtained using the recommended methods provided by the *Fermi* science support guides to perform likelihood tests and periodicity analyses on AR Sco above 100 MeV.

[1]Galactic diffuse background model version: `gll_iem_v07`
Isotropic background model version: `iso_P8R3_SOURCE_V3_v1`

4.2 *Fermi*-LAT telescope

The Large Area Telescope (LAT) on board the *Fermi* Gamma-ray Space Telescope (hereafter *Fermi*) has been in operation since August of 2008. It was first launched by NASA on 11 June 2008 aboard the Delta II heavy launch vehicle into a low-earth orbit (altitude of $\sim$ 550 km) where it allows for all-sky observations. The LAT is the primary instrument (see Fig. 4.1) aboard the *Fermi* telescope, which serves as an imaging, wide Field of View (FoV), high-energy γ-ray telescope covering an energy range from 20 MeV to more than 300 GeV (Abdollahi et al., 2020; Atwood et al., 2009). The telescope's wide FoV (2.4 str at 1 GeV) covers the entire γ-ray sky, ensuring all-sky coverage every 3 hours to allow for most γ-ray photons to be observed and used for energy measurement.

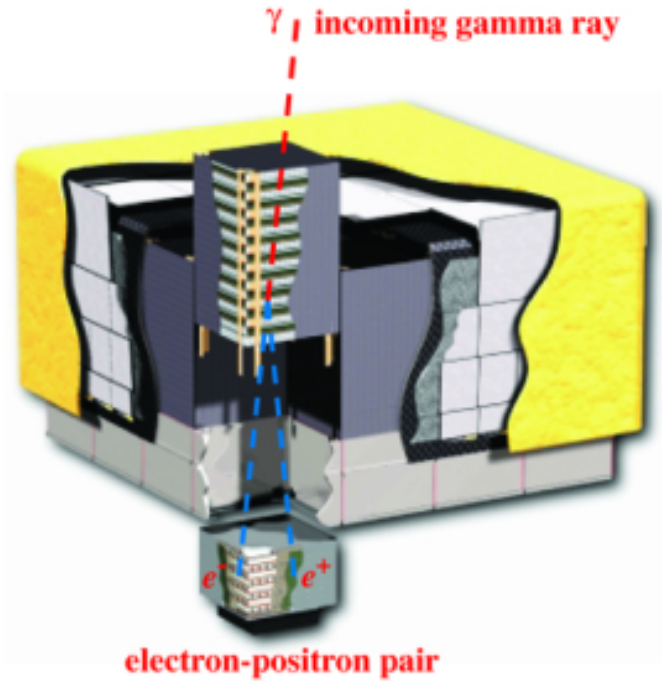

Figure 4.1: Illustration of the primary *Fermi* γ-ray detector, i.e., the LAT, which can detect γ-rays with energies ranging from 20 MeV to more than 300 GeV. Adopted from Atwood et al. (2009).

The technique used by *Fermi* for particle detection of lower-energy γ-ray photons (50 MeV to 300 GeV) includes the production of $e^{\pm}$-pairs through the interaction with metal. The primary γ-ray detector structure on the telescope consists of a cube-like detector surrounded by a segmented anticoincidence detector (ACD) that is used to identify and reject events triggered by background cosmic-rays, while maximising detected γ-ray events. The cube consists of a series of modular "towers" (4 x 4 array of modules with 18 tracking planes) made of thin layers of tungsten foil and silicon strip detectors. The progress of detected charged particles are tracked through the 18 alternating X and Y tracking planes, which helps with background cosmic-ray rejections. The tungsten foil is used to produce a $e^{\pm}$-pair when one of the tungsten atoms interacts with an incoming γ-ray. A caesium iodide (CsI) calorimeter (or scintillator) is then used to measure the total energy of the charged particle pair. The combined information from the ACD, silicon tracker and calorimeter is used to determine the direction and energy of the observed γ-ray[2]. Due to the LAT tracker's overall aspect ratio (height/width = 0.4) it ensures that nearly all pair-conversion events initiated in the tracker passes into the calorimeter for energy measurement.

The main objective of the *Fermi*-LAT telescope mission is to continuously survey the sky and detect high-energy γ-ray emission above the diffuse Galactic background. These efforts resulted in an extensive catalog of several thousand high-energy sources obtained from the *Fermi* mission[3]. With the LAT's larger effective area (~ 9500 cm^2) it is possible to detect more sources that could not be detected or identified by previous, phased-out γ-ray telescopes, e.g., the Energetic Gamma-ray Experimental Telescope (EGRET), which was *Fermi*'s predecessor and only had an effective area of ~ 1500 cm^2 (Mattox et al., 1996; Thompson et al., 1993). This makes *Fermi* more sensitive to detecting γ-ray sources, increasing the low energy sensitivity range of 30 MeV to 30 GeV using EGRET to a larger energy range of 20 MeV $-$ 1 TeV from *Fermi*.

[2]Refer to Atwood et al. (2009) and Ackermann et al. (2012) for a more detailed discussion regarding the *Fermi*-LAT instrumentation and technical specifications.
[3]Latest catalogue (4FGL) contains 5064 sources.

Other scientific goals set out by *Fermi* include, among other: determining the nature of unidentified sources and the origins of diffuse emission revealed by EGRET, understanding the mechanisms of particle acceleration operating in celestial sources, such as AGNs, pulsars and Supernovae Remnants (SNR) in particular, and understanding the high-energy behaviour of GRBs and transients (Abdollahi et al., 2020).

Both EGRET and *Fermi* have contributed significantly to our understanding of the high-energy universe and provided insights into Galactic and extragalactic γ-ray emission. For the past decade since its launch, *Fermi*-LAT has been primarily used in an all-sky survey mode to observe and detect nearby γ-ray sources. Over 5000 sources above a 4σ threshold has been detected, observed and listed in the 4FGL[4]. Relative to the previous Third *Fermi* Gamma-ray LAT Catalogue (3FGL), which lists 3033 sources, the 4FGL catalog (5064 sources) benefits from twice as much exposure time as well as a number of analysis improvements including an updated model for the Galactic diffuse background. This allows for more source detections in the broader energy regime ranging from 20 MeV - 1 TeV, relative to the initial 20 MeV - 300 GeV range (Abdollahi et al., 2020).

The initial Pass 6 iteration/data framework (e.g., Ackermann et al., 2012), has also been improved to the latest Pass 8 framework where improvements have been made in terms of energy resolution as well as better determination of the diffuse Galactic γ-ray emission (Abdollahi et al., 2020). Relative to the previous version used in the 3FGL catalog, i.e., Pass 7 P7REP data (Bregeon et al., 2013), the Pass 8 P8R3 (Bruel et al., 2018) data provide improved angular resolution above 3 GeV, a narrower Point Spread Function (PSF) at higher energies and about 20% more event acceptance at all energies (see Fig. 4.2). This makes future studies of fainter γ-ray sources, which are more difficult to detect, much more effective.

[4]Based on the first 8 years of data.

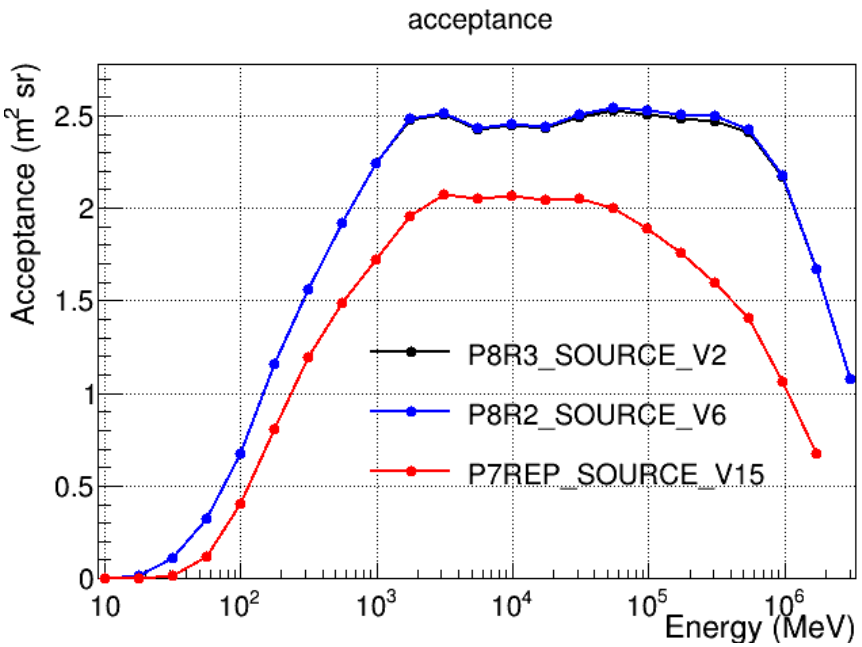

Figure 4.2: Diagram showing the comparison of photon acceptance per sr and energy between the *Fermi* Pass 8 and Pass 7 source event files. Adopted from `https://www.slac.stanford.edu/exp/glast/groups/canda/lat_Performance.htm`. Accessed 15/10/2021.

4.3 *Fermi*-LAT likelihood analysis

The analysis of LAT data begins with a list of counts, or photon events, detected by the LAT. These photon events are released to the public through the LAT data archive with the help of the *Fermi* Science Support Center (FSSC) at HEASARC[5]. The FSSC also provides suitable software tools and tutorials for reduction and analysis of LAT data[6]. A likelihood analysis of the photon events are done to determine whether a source exists above the *Fermi* threshold, and to find the best model fit parameters describing the source's spectrum and position. In this study, the first step was to inspect *Fermi*-LAT catalogs for any possible source detections in the region centred on AR Sco (RA:$16^h21^m47.28^s$, Dec:$-22°53'10.39''$, J2000). *Fermi* had a few notable sources close to the coordinates centred at AR Sco, with an un-associated source, 4FGL J1623.7-2315, being the closest (0.56°). Due

[5]`https://fermi.gsfc.nasa.gov/cgi-bin/ssc/LAT/LATDataQuery.cgi`. Accessed 15/10/2021
[6]`https://fermi.gsfc.nasa.gov/ssc/data/analysis/scitools/`. Accessed 15/10/2021

to *Fermi's* poor spatial resolution, especially at lower energies (0.6° at 1 GeV, Atwood et al. 2009), it cannot be confirmed that this source may indeed be AR Sco. Hence, after inspection, it was concluded that AR Sco is probably not listed in any of *Fermi*-LAT catalogs.

Thus, the next point of interest was the *Fermi* data archive where a *Fermi*-LAT dataset from the past decade (4 August 2008 - 18 March 2019) was extracted. The event files, i.e., the photon event files and spacecraft file, were chosen to have a Region of Interest (ROI) of 10° centred on AR Sco (RA: 245.447°, Dec:−22.886°, J2000, Decimal Equatorial) within the energy range of 100 MeV to 500 GeV. The spacecraft file contains the telescope telemetry data and is necessary to determine good time interval values required for barycentric corrections. From these extracted files the necessary procedures could be followed to perform a standard likelihood analysis centred on the position of AR Sco.

The analysis was performed using the recently released *Fermi*-Tools software, *Fermi/1.0.1*, in a Linux based `Fedora-MATE` system. A `python` environment (`python` 2.7) was chosen to do the analyses since the same likelihood analysis done using the standard command line tools can be done with more direct access to all of the model parameters in the `python` environment. Due to the size of the data set extracted, the analysis was performed utilising the High Performance Computer (HPC) facility available at the UFS.

4.3.1 Likelihood statistics

To analyse LAT data, a likelihood test was performed on a selection of extracted data, where-after this likelihood was used to find the best spectral model fit parameters. The likelihood (L) is the probability of detection of the observed event data for a specific input model of γ-ray emission[7]. The input model is the distri-

[7]See `https://fermi.gsfc.nasa.gov/ssc/data/analysis/documentation/Cicerone/Cicerone_Likelihood/Likelihood_formula.html` for a detailed discussion. Accessed 15/10/2021.

bution of observable γ-ray sources in the γ-ray sky, and includes their spectra and intensity. The likelihood can be defined as the product of the probability for each pixel (which is based upon γ-ray counts maps):

$$L = \prod_{ij} p_{ij}, \tag{4.1}$$

where

$$p_{ij} = \frac{\theta_{ij}^{n_{ij}} e^{-\theta_{ij}}}{n_{ij}!} \tag{4.2}$$

is the Poison probability of observing n_{ij} counts in pixel ij when the number of counts predicted by the model is θ_{ij}.

For the sake of convenience, the logarithm of the likelihood is more commonly used as:

$$\ln L = \Sigma_{ij} n_{ij} \ln(\theta_{ij}) - \Sigma_{ij}\theta_{ij} - \Sigma \ln(n_{ij}!). \tag{4.3}$$

Since the last term is not model-dependent, and serves no purpose for the likelihood ratio tests, it can be neglected, i.e.

$$\ln L = \Sigma_{ij} n_{ij} \ln(\theta_{ij}) - \Sigma_{ij}\theta_{ij}. \tag{4.4}$$

In the above equation (eq. 4.4), the first term causes $\ln L$ to increase as the model predicts the counts in pixels where they actually occur. The second term demands that the model counts be scarcely allocated.

Optimisers in the input model find the best spectral fit parameters of the observed counts, but not the source's location. However, a tool is provided that

performs a grid search, mapping out the maximum likelihood value over a grid of locations. This quantity is called the Test Statistic (TS)[8], and is defined as

$$\mathrm{TS} = -2\ln(L_{\mathrm{max},0}/L_{\mathrm{max},1}), \tag{4.5}$$

where $L_{\mathrm{max},0}$ is the maximum likelihood value for a model where no source is present (i.e. the "null hypothesis") and $L_{\mathrm{max},1}$ is the maximum likelihood value for a model with a source at a specified location. TS is an increasing function of $L_{\mathrm{max},1}$, meaning that the TS will be maximised when the likelihood is maximised. In the case of a large number of counts, Wilks Theorem (Wilks, 1938) states that the TS for the null hypothesis is asymptotically distributed as χ^2_1, which means that the TS departs from this distribution if no source is present, and an apparent source will be visible. Hence, a larger TS suggest that the null hypothesis is incorrect, i.e. a source exists and its parameters can be quantified[9]. For example, if $L_{\mathrm{max},1}$ is large, the natural logarithm (ln) of the ratio will tend to zero and the TS value will be larger than zero. If $L_{\mathrm{max},1}$ is small then the ratio will increase and TS will tend to zero:

$$\begin{aligned} \text{Source present}: &\quad L_{\mathrm{max},1} > L_{\mathrm{max},0},\ \mathrm{TS} > 0 \\ \text{Source not present}: &\quad L_{\mathrm{max},1} \to L_{\mathrm{max},0},\ \mathrm{TS} \to 0. \end{aligned} \tag{4.6}$$

This method is also used to measure the significance of the fit (spectral or spatial), where the TS is maximised when the likelihood is at its maximum. Adopting the common practice and as a basic rule of thumb, the square root of the TS ($\sqrt{\mathrm{TS}}$) is approximately equal to the significance of detection (σ) for any given source (e.g., Mattox et al., 1996).

[8] `https://fermi.gsfc.nasa.gov/ssc/data/analysis/documentation/Cicerone/Cicerone_Likelihood/Likelihood_overview.html` Accessed 25/01/2022

[9] See Mattox et al. (1996) for a more detailed statistical approach.

4.3.2 Binned likelihood analysis

The analysis method to search for γ-ray emission from AR Sco was initiated by doing a standard binned likelihood analysis (as pre-scribed by the FSSC Web-based tutorials[10]) over the whole 10-year dataset in an attempt to search for possible long-term continuous, or pulsed, high-energy emission. The selected photon event files, for the above-mentioned period (4 August 2008 - 18 March 2019) in an energy range of 100 MeV to 500 GeV centred on the coordinates of AR Sco within a ROI = 10°, were filtered by considering only `SOURCE` class event files (`evclass=128, evtype=3`) corresponding to the Pass 8 `P8R3-SOURCE-V6` instrument response function. Also, to minimise contamination from background photons from the earth's limb, the value of the zenith angle was set to `zmax` = 90° (the value most commonly used). These filtered files were further reduced using the relational filter (`DATA_QUAL>0 and LAT_CONFIG==1`) to select good time intervals in which the satellite was working in standard data taking mode and where the quality of the data was good. A counts map (see Fig. 4.3) was created of the ROI in order to identify candidate sources and to ensure that the ROI field looks sensible. From this counts map some excess in counts can be seen in close proximity to AR Sco's coordinates.

All the 4FGL sources located within the ROI, including the latest isotropic background and Galactic diffuse emission models at the time, were used to generate a background model file for background subtraction. The spectral shapes of all the point sources within the model file were kept the same as defined in the 4FGL catalogue. Since AR Sco is not listed within the 4FGL catalogue, the methodology of manually adding the source to the model centred at its coordinates was used, parameterising it with a power-law (PL) spectral shape at first. A power-law model was chosen for AR Sco since it is the simplest model to use for non-thermal processes. Takata et al. (2017) also suggested that the magnetic dissipation on the companion star surface accelerates charge particles to relativistic energies to form a

[10] `https://fermi.gsfc.nasa.gov/ssc/data/analysis/scitools/binned_likelihood_tutorial.html` Accessed 15/10/2021

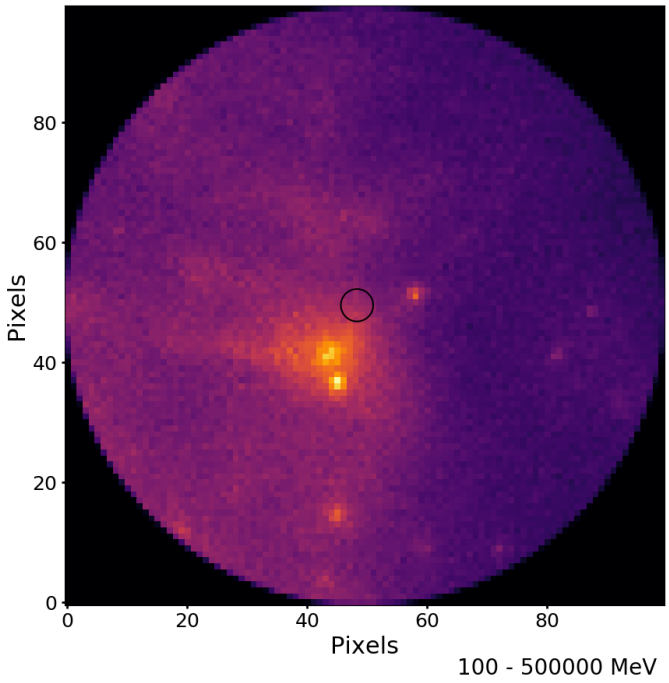

Figure 4.3: Counts map centred on AR Sco (100 x 100 pixels). The black circle represents coordinates centred on AR Sco.

power-law over several decades in energy, assuming a power-law index of the order $p \sim 2.5$. The associated spectral parameters of all the sources within a 1° radius, including those of AR Sco, were left free to vary during the binned likelihood fitting, along with the Galactic and isotropic background models. Alternative to the power-law model, both broken-power-law (BPL) and log-parabola (LP) models were also explored to do a likelihood fit. The resulting integrated flux above 100 MeV with corresponding model parameters from the different models used during binned likelihood analyses are presented in Table 4.1.

These results of our present binned analysis ($\leq 4.31\sigma$) in the energy range of 100 MeV - 500 GeV reveal low-level emission from the position of AR Sco, best described using a broken power-law model (see Fig. 4.4), where the statistical significance is calculated via $\sigma = \sqrt{\mathrm{TS}}$, (e.g., Mattox et al., 1996).

Table 4.1: Spectral model parameters obtained for the region centred on AR Sco in the energy interval 100 MeV - 500 GeV using binned likelihood analysis. Optimisation of AR Sco was done using an PL (Γ= - (2.7 $\pm$ 0.8)), BPL ($\Gamma_1 = -(1.00 \pm 0.31)$, $\Gamma_2 = -(3.83 \pm 1.81)$) and LP ($\alpha = (1.30 \pm 0.38)$, $\beta = (0.92 \pm 0.32)$) to determine the likelihood of detection of γ-rays from the ROI centred on AR Sco. Here $N_{\rm pred}$ refers to number of predicted counts.

Binned Likelihood Analysis for AR Sco				
Spectral model	Flux(photons/cm^2/s)	$N_{\rm pred}$	TS	Significance
Power-Law	$5.75 \pm 3.08 \times 10^{-9}$	1116.91	9.02	$\leq 3.00\sigma$
Broken-Power-Law	$4.39 \pm 3.24 \times 10^{-9}$	1109.37	18.54	$\leq 4.31\sigma$
Log-Parabola	$2.86 \pm 2.12 \times 10^{-9}$	823.98	15.15	$\leq 3.89\sigma$

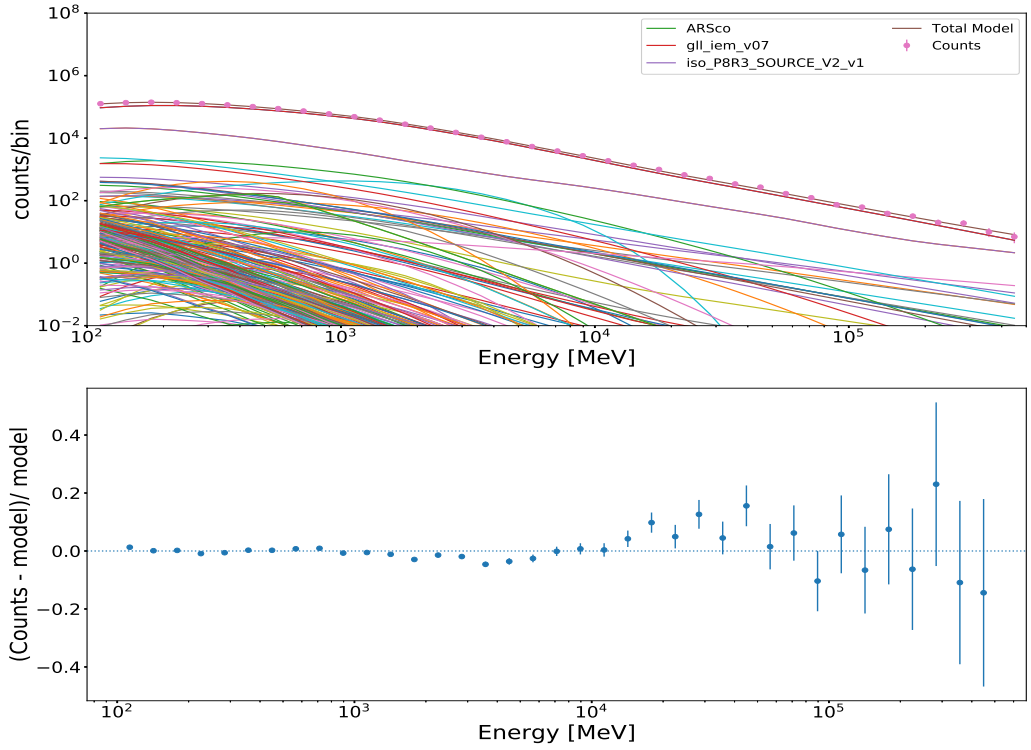

Figure 4.4: Model fit (top) and residual fit (bottom) of AR Sco's model fit (brown) in relation to 4FGL sources within the ROI (other colours), isotropic background model (purple) and Galactic diffuse model (red) using the BPL model. The residual fit is the fit for the chosen model for AR Sco relative to the observed counts.

After the likelihood analysis had been performed, an SED was plotted using the power-law model over 9 energy bins (see Fig. 4.5a). The SED was obtained using the *Fermi* build-in function `bdlikeSED` with the binned likelihood results. The energy flux values can be considered as 2σ upper-limits (with a 3σ data point) based on a limiting TS < 9 value per bin due to the low overall significance of AR Sco ($\sim 3\sigma$) using a power-law model. The distribution of TS values per energy bin (see Fig. 4.5b) also illustrates that the most significant emission is concentrated in the energy bins below 3 GeV.

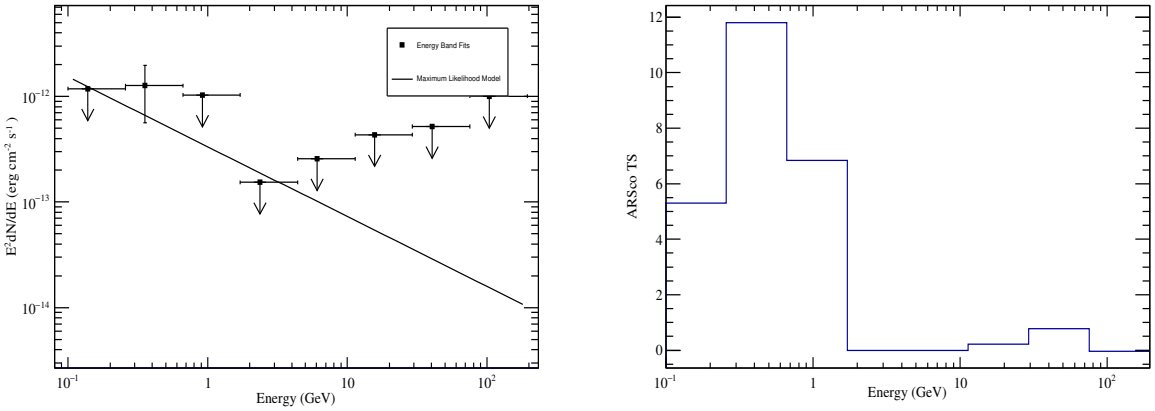

(a) Energy flux SED obtained using `bdlikeSED`.

(b) TS values vs energy of γ-ray photons.

Figure 4.5: (a) High-energy flux SED of AR Sco. The flux values are 2σ upper-limits (with a 3σ data point) based on a limiting TS < 9 value per bin. (b) Distribution of energy vs TS. The distribution indicates that there is a higher probability of photons being detected from AR Sco at lower energies.

An updated broadband SED (see Fig. 4.6) for AR Sco was produced. It indicates that the flux upper-limits for energies between 100 MeV and 500 GeV from AR Sco in the ROI coincides with the *Fermi*-LAT (10 year) sensitivity curve,[11] though γ-ray upper-limit values are below the recommended 5σ threshold for first-time detections. Due to *Fermi's* low spatial resolution at lower energies, it may be possible for other nearby sources (for example *4FGL-J1623.7-2315*) to still contribute to the observed emission, resulting in larger significance values.

[11] `http://www.slac.stanford.edu/exp/glast/groups/canda/lat_Performance.htm` Accessed 15/10/2021

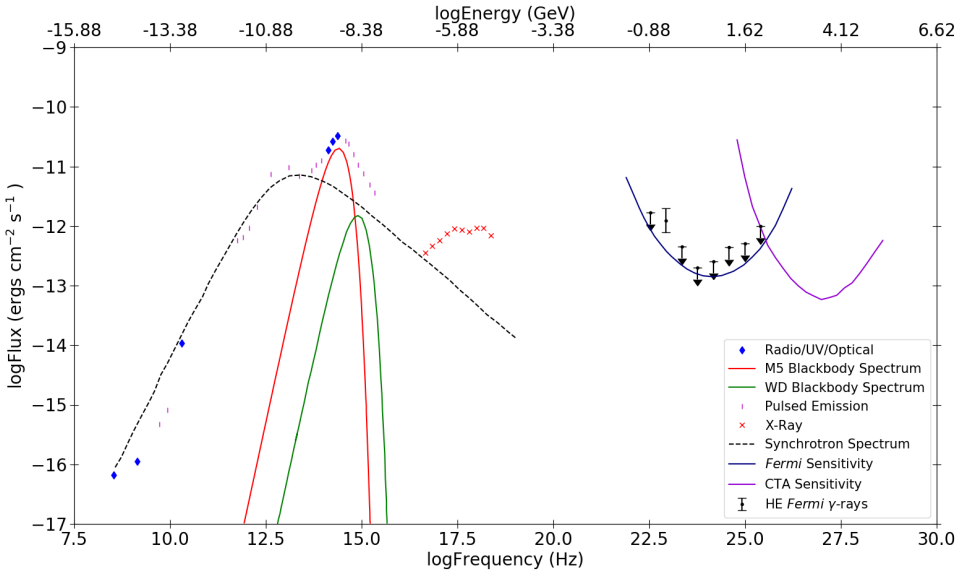

Figure 4.6: Updated broadband SED of AR Sco showing γ-ray upper-limits (black), with a 3σ data point, in relation to the *Fermi*-LAT (blue) and CTA-South 50 hour (violet) sensitivity curves. Red and green curves represent model atmospheres the M5 secondary dwarf star (T = 3100 K) and white dwarf (T = 9750 K) respectively, (Marsh et al., 2016). Red crosses represents observed X-ray emission, (Takata et al., 2018). Blue diamonds and purple dashes represents radio to optical emission obtained from Marsh et al. (2016).

Relevant residual and TS maps were created to examine different emission regions within the ROI and to visualise the spatial distribution of emission excess, if any, from the coordinates centred on AR Sco (see Fig 4.7). From a few apparent "bright pixels" around the coordinates of AR Sco, some level of emission excess around these coordinates can be observed and speculated. Further investigation, however, still has to be done to verify that the upper-limit emission detection originates from the coordinates centred on AR Sco and not from nearby sources within the ROI since it is difficult to constrain the exact emission region due to the low overall significance that was obtained.

Since most of the emission originates at energies below 3 GeV (see Fig. 4.5b) and the fact that AR Sco lies near the Galactic plane and Rho Ophiuchi (henceforth Rho Oph) cloud complex, it is difficult to distinguish if the detected γ-rays come from AR Sco or from the surrounding region due to *Fermi's* low spatial resolution

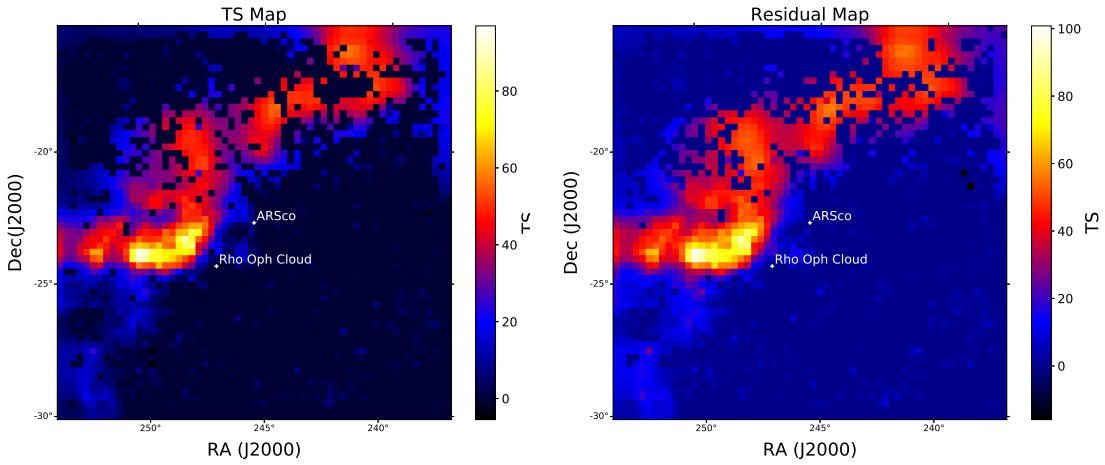

(a) TS map centred on AR Sco

(b) Residual map centred on AR Sco

Figure 4.7: Plots of AR Sco's TS values within its ROI where (a) shows the TS map centred on AR Sco and (b) shows the residual map centred on AR Sco. By comparing these two maps very low emission excess (a few bright pixels) can be seen at the coordinates centred on AR Sco in (a) but not in (b).

at lower energies. It can be seen from Fig. 4.7 that a significant amount of residual emission is noticeable to the left of the position centred on AR Sco, which may well be attributed to the contribution from the Galactic plane or the Rho Oph cloud. This, however, needs to be confirmed in future studies since both Galactic and isotropic background models were included during analysis. Due to the complexity of the Rho Oph cloud complex, it is difficult to incorporate an exact model for the molecular cloud. Since the cloud complex is not located within the 4FGL catalog, further modeling of the cloud needs to be done and added to the 4FGL catalogue in an attempt to reduce or remove the cloud from future *Fermi*-LAT analyses.

4.3.3 Un-binned likelihood analysis

Similar conditions as those of binned analyses were used during un-binned likelihood analysis, where the same ROI (10°) and model parameters were used. However, due to convergence issues, source spectral models for the broken power-law model further than 15° with insignificant TS have been discarded to allow for a better overall convergence and fit. The results are presented in Table 4.2.

Table 4.2: Spectral model parameters obtained for the region centred on AR Sco in the energy interval 100 MeV - 500 GeV using un-binned likelihood analysis. Optimisation of AR Sco was done using an PL (Γ= - (2.8 $\pm$ 0.29)), BPL ($\Gamma_1 = -(1.34 \pm 0.28)$, $\Gamma_2 = -(4.99 \pm 0.43)$ and LP ($\alpha = (0.03 \pm 0.20)$, $\beta = (1.06 \pm 0.78)$) to determine the likelihood of detection of γ-rays from the ROI centred on AR Sco. Where $N_{\rm pred}$ again refers to number of predicted counts.

Un-binned Likelihood Analysis for AR Sco				
Spectral model	Flux(photons/cm^2/s)	$N_{\rm pred}$	TS	Significance
Power-Law	$4.95 \pm 2.82 \times 10^{-9}$	967.93	6.52	$\leq 2.55\sigma$
Broken-Power-Law	$3.57 \pm 1.10 \times 10^{-9}$	941.23	13.68	$\leq 3.69\sigma$
Log-Parabola	$2.70 \pm 1.96 \times 10^{-9}$	752.31	13.52	$\leq 3.67\sigma$

As is with the binned analysis, the un-binned analysis reveal similar results ($\leq 3.40\sigma$) in the energy range 100 MeV - 500 GeV where the low-level emission from the position of AR Sco is best described using a broken-power-law model. Due to the upper-limit detection threshold ($< 5\sigma$), the likelihood of detection (or even excess values above background) that could be seen as significant and worthy of analysis, was found to be unlikely. No further investigations were therefore performed.

4.3.4 Light curves

To determine if the upper-limit emission is periodic over the past decade and to search for possible flaring events, *Fermi*-LAT light curves were produced for further study. This was done using un-binned likelihood analysis, since it is recommended to use un-binned likelihood analysis when considering data over short periods of time, with low photon counts. A 10-year light curve was produced for AR Sco over a 30-day (1 month) binning period to investigate any periodicity of the close binary system at higher energies (see Fig. 4.8). A yearly binned light curve was also produced to include more photons per bin (see Fig. 4.9), in an attempt to increase the significance of detection. Upper-limit flux points within the yearly binned light curve corresponds to 2σ upper limits on the integral flux.

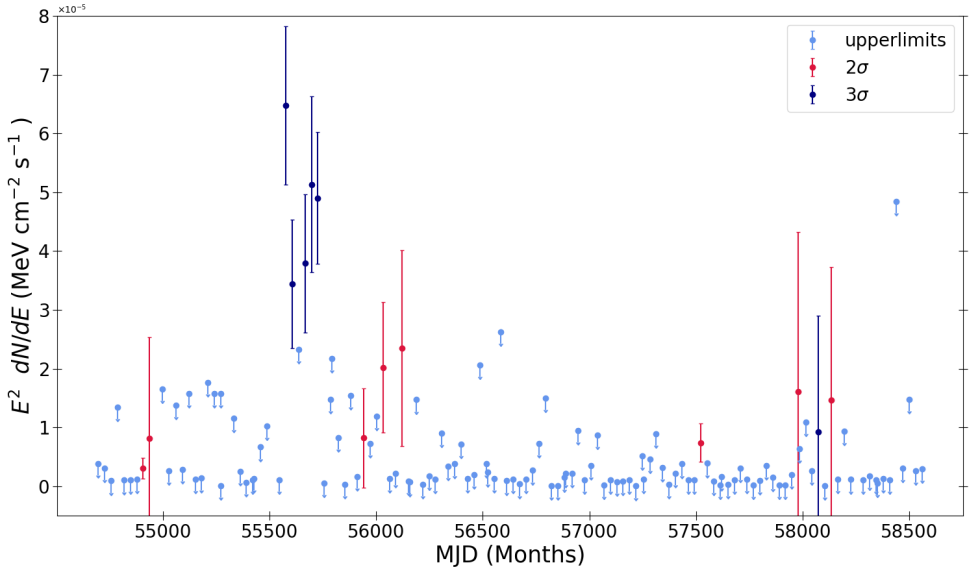

Figure 4.8: 10-year light curve of AR Sco from 4 August 2008 - 18 March 2019 binned at 30-day intervals. An increase in brightness is visible during a period of 2010 - 2011. Red (2σ) and navy (3σ) correspond to events where the model converged well. Blue represents upper-limits.

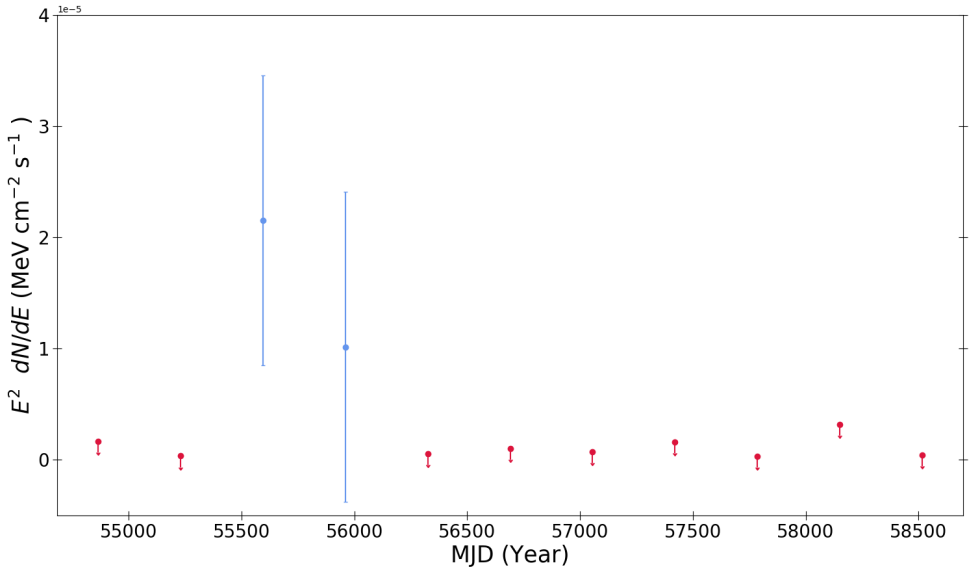

Figure 4.9: 10-year light curves of AR Sco from 4 August 2008 - 18 March 2019 with yearly binned intervals. Upper-limits correspond to 2σ limits on the integral flux.

From both the light curves produced (see Fig. 4.8 and 4.9), an increase in flux during a period between 2010 and 2011 can be seen, which sparked curiosity for further investigation. Binned likelihood analysis was performed specifically over the short period from January - June 2011 to investigate this increase in brightness. During this period a much larger significance of detection and overall flux levels of the region centred on AR Sco is observed and is well above the current 5σ *Fermi*-LAT threshold, see Table 4.3. Here, the power-law and log-parabola models struggled to get good convergence.

Table 4.3: Spectral model parameters obtained for AR Sco during the period of Jan-June 2011 using binned likelihood analysis. Optimisation was done using a PL, BPL and LP to determine the likelihood fit during the flaring period.

Binned Likelihood Analysis for AR Sco During Jan-June 2011				
Spectral model	IntFlux(photons/cm^2/s)	N_{pred}	TS	Significance
Power-Law	1.293 ± 0.177 x 10^{-7}	711.16	66.892	$\leq 8.17\sigma$
Broken Power-Law	1.293 ± 0.181 x 10^{-7}	738.88	74.173	$\leq 8.61\sigma$
Log Parabola	1.299 ± 0.178 x 10^{-7}	741.59	74.280	$\leq 8.61\sigma$

However, TS and residual maps (see Fig. 4.10a and 4.10b) revealed a significant excess in brightness from the nearby source PKS1622-253, which is a powerful quasar (e.g., Punsly et al., 2005) located $\sim 2.7^\circ$ from the region centred on AR Sco. Table 4.4 shows significantly large binned likelihood results obtained for PKS1622-253, using the recommended source model parameters present in the 4FGL catalogue. This excess in flux may lead to contamination, especially at lower energies, of any γ-rays observed from AR Sco since the region of γ-ray emission from this quasar is extended to the region centred around AR Sco. This may explain the increase in brightness from the region of AR Sco during the same period around 2011, but can not be confirmed at this stage.

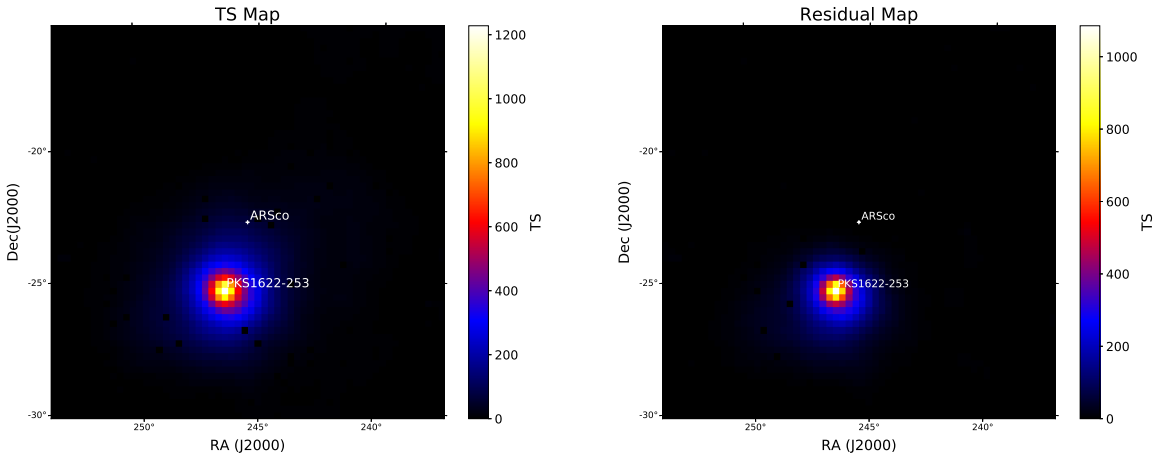

(a) TS map of AR Sco.

(b) Residual map of AR Sco.

Figure 4.10: Plots of AR Sco's TS values during the period of Jan-June 2011 within its ROI where (a) shows the TS map centred on AR Sco and (b) shows the residual map centred on AR Sco.

Table 4.4: Spectral model parameters obtained for PKS1622-253 using a binned likelihood analysis in the energy range 100 MeV to 500 GeV. Optimisation was done using an LP model to determine the likelihood fit of this bright quasar during the full 10-year period and the possible flaring period. The LP model is the pre-defined model used in the 4FGL catalog.

Binned Likelihood Analysis for PKS1622-253				
Spectral model	IntFlux(photons/cm^2/s)	N_{pred}	TS	Significance
LP (10 Years)	$5.851 \pm 0.271 \times 10^{-8}$	14057.14	2654.592	$\leq 51.53\sigma$
LP (Jan-June 2011)	$4.727 \pm 0.204 \times 10^{-7}$	3737.40	2607.674	$\leq 51.38\sigma$

A *Fermi*-LAT light curve over the past decade was also produced for PKS1622-253 to investigate the observed emission, see Fig. 4.11. During the period of October 2010 and November 2012 the source went into a flaring state, and our light curve is comparable to the light curve currently available in the *Fermi*-LAT Monitored Source list (see Fig. 4.12), where a section from the flaring period can be seen, (e.g., Abdo et al., 2009).

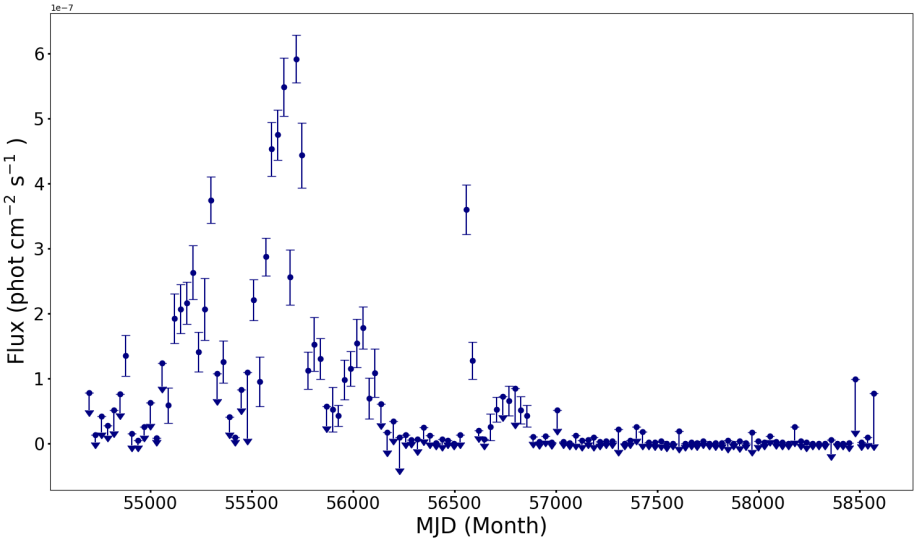

Figure 4.11: 10-year light curves of PKS1622-253 from 4 Augustus 2008 - 18 March 2019, in the energy range 100 MeV to 500 GeV, binned over 1-month intervals. Upper-limits are based on *Fermi*'s $\leq 5\sigma$ threshold.

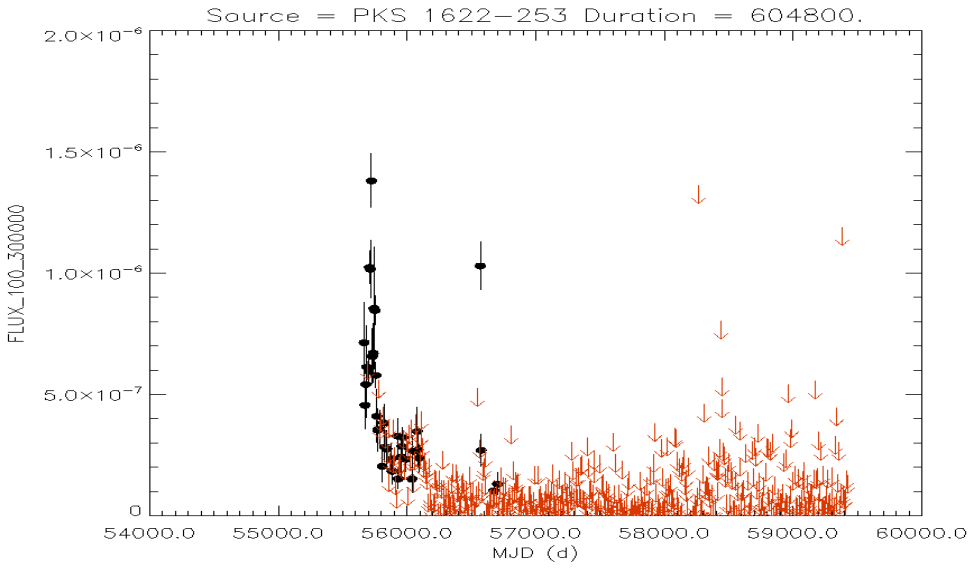

Figure 4.12: Weekly binned light curve of PKS1622-253 that is currently in the *Fermi*-LAT Monitored Source list. Adopted from `https://fermi.gsfc.nasa.gov/ssc/data/access/lat/msl_lc/source/PKS_1622-253`. Accessed 15/10/2021.

By comparing the TS and residual maps of PKS1622-253 for the same 10-year period (4 August 2008 - 18 March 2019) to the flaring period (January - June 2011) some excess can be observed from the source during the flaring period. See

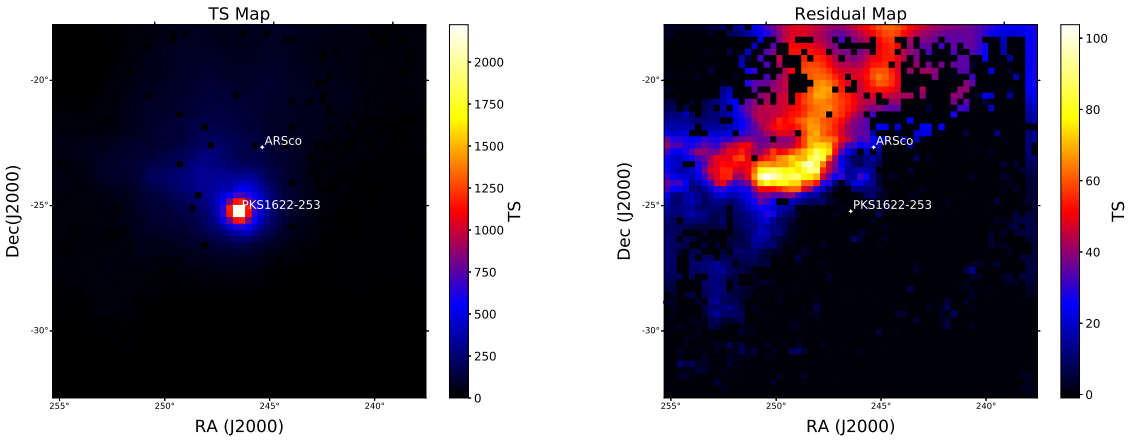

(a) TS map of PKS1622-253.

(b) Residual map of PKS1622-253.

Figure 4.13: TS (a) and residual map (b) centred on PKS1622-253 for the 10-year period (4 August 2008 - 18 March 2019).

Fig. 4.13 and 4.14 respectively. By comparing Fig. 4.13a with Fig. 4.14a an increase in TS, and consequently flux, can be observed resulting in a larger region to be influenced. An assumption can be made that this may have an effect on the brightness increase seen in AR Sco's 10-year light curve and can explain why larger TS values are observed during the period of January - June 2011.

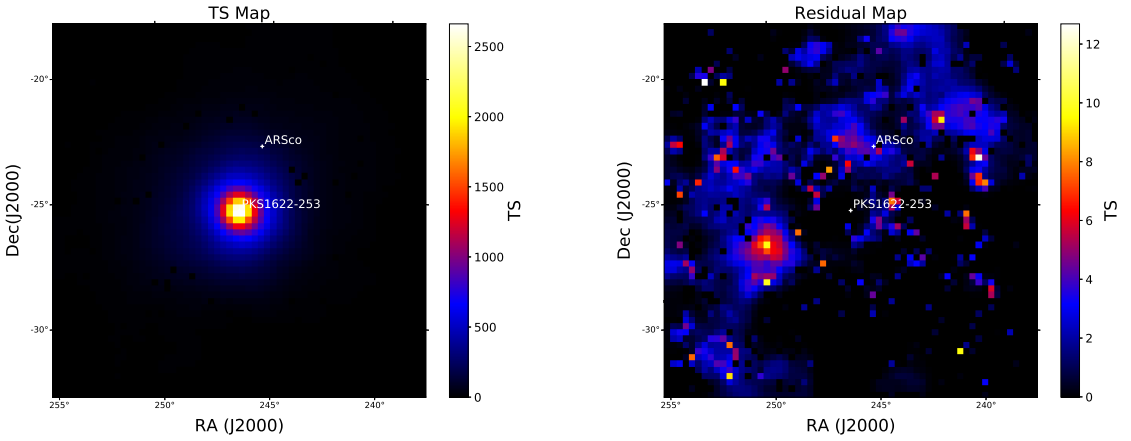

(a) TS map of PKS1622-253.

(b) Residual map of PKS1622-253

Figure 4.14: TS (a) and residual map (b) centred on PKS1622-253 for the period of January - June 2011 during flaring.

4.4 Periodic analysis

Considering the results obtained from the likelihood analysis, where a low-level upper-limit value of γ-ray emission centred at the coordinates of AR Sco was placed, along with the assumption of contribution from the Galactic Plane, the Rho Oph cloud complex and high-energy sources in the surrounding region, a search for emission at noise level was conducted. By doing a period analysis, a search for uniformity of a phase distribution at a certain predetermined period can be investigated.

Since the spin (P_s = 117 s) and beat period (P_b = 118.2 s) for the rapidly rotating white dwarf is known and detectable from radio to X-ray (e.g., Marsh et al., 2016; Takata et al., 2017), accompanied by the argument that the white dwarf in AR Sco has similar features to that of spun-up pulsars (e.g., Buckley et al., 2017), a search for any periodicities around these periods was justified. A *Fermi*-LAT dataset covering the same 10-year period (4 August 2008 - 18 March 2019) in the energy range 100 MeV to 30 GeV, including the latest spacecraft file at the time of analysis, was used to do a standard period search and obtain power spectra (periodograms) with the help of the `gtpsearch` tool. The `gtpsearch` tool automatically corrects for the barycentre by converting the detected event times to barycentric time using the spacecraft file, which contains the telescope's telemetry data. The ROI was left at 10°.

4.4.1 Rayleigh power statistics

A very functional test for broad sinusoidal pulse profiles in sparsely distributed data is the Rayleigh test (Mardia, 1972). The general form of Rayleigh statistic is given as

$$2n\bar{R_l}^2 = 2n(\bar{C_l}^2 + \bar{S_l}^2), \tag{4.7}$$

with n the number of data points and l the number of harmonics.

Here the cosine and sine components are respectively defined as:

$$\bar{C}_l = \frac{1}{n}\sum_{i=1}^{n}\cos(2\pi l\theta_i) \tag{4.8}$$

$$\bar{S}_l = \frac{1}{n}\sum_{i=1}^{n}\sin(2\pi l\theta_i). \tag{4.9}$$

Here θ_i is defined as pulse phase of each arrival from the pulsed emission. The Rayleigh power ($n\bar{R_l}^2$), which is half of the Rayleigh statistic, is similar to that of Fourier power in Fast Fourier Transform (FFT) analysis, and can be written as a function of signal strength (p) (de Jager et al., 1989):

$$n\bar{R_l}^2 = \frac{np^2}{4} + 1. \tag{4.10}$$

In the case of uniformly-distributed data, the distribution of Rayleigh statistic (eq. 4.7) should follow a χ^2 distribution with 2 degrees of freedom. The probability that θ_i follows a uniform distribution (in the absence of a periodic signal) is given by

$$Pr(> n\bar{R_l}^2) = \exp(-n\bar{R_l}^2). \tag{4.11}$$

A very convenient way to illustrate the significance of a peak graphically in a power spectrum is by calculating the logarithm of the probability:

$$-\,log_{10}Pr = 0.434n\bar{R_l}^2. \tag{4.12}$$

The distribution of Rayleigh statistics can be tested by sampling the Rayleigh power around a specific frequency, i.e., the source frequency, with independently-spaced Fourier frequencies. These Fourier frequencies are then spaced by $1/T$, where T is defined as the observation time of the data set. On a semi-logarithm plot, the differential number distribution of these independent Rayleigh test values should show a linear dependence with a gradient of 0.5, in the event that the data follows a pure white noise profile. Due to sparsity of data from AR Sco obtained using *Fermi*-LAT, a Rayleigh test will serve as the most powerful and effective test to search for periodicities at the spin and beat frequencies.

4.4.2 Rayleigh periodograms

Rayleigh periodograms for AR Sco were produced by using the ephemeris from (Takata et al. 2018; see Table 4.5), with a reference time of $T_{s,ref} = 57641.546$ MJD and the spin frequency $\nu_{\rm spin} = 8.5390$ mHz (117.1 s). The spin-down frequency of AR Sco's white dwarf adopted from Marsh et al. (2016), $\dot{\nu} = -2.86 \pm 0.36 \times 10^{-17}$ Hz s^{-1}, was also used.

Table 4.5: X-ray ephemeris of AR Sco used in period analysis. Adapted from Takata et al. (2018).

$T^a_{orb,ref}$ (MJD)	$T^b_{s,ref}$ (MJD)	ν^c_b (mHz)	ν^d_s (mHz)	ν^e_{orb} (mHz)
57264.09615	57641.54629	8.4611	8.5390	0.07792

[a] Reference time for the orbital phase.
[b] Reference time for the spin phase.
[c] Beat frequency.
[d] Spin frequency.
[e] Orbital frequency.

A Rayleigh power spectrum (Fig. 4.15) centred on the coordinates of AR Sco was produced, folded on the spin frequency of the white dwarf. Considering the long baseline of events in the dataset, a step size (1.493×10^{-6} Hz) of 500 times the Fourier resolution ($\nu = 2.985 \times 10^{-9}$ Hz) was used with a number of trials

as 5000 centred on the fundamental frequency of $\nu_{\rm spin} = 8.53885$ mHz (117.11 s). From a power spectrum with a smaller frequency (see Fig. 4.16) there appears to be some level of Rayleigh power visible above the noise level.

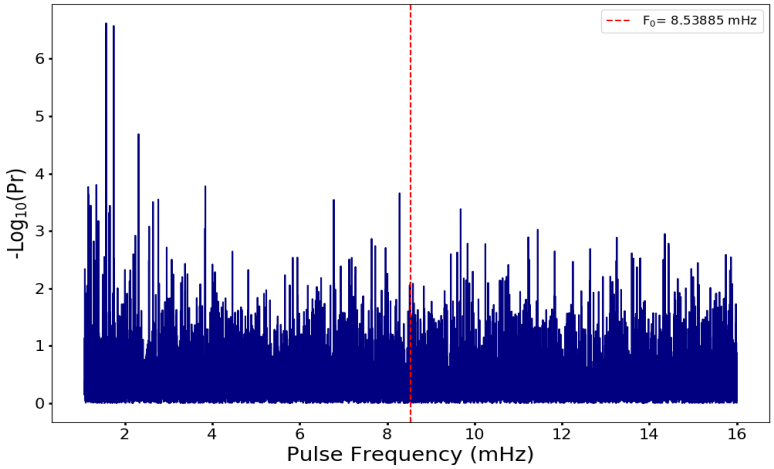

Figure 4.15: 10-year (4 August 2008 - 18 March 2019) Rayleigh periodogram of AR Sco in the energy range of 100 MeV to 30 GeV, covering frequencies from $1.5-16$ mHz. Additional line marker added showing the current model for the fundamental spin frequency ($F_0 = 8.53885$ mHz) of the white dwarf in AR Sco.

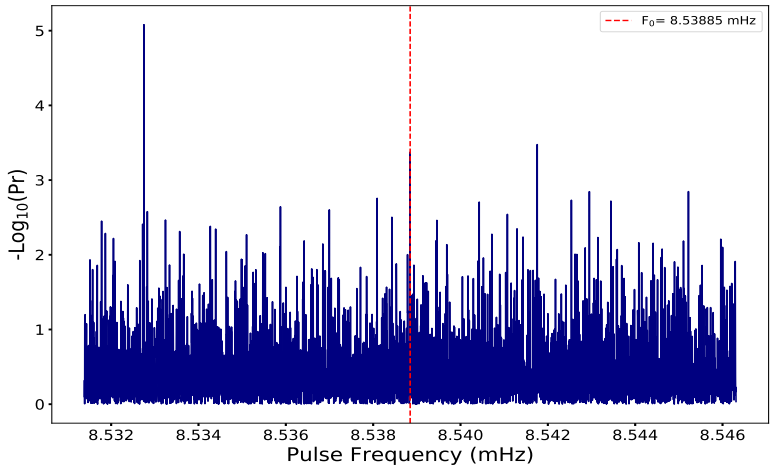

Figure 4.16: 10-year (4 August 2008 - 18 March 2019) Rayleigh periodogram of AR Sco in the energy range of 100 MeV to 30 GeV, focusing on the spin period frequency range, covering frequencies from $8.530-8.547$ mHz. Additional line marker added showing the fundamental spin frequency ($F_0 = 8.53885$ mHz) of the white dwarf in AR Sco.

A narrower Rayleigh power spectrum (Fig. 4.17), with accompanying phasogram (Fig. 4.19), with step size (1.493×10^{-9} Hz) of 0.5 times the Fourier resolution of ($\nu = 2.985 \times 10^{-9}$ Hz) and number of trials 500, centred on the fundamental frequency of $\nu_{\rm spin} = 8.53885$ mHz (117.11 s) were obtained, covering frequencies from $8.5384 - 8.5393$ mHz. From this Rayleigh power an apparent signal at the fundamental spin frequency seems to be visible, albeit not at a significant level.

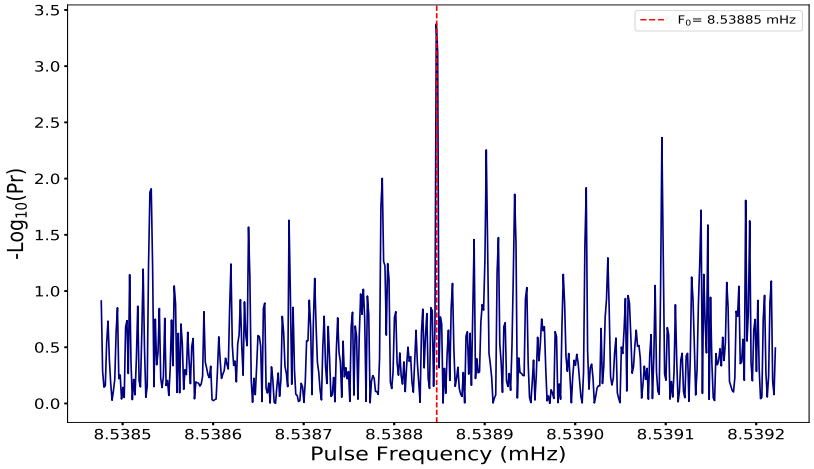

Figure 4.17: Narrower 10-year (4 August 2008 - 18 March 2019) Rayleigh periodogram of AR Sco in the energy range of 100 MeV to 30 GeV, covering frequencies from $8.5384 - 8.5393$ mHz. Additional line marker added showing the current model for the fundamental spin frequency ($F_0 = 8.53885$ mHz) of the white dwarf in AR Sco.

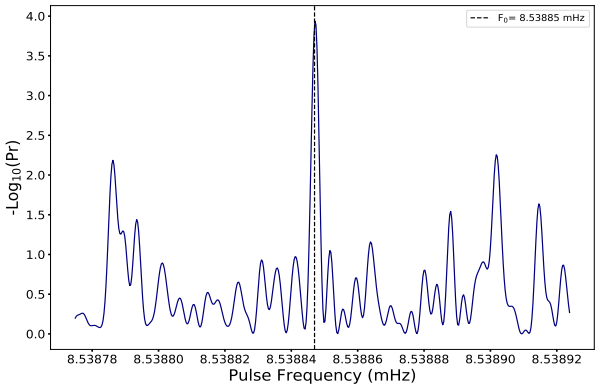

Figure 4.18: AR Sco 10-year (4 August 2008 - 18 March 2019) Rayleigh periodogram for the spin period covering a narrower frequency range from $8.53877 - 8.53893$ mHz.

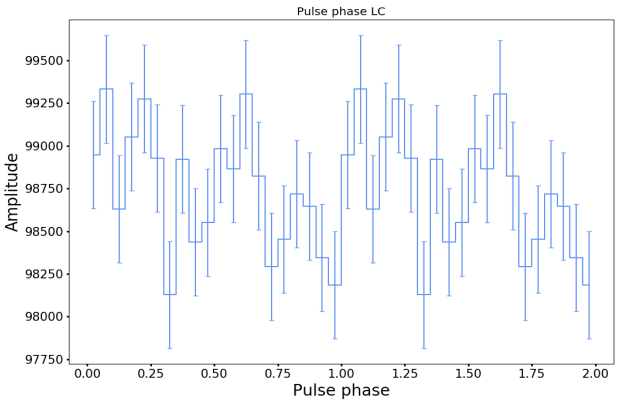

Figure 4.19: AR Sco 10-year (4 August 2008 - 18 March 2019) pulse/phase profile folded on the fundamental spin frequency ($F_0 = 8.53885$ mHz).

A Rayleigh power spectrum (see Fig. 4.20) with accompanying pulse/phase profile (see Fig. 4.21) for the beat period was also produced, using similar Fourier parameters as in Fig 4.17. No clear or significant signal can be observed within this periodogram, hence any further analysis at the beat frequency of AR Sco can be considered as impractical at this stage. No further investigation was therefore conducted. An alternative ephemeris (Gaibor et al., 2020) for the beat period was, however, tested and is presented in Appendix B.

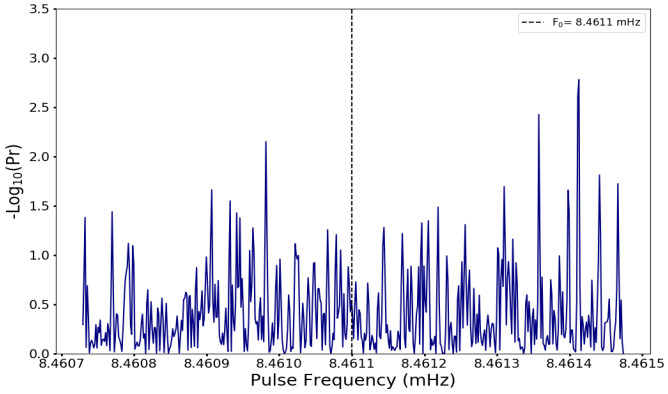

Figure 4.20: AR Sco 10-year (4 August 2008 - 18 March 2019) Rayleigh periodogram for the beat period covering a frequency range from 8.4607 – 8.4615 mHz. Additional line marker added showing the current model for the fundamental beat frequency (F_0 = 8.4611 mHz) of the white dwarf in AR Sco.

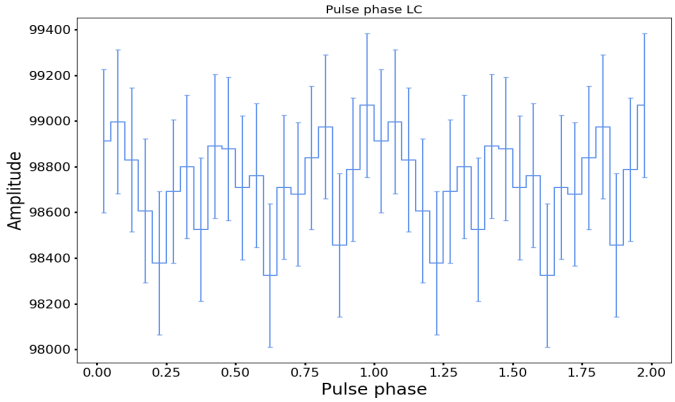

Figure 4.21: AR Sco 10-year (4 August 2008 - 18 March 2019) pulse/phase profile folded on the fundamental beat frequency (F_0 = 8.4611 mHz).

4.4.3 Periodogram control tests

Due to the overall low significance within the spectra, the Rayleigh spectrum for the spin period was subjected to noise structure analysis by focusing on the much narrower frequency range (see Fig 4.18). A histogram (see Fig. 4.22) of $\log_{10}(\mathrm{dN/dZ})$ versus Rayleigh statistics (Z) was generated, where the graph for a white noise profile will have an inverse linear trend in power distribution. If any deviation from this linear trend in the histogram occurs, it can be considered that the distribution of Rayleigh statics does not form part of the white noise profile and is suggestive of a possible signal within the data.

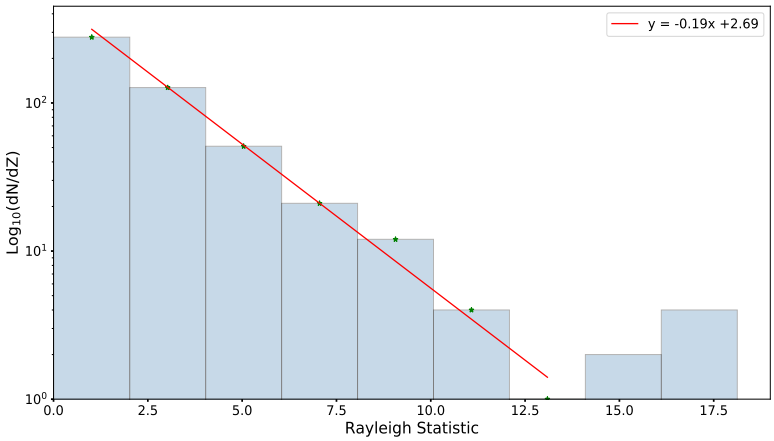

Figure 4.22: Histogram of the Rayleigh distribution for AR Sco, in the frequency range of 8.53887 - 8.53893 mHz.

4.4.3.1 Off-source periodogram control test

Another method to determine the validity of the power spectra, was by doing a search for a similar signal within the extracted *Fermi*-LAT dataset at locations farther away from the position centred on AR Sco (within the ROI), where no γ-ray sources are detected, and the γ-ray background is at a significantly lower level (see Fig. 4.23). If a signal is detected at any of these independent locations at the same spin frequency with the same properties as AR Sco, then the proposed

signal detected in the power spectra from AR Sco could possibly be inherent to the analysis technique or dataset. However, if the data reveals white noise structures, with no clear signals at locations without any suspected γ-ray sources, it will strengthen the case that the analysis technique and results obtained are justified.

Rayleigh periodograms compared to each region within the ROI (centred on AR Sco) are presented in Fig. 4.25, along with the individual periodograms and accompanied histogram distributions at each region (see Fig. 4.24). Regions were chosen to be 2°, 3°, 5° and 8° away from the ROI centre, where low-level γ-ray emission is present[12]. However, from Fig. 4.24h a deviation from the white noise profile seems to be present. This may be due to the increase in Rayleigh statistic at 8.53879 Hz which causes a deviation from the noise profile. Hence an alternative control test is needed.

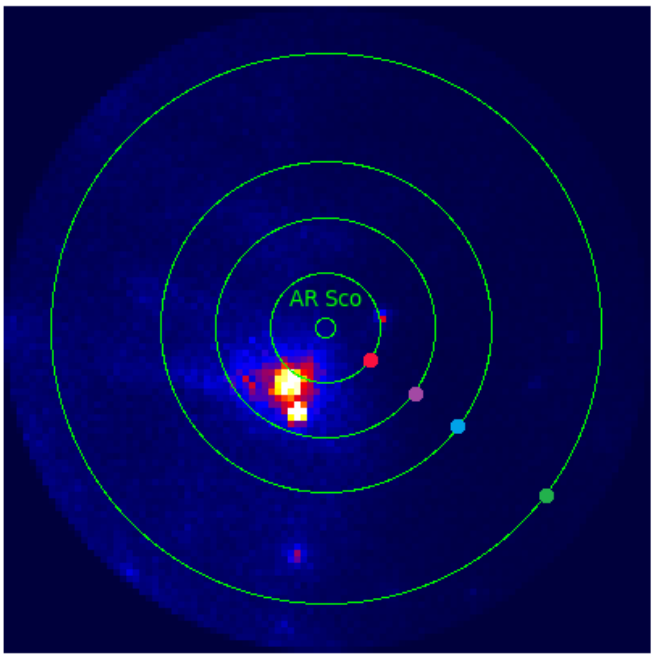

Figure 4.23: Counts map (100 x 100 pixels) centred on AR Sco. Green circles represent locations 2° (red), 3° (purple), 5° (blue) and 8° (green) away from the coordinates centred on AR Sco.

[12]See Appendix C for a control test at locations in the opposite direction.

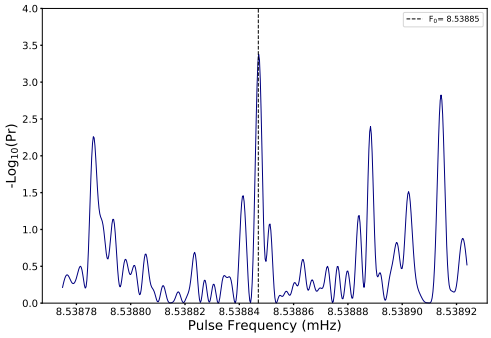

(a) Rayleigh probability at 2° away.

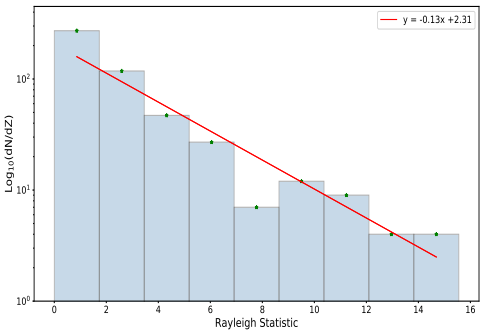

(b) Rayleigh histogram at 2° away.

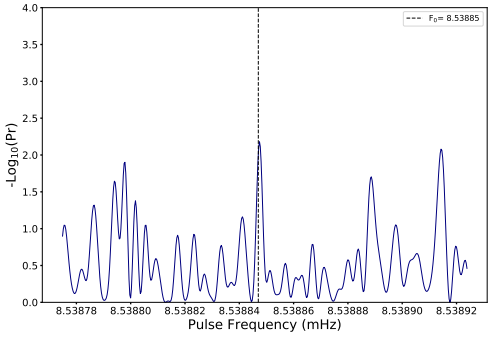

(c) Rayleigh probability at 3° away.

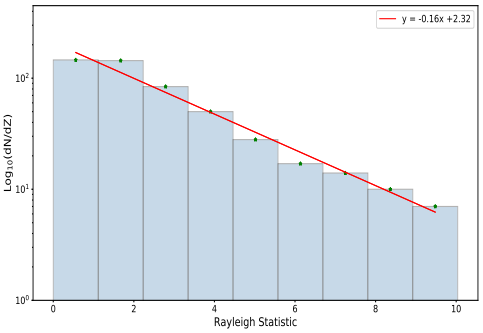

(d) Rayleigh histogram at 3° away.

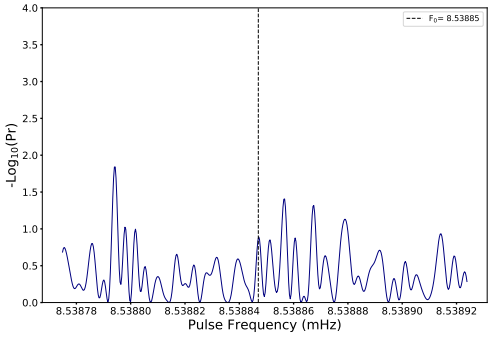

(e) Rayleigh probability at 5° away.

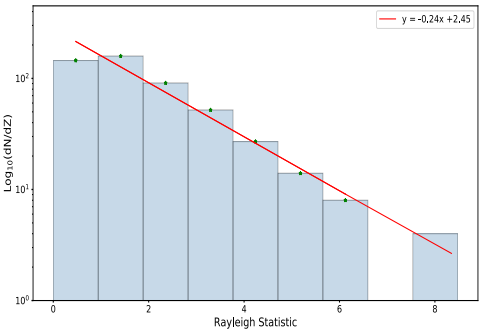

(f) Rayleigh histogram at 5° away.

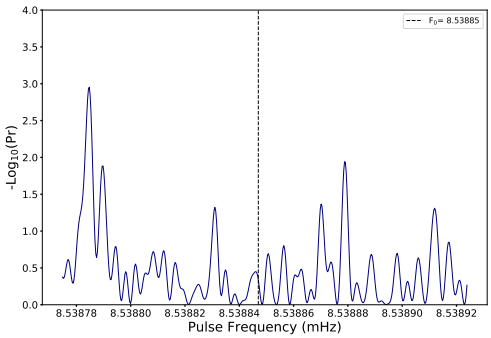

(g) Rayleigh probability at 8° away.

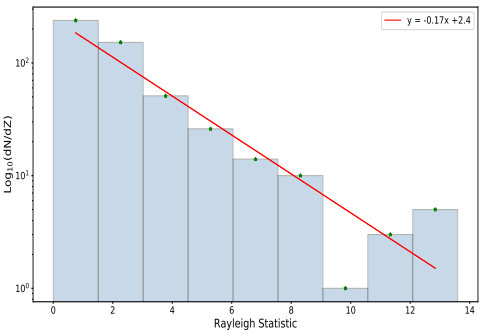

(h) Rayleigh histogram at 8° away.

Figure 4.24: Rayleigh probability spectra and histogram distributions at regions of 2°, 3°, 5° and 8° away from the coordinates centred on AR Sco.

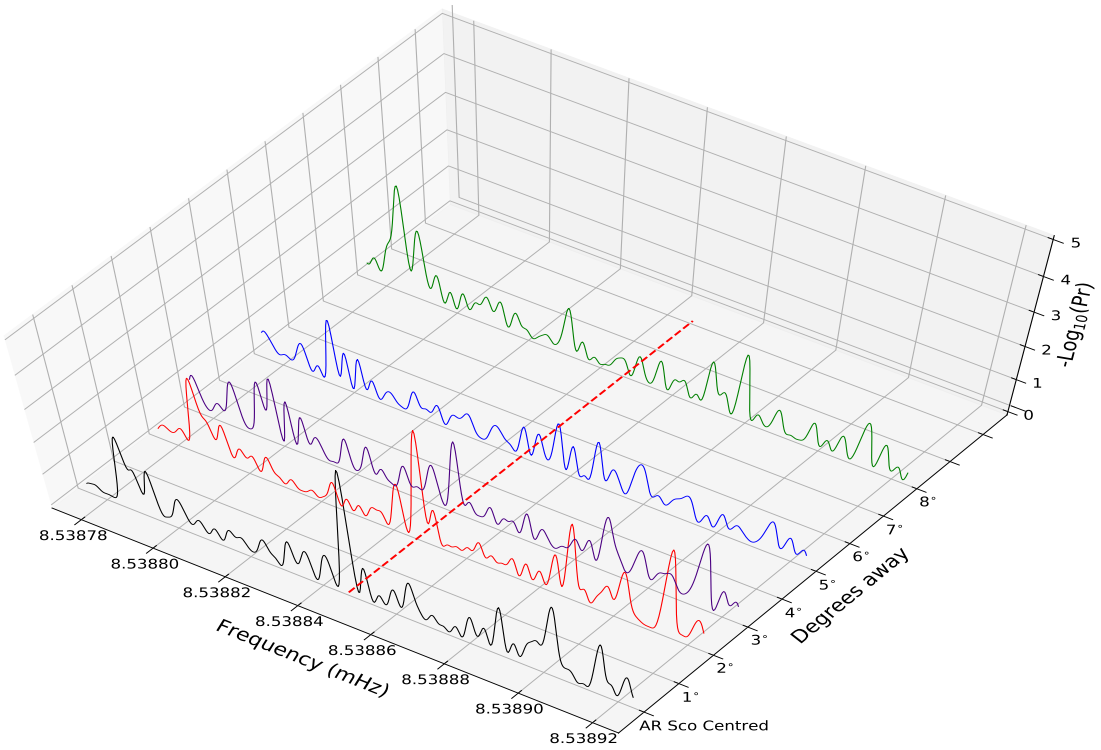

Figure 4.25: AR Sco power spectra (black) compared to regions 2° (red), 3° (violet), 5° (blue) and 8° (green) away from the coordinates centred on AR Sco.

Two independent, known *Fermi*-LAT sources, i.e., 4FGL J1648.1-1547 and 4FGL J1555.7-2908[13], close to the coordinates of AR Sco were also subjected to a period analysis. By using the same ephemeris as AR Sco an alternative control test can be conducted in an attempt to test the validity of the possible signal obtained at the spin period of AR Sco. Again, if similar signatures from the AR Sco's power spectra (see Fig. 4.18) are observed in the power spectra from these two independent sources, the proposed signal detected could be inherent to the data or analysis technique. Alternatively, if the signatures in the power spectra are different to that obtained for AR Sco, the detected signal can be considered as inherent at AR Sco's coordinates. The ROIs of these sources (see Fig. 4.26) were chosen in such a way that AR Sco will still be included within their respective ROIs, along with the selected locations farther away from AR Sco as previously discussed (see Fig. 4.23).

[13]These source are currently listed within the 4FGL catalog.

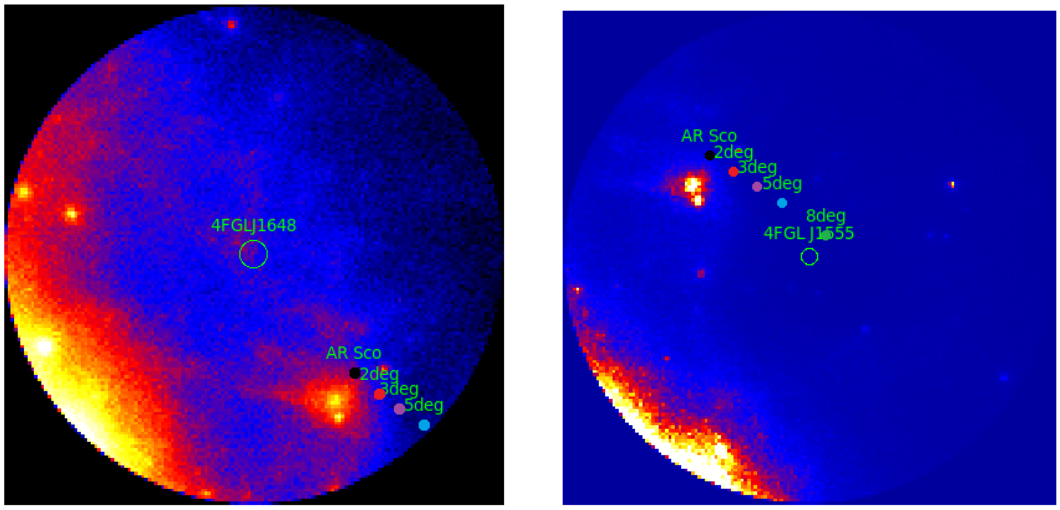

(a) *4FGL J1648.1-1547* (b) *4FGL J1555.7-2908*

Figure 4.26: Counts maps centred on 4FGL J1648.1-1547 and 4FGL J1555.7-2908. Markers represents locations 2° (red), 3° (purple), 5° (blue) and 8° (green) away from the coordinates centred on AR Sco (black).

Spectral model parameters, as well as TS and residual maps for each source (see Fig. 4.27 and 4.28 respectively) were obtained to show their respective likelihood within the selected ROIs. Rayleigh periodograms were also produced for AR Sco, and the surrounding regions within the ROI of 4FGL J1648.1-1547 and 4FGL J1555.7-2908 respectively, (see Fig. 4.29 and 4.30). If similar features are observed as in the power spectra obtained in Fig 4.25, it suggests that the observed decrease in signals are analogous to the surrounding region of AR Sco, regardless of where the ROI is centred and the dataset used.

Table 4.6: Spectral model parameters obtained for 4FGL J1648.1-1547 and 4FGL J1555.7-2908 using binned likelihood analysis in the energy range 100 MeV to 500 GeV over the past decade. Optimisation was done using the pre-defined PL models used in the 4FGL catalog for both sources.

Binned Likelihood Analysis				
Source	IntFlux(photons/cm^2/s)	N_{pred}	TS	Significance
4FGL J1648.1-1547	$1.392 \pm 0.632 \times 10^{-9}$	337.25	53.796	$\leq 7.33\sigma$
4FGL J1555.7-2908	$9.034 \pm 1.551 \times 10^{-9}$	1928.01	81.734	$\leq 9.04\sigma$

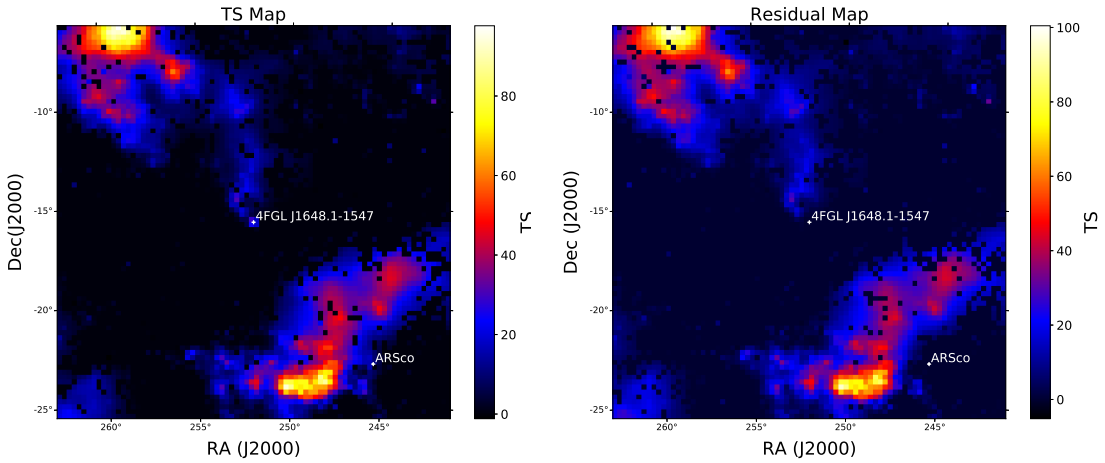

(a) TS map. (b) Residual map.

Figure 4.27: TS (a) and residual map (b) centred on 4FGL J1648.1-1547 (RA:252.027°, Dec:-15.793, J2000, Decimal Equatorial) for the 10-year period (4 August 2008 to 18 March 2019), including AR Sco (bottom right).

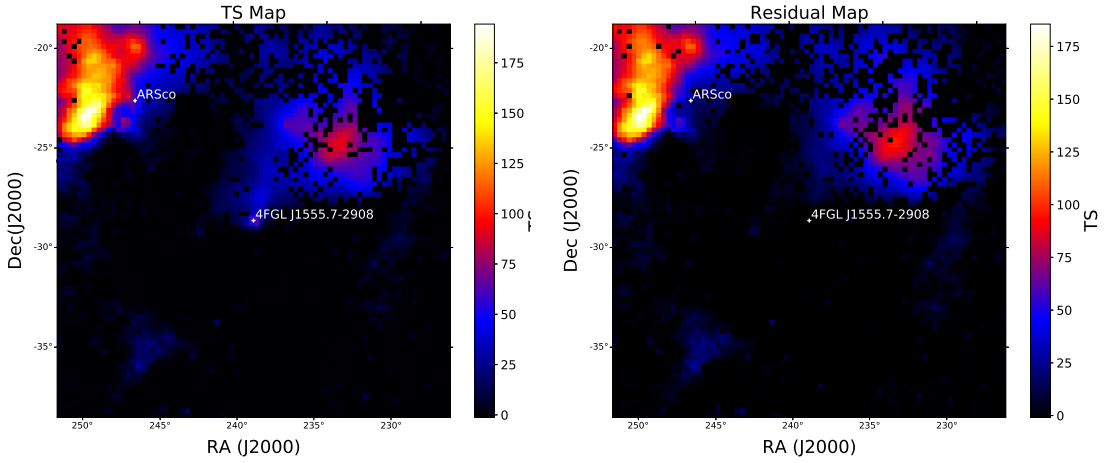

(a) TS map. (b) Residual map.

Figure 4.28: TS (a) and residual map (b) centred on 4FGL J1555.7-2908 (RA:238.921°, Dec:-29.137, J2000, Decimal Equatorial) for the 10-year period (4 August 2008 to 18 March 2019), including AR Sco (top left).

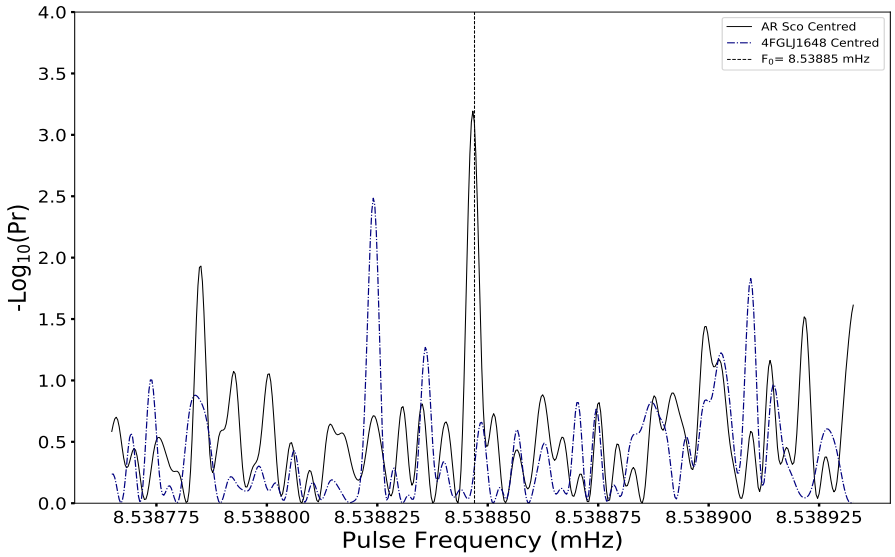

Figure 4.29: Rayleigh power spectra for 4FGL J1648.1-1547 (dot-dash line) compared to regions 2° (red), 3° (violet) and 5° (blue) away from the coordinates centred on AR Sco (black).

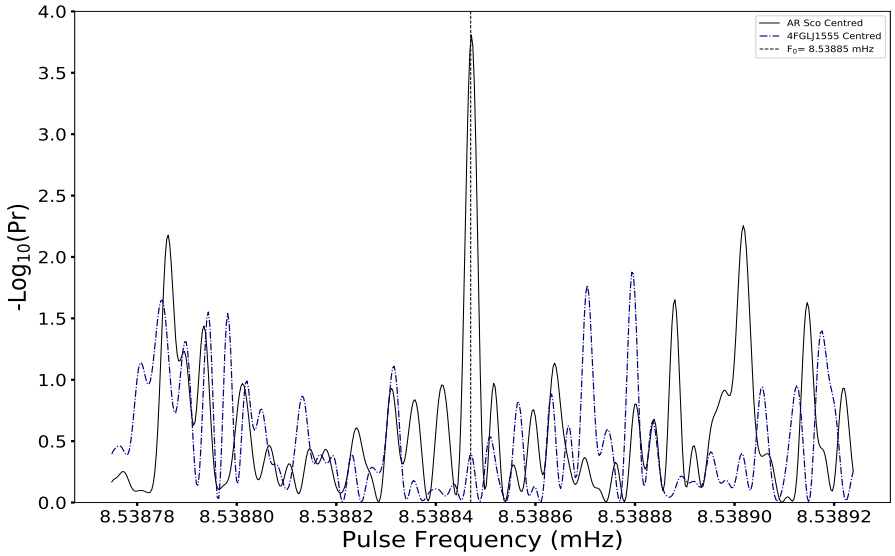

Figure 4.30: Rayleigh power spectra for 4FGL J1555.7-2908 (dot-dash line) compared to regions 2° (red), 3° (violet), 5° (blue) and 8° (green) away from the coordinates centred on AR Sco (black).

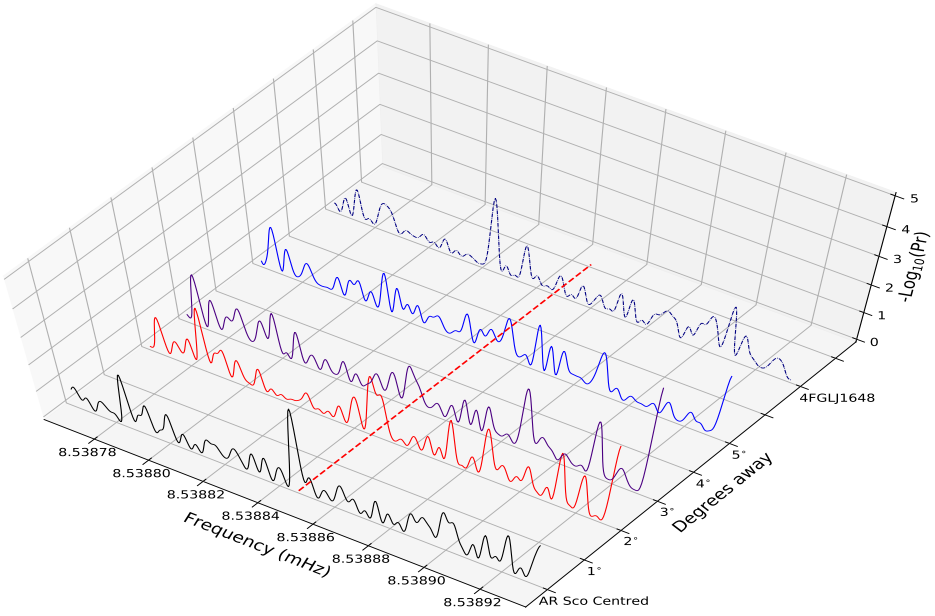

Figure 4.31: Rayleigh power spectra for 4FGL J1648.1-1547 (dot-dash line) compared to regions 2° (red), 3° (violet), 5° (blue) away from the coordinates centred on AR Sco (black).

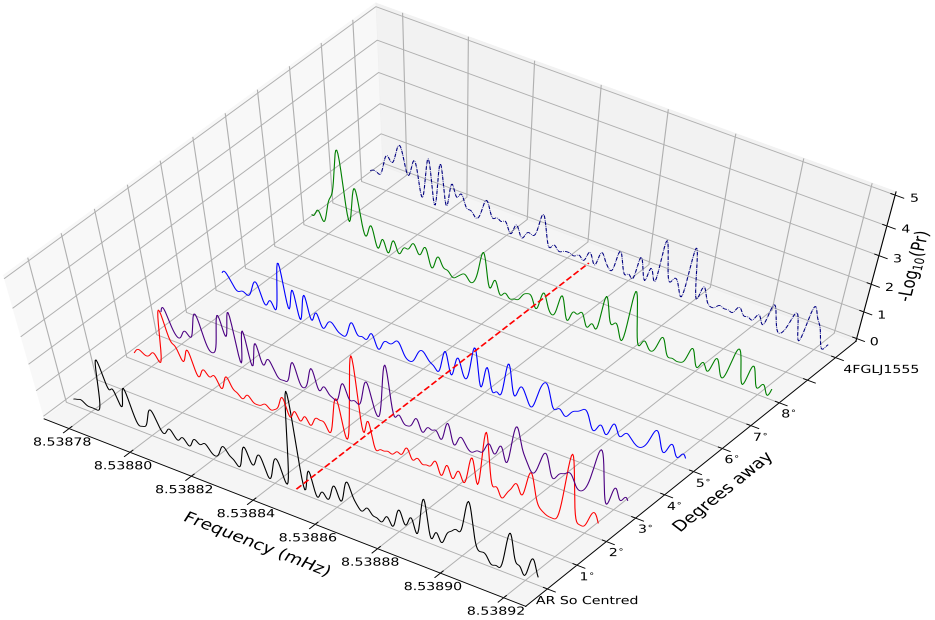

Figure 4.32: Rayleigh power spectra for 4FGL J1555.7-2908 (dot-dash line) compared to regions 2° (red), 3° (violet), 5° (blue) and 8° (green) away from the coordinates centred on AR Sco (black).

4.4.4 Event selection periodograms

Rayleigh tests were also performed over shorter periods within the 10-year light curve (see Fig. 4.8), where a bin size of two weeks were chosen for period analysis over the past decade. Selected events with likelihood TS values greater than zero (TS ≥ 0), and where good convergence were obtained, were extracted and used to construct power spectra.

Due to the immense size of the data set, and the fact that the majority of the power spectra obtained show pulsations at noise level[14], only selected spectra where events are above 2σ and which show possible pulsations at the fundamental frequency ($F_0 = 8.53885$ mHz), were used for further analysis. Periodograms were subjected to a frequency range of $8.43552 - 8.64177$ mHz, with a step size ($\nu = 4.134 \times 10^{-7}$ Hz) 0.5 times the Fourier resolution ($\nu = 8.267 \times 10^{-7}$ Hz) and the number of trials set to 500.

Given that a consistent binned timescale is used for each two-week interval within the 10-year data, and that the frequency is consistent within the margin of $\frac{1}{\Delta t}$ (where Δt is the binned interval), the chance probability of n interval ($Pr_i, i = 1, ..., n$) at a given frequency can be combined incoherently (Eadie et al., 1971). This method results in a loss of phase information of the pulsed emission and only requires the summation of power at fixed frequencies, which will give a χ^2 distributed statistic with $2k$ degrees of freedom in the absence of a signal,

$$\chi^2_{2k}(\nu) = -2 \sum_{i=1}^{k} ln(Pr_i^{\nu}). \tag{4.13}$$

If a consistent but weak signal is present in each individual interval, it will result in a summation and eventually lead to a more significant detection. A combined spectrum of the selected spectra above 2σ (see Fig. 4.34) used is shown in Fig. 4.33. The χ^2_{2k} probability distribution was calculated using `scipy`'s built-in statistical

[14]See Appendix B for power spectra obtained at noise level.

function `chi2.pdf`[15]. This distribution is known as the probability distribution function (pdf). A notable peak to the left of the spin frequency is more than one Fourier spacing away, which dissociates it from the fundamental spin frequency. Due to the overall low significance of possible signals at the fundamental spin frequency only the previously mentioned events were chosen for stacking, in an attempt to minimise the possibility of stacking noise. The possibility, however, still exist that these selected events may just be noise. Hence, control tests are needed to verify the validity of the signal.

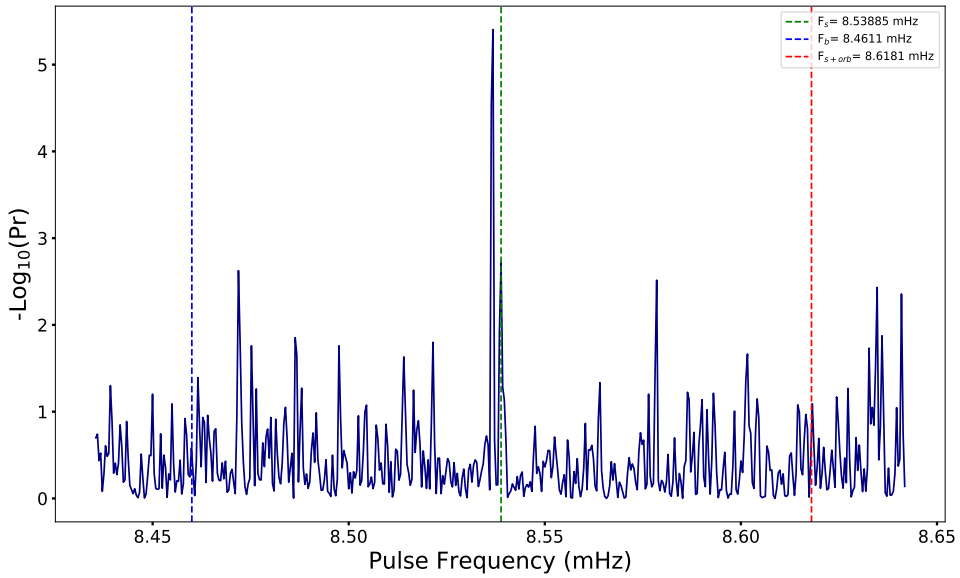

Figure 4.33: Combined Rayleigh power spectrum, with $2k = 12$ degrees of freedom in the energy range 100 MeV - 30 GeV for AR Sco. Line markers added showing the fundamental spin frequency ($F_s = 8.53885$ mHz), beat frequency ($F_b = 8.4611$ mHz) and the spin plus orbital frequency ($F_{s+orb} = 8.6181$ mHz) of the white dwarf in AR Sco.

[15] `https://docs.scipy.org/doc/scipy/reference/reference/generated/scipy.stats.chi.html` for reference. Accessed 15/10/2021.

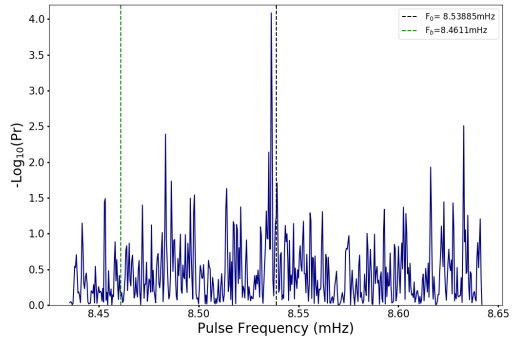

(a) 2009-08-18 (55061 MJD)

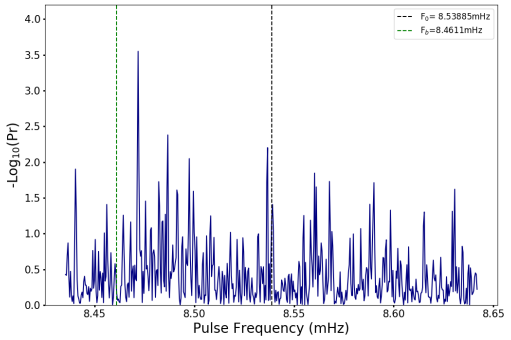

(b) 2010-11-24 (55524 MJD)

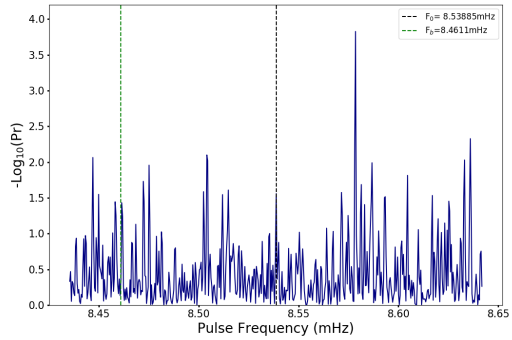

(c) 2011-05-11 (55692 MJD)

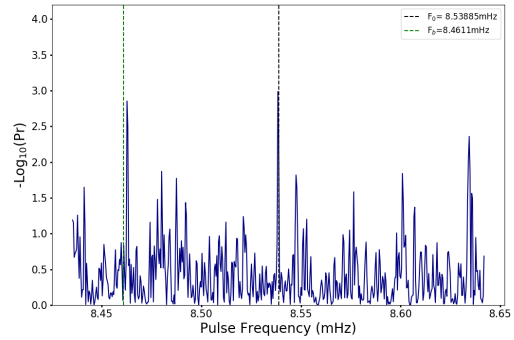

(d) 2014-09-01 (56901 MJD)

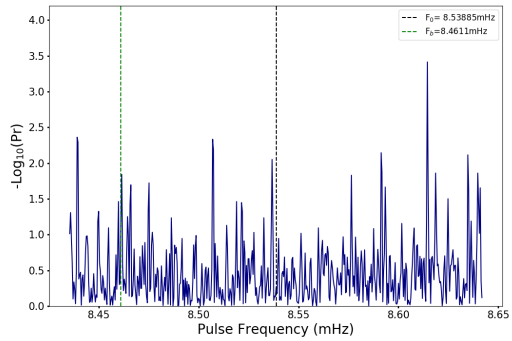

(e) 2017-01-05 (57758 MJD)

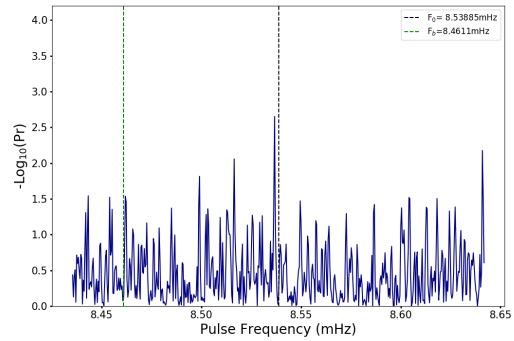

(f) 2017-12-08 (58095 MJD)

Figure 4.34: AR Sco Rayleigh power spectra over selected periods in the 10-year data set. Additional line markers added showing the current model for the fundamental spin frequency (F_0) and beat frequency (F_b) of the white dwarf in AR Sco.

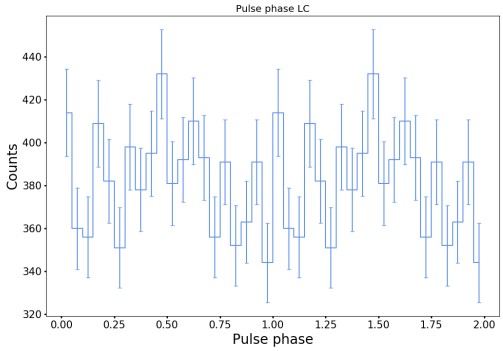

(a) 2009-08-18 (55061 MJD)

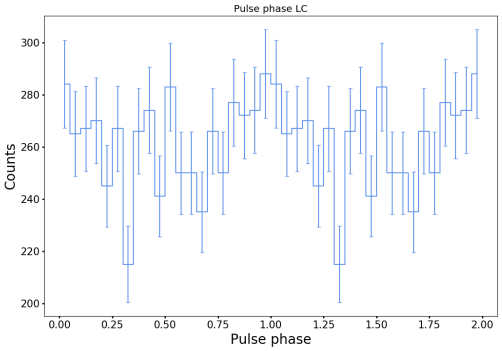

(b) 2010-11-24 (55524 MJD)

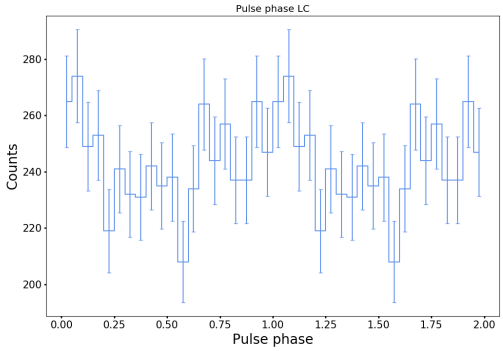

(c) 2011-05-11 (55692 MJD)

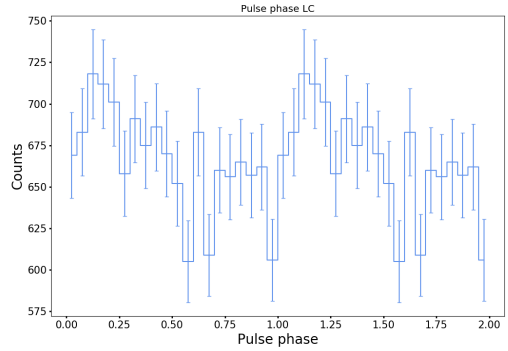

(d) 2014-09-01 (56901 MJD)

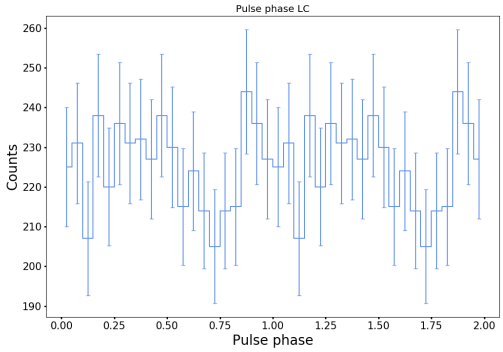

(e) 2017-01-05 (57758 MJD)

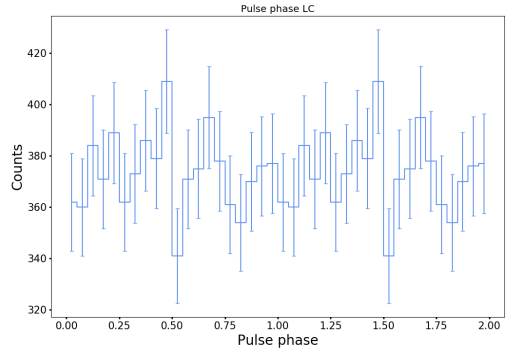

(f) 2017-12-08 (58095 MJD)

Figure 4.35: AR Sco pulse phase profiles over selected periods in the 10-year data set, folded on the fundamental frequency ($F_0 = 8.53885$ mHz).

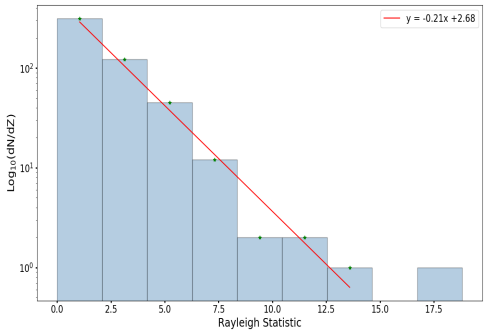

(a) 2009-08-18 (55061 MJD)

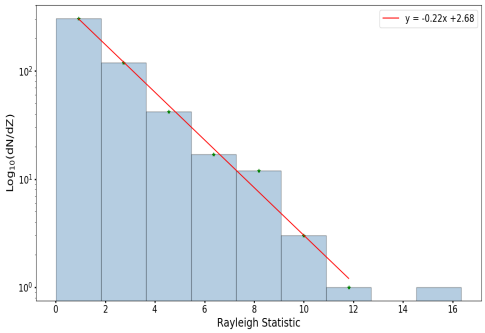

(b) 2010-11-24 (55524 MJD)

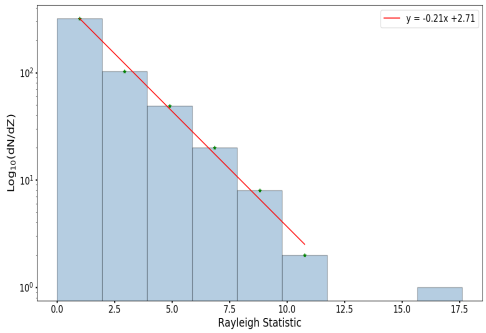

(c) 2011-05-11 (55692 MJD)

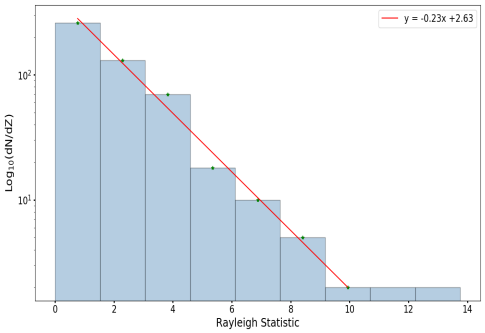

(d) 2014-09-01 (56901 MJD)

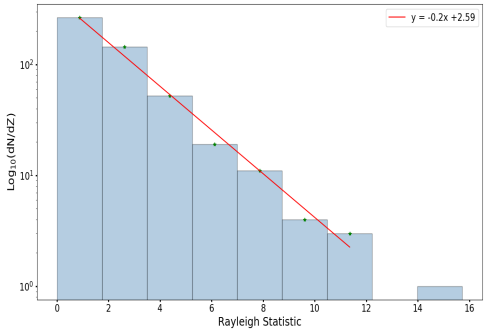

(e) 2017-01-05 (57758 MJD)

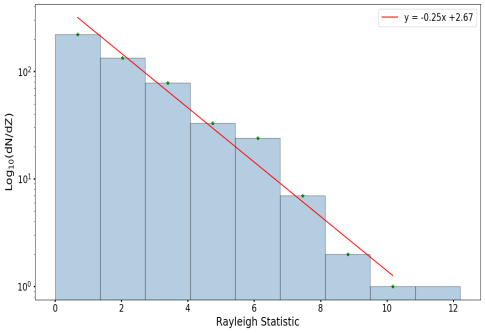

(f) 2017-12-08 (58095 MJD)

Figure 4.36: AR Sco histogram of the Rayleigh distribution in the energy range 100 MeV − 30 GeV for selected events.

4.4.5 Event selection control test

The selected events periodograms were subjected to the same control test at region farther away from AR Sco's coordinates (see Fig. 4.37 and 4.38). A region of 5° away (see Fig 4.23), was chosen to determine if the Rayleigh power decreases in strength as one move farther away from the coordinates centred on AR Sco.

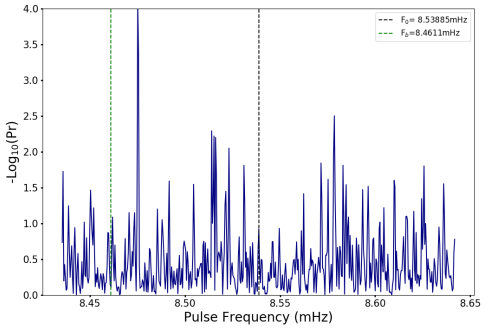

(a) 2011-05-11 (55692 MJD)

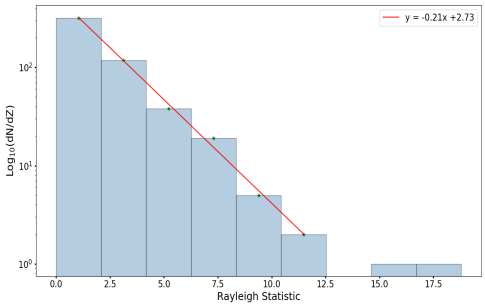

(b) 2011-05-11 (55692 MJD)

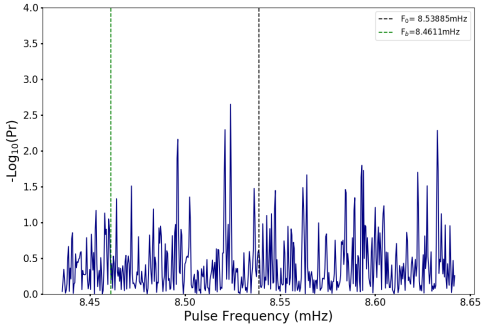

(c) 2009-08-18 (55061 MJD)

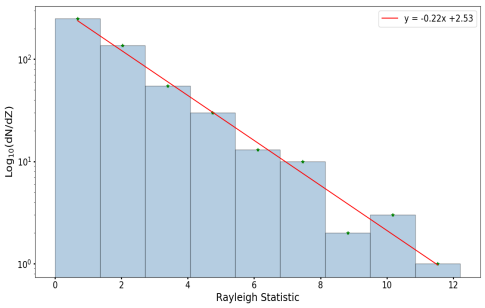

(d) 2009-08-18 (55061 MJD)

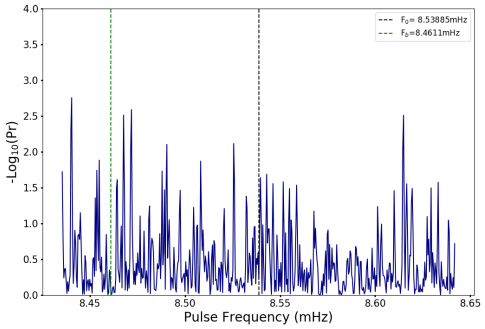

(e) 2010-11-24 (55524 MJD)

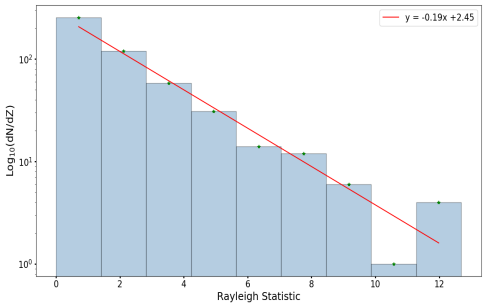

(f) 2010-11-24 (55524 MJD)

Figure 4.37: AR Sco Rayleigh spectra and histogram of the Rayleigh distribution in the energy range 100 MeV - 30 GeV for selected events 5° away from the ROI centre.

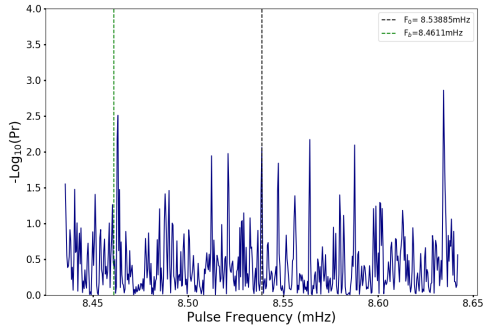

(a) 2014-09-01 (56901 MJD)

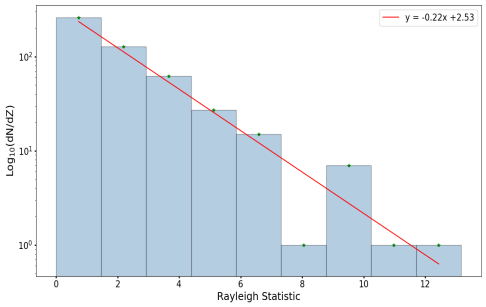

(b) 2014-09-01 (56901 MJD)

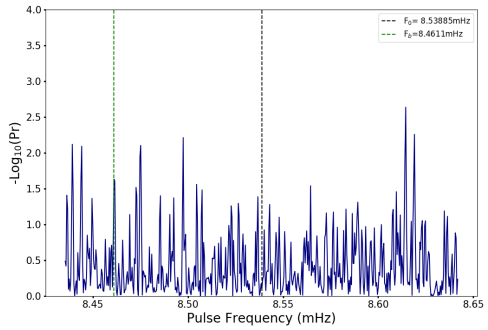

(c) 2017-01-05 (57758 MJD)

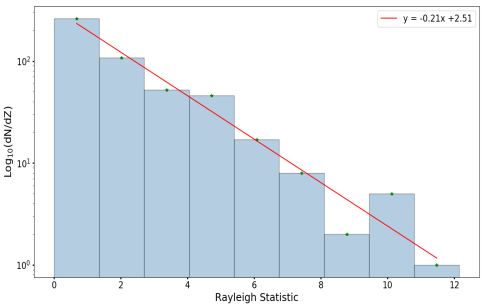

(d) 2017-01-05 (57758 MJD)

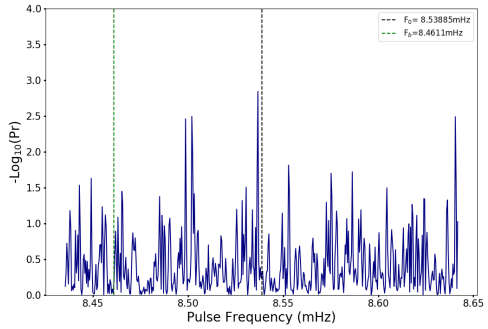

(e) 2017-12-08 (58095 MJD)

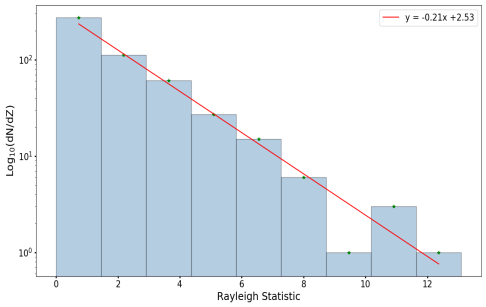

(f) 2017-12-08 (58095 MJD)

Figure 4.38: AR Sco Rayleigh spectra and histogram of the Rayleigh distribution in the energy range 100 MeV - 30 GeV for selected events 5° away from the ROI centre, continued.

From the results obtained in Fig. 4.17, there appears to be evidence of a power peak centred at the current ephemeris model frequency for the spin period $\nu_{\rm spin}$ = 8.53885 mHz (117.11 s). Compared to the model frequency obtained by Takata et al. (2018), $\nu_{\rm spin}$ = 8.5390 mHz (117.1 s), the periodogram frequency of our current analysis is much narrower and focused on a more precise value for the

white dwarf's spin frequency. This value is well within the power peaks from the periodograms (see Fig. 2.18) obtained by Takata et al. (2018).

Validity tests performed also appears to suggest a possible low-level pulsation at the spin frequency. The histogram of Rayleigh power distribution considering the 10-year period (see Fig. 4.22) reveals a deviation from the white noise profile at higher Rayleigh statistics, suggesting pulsed power above the noise level. Compared to regions farther away from the ROI centre (see Fig. 4.23), where no known γ-ray emission is visible and only background noise is considered, it appears that the Rayleigh power at the fundamental spin frequency is decreasing in strength as one moves farther away from the position centred on the coordinates of AR Sco. Independent source analysis, considering the same locations from AR Sco and its surrounding regions within the ROI, also appears to show similar features of a decrease in Rayleigh power, regardless of how the ROI is chosen. Even though the validity test appears to show a possible signal within the noise structure, confirmation of this signal can only be considered through farther examination and studies.

Considering certain event selection periodograms within the 10-year period, power peaks also appear to be visible at selected events. Control tests for these periodograms also appear to show a decrease in signal strength farther away from the source, except on 8 December 2017 (58095 MJD). Hence, no confirmation of a signal on this date can be justified. Further investigation, e.g., using an updated ephemeris or more sensitive instruments, is however necessary to confirm the nature of these periodograms, and constrain the necessary parameters for future studies. It is, however, possible to isolate these events and explore them on shorter time scales, but due to lower photon counts at these time scales using *Fermi*, and influences from the surrounding regions, it will prove difficult to obtain significant detections.

Chapter 5

Discussion and Conclusion

The aim of this study was to search for high-energy non-thermal emission from the close binary AR Sco. A general overview was given regarding the main properties of AR Sco to identify signatures at other wavelengths which could be used to search for similar features at higher energies, such as pulsed non-thermal emission. Previous studies revealed that AR Sco shows pulsed non-thermal synchrotron emission from radio (e.g., Marcote et al., 2017; Marsh et al., 2016; Stanway et al., 2018) to X-ray (e.g., Takata et al., 2018) wavelengths. In addition, optical observations also show pulsed emission, with high levels of linear polarisations from the white dwarf indicating a non-thermal synchrotron component (Buckley et al., 2017). Also, due to the absence of accretion in the system pulsar-like scenarios and mechanisms are inferred for particle acceleration within AR Sco.

Therefore, LAT data from the past decade (2008-2019) utilising the *Fermi* γ-ray space telescope was used to search for high-energy non-thermal emission above 100 MeV. Binned and un-binned likelihood analyses using *Fermi*-LAT data did not result in any significant detection ($\sim 3\sigma$), but did however produce upper-limit values between 100 MeV and 500 GeV. A 10-year light curve revealed an increase in photon flux over certain periods in the past decade. Upon further investigation, an external source (revealed to be a powerful quasar) went into a

flaring period, contributing to the observed emission from AR Sco's ROI. Due to AR Sco's location close to the Galactic Plane and the Rho Oph cloud, as well as the fact that only upper-limit values were obtained during this study, it is difficult to constrain the emission from AR Sco's coordinates, especially with *Fermi*-LAT's low spatial resolution at lower energies. However, based on the non-thermal emission from X-ray observations (Takata et al., 2018), as well as the observed upper-limit values from *Fermi*-LAT data between 100 MeV and 500 GeV, the possibility for high-energy emission from AR Sco cannot be excluded.

As part of this study, the observed upper-limit values were included in an updated SED (see Fig. 4.6), along with archival data from radio to X-ray. From the SED it can be seen that the observed upper-limit flux is around the *Fermi*-LAT's sensitivity threshold, however the low-level emission from AR Sco cannot definitively be resolved. The SED also shows that additional analyses from hard X-ray and soft γ-rays should be included in an attempt to resolve the possible non-thermal emission over multiple wavelengths, and identify the exact nature of a particle accelerator in the system. As previously described, one of the possibilities to accelerate charged particles is the rapid rotation in conjunction to the strong magnetic field of the white dwarf, which can drive synchrotron emission across most of the electromagnetic spectrum (e.g., Buckley et al., 2017; Geng et al., 2016; Marsh et al., 2016; Takata et al., 2017).

Hence, due to the external contributing factors, timing analyses were therefore performed on the extracted *Fermi*-LAT data (covering energies of 100 MeV to 30 GeV) to search for any periodicities at noise level. This energy range was chosen to include Galactic background noise to act as a white noise "buffer" at lower energy intervals (100 MeV - 250 GeV), as well as include any possible signals from AR Sco above the background noise. Since periodograms at radio, optical (e.g., Marsh et al., 2016) and X-ray Takata et al. (2018) all appear to show a signal at the spin ($P_s = 117$ s) and beat period ($P_b = 118.2$ s) of the white dwarf, Rayleigh periodograms were produced to search for similar signals at higher energies. From

these periodograms there appears to be a low-power signal at the spin period, but not at the beat period of the white dwarf. To test whether this signal is part of the noise structure, control tests at regions farther away from AR Sco's coordinates (where no γ-ray emission is present) were conducted, along with period analyses at independent γ-ray sources to confirm if the signal is not part of the data set or analysis technique. From these control tests a decrease in Rayleigh power can be observed as the distance away from AR Sco increases, along with dissimilar features within the power spectra of the independent sources compared to that obtained from AR Sco. This strengthens the notion of an apparent signal at the fundamental spin period inherent to the ROI centred on AR Sco.

Alternatively, the possibility exists that high-energy emission can be detected and better constrained with the increased sensitivity of CTA. Compared to *Fermi*-LAT, CTA offers a larger collection area and better angular resolution, which makes observations of faint γ-ray sources much more efficient. Overlapping regions of energy between these two observatories also show that at an energy of about 40 GeV, *Fermi* will be doing measurements within a 10-year period that is comparable in quality to measurements of 100-hour observations with CTA (see Fig. 5.1a). CTA therefore has an advantage over *Fermi*-LAT in terms of observation time and sensitivity (see Fig. 5.1b), which will prove helpful in observations of faint γ-ray sources as well as short-period transient objects. The future CTA system could therefore increase the probability of detection of low-level pulsed high-energy or VHE emission from AR Sco. However, future studies of AR Sco with CTA, and possibly other Cherenkov telescope arrays (e.g., H.E.S.S), should be conducted with close correlation to other multi-wavelength platforms (especially *Fermi*-LAT) to determine the parameters and origin of the postulated high-energy non-thermal emission.

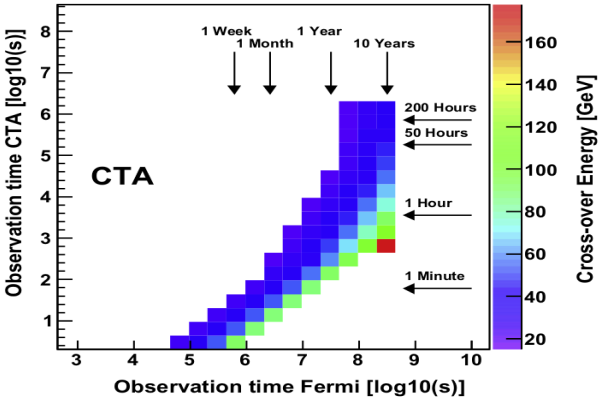

(a)

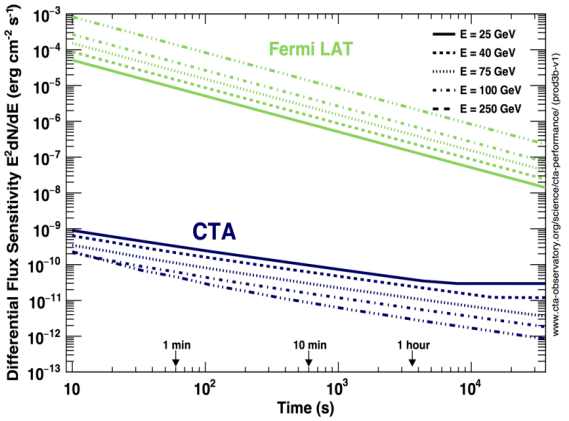

(b)

Figure 5.1: Comparison of *Fermi*-LAT and CTA energy region relative to observation time. Where (a) is the cross-over energy as a function of *Fermi*-LAT and CTA observation time and (b) the differential sensitivity at selected energies as a function of observation time. Adopted from Funk et al. (2012).

AR Sco is relatively new in the astrophysical community and more studies should be performed over the electromagnetic spectrum to constrain the source's emission properties and evolution. This may help to find similar sources of this nature, if any, and/or determine the class of binary sources to which AR Sco belongs.

Bibliography

Abdo, A. A., Ackermann, M., Ajello, M., et al. 2009, Bright Active Galactic Nuclei Source List from the First Three Months of the Fermi Large Area Telescope All-Sky Survey, ApJ, 700, 597, doi: 10.1088/0004-637X/700/1/597

Abdo, A. A., Ackermann, M., Ajello, M., et al. 2010, The First Fermi Large Area Telescope Catalog of Gamma-ray Pulsars, ApJS, 187, 460, doi: 10.1088/0067-0049/187/2/460

Abdo, A. A., Ajello, M., Allafort, A., et al. 2013, The Second Fermi Large Area Telescope Catalog of Gamma-Ray Pulsars, ApJS, 208, 17, doi: 10.1088/0067-0049/208/2/17

Abdollahi, S., Acero, F., Ackermann, M., et al. 2020, Fermi Large Area Telescope Fourth Source Catalog, ApJS, 247, 33. https://arxiv.org/abs/1902.10045

Achterberg, B. 2008, Cosmic Accelerators, in Notes prepared for the AIC2008

Ackermann, M., Ajello, M., Albert, A., et al. 2012, The Fermi Large Area Telescope on Orbit: Event Classification, Instrument Response Functions, and Calibration, ApJS, 203, 4, doi: 10.1088/0067-0049/203/1/4

Ackermann, M., Ajello, M., Albert, A., et al. 2014, Fermi establishes classical novae as a distinct class of gamma-ray sources, Science, 345, 554, doi: 10.1126/science.1253947

Ajello, M., Arimoto, M., Axelsson, M., et al. 2019, A Decade of Gamma-Ray Bursts Observed by Fermi-LAT: The Second GRB Catalog, ApJ, 878, 52, doi: 10.3847/1538-4357/ab1d4e

Atwood, W. B., Abdo, A. A., Ackermann, M., et al. 2009, The Large Area Telescope on the Fermi Gamma-Ray Space Telescope Mission, ApJ, 697, 1071, doi: 10.1088/0004-637X/697/2/1071

Badhwar, G. D., Daniel, R. R., Cleghorn, T., et al. 1977, The cosmic-ray antiproton flux: an upper limit near that predicted for secondary production., ApJ, 217, L135, doi: 10.1086/182556

Barrett, P., Schlegel, E., de Jager, O. C., & Chanmugam, G. 1995, High-Energy Gamma Rays from Polars, ApJ, 450, 334, doi: 10.1086/176143

Barrett, P. E., Dieck, C., Beasley, A. J., Singh, K. P., & Mason, P. A. 2017, A Jansky VLA Survey of Magnetic Cataclysmic Variable Stars. I. The Data, AJ, 154, 252, doi: 10.3847/1538-3881/aa93ff

Bastian, T. S., Dulk, G. A., & Chanmugam, G. 1988, Radio Flares from AE Aquarii: A Low-Power Analog to Cygnus X-3?: Erratum, ApJ, 330, 518, doi: 10.1086/166489

Becker, W., & Trumper, J. 1997, The X-ray luminosity of rotation-powered neutron stars., A&A, 326, 682. https://arxiv.org/abs/astro-ph/9708169

Bednarek, W. 2018, Hadronic model for the non-thermal radiation from the binary system AR Scorpii, MNRAS, 476, L10, doi: 10.1093/mnrasl/sly022

Bregeon, J., Charles, E., & Wood, M. 2013, Fermi-LAT data reprocessed with updated calibration constants, arXiv e-prints, arXiv:1304.5456. https://arxiv.org/abs/1304.5456

Bruel, P., Burnett, T. H., Digel, S. W., et al. 2018, Fermi-LAT improved Pass~8 event selection, arXiv e-prints, arXiv:1810.11394. https://arxiv.org/abs/1810.11394

Buckley, D. A. H., Meintjes, P. J., Potter, S. B., Marsh, T. R., & Gänsicke, B. T. 2017, Polarimetric evidence of a white dwarf pulsar in the binary system AR Scorpii, Nature Astronomy, 1, 0029, doi: 10.1038/s41550-016-0029

Butters, O. W., Katajainen, S., Norton, A. J., Lehto, H. J., & Piirola, V. 2009, Circular polarization survey of intermediate polars I. Northern targets in the range 17 h $<$ RA $<$ 23 h, A&A, 496, 891, doi: 10.1051/0004-6361/200811058

Carroll, B. W., & Ostlie, D. A. 2014, An introduction to modern astrophysics and cosmology (Pearson Education Ltd.)

Cerutti, B., & Beloborodov, A. M. 2017, Electrodynamics of Pulsar Magnetospheres, Space Sci. Rev., 207, 111, doi: 10.1007/s11214-016-0315-7

Charpinet, S., Fontaine, G., & Brassard, P. 2009, Seismic evidence for the loss of stellar angular momentum before the white-dwarf stage, Nature, 461, 501, doi: 10.1038/nature08307

Cheng, A. F. 1989, Eclipsing Millisecond Pulsar: Excitation of the Companion Wind, ApJ, 339, 291, doi: 10.1086/167296

Cheng, K. S., Ho, C., & Ruderman, M. 1986, Energetic Radiation from Rapidly Spinning Pulsars. II. VELA and Crab, ApJ, 300, 522, doi: 10.1086/163830

Cheung, C. C., Jean, P., Shore, S. N., et al. 2016, Fermi-LAT Gamma-Ray Detections of Classical Novae V1369 Centauri 2013 and V5668 Sagittarii 2015, ApJ, 826, 142, doi: 10.3847/0004-637X/826/2/142

Coppejans, D. L., Körding, E. G., Miller-Jones, J. C. A., et al. 2016, Dwarf nova-type cataclysmic variable stars are significant radio emitters, MNRAS, 463, 2229, doi: 10.1093/mnras/stw2133

Coroniti, F. V. 1990, Magnetically Striped Relativistic Magnetohydrodynamic Winds: The Crab Nebula Revisited, ApJ, 349, 538, doi: 10.1086/168340

Cropper, M. 1990, The Polars, Space Sci. Rev., 54, 195, doi: 10.1007/BF00177799

de Jager, O. C., Raubenheimer, B. C., & Swanepoel, J. W. H. 1989, A powerful test for weak periodic signals with unknown light curve shape in sparse data., A&A, 221, 180

Drake, A. J., Djorgovski, S. G., Mahabal, A., et al. 2009, First Results from the Catalina Real-Time Transient Survey, ApJ, 696, 870, doi: 10.1088/0004-637X/696/1/870

du Plessis, L., Venter, C., Wadiasingh, Z., et al. 2022, Probing the non-thermal emission geometry of AR Sco via optical phase-resolved polarimetry, MNRAS, 510, 2998, doi: 10.1093/mnras/stab3595

Du Plessis, L., Wadiasingh, Z., Venter, C., et al. 2018, Modelling the polarisation signatures detected from the first white dwarf pulsar AR Sco., in High Energy Astrophysics in Southern Africa (HEASA2018, 27

Dubus, G., Taam, R. E., Hull, C., Watson, D. M., & Mauerhan, J. C. 2007, Spitzer Space Telescope Observations of the Magnetic Cataclysmic Variable AE Aquarii, ApJ, 663, 516, doi: 10.1086/518407

Eadie, W. T., Drijard, D., & James, F. E. 1971, Statistical methods in experimental physics (Amsterdam : North-Holland)

Fermi, E. 1949, On the Origin of the Cosmic Radiation, Physical Review, 75, 1169, doi: 10.1103/PhysRev.75.1169

Ferrario, L. 1996, Accretion curtains in magnetic CVs, PASA, 13, 87

Ferrario, L., de Martino, D., & Gänsicke, B. T. 2015, Magnetic White Dwarfs, Space Sci. Rev., 191, 111, doi: 10.1007/s11214-015-0152-0

Fruchter, A. S., Gunn, J. E., Lauer, T. R., & Dressler, A. 1988, Optical detection and characterization of the eclipsing pulsar's companion, Nature, 334, 686, doi: 10.1038/334686a0

Gaibor, Y., Garnavich, P. M., Littlefield, C., Potter, S. B., & Buckley, D. A. H. 2020, An improved spin-down rate for the proposed white dwarf pulsar AR scorpii, MNRAS, 496, 4849, doi: 10.1093/mnras/staa1901

Garnavich, P., Littlefield, C., Kafka, S., et al. 2019, Driving the Beat: Time-resolved Spectra of the White Dwarf Pulsar AR Scorpii, ApJ, 872, 67, doi: 10.3847/1538-4357/aafb2c

Geng, J.-J., Zhang, B., & Huang, Y.-F. 2016, A Model of White Dwarf Pulsar AR Scorpii, ApJ, 831, L10, doi: 10.3847/2041-8205/831/1/L10

Ghisellini, G. 2013, Radiative Processes in High Energy Astrophysics, Vol. 873, doi: 10.1007/978-3-319-00612-3

Giovannelli, F. 2008, Cataclysmic Variables: A Review, Chinese Journal of Astronomy and Astrophysics Supplement, 8, 237

Gold, T. 1968, Rotating Neutron Stars as the Origin of the Pulsating Radio Sources, Nature, 218, 731, doi: 10.1038/218731a0

Goldreich, P., & Julian, W. H. 1969, Pulsar Electrodynamics, ApJ, 157, 869, doi: 10.1086/150119

Haerendel, G. 1994, Acceleration from Field-Aligned Potential Drops, ApJS, 90, 765, doi: 10.1086/191901

Hellier, C. 2001, Cataclysmic Variable Stars: How and why they vary? (Springer in accosiation with Praxis Publishing Ltd. Chichester, UK)

Hewish, A., Bell, S. J., Pilkington, J. D. H., Scott, P. F., & Collins, R. A. 1968, Observation of a Rapidly Pulsating Radio Source, Nature, 217, 709, doi: 10.1038/217709a0

Hilditch, R. W. 2001, An Introduction to Close Binary Stars (Cambridge University Press)

Hillas, A. M. 1984, The Origin of Ultra-High-Energy Cosmic Rays, ARA&A, 22, 425, doi: 10.1146/annurev.aa.22.090184.002233

Irwin, J. A. 2007, Astrophysics: Decoding the Cosmos (A Wiley-Interscience publication. Wiley-VCH, Wenheim Germany.)

Jackson, J. D. 1998, Classical Electrodynamics, 3rd Edition (A Wiley-Interscience publication. Wiley-VCH, San Francisco.)

Joshi, G. 2019, The introductory characteristics of variable stars and their importance

Kamae, T., Lee, S.-H., Makishima, K., Shibata, S., & Shigeyama, T. 2018, Evidence for GeV cosmic rays from white dwarfs in the local cosmic ray spectra and in the gamma-ray emissivity of the inner Galaxy, PASJ, 70, 29, doi: 10.1093/pasj/psy010

Katz, J. I. 2017, AR Sco: A Precessing White Dwarf Synchronar?, ApJ, 835, 150, doi: 10.3847/1538-4357/835/2/150

Kuiper, L., Hermsen, W., Cusumano, G., et al. 2001, The Crab pulsar in the 0.75-30 MeV range as seen by CGRO COMPTEL. A coherent high-energy picture from soft X-rays up to high-energy gamma-rays, A&A, 378, 918, doi: 10.1051/0004-6361:20011256

Littlefield, C., Garnavich, P., Kennedy, M., et al. 2017, Long-term Photometric Variations in the Candidate White-dwarf Pulsar AR Scorpii from K2, CRTS, and ASAS-SN Observations, ApJ, 845, L7, doi: 10.3847/2041-8213/aa8300

Longair, M. S. 1992, High energy astrophysics. Vol.1: Particles, photons and their detection (Cambridge University Press)

Lyutikov, M., Barkov, M., Route, M., et al. 2020, Magnetospheric interaction in white dwarf binaries AR Sco and AE Aqr, arXiv e-prints, arXiv:2004.11474. https://arxiv.org/abs/2004.11474

Marcote, B., Marsh, T. R., Stanway, E. R., Paragi, Z., & Blanchard, J. M. 2017, Towards the origin of the radio emission in AR Scorpii, the first radio-pulsing white dwarf binary, A&A, 601, L7, doi: 10.1051/0004-6361/201730948

Mardia, K. 1972, Statistics of Directional Data (Academic Press Inc., London), 77

Marsh, T. R., Gänsicke, B. T., Hümmerich, S., et al. 2016, A radio-pulsing white dwarf binary star, Nature, 537, 374, doi: 10.1038/nature18620

Mattox, J. R., Bertsch, D. L., Chiang, J., et al. 1996, The Likelihood Analysis of EGRET Data, ApJ, 461, 396, doi: 10.1086/177068

Mauche, C. W., Abada-Simon, M., Desmurs, J. F., et al. 2012, Multiwavelength campaign of observations of AE Aqr., Mem. Soc. Astron. Italiana, 83, 651. https://arxiv.org/abs/1111.1190

Meintjes, P. 2015, The Physics of Transient High-Energy Cosmic Sources: from Radio to VHE Gamma-rays, in XI Multifrequency Behaviour of High Energy Cosmic Sources Workshop (MULTIF15), 31

Meintjes, P. 2017, On the multi-frequency emission and evolution of the white dwarf pulsar binary system AR Scorpii, in XII Multifrequency Behaviour of High Energy Cosmic Sources Workshop (MULTIF2017), 44

Meintjes, P. J. 2004, Magnetized fragmented mass transfer in cataclysmic variables: AE Aquarii, a trial case, MNRAS, 352, 416, doi: 10.1111/j.1365-2966.2004.07898.x

Meintjes, P. J. 2018, On the multi-frequency emission and evolution of the white dwarf pulsar binary system AR Scorpii, PoS, MULTIF2017, 044, doi: 10.22323/1.306.0044

Meintjes, P. J., & Breedt, E. 2015, Magnetic viscosity: outbursts and outflows in accretion driven systems, Mem. Soc. Astron. Italiana, 86, 89

Meintjes, P. J., & de Jager, O. C. 2000, Propeller spin-down and the non-thermal emission from AE Aquarii, MNRAS, 311, 611, doi: 10.1046/j.1365-8711.2000.03125.x

Meintjes, P. J., & Jurua, E. 2006, Secondary star magnetic fields in close binaries, MNRAS, 372, 1279, doi: 10.1111/j.1365-2966.2006.10933.x

Meintjes, P. J., Raubenheimer, B. C., de Jager, O. C., et al. 1992, AE Aquarii: an Emitter of Pulsed TeV Gamma Rays Resembling Optical Emission during Flares, ApJ, 401, 325, doi: 10.1086/172063

Meintjes, P. J., de Jager, O. C., Raubenheimer, B. C., et al. 1991, Transient Quasi Coherent Tev Gamma-Rays from AE Aquarii, in IAU Colloq. 129: The 6th Institute d'Astrophysique de Paris (IAP) Meeting: Structure and Emission Properties of Accretion Disks, ed. C. Bertout, S. Collin-Souffrin, & J. P. Lasota, 483

Oruru, B., & Meintjes, P. J. 2012, X-ray characteristics and the spectral energy distribution of AE Aquarii, MNRAS, 421, 1557, doi: 10.1111/j.1365-2966.2012.20410.x

Parker, E. N. 1976, The Acceleration of Particles to High Energy, in NATO Advanced Study Institute (ASI) Series C, Vol. 28, The Physics of Non-Thermal Radio Sources, ed. G. Setti, 137

Patterson, J. 1994, The DQ Herculis Stars, PASP, 106, 209, doi: 10.1086/133375

Potter, S. B., & Buckley, D. A. H. 2018a, A reevaluation of the proposed spin-down of the white dwarf pulsar in AR Scorpii, MNRAS, 478, L78, doi: 10.1093/mnrasl/sly078

Potter, S. B., & Buckley, D. A. H. 2018b, Time series photopolarimetry and modelling of the white dwarf pulsar in AR Scorpii, MNRAS, 481, 2384, doi: 10.1093/mnras/sty2407

Potter, S. B., Romero-Colmenero, E., Kotze, M., et al. 2012, On the spin modulated circular polarization from the intermediate polars NY Lup and IGR J15094-6649, MNRAS, 420, 2596, doi: 10.1111/j.1365-2966.2011.20232.x

Pretorius, M. L., & Mukai, K. 2014, Constraints on the space density of intermediate polars from the Swift-BAT survey, MNRAS, 442, 2580, doi: 10.1093/mnras/stu990

Punsly, B., Rodríguez, L. F., Tingay, S. J., & Cellone, S. A. 2005, PKS 1622-253: A Weakly Accreting, Powerful Gamma-Ray Source, ApJ, 633, L93, doi: 10.1086/498307

Ritter, H. 1988, Turning on and off mass transfer in cataclysmic binaries., A&A, 202, 93

Roberts, M. S. E. 2013, Surrounded by spiders! New black widows and redbacks in the Galactic field, in Neutron Stars and Pulsars: Challenges and Opportunities after 80 years, ed. J. van Leeuwen, Vol. 291, 127–132, doi: 10.1017/S174392131202337X

Rybicki, G. B., & Lightman, A. P. 2004, Radiative Processes in Astrophysics (A Wiley-Interscience publication. Wiley-VCH,, Wenheim Germany)

Sato, M. 1958, Notes on the Magnetic Mirror Effect, Progress of Theoretical Physics, 20, 737, doi: 10.1143/PTP.20.737

Satyvaldiev, V. 1971, On seventeen variable stars., Astronomicheskij Tsirkulyar, 633, 7

Schlegel, E. M., Barrett, P. E., de Jager, O. C., et al. 1995, Gamma-Ray Emission from Cataclysmic Variables. I. The Compton EGRET Survey, ApJ, 439, 322, doi: 10.1086/175175

Singh, K. K., Meintjes, P. J., Kaplan, Q., Ramamonjisoa, F. A., & Sahayanathan, S. 2020, Modelling the broadband emission from the white dwarf

binary system AR Scorpii, Astroparticle Physics, 123, 102488, doi: 10.1016/j.astropartphys.2020.102488

Smak, J. 1985, Cataclysmic variables, in Multifrequency Behaviour of Galactic Accreting Sources, 3

Smith, R. C. 2007, Cataclysmic Variables, arXiv e-prints, astro. https://arxiv.org/abs/astro-ph/0701654

Spitzer, L. 1956, Physics of Fully Ionized Gases (Interscience Publishers Inc., New York)

Stanway, E. R., Marsh, T. R., Chote, P., et al. 2018, VLA radio observations of AR Scorpii, A&A, 611, A66, doi: 10.1051/0004-6361/201732380

Stephens, S. A., & Badhwar, G. D. 1981, Production Spectrum of Gamma-Rays in Interstellar Space Through Neutral Pion Decay, Ap&SS, 76, 213, doi: 10.1007/BF00651256

Sterken, C., & Jaschek, C. 2005, Light Curves of Variable Stars (Cambridge University Press)

Stiller, R. A., Littlefield, C., Garnavich, P., et al. 2018, High-time-resolution Photometry of AR Scorpii: Confirmation of the White Dwarf's Spin-down, AJ, 156, 150, doi: 10.3847/1538-3881/aad5dd

Szkody, P., & Gaensicke, B. T. 2012, Cataclysmic Variables, Journal of the American Association of Variable Star Observers (JAAVSO), 40, 563

Takata, J., Hu, C. P., Lin, L. C. C., et al. 2018, A Non-thermal Pulsed X-Ray Emission of AR Scorpii, ApJ, 853, 106, doi: 10.3847/1538-4357/aaa23d

Takata, J., Yang, H., & Cheng, K. S. 2017, A Model for AR Scorpii: Emission from Relativistic Electrons Trapped by Closed Magnetic Field Lines of Magnetic White Dwarfs, ApJ, 851, 143, doi: 10.3847/1538-4357/aa9b33

Terada, Y., Ishida, M., Mukai, K., et al. 2007, A High Sensitive Suzaku Observation of Possible Non-Thermal Emission from a White Dwarf, in ESA Special Publication, Vol. 622, The Obscured Universe. Proceedings of the VI INTEGRAL Workshop, 521

Thompson, D. J., Bertsch, D. L., Fichtel, C. E., et al. 1993, Calibration of the Energetic Gamma-Ray Experiment Telescope (EGRET) for the Compton Gamma-Ray Observatory, ApJS, 86, 629, doi: 10.1086/191793

Usov, V. V. 1988, Generation of Gamma-Rays by a Rotating Magnetic White Dwarf, Soviet Astronomy Letters, 14, 258

van den Heuvel, E. P. J., & van Paradijs, J. 1988, Fate of the companion stars of ultra-rapid pulsars, Nature, 334, 227, doi: 10.1038/334227a0

van Heerden, H. 2015, PhD thesis, University of the Free State. https://scholar.ufs.ac.za/handle/11660/2124

van Soelen, B. 2012, PhD thesis, University of the Free State. https://scholar.ufs.ac.za/xmlui/handle/11660/1919

Warner, B. 2003, Cataclysmic Variable Stars (Cambridge University Press)

Wickramasinghe, D. T., & Ferrario, L. 2000, Magnetism in Isolated and Binary White Dwarfs, PASP, 112, 873, doi: 10.1086/316593

Wickramasinghe, D. T., & Ferrario, L. 2005, The origin of the magnetic fields in white dwarfs, MNRAS, 356, 1576, doi: 10.1111/j.1365-2966.2004.08603.x

Wilks, S. S. 1938, The Large-Sample Distribution of the Likelihood Ratio for Testing Composite Hypotheses, The Annals of Mathematical Statistics, 9, 60 , doi: 10.1214/aoms/1177732360

Wynn, G. A. 2000, Accretion flows in magnetic CVs, New A Rev., 44, 75, doi: 10.1016/S1387-6473(00)00017-8

Appendix A

Particle Acceleration and γ-ray Production

A.1 Introduction

In this chapter a selection of radiative processes will be presented for background theory required to analyze the system in question, i.e. AR Sco. Although this system has both thermal and non-thermal emission properties (Marsh et al., 2016), the primary aim of this study was to search for possible non-thermal γ-ray emission above 100 MeV. Thus, a selection of non-thermal emission and particle acceleration mechanisms will be discussed, primarily focusing on e.g. synchrotron radiation, inverse-Compton (IC) radiation, interactions between particle pairs and decay of radioactive material in the form of π°-decay. The background theory presented here will serve as a framework to either strengthen or eliminate cases put forward for the non-thermal radiative models developed for AR Sco, as presented in Chapter 3. The following brief discussions on particle acceleration and γ-ray production, unless specifically indicated, are referenced from the following sources: Ghisellini 2013; Irwin 2007; Rybicki & Lightman 2004.

A.2 Particle acceleration

Particle acceleration and scattering can be considered as one of the main ingredients in active astrophysical environments, where the acceleration of particles occurs under violent and turbulent conditions, making it difficult to treat analytically. The majority of all cosmic sources radiate their energy through space in the form of thermal and non-thermal radiation. (there are also contributions from escaping particles that carry away significant amounts of energy.) Thermal plasmas are characterised by a Maxwellian distribution of particles and has relatively low temperatures ($\leq 10^{7-8}$K), (e.g., Irwin, 2007), whereas non-thermal plasmas are associated with the acceleration of charged particles in a magnetic or electric field, and require different means to explain their energy distribution.

For particle acceleration to occur in astrophysical plasmas some requirements have to be met, (e.g., Achterberg, 2008)[1]. Firstly the plasmas should be collisionless, otherwise particle-particle collisions will result in thermalization and not acceleration, resulting in thermal radiation. The second requirement is that the plasma should be highly conductive so that ideal Magnetohydrodynamics (MHD) can be satisfied. The following section is based on the discussions made by Achterberg (2008); Meintjes (2015). It can be shown that the magnetic and electric fields in a reference frame co-moving with a highly conducting fluid or plasma can be expressed as

$$\begin{aligned} E' &= \Gamma(E + \frac{1}{c}(\vec{\mathbf{v}} \times B)) \\ B' &= \Gamma(B - \frac{1}{c}(\vec{\mathbf{v}} \times E)), \end{aligned} \tag{A.1}$$

where the primed, $(E'; B')$, and un-primed, $(E; B)$, variables represents the fields in the co-moving (K') and stationary (K) observer's rest frames (i.e. the

[1]See `http://www.rci.uct.ac.za/sites/default/files/image_tool/images/395/Course_Resources/Pieter_Meintjies/ba-lecture.pdf` for reference.

laboratory frame) respectively. Here $\vec{\mathbf{v}} = \vec{\beta}c$ represents the relative bulk flow velocity between the co-moving frame and laboratory frame and $\Gamma = 1/\sqrt{1-\beta^2}$ represents the bulk Lorentz factor.

For a fluid which is highly conductive (i.e., the electrical conductivity $\sigma \longrightarrow \infty$) the electric field in the co-moving frame will reduce to zero ($E' \longrightarrow 0$) which causes the field quantities to change to

$$\begin{aligned} E &= -\Gamma(\beta \times B') \\ B &= \Gamma B', \end{aligned} \tag{A.2}$$

where $\beta = \frac{\vec{\mathbf{v}}}{c}$. This means that the induced electric field plays an important role in the acceleration of individual charged particles and that the motion of these particles is proportional to the bulk flow velocity ($\vec{\mathbf{v}}$) of the magnetized fluid with respect to the laboratory (stationary) reference frame.

It is important to understand that the electric field is responsible for the acceleration of particles and that the magnetic Lorentz force does not accelerate or change the energy of the the particle, but merely deflects the charge. For example, it can be shown that rate of change of kinetic energy of a particle as a result of the magnetic component is given by

$$\begin{aligned} \frac{d\epsilon_{KE}}{dt} &= \vec{\mathbf{v}_p} \cdot \vec{F_{m,L}} \\ &= c\vec{\beta_p} \cdot q\left[\frac{1}{c}(\vec{\mathbf{v}_p} \times \vec{B})\right] \\ &= 0, \end{aligned} \tag{A.3}$$

where $\vec{F_{m,L}}$ is defined as the Lorentz force of the magnetic component. Hence, the magnetic field cannot increase the kinetic energy of the particles, since $\vec{\beta_p} \perp (\vec{\beta_p} \times \vec{B})$. The magnetic field, however, can act as scattering centre for particles,

given that the magnetic fields are transported with the bulk flow velocity ($\vec{\mathbf{v}}$):

$$\begin{aligned}
\frac{d\epsilon_{KE}}{dt} &= \vec{\mathbf{v}_p} \cdot \vec{F_{m,L}} \\
&= \vec{\mathbf{v}_p} \cdot q \left[\vec{E} + (\frac{\vec{\mathbf{v}_p}}{c} \times \vec{B}) \right] \\
&= q\vec{\mathbf{v}_p} \cdot \vec{E} + \frac{q}{c}\vec{\mathbf{v}_p}. \left(\vec{\mathbf{v}_p} \times \vec{B} \right) \\
&= qc\vec{\beta_p} \cdot \vec{E} + qc\vec{\beta_p} \cdot \left(\vec{\beta_p} \times \vec{B} \right) \\
&= qc\vec{\beta_p} \cdot \left(-\vec{\beta} \times \vec{B} \right) + qc \left[\vec{\beta_p} \cdot \left(\vec{\beta_p} \times \vec{B} \right) \right]
\end{aligned} \tag{A.4}$$

By doing some manipulations of vectors and taking note that $\vec{\beta_p} \perp \left(\vec{\beta_p} \times \vec{B} \right) = 0$, the equation reduces to

$$\begin{aligned}
\frac{d\epsilon_{KE}}{dt} &= -qc\vec{\beta_p} \cdot \left[(\vec{\beta} \times \vec{B}) \right] \\
&= -qc\vec{\beta} \cdot \left[(\vec{B} \times \vec{\beta_p}) \right] \\
&= qc\vec{\beta} \cdot \left[(\vec{\beta_p} \times \vec{B}) \right] \\
&= \vec{\beta} \cdot \left[qc(\vec{\beta_p} \times \vec{B}) \right] \\
&= \vec{\beta} \cdot \vec{F}_{m,L},
\end{aligned} \tag{A.5}$$

where $\vec{\beta}$ is the bulk flow velocity and $\vec{F}_{m,L}$ represents the magnetic Lorentz force. These arguments show that particle acceleration in highly conductive magnetized plasmas is in principle a scattering process and applies to the majority of astrophysical environments.

These properties of MHD and astrophysical particle acceleration in magnetized fluids make it possible to place a limit on the energy particles can reach in cosmic accelerators. By integrating over the path length of the particle that is subjected to in the electric field (i.e. ds), the maximum energy which can be achieved by a

charged particle can be determined using:

$$\begin{aligned} \epsilon_{\max} &= Ze \int E.ds \\ &= q\beta\Gamma R_s B', \end{aligned} \tag{A.6}$$

with Ze defined as the charge, $\beta = (\nu/c)$ the velocity and Γ the Lorentz factor. In a fast rotating magnetosphere of a compact object (e.g. NS or an isolated white dwarf), these parameters are associated with the rotational velocity of the source with respect to a stationary observer (K). In the above equation B' and R_s represent the magnetic field in the frame of the source and the size of the source respectively, where $\beta\Gamma$ is associated with the rotational velocity of the compact object's magnetosphere relative to a stationary observer

Thus, equation A.6 plays an important role to calculate the potential of rotating magnetized compact objects, as postulated by Goldreich & Julian (1969), to accelerate charged particles to VHE. The electric field can then be considered as an induced *emf* parallel to the magnetic field lines, as long as there is relative motion between the co-moving frame and the observer. This allows for a very effective mechanism to accelerate charged particles in the magnetosphere of rapidly rotating, highly magnetized compact objects. It can be shown, see Fig. A.1, that charged particles can be accelerated to energies of the order of $\epsilon_{\max} \sim 10^{20}$ eV for white dwarfs with magnetic fields ranging between $\sim 10^5\mathrm{G} - 10^8\mathrm{G}$, (Hillas, 1984).

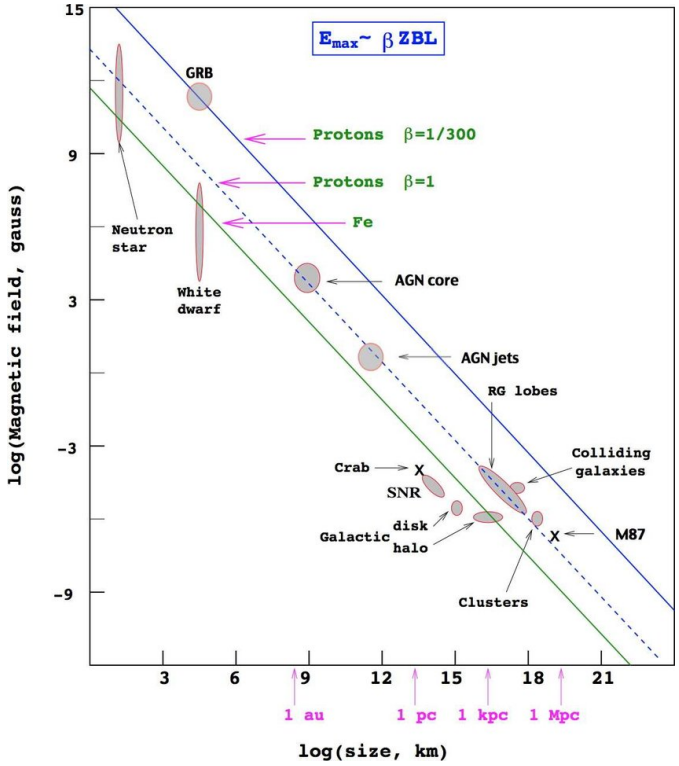

Figure A.1: The Hillas diagram. The typical size of the source is given on the horizontal axis whereas the vertical axis gives the magnetic field strength of a source. The dashed diagonal line correspond to the requirements for a proton with energy 10^{20} eV. Adapted from Hillas (1984).

It was however shown by Usov (1988) that is also possible for fast rotating magnetic white dwarfs to produce γ-ray emission through relativistic particle acceleration. Some white dwarfs have magnetic field strengths and rotation periods similar to that of NS, making fast rotating magnetized white dwarfs a site for particle acceleration processes accompanied with the production of γ-rays, as in the magnetospheres of NS pulsars, (e.g., Cerutti & Beloborodov, 2017). The acceleration of particles in the magnetosphere of a rotating magnetic star is controlled by the electric field structure which is determined by the distribution of ionized gas around the star. Hence, if we consider the scale height of a typical isolated white dwarf, with mass $\approx 1\ M_{\odot}$, size $R_{\rm WD} \approx 10^9$ cm and surface temperature $T_s \leq 10^5$ K to be

$$h \approx \frac{kT_s R^2}{m_p GM} \approx 10^5 \left(\frac{R}{10^9 \mathrm{cm}}\right)^2 \left(\frac{M}{1M_\odot}\right)^{-1} \left(\frac{T_s}{10^5 \mathrm{K}}\right) \mathrm{cm}, \tag{A.7}$$

the particle density in the atmosphere of the white dwarf will consequently drop to zero at a distance of $10^2 h \ll R$. Thus, the white dwarf lacks a hot corona and is not experiencing massive amounts of accretion of gas, effectively making the surrounding area a vacuum. As a result, an electric field is introduced along the conducting magnetic field line with a non-zero component, i.e.

$$E_\parallel = (\mathbf{E} \cdot \mathbf{B}) / B. \tag{A.8}$$

Thus, close to the surface of a fast rotating magnetized white dwarf the force that the electric field exerts on a charged particle will exceed the force from gravitational attraction. This will cause charged particles to flow away from the stellar surface, forming a magnetosphere around it with particle density of approximately

$$n_{\mathrm{GJ}} = \frac{B}{P_s ce} = 7 \times 10^5 \left(\frac{B_p}{10^8 \text{ G}}\right) \left(\frac{P_s}{10 \text{ s}}\right)^{-1} \left(\frac{R}{r}\right)^3 \mathrm{cm}^{-3}, \tag{A.9}$$

where n_{GJ} represents the Goldreich-Julian particle density, (Goldreich & Julian, 1969), P_s the white dwarf's rotation period and $B = B_p(R/r)^3$ represents the field strength at a distance r from the centre. The electric field will nearly be canceled out by the outflowing particles in this region away from the white dwarf, except in the regions that are penetrated by the magnetic field lines that extends beyond the star's light cylinder. In these regions the cancellation of the electric field is incomplete and the particles emerging from the white dwarf are then accelerated. Or gaps may form even within the magnetosphere as sites of particle acceleration.

In terms of energy, these ultra-relativistic particles with Lorentz factors $\approx 10^6$, can generate curvature radiation whose photons have a typical energy of

$$\begin{aligned} E_\gamma &= \frac{3}{2}\frac{c\hbar\gamma^3}{R_c} \\ &= 10^6 \text{ eV}, \end{aligned} \tag{A.10}$$

where $R_c \simeq (cr/\Omega)^{\frac{1}{2}}$ represents the radius of curvature of the field lines, Usov (1988). Curvature radiation is primarily due to field line curvature where the particle slide along the field line. Thus the average energy of the curvature photons generated by the outflowing particles rises with distance from the star, resulting in γ-ray radiation.

Another possibility can be due to burst-like particle acceleration events associated with magnetic reconnection, or double layers, as is the case in AE Aqr, (Meintjes & de Jager, 2000). Strong field-aligned currents in the magnetosphere of the white dwarf can result in the acceleration of particles in strong localized field-aligned potential drops, known as double layers. Consider two plasma regions of different densities, which consequently leads to different conductivities. In the regions of relatively low conductivity the currents will reach a critical value and become unstable, i.e.

$$j_\parallel = j_{crit} = e n_\mathrm{e} f c_s, \tag{A.11}$$

where n_e and c_s represents the electron density and speed of sound respectively. As f reaches a critical limit ($f \to 10$) it will trigger micro-instabilities, resulting in an increase in resistivity of the plasma. The acceleration of field-aligned potential drops are a conversion process from free magnetic energy to kinetic energy of particle beams. This will only apply to regions where $j_\parallel$ is sufficiently concentrated, i.e. j_{crit}, in order to cause the high resistivity from micro-instabilities. Hence, the potential drops along the field lines can be determined using energy conservation arguments. By comparing the electromagnetic Poynting flux flowing into the

double layer to the particle flux flowing out of the double layer, it can be shown that,

$$\begin{aligned}\Phi_{\parallel} &= \left(\frac{\text{e-m energy into double layer}}{\text{particle flux outflow of double layer}}\right) \\ &= \left(\frac{B^2\nu_a}{8\pi e n_e f c_s}\right),\end{aligned} \tag{A.12}$$

where $\nu_e = B/\sqrt{4\pi\rho_e}$ represents the Alfvén velocity. In some regions where the electron density is extremely low, the formation of double layers leads to an interesting consequence where the electric field becomes large and out of control, resulting in the explosion of double layer. In such an event, a total release of an energy reservoir will follow,

$$P_{\rm dl} = 1/2LI^2. \tag{A.13}$$

Here L is the total inductance of the circuit and $I \sim jd^2 \sim en_pcd^2$ is the current of the relativistic particle crossing the double layer of width d. Hence the total power that can be released through the accelerated particle can be given as

$$\begin{aligned}P_{\rm dl} &= \int j.EdV \\ &= en_e c\Phi_{\parallel}d^2\end{aligned} \tag{A.14}$$

A.2.1 Particle acceleration through scattering

The principle of bulk flow motion is of great importance for particle acceleration and serves as a template for all subsequent work. It was first realized by Enrico Fermi who developed two simple models for acceleration, namely Stochastic

(Fermi-II) acceleration by scattering of randomly magnetized clouds, and Regular (Fermi-I) acceleration through scattering and reflections of shocks, (Fermi, 1949). For Stochastic acceleration the randomly moving particles diffuse in energy space in such a way that the mean energy increases, due to the fact that head-on interactions gains more energy than overtaking interactions. In regular Fermi acceleration the particles all move in the same direction where they are forced to reflect back from a shock, again and again. In both scenarios these particles will gain energy and collide with photons to produce high-energy radiation. See Achterberg (2008) for a more detailed discussion.

Another scenario in which particles can be accelerated is through the magnetic mirror effect (e.g., Parker, 1976; Sato, 1958; Spitzer, 1956). Assume a particle follows a spiral motion along a field line where the particle with a pitch angle θ_0 in a field B_0 is trapped between two approaching Alfvén waves of maximum field density $B_w > B_0$ (Parker, 1976). See Fig. A.2 for illustration. The particle will then reflect back and forth between the two regions.

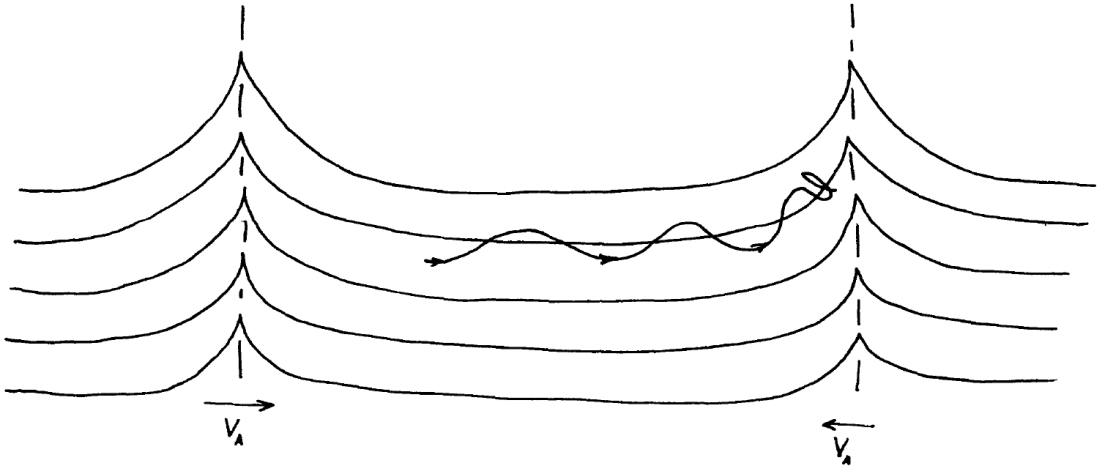

Figure A.2: Illustrative sketch of two Alfvén waves approaching each other along a uniform magnetic field B_0. Adopted from Parker (1976).

The kinetic energy of the particle's motion perpendicular to the field satisfies

$$\frac{1}{2}Mw_{\perp}^2/B = \text{constant}. \tag{A.15}$$

This value does not change in the uniform field B_0 between the waves. If θ is the angle between the velocity vector and the z-axis, then the ratio of the perpendicular velocity ($w_{\perp}$) to the total velocity will be $\sin\theta$. As B increases, the uniformity of the magnetic moment implies that $w_{\perp}$ increases proportionally to $B^{1/2}$, meaning

$$\sin^2\theta = \frac{B_0}{B_w}\sin^2\theta_0. \tag{A.16}$$

Let θ_0 be the initial value of θ where $B = B_0$. When B/B_0 rises to $1/\sin^2\theta_0$ then all the energy of the particle has been transformed into transverse kinetic energy, the parallel gyrating velocity ($w_{\parallel}$) will fall to zero and the particle is then reflected back into the region of lesser field. Contrarily, if B is the maximum value reached by the magnetic field, all particles will be reflected for which $\sin^2\theta_0$ exceed B_0/B_w.

This method of particle acceleration is subject to one important limitation. As $w_{\parallel}$ increases, θ decreases, and the particle is ultimately no longer trapped. To obtain continuous acceleration of particles it must be assumed that collisions re-establish an isotropic velocity distribution after the $w_{\parallel}$ has increased, and that the particles then become trapped and accelerated again. The particles can then be divided into two groups according to the magnitude of θ, i.e. the reflecting group for which $\theta > \theta_{crit}$ and the escaping group for which $\theta < \theta_{crit}$ (see Fig. A.3).

In the mechanism proposed by Fermi, a charged particle is moving in a magnetic field between two clouds. If the magnetic field in the clouds is assumed to be greater than in the intervening region, the particle is trapped between two magnetic

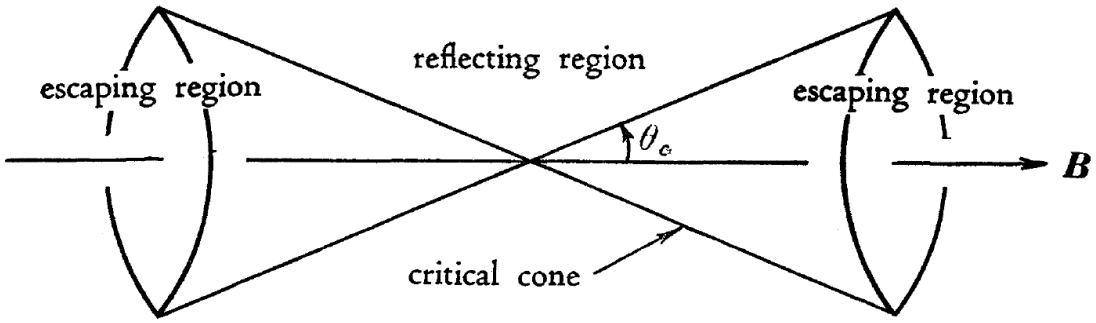

Figure A.3: Illustrative sketch of the escaping and reflecting region in the magnetic mirror effect. Adopted from Sato (1958).

mirrors. Such trapping will occur only for particles whose velocity is inclined to the magnetic field at a sufficient angle, i.e. the pitch angle θ. The clouds comprising of the two mirrors are assumed to be moving towards each other at a relative velocity. The charged particle now gains energy on each reflection from the mirror[2].

A.3 Synchrotron radiation

It has been established that the majority of high-energy astrophysical sources are magnetized and contains particles, i.e. electrons and positrons, that move at relativistic and non-relativistic speeds. In the presence of a negligible electric field, the driving mechanism for the motion of these particles in a magnetic field is known as the Lorentz force, which is responsible for an electron to gyrate around the magnetic field lines, i.e. in a spiral-like trajectory. The direction of the force is perpendicular to both $\vec{v}$ and $\vec{B}$, where the magnitude of the force is given as:

$$F_L = \frac{e\vec{v}}{c}\vec{B}\sin\phi. \tag{A.17}$$

Here, ϕ represents the pitch angle between the velocity, $\vec{v}$, and magnetic field,

[2]See Spitzer (1956) for a more detailed discussion and derivation.

$\vec{B}$. If the motion of the electron is perpendicular to the magnetic field, the electron will experience a maximum force, circle around the field line and radiate. If the motion is parallel to the magnetic field, no force is experienced and it will not radiate. Thus, these gyrations of non-relativistic and relativistic electrons in a magnetic field will give rise to cyclotron and synchrotron radiation respectively (see Fig. A.4). Over the period of gyrations the speed of the electron does not change due to the Lorentz force, but this motion constitutes an acceleration due to change in direction.

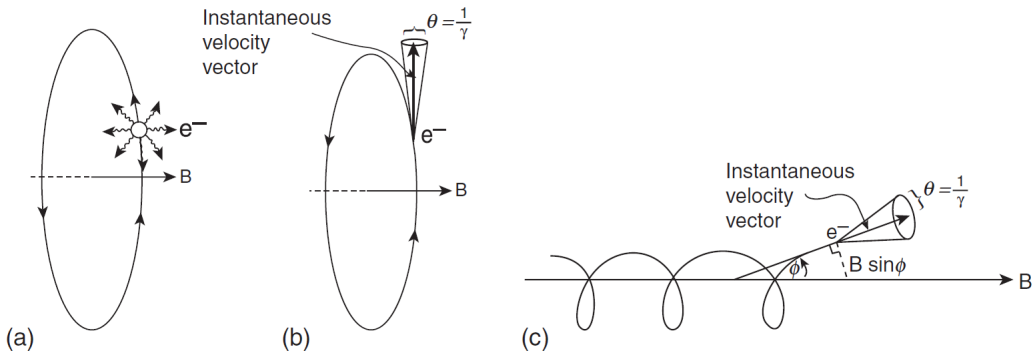

Figure A.4: Illustrations of radiation given off by an electron with velocity $\vec{v}$ orbiting a magnetic field of strength B. (a) Cyclotron emission from a non-relativistic electron whose velocity is perpendicular to the direction of the magnetic field. (b) Synchrotron emission from a relativistic electron, where the emission is beamed in the forward direction into a cone of angular radius $\theta = 1/\gamma$, (γ represents the Lorentz factor). (c) A more realistic scenario where the electron has velocity components both parallel and perpendicular to the direction of B, where ϕ represents the pitch angle between $\vec{v}$ and $\vec{B}$. Adopted from Irwin (2007).

Synchrotron radiation occurs when charged particles, primarily electrons, move along a magnetic field line in a gyrating motion at relativistic velocities. The nature of emission appears to show a continues spectrum over a broad range of frequencies. These radially accelerated and gyrating particles also has a characteristic polarization, which can be observed from radio to hard X-rays and even γ-rays.

Following the discussions from Chapter 2 and 3, it clear that the highly magnetic white dwarf in AR Sco shows strong evidence of synchrotron emission (e.g., Buckley et al., 2017; Takata et al., 2017). Observations from radio to X-ray indicate that emission can be produced from relativistic particles, such as electrons, in or near the magnetosphere of the white dwarf. The produced SED is characteristic of synchrotron emission from radio to X-ray, with underlying thermal emission from the M-dwarf companion. Also, clear evidence of strong linear polarized emission ($\sim$ 40%) compared to low circular polarization at optical wavelengths (Buckley et al., 2017), also support the notion that AR Sco can be a source of synchrotron emission.

A.3.1 Synchrotron emissivity (power)

Consider the simple case of a single electron. As mentioned, the Lorentz force causes a gyration of the particles around the magnetic field lines and induces acceleration. By considering an electron that is momentarily at rest, it is possible to calculate the total integrated power. In this frame the velocity of the particle is zero but not its acceleration. By making use of the fact that the total emitted power is Lorentz-invariant, it can be shown using the Larmor formula that:

$$P_e = \frac{2e^2}{3c^3}[a_{\parallel}^2 + a_{\perp}^2], \tag{A.18}$$

where P_e is the total emitted power radiated from the accelerated electron. Using the acceleration Lorentz transformation, where $a'_{\parallel} = \gamma^3 a_{\parallel}$ and $a'_{\perp} = \gamma^2 a_{\perp}$ the Larmor formula becomes:

$$P_e = \frac{2e^2}{3c^3}\gamma^4[\gamma^2 a_{\parallel}^2 + a_{\perp}^2] \tag{A.19}$$

By taking into account the involved parameters, e.g. the Lorentz force, Larmor

radius, pitch angles (θ) and fundamental frequency, the isotropic power distribution over a solid angle becomes

$$\langle P \rangle = \frac{4c}{3}\sigma_T U_B \gamma^2 \beta^2, \tag{A.20}$$

where σ_T represents the Thomson scattering cross section, U_B the magnetic energy density, c is the speed of light, γ the Lorentz factor and $\beta = \frac{\mathrm{v}}{c}$ is the velocity of the particle[3].

In the case of a "many-electron" model, the synchrotron emission is often based on a power-law distribution, which is routinely used in high-energy astrophysics to explain particle energy distributions, i.e.

$$N(\gamma) = K\gamma^{-p} = N(E)\frac{dE}{d\gamma} \qquad (\gamma_{min} < \gamma < \gamma_{max}). \tag{A.21}$$

Assuming that the distribution of pitch angle is equal for both high and low values of the γ range, the emissivity of many electrons can be determined as follows. By taking the power-law density function and integrating over the γ range of a single electron, and assuming the emission is isotropic, the specific emissivity can be calculated as:

$$\epsilon_s(\nu, \theta) = \frac{1}{4\pi}\int_{\gamma_{min}}^{\gamma_{max}} N(\gamma) P(\gamma, \nu, \theta) d\gamma \tag{A.22}$$

Solving the integral for an appropriate range of frequencies will lead to

$$\epsilon_s(\nu, \theta) \propto K B^{(p+1)/2} \nu^{-\alpha} \tag{A.23}$$

where B the magnetic field strength and $\alpha = (p-1)/2$ the spectral index of

[3]See Ghisellini (2013), page 56-58, for a more detailed derivation.

the radiation. If we consider an optically thin, homogeneous source with a volume $V \propto R^3$ at a distance d_L, the received flux will then be:

$$\begin{aligned} F_s(\nu) &= 4\pi\epsilon(\nu)\frac{V}{4\pi d_L^2} \\ &\propto \frac{R^3}{d_L^2} K B^{1+\alpha}\nu^{-\alpha} \\ &\propto \theta_s^2 R K B^{1+\alpha}\nu^{-\alpha}, \end{aligned} \tag{A.24}$$

where θ_s is the angular radius of the source. Hence, observing a source at multiple frequencies, allows the determination of the slope α of the particle energy distribution.

A.3.2 Synchrotron spectrum

For simplicity, again consider the case of a single electron. The synchrotron process is associated with a typical frequency. In the case of a relativistic electron, the frequency associated with the radiation is coupled with the timescale during each revolution the radiation cone points in the direction of the observer. The time in which an electron will emit photons in any given direction can be described by

$$\Delta t_e \sim \frac{2}{2\pi}\frac{1}{\gamma\nu_B}, \tag{A.25}$$

with ν_B the magnetic gyro-frequency. The arrival time of the photon can then be written as $\Delta t_A = \Delta t_e(1-\beta) = 1/2\pi\gamma^3\nu_B$. The frequency at which the photon emits most of its power, i.e the synchrotron frequency, will then be:

$$\nu_s = \frac{1}{2\pi\Delta t_A} = \gamma^2\frac{eB}{2\pi m_e c}. \tag{A.26}$$

Thus the final derivation for the power per unit frequency of an electron, with energy $\gamma m_e c^2$ in a magnetic field B moving at a pitch angle of θ, summed over polarizations is then given by:

$$P_s^{sy}(\nu, \gamma, \theta) = \frac{\sqrt{3} e^3 B \sin\theta}{m_e c^2} F(\nu/\nu_c), \tag{A.27}$$

with

$$F(\nu/\nu_c) \equiv \frac{\nu}{\nu_c} \int_{\nu/\nu_c}^{\infty} K_{5/3}(\xi) d\xi \tag{A.28}$$

$$\nu_c \equiv \frac{3}{2} \nu_s \sin\theta. \tag{A.29}$$

This represents the power integrated over the emission pattern and can be interpreted as the synchrotron spectrum. Here, $K_{5/3}(\xi)$ is the modified Bessel function of the second kind of order 5/3 and ν_s is the given synchrotron frequency.

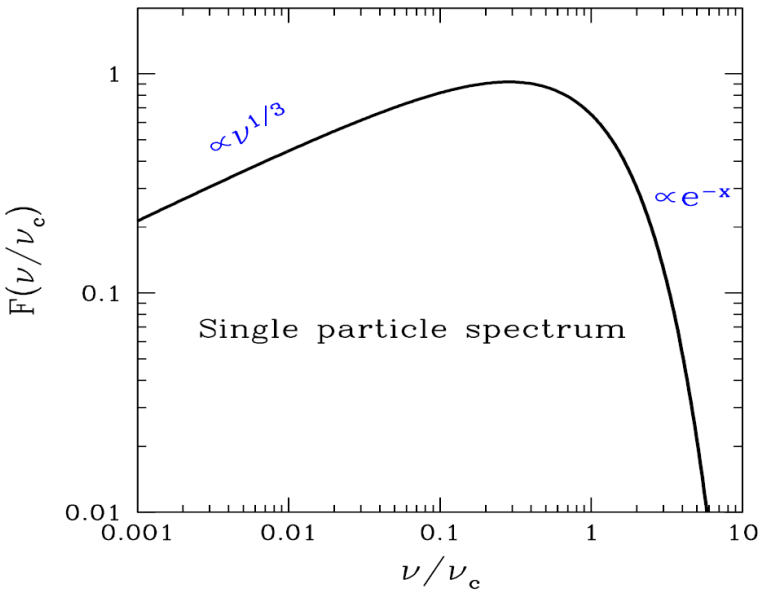

Figure A.5: A single-particle spectrum where the flux is frequency-dependent. Adopted from Ghisellini (2013).

The dependence upon frequency is contained in the function $F(\nu/\nu_c)$ which is plotted in Fig. A.5. The flux function, eq. A.28, peaks at $\nu \sim 0.29\nu_c$ with the low-frequency part approximated by a power-law function with a slope of 1/3,

$$F(\nu/\nu_c) \longrightarrow \frac{4\pi}{\sqrt{3}\Gamma(1/3)} \left(\frac{\nu}{2\nu_c}\right)^{1/3} \qquad (\nu \ll \nu_c) \tag{A.30}$$

and at frequencies above $\nu \gg \nu_c$ the spectrum will decay exponentially and can be approximated by

$$F(\nu/\nu_c) \longrightarrow \left(\frac{\pi}{2}\right)^{1/2} \left(\frac{\nu}{2\nu_c}\right)^{1/2} e^{-\nu/\nu_c} \qquad (\nu \gg \nu_c) \tag{A.31}$$

A.3.3 Synchrotron cooling timescale

As in any instance, to determine the timescale of any quantity, an order of magnitude estimate can be made by using $t = A/\dot{A}$. Hence, the time it takes for an electron to lose its energy (E) through synchrotron radiation can be calculated as:

$$\begin{aligned} t_{syn} &= \frac{E}{\langle P_{syn} \rangle} \\ &= \frac{3\gamma m_e c^2}{4\sigma_T c U_B \gamma^2 \beta^2}, \end{aligned} \tag{A.32}$$

where σ_T is the Thomson cross section, and $U_B = B^2/8\pi$.

A.3.4 Synchrotron absorption

Synchrotron absorption for non-thermal relativistic particles can not be determined in the same manner as for a Maxwellian distribution, i.e. Kirchoff's law. Instead it is better to consider the relationship between the A and B Einstein coef-

ficients related to spontaneous and stimulated emission. For relativistic electrons in a plasma it is expected that there will be an equilibrium between the energy of the thermal plasma ($\sim kT$) and the population of relativistic electrons. Considering this, the intensity of a source can be determined by equating the brightness temperature to the kinetic temperature of the emitting electrons:

$$\begin{aligned} I(\nu) &= 2kT\frac{\nu^2}{c^2} \qquad (kT \sim \gamma m_e c^2) \\ &\sim 2m_e\nu^2(\frac{\nu}{\nu_L})^{1/2} \\ &\propto B^{-1/2}\ \nu^{5/2} \end{aligned} \tag{A.33}$$

This is only true as long as a specific γ can be associated to any given ν. By integrating the intensity over the angular dimension of the source, the flux can be calculated as:

$$\begin{aligned} F(\nu) &\propto \theta_s^2\frac{\nu^{5/2}}{B^{1/2}} \qquad (h\nu \ll kT) \\ &\propto \theta_s^2\frac{B^{(p+1)/2}}{\nu^{(p-1)/2}} \qquad (h\nu \gg kT) \end{aligned} \tag{A.34}$$

Based on model fitting of a synchrotron spectrum the magnetic field B can be constrained where the source is optically thick while the normalization K and electron spectral index p can be determined from the thin part (see Fig. A.6).

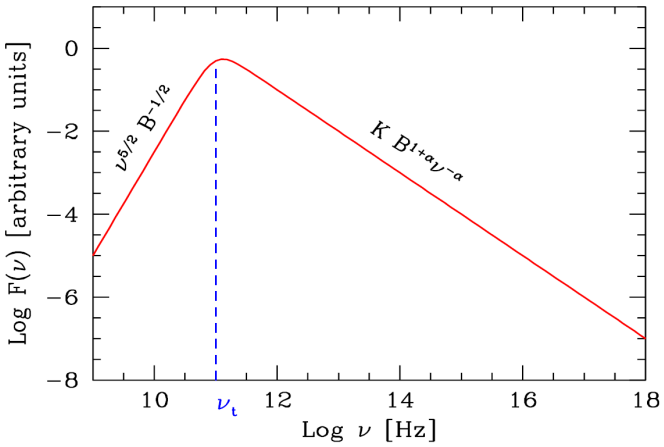

Figure A.6: Synchrotron spectrum for a partially self-absorbed source. With the self-absorbed part to the left of the boundary frequency ν_t, and the optically thin part towards the right. Adopted from Ghisellini (2013).

A.4 Compton scattering

It is established that the simplest interaction between photons and electrons is scattering. In order to explain γ-ray emission at VHE, we first have to give some background information regarding interactions between photons and electrons. In the simple case of an incoming photon interacting with a stationary electron, where energy is transferred from the photon to the electron, the process is called *Compton scattering*. When the energy of an incoming photon is small compared to the rest-mass energy of an electron, the process is called *Thomson scattering*, which can be treated within the framework of classical electrodynamics. If the energy of the incoming photon increases, and becomes greater than or comparable to $m_e c^2$, a quantum treatment has to be considered, i.e. the *Klein-Nishina regime*.

Consider the simple case of Thomson scattering, when a low-energy photon, $h\nu \ll mc^2$, strikes an electron which is at rest. The energy of the photon before and after scattering can be given as ϵ_0 and ϵ_1 respectively. In this case $\epsilon_0 = \epsilon_1$ and the scattering becomes elastic. The result of this interaction (or collision) can be determined by considering the four-momentum before and after the collision.

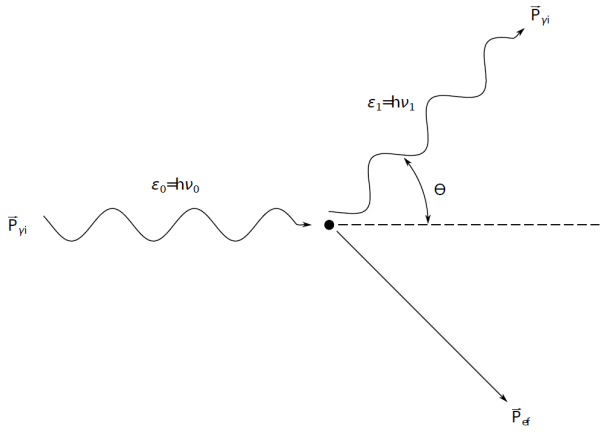

Figure A.7: Schematic illustration of Compton scattering. Figure adapted by van Soelen (2012) from Rybicki & Lightman (2004).

The initial and final four-momenta of the photon are given by

$$\begin{aligned} \vec{P}_{\gamma i} &= [\frac{h\nu_i}{c}, \frac{h\nu_i}{c}]\vec{n}_i \\ &= (\epsilon_0/c)[1, \vec{n}_i] \end{aligned} \tag{A.35}$$

and

$$\begin{aligned} \vec{P}_{\gamma f} &= [\frac{h\nu_f}{c}, \frac{h\nu_f}{c}]\vec{n}_f \\ &= (\epsilon_1/c)[1, \vec{n}_f], \end{aligned} \tag{A.36}$$

where $\vec{P}_{\gamma i}$ and $\vec{P}_{\gamma f}$ are the initial and final four-momentum of the photon respectively. The same approach is taken for a stationary electron where the initial four-momenta of an electron before scattering is:

$$\vec{P}_{\gamma f} = [m_e c, 0]. \tag{A.37}$$

It is assumed that the electron's motion after scattering is non-relativistic. By using the conservation of momentum and energy, which is expressed as $\vec{P}_{ei} + \vec{P}_{\gamma i} = \vec{P}_{ef} + \vec{P}_{\gamma f}$, and by re-arranging and doing some squaring it follows that $(\vec{P}_{ei} + \vec{P}_{\gamma i} - \vec{P}_{\gamma f})^2 = \vec{P}_{ef}^2$. From this and using the fact that $\vec{P}_{\gamma f}^2 = m_e^2 c^2$, it is possible to show that the energy of scattered photons is given by

$$\epsilon_1 = \frac{\epsilon_0}{1 + x_0(1 - \cos\theta)}, \tag{A.38}$$

where θ is the scattering angle of the photon from its initial path and $x_0 = \epsilon_0/m_e c^2$ (see Fig. A.7). In terms of wavelength, it can be expressed as

$$\Delta\lambda = \lambda_1 - \lambda_0 = \lambda_c(1 - \cos\theta), \tag{A.39}$$

where the Compton wavelength, λ_c, is defined as

$$\lambda_c = \frac{h}{m_e c}. \tag{A.40}$$

If the photon's wavelength is much larger than the Compton wavelength the scattering can be closely considered as elastic and we can assume there is no change in photon energy in the rest frame of the electron.

A.4.1 Thomson cross section

The probability that a photon will scatter from an electron is determined by the scattering cross sections. Again we have the two aforementioned regimes, i.e. Thomson (classical) and Klein-Nishina (quantum). The pattern of scattered radiation will follow the pattern of the cross section. In the classical case, assume an electron is at rest and an electromagnetic wave is impinging with an energy of $h\nu \ll m_e c^2$ and that the incoming wave is completely linearly polarized. Since the

Thomson limit is a non-relativistic case ($v \ll c$), it means that the incoming wave is of low-amplitude and causes the electron to oscillate, hence the average square acceleration during one cycle can be given by:

$$\langle a^2 \rangle = \frac{e^2 E_0^2}{2m_e^2}. \tag{A.41}$$

Also, from the Larmor formula it is given that the emitted power per solid angle is

$$dP/d\Omega = e^2 a^2 \sin^2\theta/(4\pi c^3), \tag{A.42}$$

where θ is the angle between the acceleration vector and the propagating vector of the emitted radiation. Then by substituting the average acceleration we get:

$$\frac{dP_e}{d\Omega} = \frac{e^4 E_0^2}{8\pi m_e^2 c^3} \sin^2\theta. \tag{A.43}$$

Since the scattered radiation is completely linearly polarized in the plane defined by the incident polarization vector of the incoming photon and the resultant scattered photon, with the flux of the incoming wave being $S_i = cE_0^2/8\pi$. Thus the differential cross section of an electron of charge, e, and mass, m_e, is given by

$$\frac{d\sigma}{d\Omega} = \frac{dP_e/d\Omega}{S_i} = \frac{e^4}{m_e^2 c^4} \sin^2\theta = r_0^2 \sin^2\theta, \tag{A.44}$$

where $d\sigma$ is the differential cross section, $d\Omega$ is the solid angle in the direction of the scattering and

$$r_0 = \frac{e^2}{m_e c^2} \tag{A.45}$$

is known as the classic electron radius, $r_0 = 2.82 \times 10^{-13}$ cm. Integrating over the entire solid angle will give,

$$\begin{aligned} \sigma_T &= \int \frac{d\sigma}{d\Omega} d\Omega \\ &= \int_0^{2\pi} \int_0^{\pi} r_0^2 \sin^2\theta \sin\theta d\theta d\phi \\ &= \frac{8\pi}{3} r_0^2, \end{aligned} \tag{A.46}$$

where σ_T is the total scattering cross section, known as the Thomson cross-section, which for a classical electron is $\sigma_T = 6.65 \times 10^{-25}$ cm^2.

A.4.2 Klein-Nishina cross section

The Klein-Nishina cross section is a more general case than the classical limit of the Thomson cross-section, and takes into account quantum electrodynamics. The differential cross-section of the Klein-Nishina limit is given by

$$\frac{\sigma_{KN}}{d\Omega} = \frac{3}{16\pi} \sigma_T \frac{\epsilon_1^2}{\epsilon_0^2} \left(\frac{\epsilon_0}{\epsilon_1} + \frac{\epsilon_1}{\epsilon_0} - \sin^2\theta \right), \tag{A.47}$$

where ϵ_0 and ϵ_1 are the energies of the incoming and scattered photons respectively. The total cross section can then be given by integrating over the solid angle as, see Rybicki & Lightman (2004), p. 197:

$$\sigma_{KN} = \sigma_T \frac{3}{4} \left[\frac{1+x}{x^3} \left\{ \frac{2x(1+x)}{1+2x} - \ln(1+2x) \right\} \frac{1}{2x} \ln(1+2x) - \frac{1-3x}{(1+2x)^2} \right], \tag{A.48}$$

where $x = h\nu / m_e c^2$.

An important feature of the Klein-Nishina equation is that the scattering cross section is reduced when the photon energy becomes large. Hence, in the Thomson limit the cross section will be larger than in the Klein-Nishina regime, implying that the probability of scattering will be greater and consequently result in a higher scattering rate from softer photons. In that case the limiting regimes of non-relativistic and relativistic, the Klein-Nishina cross section, i.e. equation A.48, becomes:

$$\sigma \approx \sigma_T \left(1 - 2x + \frac{26x^2}{5} + ...\right), \quad x \ll 1 \tag{A.49}$$

and

$$\sigma = \frac{3}{8}\sigma_T x^{-1} \left(\ln 2x + \frac{1}{2}\right), \quad x \gg 1. \tag{A.50}$$

A.5 Inverse-Compton scattering

The previous section discussed the energy transfer during scattering between a stationary electron and a low-energy photon, where the electron gains energy from the photon and in return the photon loses its energy, which results in an observed change in wavelength. In the case where energy is transfered from a relativistic electron to a low-energy photon, the process is reversed and called *Inverse-Compton (IC) scattering*. Here, the energy of the electron can be greater then the photon energy, and energy will be transferred from the electron to the photon. Since the electrons are relativistic in nature, IC can serve as a very effective mechanism to produce VHE γ-rays. Detailed IC scattering can take a lot of time to discuss, therefore a summary of the most important points will be given in the following few sections. For a more precise and detailed discussion, see e.g. Ghisellini (2013); Longair (1992); Rybicki & Lightman (2004).

A.5.1 Scattering energies

Scattering energy due to the IC process can be evaluated in two regimes, i.e. the Thomson limit and the Klein-Nishina limit. These two limits depends on the energy of the photons (as previously mentioned). First, consider the reference frame where the electron is at rest (co-moving frame, K') and evaluate the incoming energy of the photon. Hence,

$$\begin{aligned} x' &= h\nu'/m_e c^2 \ll 1, \quad \text{(Thomson limit)} \\ x' &= h\nu'/m_e c^2 \gg 1, \quad \text{(K-N limit)} \end{aligned} \tag{A.51}$$

The next step is to standardise a fixed reference frame to evaluate the angles between the incoming photon and the relativistic electron, which moves in the x-direction (see Fig. A.8).

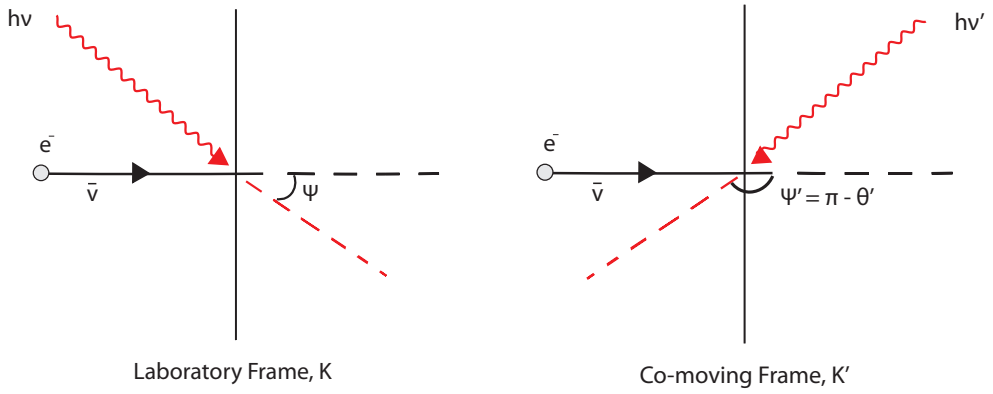

Figure A.8: Scattering geometries in the observer's frame K and in the electron's rest frame K'. In the lab frame an electron is moving with velocity $\vec{v}$ and makes an angle ψ with an incoming photon of frequency ν. In the electron's rest frame, the photon is coming from the front with frequency ν', making an angle ψ' with the direction of the velocity. Adapted from Ghisellini (2013).

This can be achieved using the Doppler shift equations to transform between reference frames, i.e.

$$\epsilon' = \epsilon\gamma(1 - \beta\cos\theta) \tag{A.52}$$

$$\epsilon = \epsilon'\gamma(1 + \beta\cos\theta), \tag{A.53}$$

where the angles between the direction of an electron and the direction of a photon are given by θ' and θ in the laboratory frame (K), and the co-moving frame (K'), respectively. The corresponding transformation of angle between the respective reference frames are

$$\cos\theta' = \frac{\cos\theta - \beta}{1 - \beta\cos\theta} \tag{A.54}$$

$$\cos\theta = \frac{\cos\theta' + \beta}{1 + \beta\cos\theta'} \tag{A.55}$$

and

$$\sin\theta' = \frac{\sin\theta}{\gamma(1 - \beta\cos\theta')} \tag{A.56}$$

$$\sin\theta = \frac{\sin\theta'}{\gamma(1 + \beta\cos\theta)}. \tag{A.57}$$

A very convenient way to treat IC scattering is to evaluate the process in the co-moving frame and then converting it to the observer's frame. Consider the "incoming photon" energy in the co-moving frame, K', of the electron:

$$\epsilon_0' = \frac{\epsilon_0}{\gamma(1 - \beta\cos\theta')}, \tag{A.58}$$

where $\beta = \mathrm{v}/c$, γ is the Lorentz factor and θ' is the angle between the direction of a photon and the direction of an electron's velocity in the co-moving reference frame. By using the transformation of angle equation, we can transform the above equation to:

$$\begin{aligned} \epsilon_0' &= \frac{\epsilon_0}{\gamma(1 - \beta\cos\Psi')}, \qquad (\Psi = \pi - \theta') \\ &= \epsilon_0\gamma(1 - \beta\cos\Psi), \end{aligned} \tag{A.59}$$

where Ψ is the angle between the photon and electron velocity in the laboratory reference frame, K. In the Thomson limit ($h\nu' \ll 1$) the scattering process can be considered elastic, (i.e. $\epsilon_1' = \epsilon'$), where ϵ_1' and ϵ' are the scattered and incoming photon's energies in the co-moving reference frame (K'). By using these transformation equations it is however possible to convert these energies between the two reference frames, i.e. converting the energies in the observer's frame to the energies in the electron's rest frame, and the other way around. Hence, these equations are normally used to determine the observed energy change during IC scattering. The photon energy can thus be transformed into the observer's reference frame (K), as

$$\epsilon_1 = \epsilon_1'\gamma(1 + \beta\cos\Psi_1'). \tag{A.60}$$

This can then be re-written, again using the transformation equations for angles, so that all quantities are in terms of the laboratory reference frame:

$$\epsilon_1 = \epsilon_0 \, \frac{1 - (\beta\cos\Psi)}{1 - (\beta\cos\Psi_1)}, \tag{A.61}$$

where, Ψ and Ψ_1 represent the incoming and scattered photon angle relative to the electron respectively.

A.5.2 Maximum and minimum energy transfers

The amount of energy transfered depends on the path of the photon and electron. The maximum energy transfer from the electron to the scattered photon is if the collision is head-on, resulting in the photon to scatter in the opposite direction from where it came from, i.e.

$$\begin{aligned}
\epsilon_{1,max} &= \epsilon_0 \ \frac{1-(\beta\cos\Psi)}{1-(\beta\cos\Psi_1)} \\
&= \epsilon_0 \ \frac{1-(\beta\cos(\pi))}{1-(\beta\cos(0))} \\
&= \Gamma^2(1+\beta)^2 \ \epsilon_0 \\
&= 4\ \gamma^2\ \epsilon_0, \qquad (\beta \to 1),\ (\Gamma \to \gamma)
\end{aligned} \tag{A.62}$$

The same approach can be taken with the minimum energy transfer, where the scattering occurs during a head-tail collision. In this case the photon approaches the electron form behind and scatters in opposite directions,

$$\begin{aligned}
\epsilon_{1,min} &= \epsilon_0 \ \frac{1-(\beta\cos\Psi)}{1-(\beta\cos\Psi_1)} \\
&= \epsilon_0 \ \frac{1-(\beta\cos(0))}{1-(\beta\cos(\pi)} \\
&= \frac{1}{\Gamma^2(1+\beta)^2} \ \epsilon_0 \\
&= \frac{1}{4\ \gamma^2} \ \epsilon_0, \qquad (\beta \to 1),\ (\Gamma \to \gamma)
\end{aligned} \tag{A.63}$$

In the case of relativistic electrons, the energies of the photon before scattering, in the rest frame of the electron, and after scattering are approximately on the orders of $[1; \gamma; \gamma^2]$, providing that the condition for Thomson scattering in the rest frame $\gamma\epsilon \ll mc^2$ is met. Therefore the process converts low-energy photons to high-energy photons by and order of γ^2.

A.5.3 Total loss rate and emission spectrum

The rate at which energy is radiated from the relativistic electron after scattering can be determined by considering all the quantities in the laboratory frame. The total loss rate, within the Thomson regime, is given by

$$P_c(\gamma) \equiv \frac{dE_e}{dt} = \frac{4}{3}\sigma_T c\gamma^2\beta^2 U_r, \tag{A.64}$$

where

$$U_r = \int \epsilon n(\epsilon) d\epsilon \tag{A.65}$$

is the energy density of the surrounding radiation field before scattering and σ_T is the Thomson cross section. The energy loss rate after scattering can also be represented as follows

$$\begin{aligned} P_c(\gamma) &= \frac{\text{numb. of collisions}}{\text{sec}} \times (\text{avg. phot. energy after scatt.}) \\ &= (\sigma_T c \frac{U_r}{< h\nu >})(\frac{4}{3} < h\nu > \gamma^2) \end{aligned} \tag{A.66}$$

By comparing equation A.66 to equation A.20 (i.e. the synchrotron energy loss) similarities can be seen in terms of the energy loss rates. Since they are identical

(with U_B switched for U_r), it means that if relativistic electrons are present in a region containing similar radiation and magnetic energy densities, the electrons will be able to emit ar equal rates through both synchrotron and IC scattering processes. For a single particle the typical frequency is also denoted by a factor of γ^2. Hence, because of the similarities between synchrotron and IC scattering, the same method can be used as in the synchrotron case, to derive the IC emissivity. The next step is to determine the spectrum of the scattered radiation. Assume a power-law energy distribution for the relativistic electrons:

$$N(\gamma) = k\gamma^{-\alpha} = N(E)\frac{dE}{d\gamma}; \qquad (\gamma_{min} < \gamma < \gamma_{max}), \tag{A.67}$$

also assuming that it describes an isotropic distribution of electrons. The assumption can also be made that the seed photons are isotropic and monochromatic with a frequency ν_0. Since there is a strong connection between the scattered frequency ν_c and the electron energy produced, the following can therefore be set

$$\nu_{IC} = \frac{4}{3}\gamma^2\nu_0 \rightarrow \gamma = \left(\frac{3\nu_{IC}}{4\nu_0}\right)^{1/2} \rightarrow \left|\frac{d\gamma}{d\nu}\right| = \frac{\nu_{IC}^{-1/2}}{2}\left(\frac{3}{4\nu_0}\right)^{1/2} \tag{A.68}$$

Using the same argument used for synchrotron emission, it can also be stated that the power lost by the electron of energy $\gamma m_e c^2$ within $m_e c^2 d\gamma$ goes into the radiation of frequency ν and $d\nu$. Hence the emissivity becomes:

$$\epsilon_{IC}(\nu_{IC})d\nu_{IC} = \frac{1}{4\pi}m_e c^2 P_c(\gamma)N(\gamma)d\gamma. \tag{A.69}$$

Integration leads to

$$\epsilon_{IC}(\nu_{IC}) = \frac{1}{4\pi}\frac{(4/3)^\alpha}{2}\sigma_T c K\frac{U_r}{\nu_0}\left(\frac{\nu_{IC}}{\nu_0}\right)^{-\alpha} \tag{A.70}$$

Here K is a constant. As in synchrotron emission, the emissivity is characteristic of a power-law distribution with the relation:

$$\alpha = \frac{1-p}{2} \tag{A.71}$$

Equation A.70 can be expressed more clearly if it is expressed in terms of photon energy, $h\nu_{IC}$, include the source radius, R, and consider a proxy for scattering optical depth of the relativistic electrons, $\tau_c = \sigma_T K R$. Hence the emissivity becomes:

$$\epsilon_{IC}(h\nu_{IC}) = \frac{1}{4\pi}\frac{(4/3)^\alpha}{2}\frac{\tau_c}{R/c}\frac{U_r}{\nu_0}\left(\frac{\nu_{IC}}{\nu_0}\right)^{-\alpha}. \tag{A.72}$$

In this form τ_c represents the fraction of seed photons $U_r/h\nu_0$ undergoing scatterings in a time R/c and $\nu_{IC}/\nu_0 \sim \gamma^2$ is the average gain in energy of the scattered photons . A typical IC scattering spectrum is illustrated in Fig. A.9.

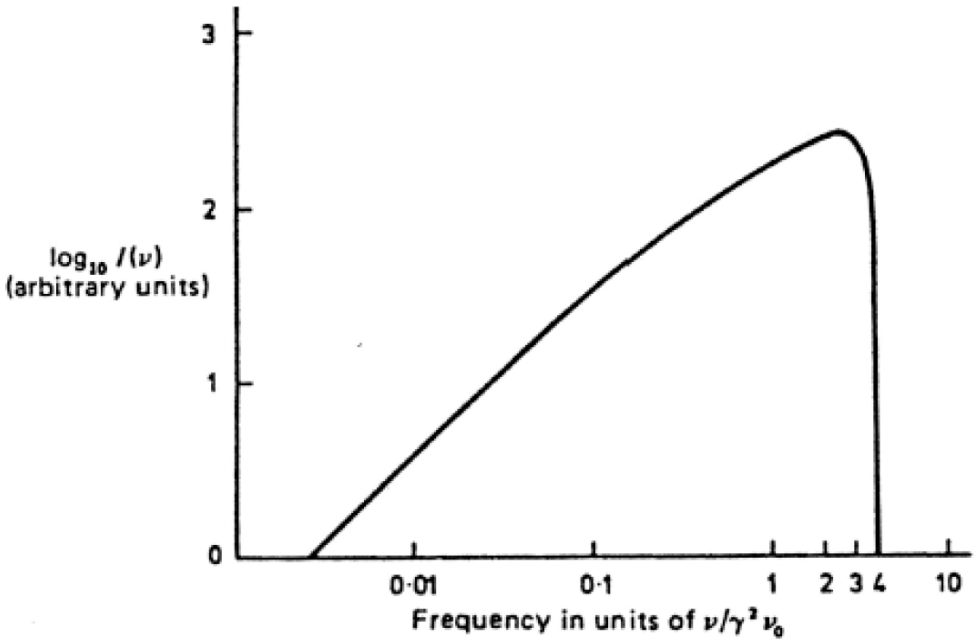

Figure A.9: Typical inverse-Compton spectrum. Adopted from Longair (1992).

A.6 π° - decay

During collisions between high-energy particles such as protons, one of the by products will a neutral π° meson. These particles are extremely unstable and quickly decay into two γ-rays. The neutral pion decay process is responsible for the continuum emission of interstellar gas at energies $\epsilon \geq 100$ MeV (Longair, 1992).

During collisions between relativistic protons and nuclei of atoms and ions within an interstellar gas, neutral pions will be generated through:

$$p + p \longrightarrow \pi^-, \pi^+, \pi^0. \tag{A.73}$$

The charged pions will then decay into neutrinos and muons, having a mean lifetime of $\sim 2.551 \times 10^{-8}$ s,

$$\begin{aligned} \pi^+ &\longrightarrow \mu^+ + \nu_\mu \\ \pi^- &\longrightarrow \mu^- + \nu_\mu. \end{aligned} \tag{A.74}$$

The charged low-energy muons will then decay into positrons, electrons and muon neutrinos, with an estimated mean lifetime of $\sim 2.200 \times 10^{-6}$ s,

$$\begin{aligned} \mu^+ &\longrightarrow e^+ + \nu_e + \nu_\mu \\ \mu^- &\longrightarrow e^- + \nu_e + \nu_\mu. \end{aligned} \tag{A.75}$$

The neutral pions by distinction will then decay into γ-ray pairs in a very short period of 1.78×10^{-16} s.

$$\pi^{\circ} \longleftrightarrow \gamma + \gamma. \tag{A.76}$$

The cross section of this π° decay can be estimated to be $\sigma_{pp \longleftrightarrow 2\gamma} \approx 10^{-30}\mathrm{m}^2$, where the emitted spectrum of γ-rays will have a broad maximum centered on a γ-ray energy of about 70 MeV, (e.g., Badhwar et al., 1977; Stephens & Badhwar, 1981).

As discussed in Chapter 3, it is speculated by Bednarek (2018) that ample target material can be provided by the secondary M-dwarf's magnetosphere and surrounding region, to produce neutral pions in AR Sco. Proton-proton collisions can also occur between the system and Rho Oph cloud complex, where AR Sco is situated. It has also been shown (e.g., Buckley et al., 2017) that the white dwarf in AR Sco has the potential to accelerate charged particles like electrons and protons to Lorentz factors ($\gamma \sim 10^6$) within the light cylinder of the rotating white dwarf, which provides a mechanism to produce γ-rays with energies around ~ 0.5 TeV through IC scattering between the relativistic electrons and the photons from the secondary star for example.

Appendix B

Period Analysis: Alternative Ephemeris

By using the ephemeris from Takata et al. (2018), Rayleigh periodograms suggest a possible signal at the fundamental spin frequency but not the beat period. Included in this appendix are Rayleigh power spectra obtained at the beat (Fig. B.1) and spin (Fig. B.2) period of the white dwarf in AR Sco using an alternative ephemeris from Gaibor et al. (2020). By using this ephemeris, there seems to be no signal at the beat or spin period, hence no further analysis was performed.

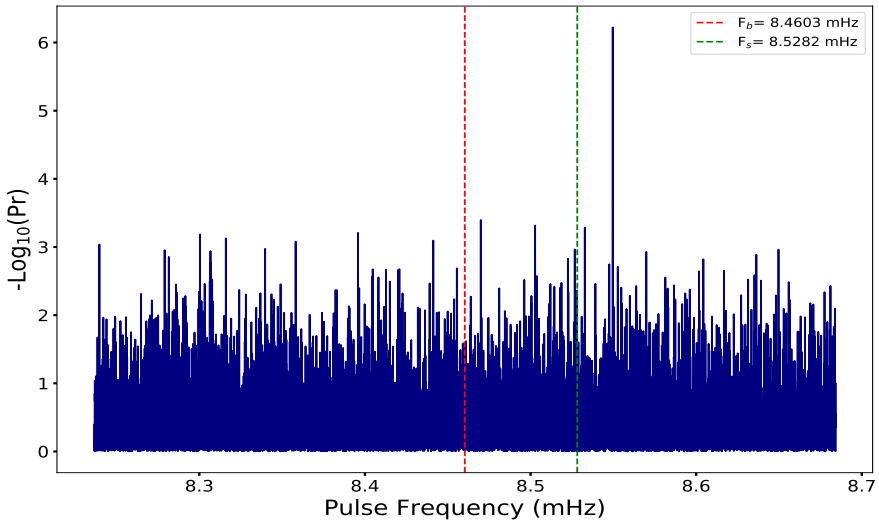

Figure B.1: 10-year (4 August 2008 - 18 March 2019) Rayleigh periodogram of AR Sco in the energy range of 100 MeV to 30 GeV, covering frequencies from $8.2 - 8.7$ mHz. Additional line marker added showing the current model for the fundamental beat (F_b = 8.4603 mHz) and spin (F_s = 8.5282 mHz) frequency of the white dwarf in AR Sco. Periodogram produced using the ephemeris from Gaibor et al. (2020).

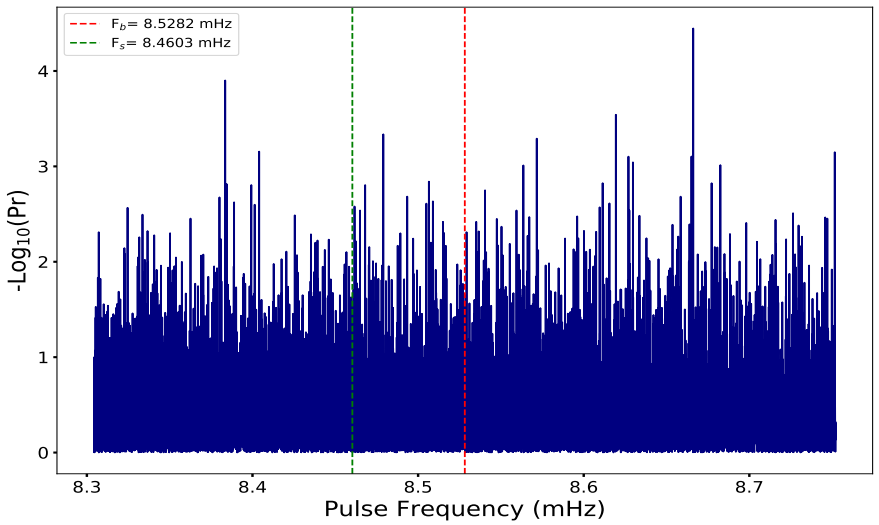

Figure B.2: 10-year (4 August 2008 - 18 March 2019) Rayleigh periodogram of AR Sco in the energy range of 100 MeV to 30 GeV, covering frequencies from $8.3 - 8.8$ mHz. Additional line marker added showing the current model for the fundamental beat (F_b = 8.4603 mHz) and spin (F_s = 8.5282 mHz) frequency of the white dwarf in AR Sco. Periodogram produced using the ephemeris from Gaibor et al. (2020).

Appendix C

Periodogram Control Test

Due to the fact that periodograms control tests (see section 4.4.3 in Chapter 4) appears to show a decrease in Rayleigh power as one moves farther away from the coordinates of AR Sco, a similar control test in an opposite direction was performed (see Fig. C.1). Hence, if similar features are observed, i.e., a decrease in power or no power at all, it suggests that the obtained signal is analogous to AR Sco's location. This method also test if the obtained results are not influenced by the surrounding regions, e.g., the Rho Oph cloud complex or nearby high energy sources. Included in this appendix are Rayleigh periodograms (see Fig. C.2 at the locations as illustrated in Fig. C.1.

From this we can see no evidence of a signal at the fundamental spin frequency, suggesting that the obtained signal (section 4.4.2 in Chapter 4) is inherent to the coordinates of AR Sco. In is also apparent that there no systematic decrease in power being observed as per Fig. 4.25. However, this still serves as evidence that the proposed signal can be associated to AR Sco coordinates. However, the exact reason why there is no systematic decrease at these location is still unclear at this stage of the analysis.

AR Sco's location is close to high energy γ-ray activity and complicates the analysis process. The possibility exist that the increase in activity to the bottom

left and bottom right does contribute to the observed results in Chapter 4. The exact nature of the observed high energy emission is still unclear, hence alternative methods and analysis techniques should be explored in an attempt to better constrain the emission from AR Sco.

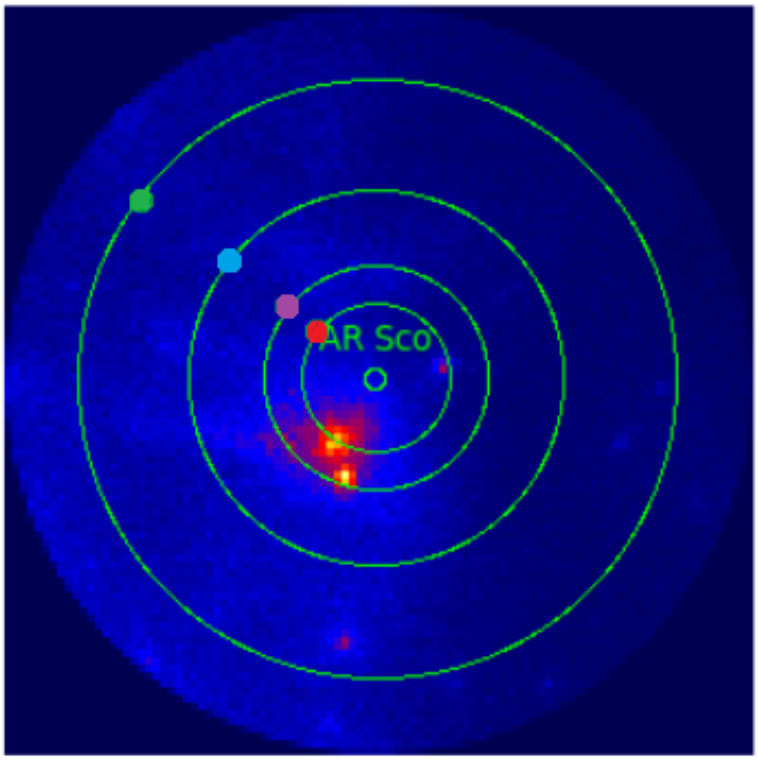

Figure C.1: Counts map (100 x 100 pixels) centred on AR Sco. Green circles represent locations 2° (red), 3° (purple), 5° (blue) and 8° (green) away from the coordinates centred on AR Sco.

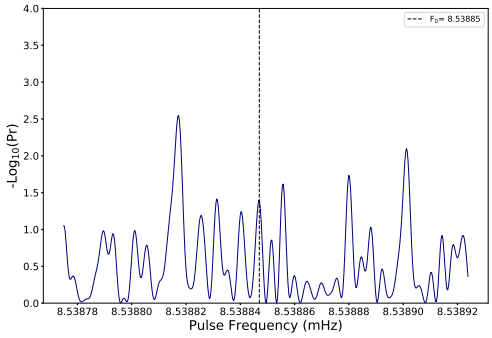

(a) Rayleigh probability at 2° away.

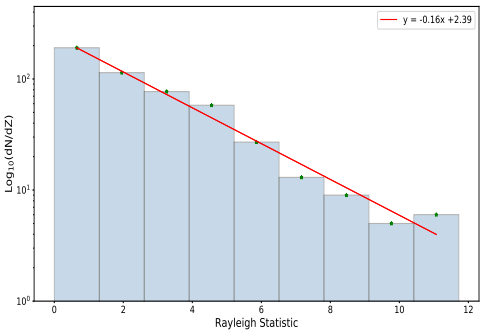

(b) Rayleigh histogram at 2° away.

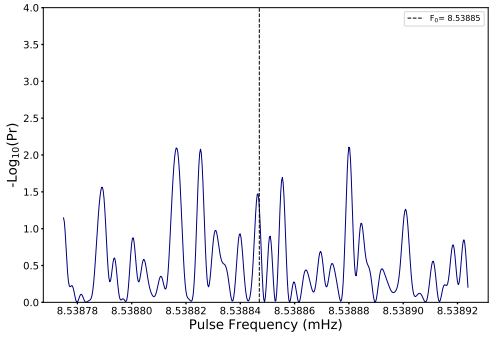

(c) Rayleigh probability at 3° away.

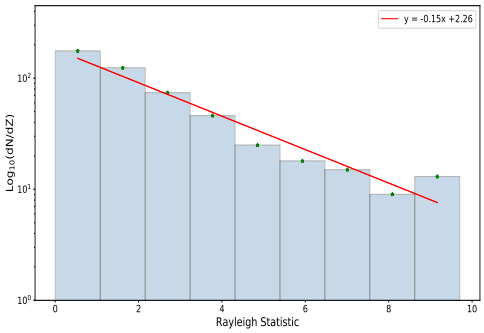

(d) Rayleigh histogram at 3° away.

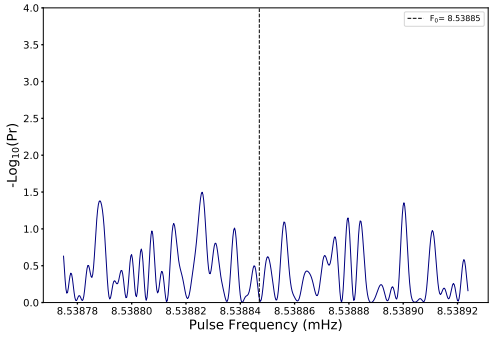

(e) Rayleigh probability at 5° away.

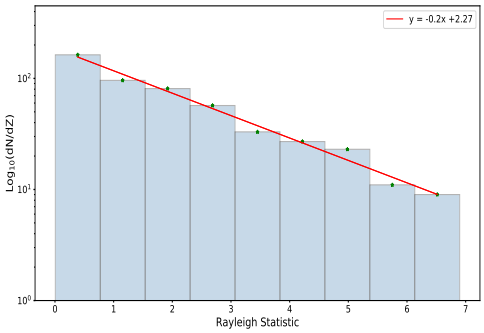

(f) Rayleigh histogram at 5° away.

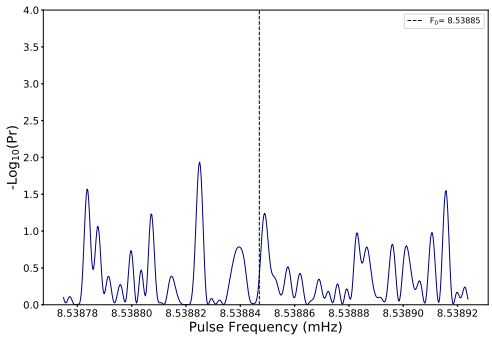

(g) Rayleigh probability at 8° away.

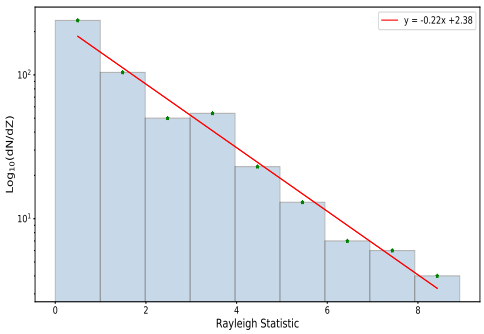

(h) Rayleigh histogram at 8° away.

Figure C.2: Rayleigh probability spectra and histogram distributions at regions of 2°, 3°, 5° and 8° away from the coordinates centred on AR Sco.

Appendix D

Noise Level Periodograms

Included in this appendix are Rayleigh power spectra of AR Sco at noise level over selected events within the 10-year data set where positive TS value events were considered. Here, no or relatively weak signals are present within the background noise at the current ephemeris for the spin frequency ($F_s = 8.53885$ mHz) and/or the beat frequency ($F_b = 8.4611$ mHz).

D.0.1 Above-2σ Periodograms

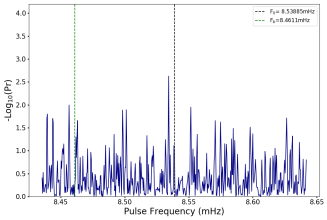

(a) 2009-09-29 (55103 MJD)

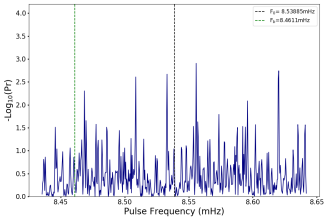

(b) 2009-12-22 (55187 MJD)

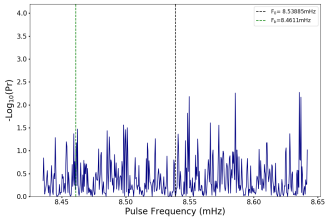

(c) 2010-03-30 (55285 MJD)

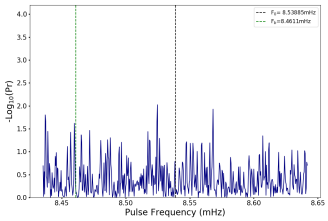

(d) 2010-04-13 (55299 MJD)

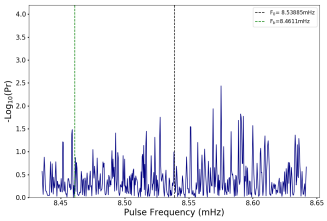

(e) 2010-09-01 (55440 MJD)

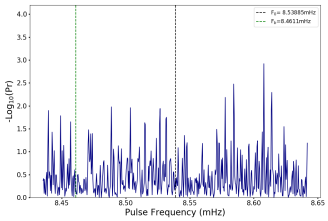

(f) 2010-09-29 (55468 MJD)

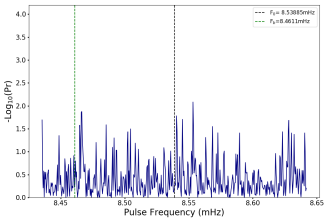

(g) 2010-10-27 (55496 MJD)

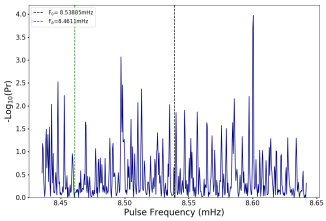

(h) 2011-01-05 (55566 MJD)

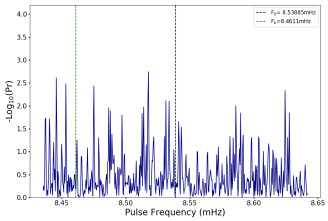

(i) 2011-04-13 (55580 MJD)

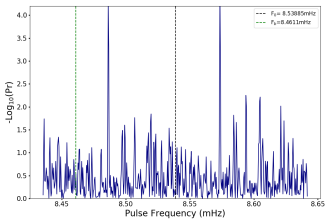

(j) 2011-02-16 (55608 MJD)

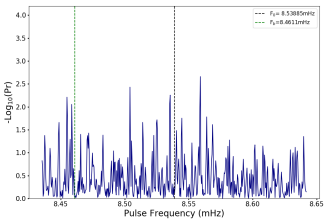

(k) 2011-03-30 (55650 MJD)

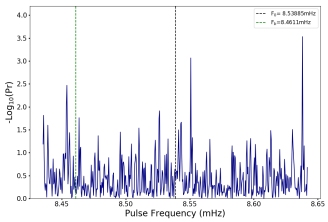

(l) 2011-05-25 (55706 MJD)

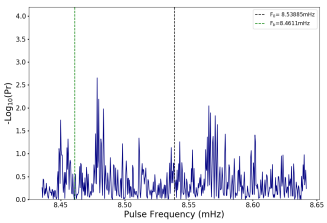

(m) 2011-06-08 (55720 MJD)

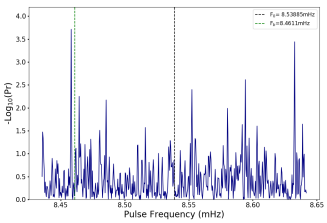

(n) 2011-06-22 (55734 MJD)

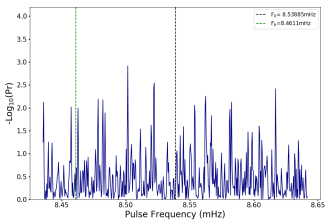

(o) 2013-01-19 (56311 MJD)

Figure D.1: AR Sco Rayleigh power spectra over selected periods in the 10-year data set at above 2σ. Additional line markers show the current model for the fundamental spin frequency (F_s) and beat frequency (F_b) of the white dwarf in AR Sco.

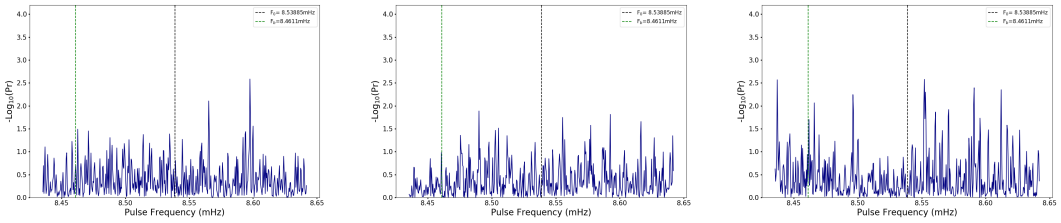

(a) 2013-09-01 (56536 MJD) (b) 2014-08-18 (56887 MJD) (c) 2014-10-13 (56943 MJD)

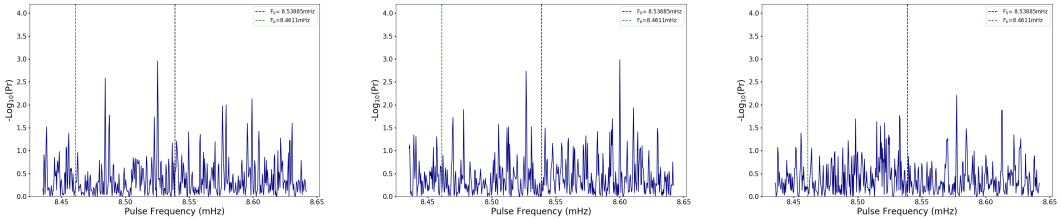

(d) 2015-02-02 (57055 MJD) (e) 2015-07-20 (57223 MJD) (f) 2016-06-07 (57546 MJD)

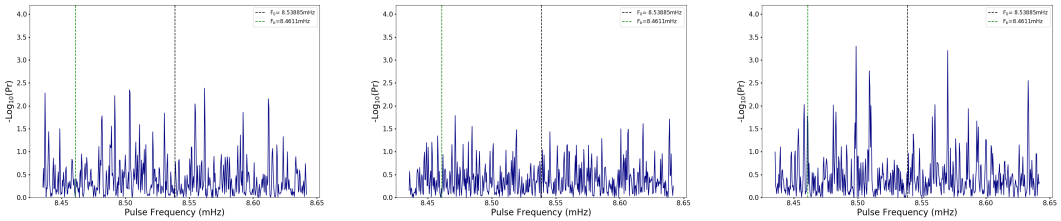

(g) 2017-08-03 (57968 MJD) (h) 2017-10-27 (58053 MJD) (i) 2017-11-24 (58081 MJD)

Figure D.2: AR Sco Rayleigh power spectra over selected 2-week periods in the 10-year data set at above 2σ, continued.

D.0.2 Below-2σ Periodograms

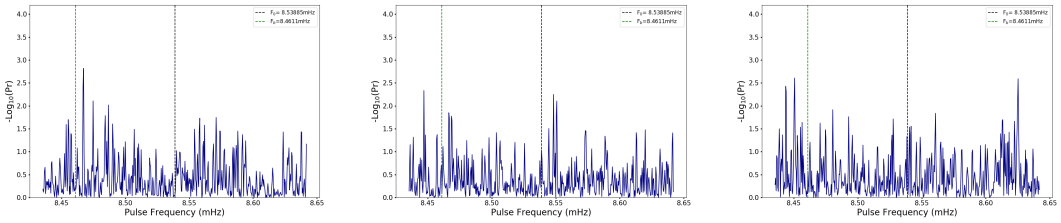

(a) 2009-10-13 (55117 MJD) (b) 2009-11-10 (55145 MJD) (c) 2009-11-24 (55159 MJD)

Figure D.3: AR Sco Rayleigh power spectra over selected 2-week periods in the 10-year data set at noise level. Additional line markers show the current model for the fundamental spin frequency (F_s) and beat frequency (F_b) of the white dwarf in AR Sco.

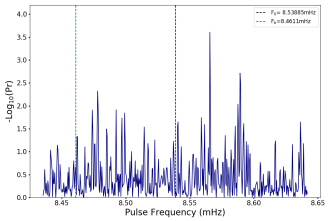

(a) 2010-01-05 (55201 MJD)

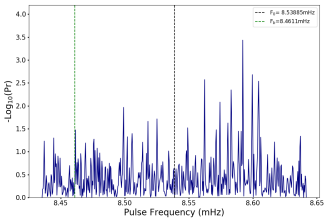

(b) 2010-01-19 (55215 MJD)

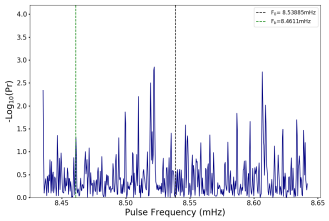

(c) 2010-02-02 (55229 MJD)

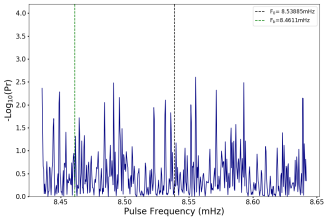

(d) 2010-02-16 (55243 MJD)

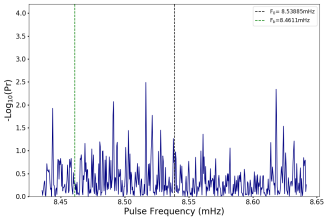

(e) 2010-03-02 (55257 MJD)

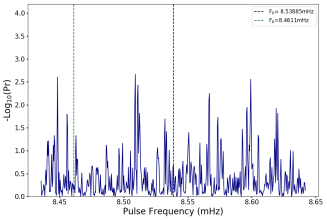

(f) 2010-05-11 (55327 MJD)

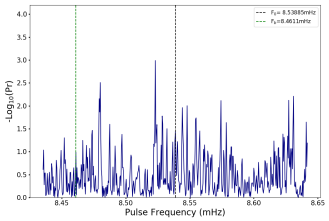

(g) 2010-09-15 (55454 MJD)

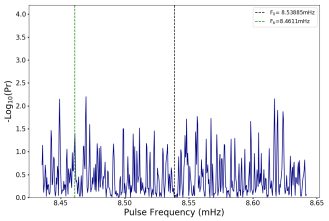

(h) 2011-01-19 (55594 MJD)

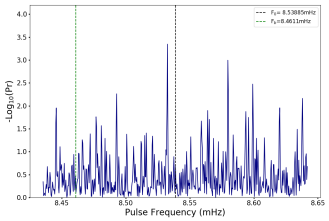

(i) 2011-03-02 (55622 MJD)

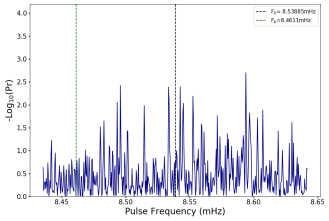

(j) 2011-03-16 (55636 MJD)

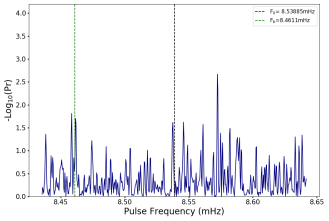

(k) 2011-04-13 (55664 MJD)

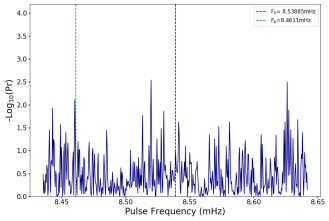

(l) 2011-04-27 (55678 MJD)

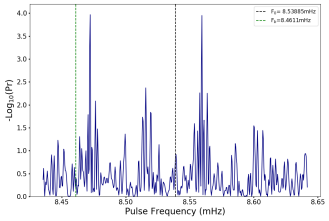

(m) 2012-09-15 (56185 MJD)

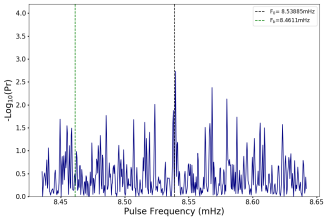

(n) 2012-09-29 (56199 MJD)

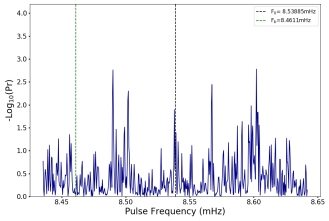

(o) 2012-10-27 (56227 MJD)

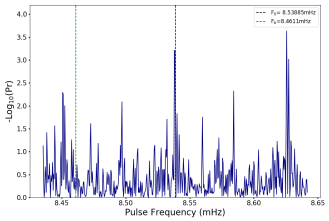

(p) 2012-11-24 (56255 MJD)

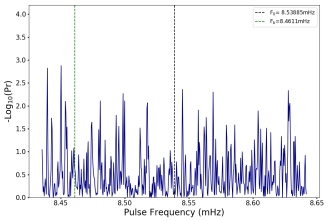

(q) 2013-01-05 (56297 MJD)

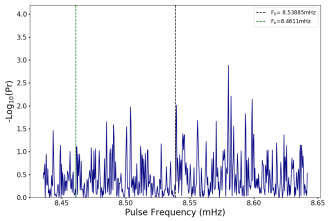

(r) 2013-02-02 (56325 MJD)

Figure D.4: AR Sco Rayleigh power spectra over selected 2-week periods in the 10-year data set at noise level, continued.

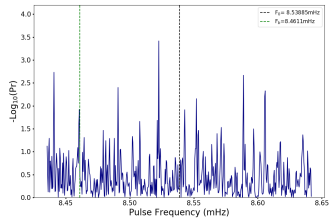

(a) 2013-02-16 (56339 MJD)

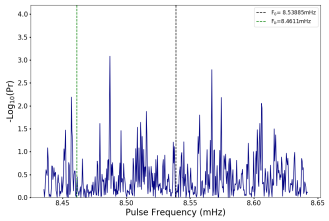

(b) 2013-03-02 (56353 MJD)

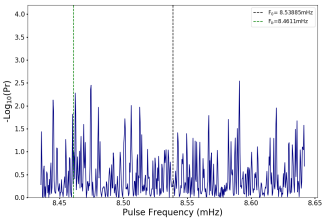

(c) 2013-03-16 (56367 MJD)

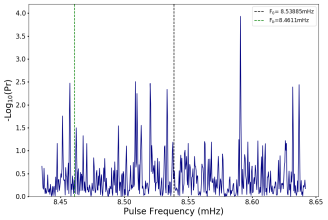

(d) 2013-03-30 (56381 MJD)

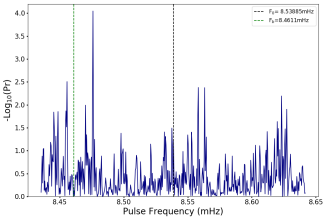

(e) 2013-05-11 (56423 MJD)

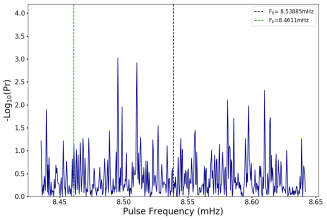

(f) 2013-06-08 (56451 MJD)

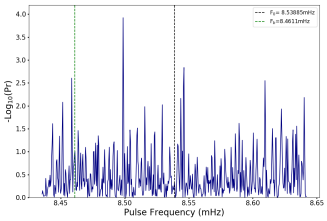

(g) 2013-06-22 (56465 MJD)

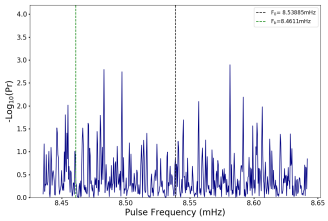

(h) 2013-12-22 (56648 MJD)

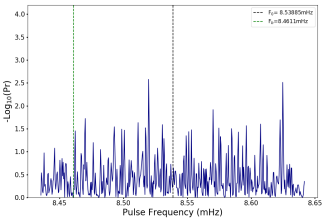

(i) 2014-02-16 (56704 MJD)

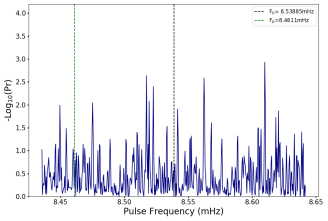

(j) 2014-04-27 (56774 MJD)

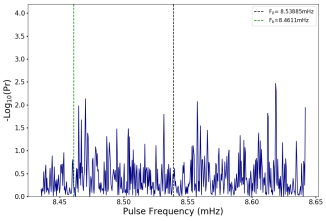

(k) 2014-05-11 (56788 MJD)

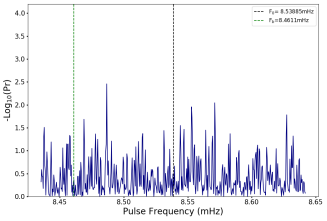

(l) 2014-08-04 (56873 MJD)

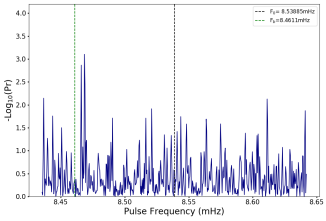

(m) 2014-09-15 (56915 MJD)

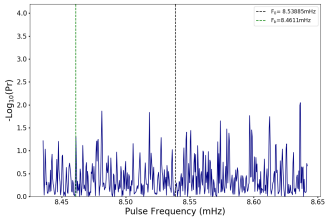

(n) 2014-11-10 (56971 MJD)

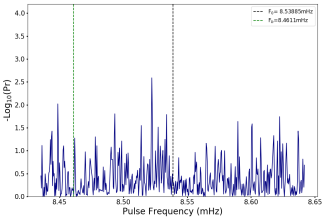

(o) 2014-11-24 (56985 MJD)

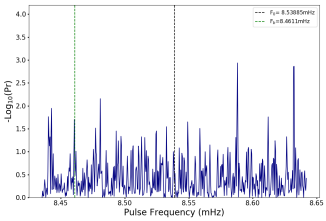

(p) 2015-01-19 (57041 MJD)

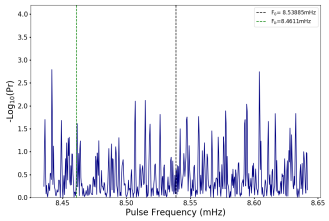

(q) 2015-02-16 (57069 MJD)

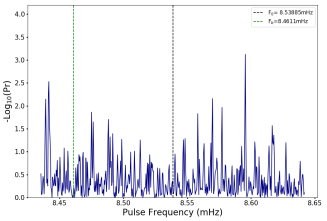

(r) 2015-04-13 (57125 MJD)

Figure D.5: AR Sco Rayleigh power spectra over selected 2-week periods in the 10-year data set at noise level, continued.

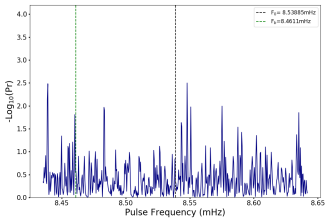

(a) 2015-05-25 (57167 MJD)

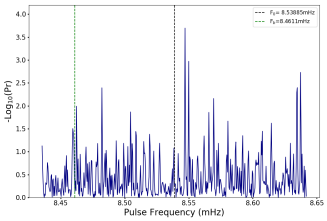

(b) 2015-06-22 (57195 MJD)

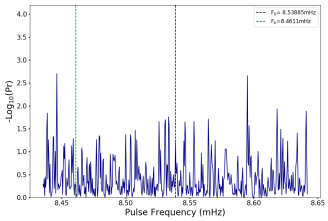

(c) 2015-08-18 (57252 MJD)

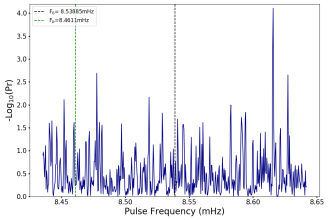

(d) 2015-09-15 (57280 MJD)

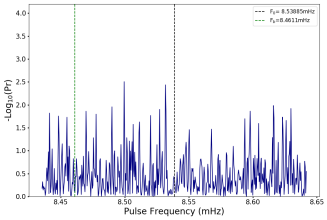

(e) 2016-01-05 (57392 MJD)

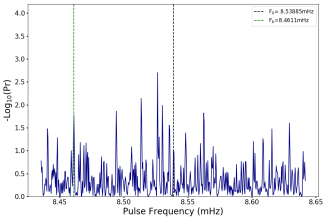

(f) 2016-01-19 (57406 MJD)

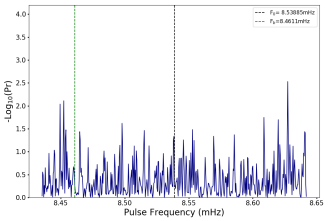

(g) 2016-04-12 (57490 MJD)

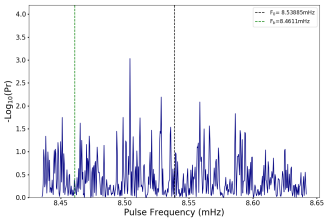

(h) 2016-05-10 (57518 MJD)

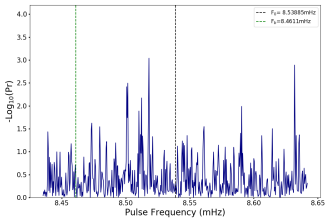

(i) 2016-06-21 (57560 MJD)

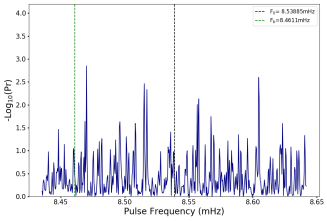

(j) 2016-07-05 (57574 MJD)

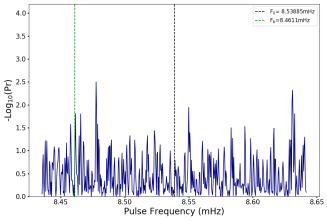

(k) 2016-09-29 (57660 MJD)

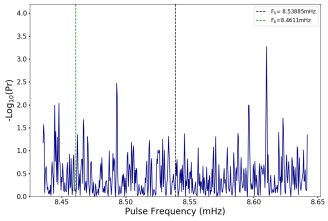

(l) 2016-10-27 (57688 MJD)

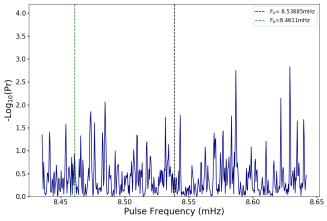

(m) 2016-11-10 (57702 MJD)

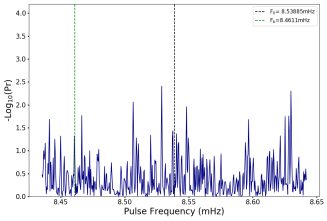

(n) 2017-03-16 (57828 MJD)

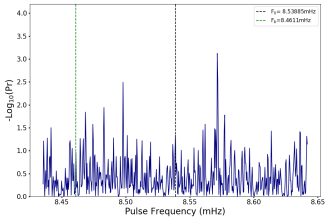

(o) 2017-04-27 (57870 MJD)

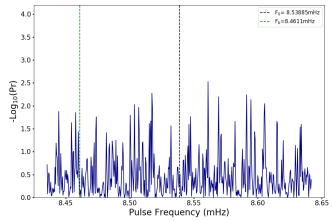

(p) 2017-07-20 (57954 MJD)

Figure D.6: AR Sco Rayleigh power spectra over selected 2-week periods in the 10-year data set at noise level, continued.

Appendix E

Contributed Papers

This research has been presented at both national and international conferences. Included in this appendix are peer-reviewed conference proceedings where *Fermi*-LAT and *Fermipy* results are presented in part, with one peer-reviewed Astroparticle Physics journal paper. Conference proceedings articles include:

- Q. Kaplan. H.J. van Heerden, P.J. Meintjes, A. Odendaal and R. Britto. Search for Gamma-ray emissionin the White Dwarf pulsar AR Sco. In Proceedings of *South African Institute of Physics (SAIP) 2018*, Bloemfontein, 25 - 29 June 2018, SA Institute of Physics, ISBN:978-0-620-85406-1, 184. *Contribution: Main Author.*

- Q. Kaplan, P.J. Meintjes, H.J. van Heerden, F. A. Ramamonjisoa, I. P. van der Westhuizen. Results from the long-term *Fermi*-LAT observations of the white dwarf binary pulsar AR Scorpii. In *36th International Cosmic Ray Conference*, PoS(ICRC 2019), 2019. *Contribution: Main Author.*

- Q. Kaplan, P.J. Meintjes, K.K. Singh, H.J. van Heerden, F.A. Ramamonjisoa. White Dwarf Pulsars as Possible Gamma-Ray Sources. In *6th Annual Conference on High Energy Astrophysics in South Africa*, PoS(HEASA 2018)037, 2018. *Contribution: Main Author.*

- Q. Kaplan, P.J. Meintjes, K.K. Singh, H.J. van Heerden. Searching for gamma-ray emission from the white dwarf pulsar system AR Sco using Pass 8 *Fermi*-LAT data. In *7th Annual Conference on High Energy Astrophysics in South Africa*, PoS(HEASA 2019)049, 2019. *Contribution: Main Author.*

- Q. Kaplan, P.J. Meintjes, H.J. van Heerden. Low-power pulsed emission at the spin period of the white dwarf in AR Scorpii? In *8th Annual Conference on High Energy Astrophysics in South Africa*, PoS(HEASA 2021)045, 2021. *Contribution: Main Author.*

- K.K. Singh, P.J. Meintjes, Q. Kaplan, F.A. Ramamonjisoa, S. Sahayanathan (2020). Modelling the broadband emission from the white dwarf binary system AR Scorpii. Astroparticle Physics, 123:102488. *Contribution: Data Analysis.*

Search for Gamma-ray emission in the White Dwarf pulsar of AR Scorpii

Q. Kaplan, H.J. van Heerden, P.J. Meintjes, A. Odendaal and R. Britto

Department of Physics, University of the Free State, Bloemfontein

E-mail: kaplanq@ufs.ac.za

Abstract. Detailed multi-frequency studies of the white dwarf pulsar AR Scorpii (AR Sco) revealed a Spectral Energy Distribution (SED) which predominantly shows features of non-thermal emission between the Radio and X-ray energies. This implies that AR Sco is a site of particle acceleration, which makes AR Sco an interesting source to investigate for possible gamma-ray emission in Fermi-LAT data (100 MeV-500 GeV). The focus of this paper was to do a preliminary analysis of the total Fermi-LAT dataset (2008-2018) by utilizing the upgraded Fermi-LAT Pass 8 data analysis pipeline to search for possible γ-ray emission in AR Sco. The detection of gamma-rays from AR Sco will be a strong motivation for possible CTA and H.E.S.S. follow-up studies. A positive detection will also be invaluable to the field of gamma-ray astronomy, establishing close binaries containing fast rotating, highly magnetic white dwarfs as a new class of γ-ray source.

1. Introduction

AR Scorpii (henceforth AR Sco) is a newly discovered close binary system consisting of a highly magnetic white dwarf pulsar and a M5 spectral type red dwarf orbiting around their Center of Mass (COM) every 3.56 h[1]. This suggest some relation to other close binary systems called Cataclysmic Variables (CV) stars. A certain subclass of CVs known as Intermediate Polars (IP), also consist of white dwarfs with strong magnetic fields ranging between 1-10 MG, which is similar to that of AR Sco. White dwarfs (WDs) are very dense stars in their final evolutionary state, supported by electron degeneracy pressure. Some of these WDs spin rapidly about their central axis, possibly due to mass transfer from their companion star. They thus mimic the properties of neutron star pulsars due to their fast rotational velocities and large magnetic fields[2]. Recently it was discovered that the rotating WD in AR Sco, with a spin period of P_s = 117 s, shows strong brightness variations across most of the electromagnetic spectrum[1], i.e. the emission predominantly modulated at the orbital (P_o = 3.56 h) and its beat period (P_b = 118 s) with spin period P_s = 117 s.

It has been shown that this close binary system is unique, since there is no evidence of mass transfer, mass accretion, or magnetospheric propelling of the mass transfer stream from the binary system[4]. It was suggested by Marsh et al.[1] that AR Sco is in the evolutionary stage of an IP, but AR Sco's optical pulsations (70%) far exceeds that of the brightest IP detected thus far, namely FO Aquarii with optical pulsations of 25%. The lack of substantial accretion is inferred from the fact that the X-ray luminosity of AR Sco is less than 1% that of a typical IP[1]. Therefore, there is no clear evidence to support the notion that AR Sco is an IP.

It was also suggested by Buckley et al.[4] that the Spectral Energy Distribution (SED) is dominated by non-thermal emission[4]. One of the most dominant emission features occurs in the radio regime, where strong modulations were found in the radio flux on the orbital period and the beat period[3] suggesting the emission originates on the M5 secondary star. Possibly in the pumped magnetospheric field of the secondary star as the WD's magnetic field sweeps across it every rotation cycle. It is also proposed that the highly magnetic WD pulsar (order of 10 MG) has the potential to accelerate charged particles like electrons and protons to high Lorentz factors ($\gamma \approx 10^6$) within the light cylinder of the rotating white dwarf[4]. This provides a vehicle to produce gamma-rays with energies above 1 TeV through e.g. inverse Compton scattering between the relativistic electrons and the photons from the secondary star[2]. However, it was also recently shown that very high energy gamma-ray production through a hadronic channel like π°-decay is also possible[5].

The aim of the study presented in this paper is to do a complete analysis of the total Fermi-LAT dataset (2008-2018) utilizing the upgraded Fermi-LAT Pass 8 data analysis pipeline to search for a gamma-ray excess from AR Sco. By using the upgraded Pass 8 data pipeline, better constraints can be put on the level of the emission above 100 MeV, which will allow the determination of a high energy SED above this threshold[6]. This will have important implications for follow-up studies with H.E.S.S. and the future CTA. This study will have a very significant impact in the field of multi-wavelength astrophysics of high energy compact sources, as well as the field of gamma-ray astronomy. The discovery of gamma-rays in AR Sco will lead to a new class of gamma-ray source and the multi-wavelength properties will result in the source being considered as a unique laboratory to study magnetospheric processes that can accelerate charged particles to very high energies.

2. Observations and Analyses

A Fermi-LAT dataset from the past decade (2008-2018) was extracted from the Fermi Science Support Center (FSSC) in the energy range between 100 MeV and 500 GeV. By using the Pass 8 data analysis pipeline, which provides a better determination of the diffuse galactic gamma-ray emission and also a significant improvement in terms of energy resolution from previous Fermi-LAT pipelines, it was possible to do a standard Binned Likelihood Analysis on the Fermi-LAT dataset[7]. The analysis was performed using Fermipy packages where a number of models were experimented with to fit and produce high energy SEDs for AR Sco. The event files, i.e. the photon and spacecraft files that were extracted from the FSSC site, were chosen to have a Region of Interest (ROI) of 30°, while a 15° ROI was chosen to extract the high energy photons of the target for analysis. All the point sources in the third Fermi-LAT catalog (3FGL) located within the ROI were modelled in the spectral fits, including the isotropic background and galactic diffuse emission. Since AR Sco is not listed in the 3FGL catalog, the source (3FGL J1616.8-2300) closest to the ROI centre (0.01° from ROI centre) was chosen to perform the event selection and create the source maps with Fermipy. AR Sco was added using its coordinates, (RA:$16^h21^m47.28^s$, Dec: $-22^{\circ}53^{'}10.39^{''}$, J2000) to the source maps and selection files with the help of Fermipy commands so that likelihood analysis could be done. The spectral shape parameters of AR Sco was set to vary during optimization and fitting. The spectral shapes used to model the spectral fit for the extracted data are as follows, namely 1.) a Power Law:

$$dN(E)/dE = N_0(E/E_0)^{\Gamma}, \tag{1}$$

with N_0 is the normalization factor and where a pivot energy (E_0) of 1 GeV was chosen to fit the model, and 2.) a Log Parabola

$$dN(E)/dE = N_0(E/E_b)^{\alpha-\beta log(E/E_b)}, \tag{2}$$

where E_b is the break value that should be set near the lower energy range of the spectrum. Here E_b was chosen to be 1 GeV.

Table 1. List of all the model parameters used during optimization to fit the Fermi-LAT data. Where the Test Statistic (TS) value is used to distinguish between flux values (TS $\geq$ 25) and 2σ upper limits.

Spectral model	TS	α	β	Γ
Power Law	7.71	N/A	N/A	2.44 $\pm$ 0.05
Log Parabola	16.17	2.29 $\pm$ 0.2	0.28 $\pm$ 0.001	N/A

3. Results and Discussion

The spectral models that were used to model the SED, as mentioned in Section 2, are the power law and log parabola functions. These models were used to determine the emission spectrum that best describes the emission properties from AR Sco. A residual model fit, see Figure 1, was also created to visually indicate how well the model has been fitted to the high energy data.

The upper limits and detected flux values were determined by using the Test Statistic (TS) values generated by the likelihood analysis. These TS values help to determine the probabillity of detecting emission from the source within each bin. Based on the parameters and overall test statistics (see Table 1) and taking in account how both the power law and log parabola fits the flux values and upper limit within the butterfly plot, see Figure 2 and 3, the best proposed significant fit for AR Sco is represented by the power law model, see Figure 2. Also, from the residual and counts fit (Figure 1), along with the produced SEDs (Figures 2 and 3), it is observed that the most of these detected flux values are within the lower energy regime (up intill $\sim$10 GeV). TS maps were also generated to show the overall significance of detection from AR Sco within the ROI, see Figure 4 and 5. The bright spot in the ROI, centred at AR Sco, in Figure 6 suggests that there is possible high energy emission from this region. Histograms of significance of all the data points in the ROI also shows the probability of detection within the standard deviation, see Figure 6 and 7. From these figures it is clear that the probability of detection is higher for the power law model as it follows a better Gaussian curve than the log parabola model.

A broadband SED was also created to show how the obtained Fermi-LAT power law spectrum, ranging from 100MeV to 500GeV, can be viewed in relation to previous multi-frequency observations (see Figure 8). The radio to optical data were extracted from the paper published by Marsh et al.[1] in 2016, whereas the X-ray data was extracted from the paper published by Geng et al.[3] in 2016.

4. Conclusion

The gamma-ray SED between 100MeV-500GeV seems to be compatible with a power law with Γ=2.4 $\pm$ 0.05. Our results seem to suggest the possibility of a low-level detection which is compatible with both hadronic and leptonic channels of gamma-ray production. Further analyses are underway to quantify the gamma-ray emission from the selected ROI centred on AR Sco. Unbinned likelihood analyses will also be performed, utilizing all the detected high energy photons, to better determine the gamma-ray excess.

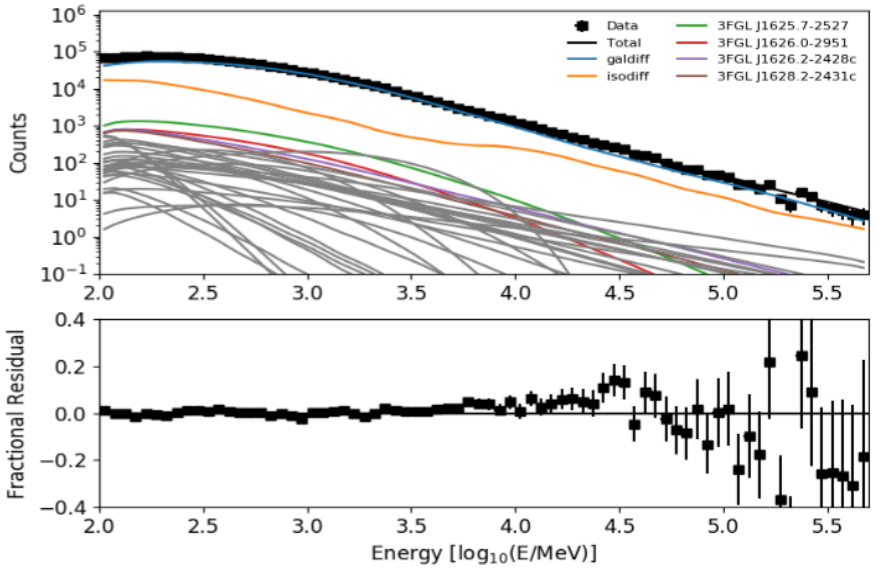

Figure 1. Residual model fit of power law model which best describes the spectral energy distribution.

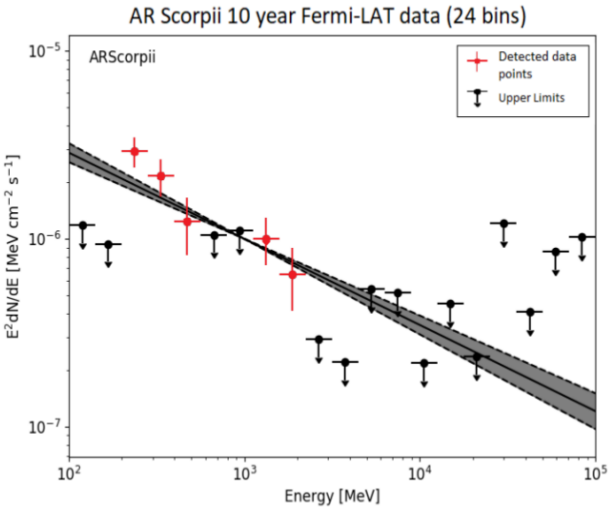

Figure 2. Spectral energy model fit of AR Sco's high energy SED represented by the Power Law function.

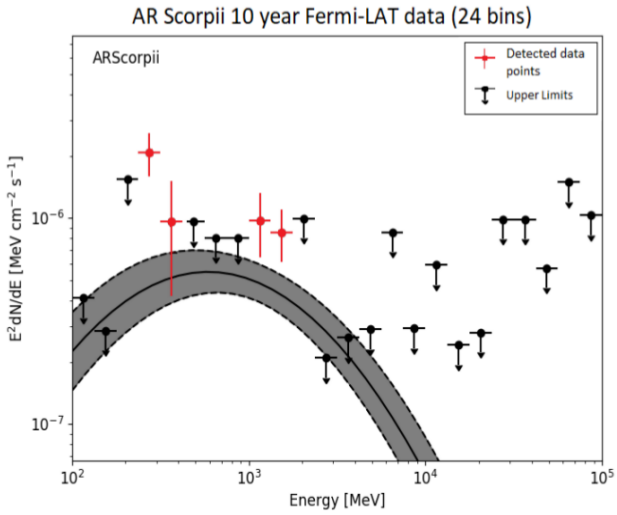

Figure 3. Spectral energy model fit of AR Sco's high energy SED represented by the Log Parabola function.

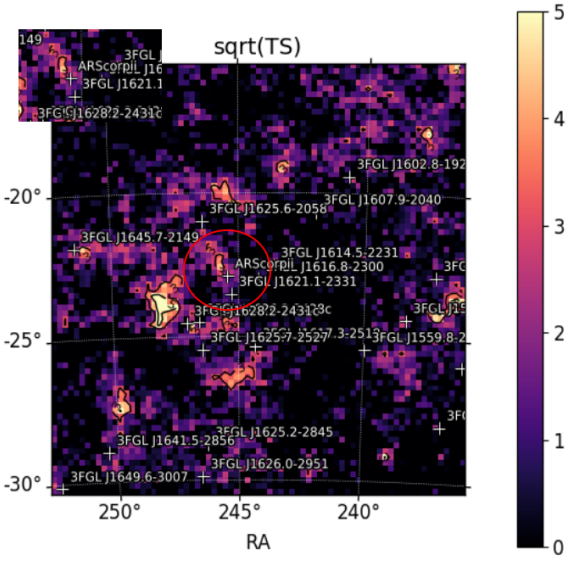

Figure 4. Test Statistic map of the source AR Sco and the galactic diffuse emission. Notice the bright pixels at the ROI centre (red circle).

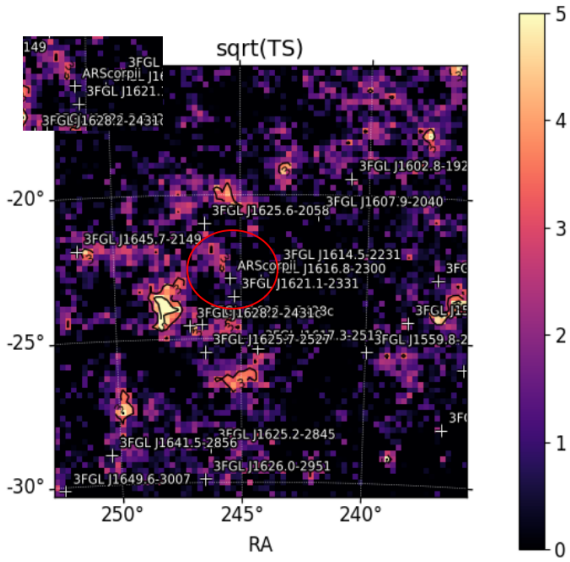

Figure 5. Test Statistic map of just the galactic diffuse emission. Notice the lack of bright pixels at the ROI centre compared to that in Figure 6.

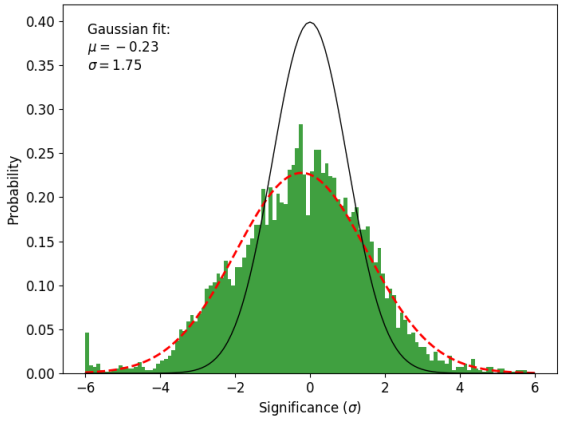

Figure 6. Histogram of significance for all the points on the map, Power Law model.

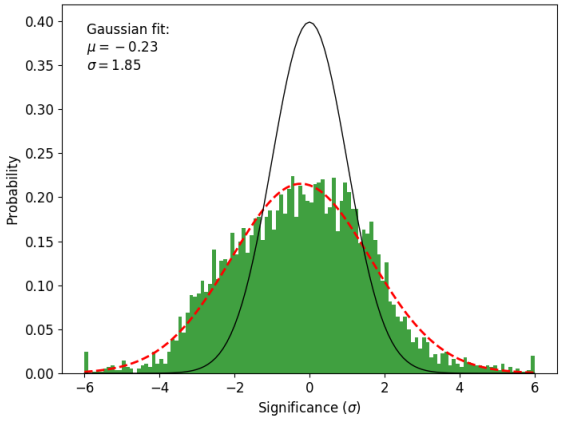

Figure 7. Histogram of significance for all the points on the map, Log Parabola model.

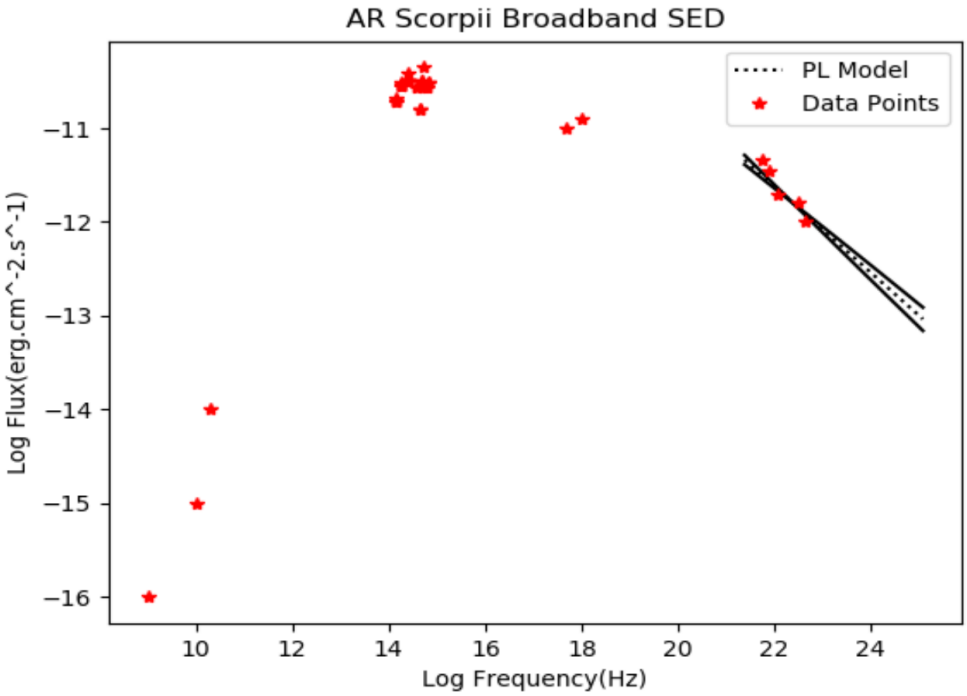

Figure 8. Proposed Broadband SED of AR Sco, ranging from radio to gamma-ray energies. Radio and optical data adapted from Marsh et al.[1] and Geng et al.[2]. The dashed and solid lines show the Power Law model butterfly plot produced by the Likelihood Analyses generated in Fermipy.

References

[1] Marsh T.R. et al. 2016, *A radio pulsating white dwarf binary star*, Nature, 537, 374.
[2] Geng J. et al. 2016, *A model of white dwarf pulsar in AR Scorpii*, ApJ, 831, L10.
[3] Stanway E.R. et al. 2018, *VLA radio observations of AR Sco*, Astronomy and Astrophysics, Volume 611, id.A66, 13 pp
[4] Buckley D.A.H et al. 2017, *Polarimetric evidence of white dwarf pulsar in the binary system AE Scorpii*, Nature Astronomy, 1, 0029.
[5] Bednarek W. 2018, *Hadronic model fro the non-thermal radiation from the binary system AR Scorpii*, MNRAS, Volume 476, L10-L14.
[6] Abdo A.A. et al. *(Fermi-LAT collaboration)*, 2010, ApJ, 723, 1082
[7] McEnery J. 2018, *Fermi Science Support Center*, https://fermi.gsfc.nasa.gov/ssc/. Date accessed: 18 June 2018

PROCEEDINGS OF SCIENCE

Results from the long-term Fermi-LAT observations of the white dwarf binary pulsar AR Scorpii

Q. Kaplan[1], **P. J. Meintjes**[1], **K. K. Singh**[1,2], **H. J. van Heerden**[1], **F. A. Ramamonjisoa**[1], **I. P. van der Westhuizen**[1*]

1.) Department of Physics, University of the Free State, PO Box 339, Bloemfontein, 9300
2.) Astrophysical Sciences Division, Bhaba Atomic Research Centre, Mumbai, India, 400085

E-mail: KaplanQ@ufs.ac.za

The discovery of the white dwarf binary system AR Scorpii (AR Sco) with its fascinating non-thermal dominated multi-frequency emission has sparked renewed interest in potential high energy gamma-ray emission from white dwarf pulsars. The Spectral Energy Distribution (SED) below and above optical shows evidence of non-thermal synchrotron emission, with pulsed emission in optical and X-ray bands at the white dwarf spin period ($P_* = 117\,$s) as well as a beat period ($P_b = 118.1\,$s) with the binary period. From an energy perspective, the highly magnetic rotating white dwarf can accelerate particles to TeV energies. In this study, a search for high energy gamma-ray emission was conducted between 100 MeV - 500 GeV by analysing the newly available Fermi-LAT Pass 8 data with the new Fermi 1.0.1 Science Tools. Binned likelihood analysis was done using power law, broken power law and log parabola models. From the selected Region of Interest (ROI) centred on AR Sco's position, we calculated a significance of $\sqrt{TS} \leq 3.87\sigma$ for the integrated gamma-ray activity between 100 MeV - 500 GeV at a photon flux level of 0.486 ± 0.261 x 10^{-8} photons cm^{-2} s^{-1} using the broken power law model. This resulted in a 3σ upper-limit detection from the position of AR Sco. The location of AR Sco inside the Rho Ophiuchi (Rho Oph) molecular cloud complex combined with the poor spatial resolution of Fermi-LAT, complicates any positive identification of low-level gamma-ray activity at the location that coincides with the position of AR Sco.

36th International Cosmic Ray Conference - ICRC2019
July 24th - August 1st, 2019
Madison, Wisconsin, USA

*Speaker.

1. Introduction

Since the discovery of the peculiar close binary system AR Scorpii (AR Sco) in 2016, ([1]) which displays non-thermal dominated multi-frequency emission from radio to X-rays (see Fig. 1), it has been the focus of intensive observational and theoretical investigation. This system consists of a 0.8 - 1.29 $M_{\odot}$ highly magnetic white dwarf with a surface field $B \leq 500\,\mathrm{MG}$ (e.g. [2, 3]) orbiting an 0.28-0.45 $M_{\odot}$ M5 dwarf star with an orbital period of $P_{\mathrm{orb}} = 3.56\,\mathrm{hours}$. Assuming the secondary star fills its Roche lobe, the distance to the system is estimated to be approximately $d \sim$ 116 pc [1].

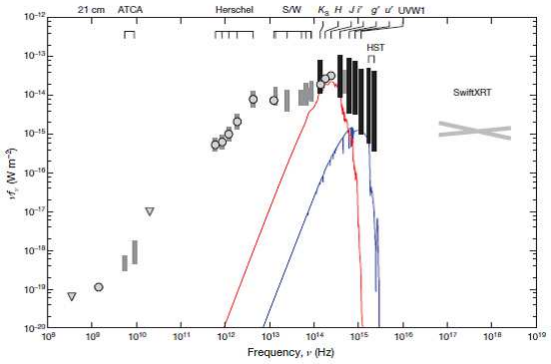

Figure 1: The multi-frequency Spectral Energy Distribution (SED) of AR Scorpii from radio to X-ray frequencies. The red and blue curves represent model atmospheres of the red M5 secondary dwarf star (T = 3100 K) and white dwarf (T = 9750 K) respectively. Adopted from [1].

In the optical part of the spectrum (see [1]) the system reveals strong brightness variations every 117 s (i.e. pulsations), which is the spin period of the white dwarf, superimposed on the orbital period as well as strong pulsations at 118.2 s, which is a beat period between the spin period and the binary orbital period (see Fig. 2). Both the spin and beat periods are clearly visible on a power spectrum (see Fig. 3), especially at the first harmonic where a clear differentiation can be distinguished between the spin and beat periods [1].

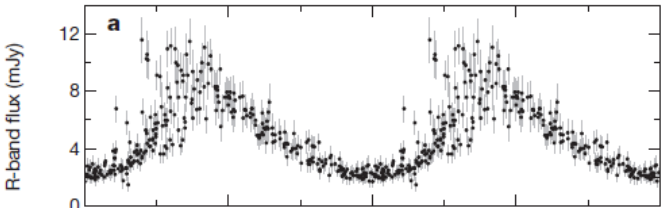

Figure 2: The orbital modulation from AR Scorpii in R-band, showing ellipsoidal variations that may be due to a Rochle lobe filling (or nearly lobe filling) secondary star. Superimposed on this orbital light curve, optical pulsations can be seen at the spin period (117 s) and beat period (118.2 s) with the binary system. Adopted from [1].

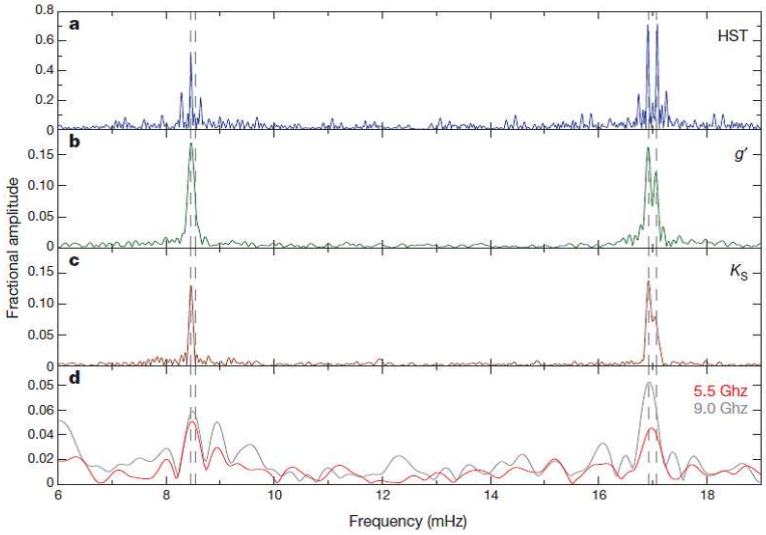

Figure 3: Periodograms from radio to optical (HST), all revealing the strong double pulse beat period between the spin and orbital periods of the system. The beat pulse and the spin frequency are most prominent at the first harmonic, close to 17 mHz. The peak on the left represents the beat while the peak on the right represents the spin frequency. Adopted from [1].

High-speed all-Stokes optical polarimetry utilizing the South African Astronomical Observatory (SAAO) HIPPO Polarimeter [4] on the 1.9 m telescope reveals strong linear polarization at levels up to 40 % with significantly lower levels of circular polarization ($< 10\%$), see Fig. 4, [2, 3]. The nature of the linear polarization profile is consistent with synchrotron emission produced in the magnetic field of a rotating magnetic dipole, strengthening the notion that the white dwarf in AR Sco is a white dwarf pulsar.

Also, the notion that nearly the entire Spectral Energy Distribution (SED) may be dominated by non-thermal emission sparked enormous interest among theorists (e.g. [5, 6]). A favorite approach was to model the emission as being the result of the interaction between a highly magnetized white dwarf pulsar and an M-type secondary dwarf star (see Fig. 5). It is proposed that the WD is a nearly perpendicular rotator where both open field lines sweep past the M-type in each rotation period. The interaction between the particle beam streaming out from the open field line regions and the M-type wind would lead to the formation of a bow shock, where the relativistic electrons can be accelerated by the large magnetic field to produce possible synchrotron radiation in the magnetic field of the magnetosphere. However, it has also been shown that very high energy gamma-ray production through a hadronic channel like π° is also possible [7], as well as inverse Compton scattering.

Recent studies of the pulsed nature of the emission in X-rays using XMM-Newton data [8] reveal pulsed emission consistent with the white dwarf spin period with a pulsed fraction of $\sim$ 14 %. Here it is suggested that the X-ray emission is produced mainly by a thermal plasma on the secondary star heated by magnetic pumping from the white dwarf's magnetic field lines that sweeps across it during every rotation cycle. The X-ray luminosity of $L_x = 4 \times 10^{30}\,\mathrm{erg\ s^{-1}}$ is

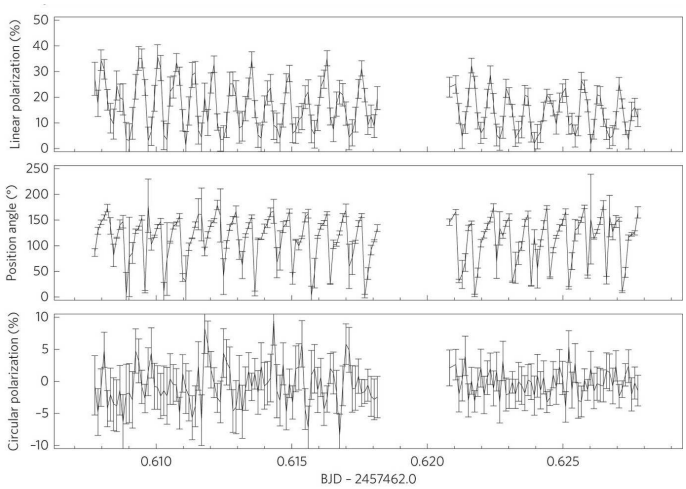

Figure 4: Time series polarimetry (10s bins) that shows the degree of linear polarization, position angle of linear polarization and the degree of circular polarization. Adapted from [2].

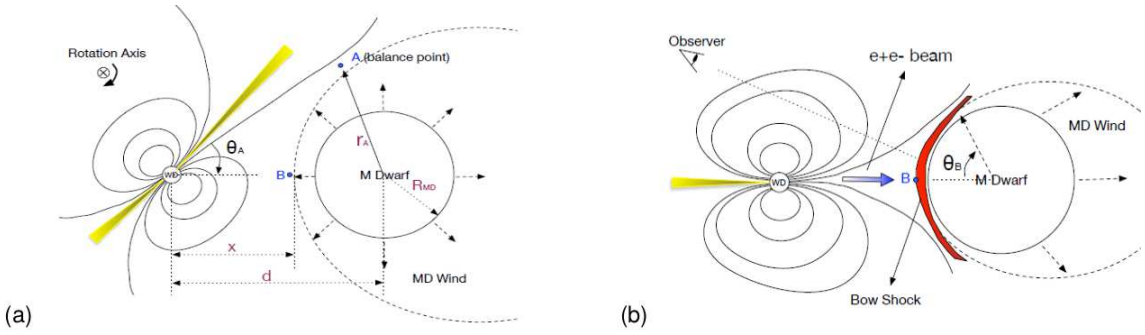

Figure 5: Proposed schematic illustration of the WD/MD binary in AR Sco, where (a) shows the increase of emission from the white dwarf as the electron/positron beam approaches the M-dwarf wind (point A), and (b) shows the episode when the open field lines of the WD interacts with the M-dwarf to form a bow shock, where electrons are accelerated to relativistic energies. Adopted from [5].

then produced mainly by the thermalized electrons on the face of the secondary star, with the non-thermal component, peaking in IR/Optical, produced by relativistic electrons accelerated in the magnetosphere of the white dwarf [8]. It is also suggested that the relativistic electrons are trapped within the white dwarf's magnetic field lines due to the magnetic mirror effect. Both the models presented by Geng et. al. [5] and Takata et. al. [8] suggest non-thermal emission inside this region.

For AR Sco the ratio of the X-ray luminosity to spin-down power, i.e. $\alpha = L_x/L_{\dot{\nu}_{\rm s,wd}} \sim 10^{-3}$, is similar to another cataclysmic variable AE Aquarii and place both AR Sco and AE Aquarii in the same class as spin-powered pulsars [9]. The high ratio of spin-down power to thermal X-ray emission provides a reservoir for particle acceleration that makes AR Sco a possible candidate for high energy gamma-ray emission like most other spin-powered pulsars [9].

2. Using 10 years of Fermi-LAT data to search for γ-ray emission

A Fermi-LAT dataset from the past decade (4Aug2008-18Mar2019) was extracted from the Fermi Science Support Center (FSSC) in the energy range of 100 MeV to 500 GeV. By using the Pass 8 data analysis pipeline, which provides a better determination of the diffuse galactic gamma-ray emission and a significant improvement in terms of energy resolution from previous Fermi-LAT pipelines, it was possible to do a standard Binned Likelihood Analysis on the Fermi-LAT dataset.

The analysis was performed using the recently released Fermi Tools software, where a number of energy ranges were experimented with to fit and produce likelihood statistics for AR Sco. The event files, i.e. the photon and spacecraft files that were extracted from the FSSC site, were chosen to have a Region of Interest (ROI) of 10° centred at ARSco (RA:$16^h21^m47.28^s$, Dec: $-22°53'10.39''$, J2000) in order to extract the high energy photons for analysis. During reduction, only SOURCE class events (`evclass=128`) were considered, along with the relational filter (`DATA_QUAL>0 and LAT_CONFIG==1`) to select good time intervals. All the point sources in the fourth Fermi-LAT catalogue (4FGL) located within the ROI were modelled in the spectral fits, including the latest isotropic background and galactic diffuse emission. All the point sources included in the background model file are the same as reported in the 4FGL catalogue.

As AR Sco is not listed in the 4FGL catalogue we have followed the same methodology as ([10]), which reported the detection of a gamma-ray flare from the high redshift blazar DA 193, by manually adding the source to the model centred at its coordinates. The associated parameters of spectral models of all the sources within a 2° radius were chosen to be free to vary while performing the likelihood fitting. Since AR Sco is not part of the 4FGL catalogue, it was first added by parameterizing a power law spectral shape where the prefactor and photon index of the model were allowed to vary during optimization. A power law model was chosen since it is the easiest to model and is analogous with non-thermal emission. After the power law model was added, both broken power law and log parabola were also used to do a likelihood fit. The final results are summarized in Table 1.

Table 1: Spectral model parameters obtained for AR Sco using Binned Likelihood Analysis. Optimization of AR Sco was done using a power law (Γ= - (2.7 $\pm$ 0.8)), broken power law and log parabola to determine the likelihood of detection of gamma-rays from the ROI centred on AR Sco.

Spectral model	IntFlux(photons/cm^2/s)	N$_{pred}$	TS	Significance
Power Law	0.565 ± 0.311 x 10^{-8}	1092.78	8.53	$\leq 2.92\sigma$
Broken Power Law	0.486 ± 0.261 x 10^{-8}	1126.57	15.04	$\leq 3.87\sigma$
Log Parabola	0.251 ± 0.179 x 10^{-8}	737.39	13.15	$\leq 3.62\sigma$

Results from a previous Fermi-LAT study, shown in Table 2 ([11]), using the methodology of removing sources with a TS value less than 25 showed a possible gamma-ray emission from the region. However, during the analysis process one of the sources closest to AR Sco,the unidentified source *4FGL J1623.7-2315* nearly 0.6° away, was not taken into account during optimization and may have contributed to emission attributed to AR Sco. These results revealed an excess at the $\sqrt{TS} \leq 4.89\sigma$ level from the position of AR Sco between the energy range of 0.1 - 500GeV. Since

all the sources closest to the ROI centre has to be taken into account, the results obtained from this method (see Table 2) needs to be adjusted by incorporating the associated parameters of spectral models of all the sources within a 2° radius mentioned earlier.

Table 2: Summary of model parameters from the power law fit for AR Sco reported in [11] **excluding** the nearby unidentified source *4FGL J1623.7-2315*. The significance levels reported by these authors ([11]) are therefore perhaps too optimistic due to contamination of this near-by (0.6°) source !!

Energy Bin	Spectral Index	N_{pred}	IntFlux(photons/cm^2/s)	TS	Significance
100MeV-500 GeV	2.70 ± 0.82	2041.91	1.076 ± 0.318 x 10^{-8}	23.93	$\leq 4.89\sigma$
100MeV-10 GeV	2.81 ± 0.22	1866.78	0.997 ± 0.317 x 10^{-8}	19.35	$\leq 4.41\sigma$
10GeV-500 GeV	6.03 ± 1.04	0.00	5.681 ± 1.160 x 10^{-16}	0	0

These new updated results (see Table 1) of our present analysis in the energy range of 0.1 - 500 GeV reveals low level emission at the $\leq 3.87\sigma$ significance level from the position of AR Sco. After the likelihood analysis has been performed, SEDs were plotted using e.g. the power law model over 9 energy bins (see Fig. 6). The SED that was obtained using the Fermi build-in function `bdlikeSED`. The energy flux values can be considered as as 2 σ upper limits based on a limiting TS < 4 value per bin. The distribution of TS values per energy bin (see Figure 7) also illustrates that the most significant emission is concentrated in the energy bins below 3 GeV.

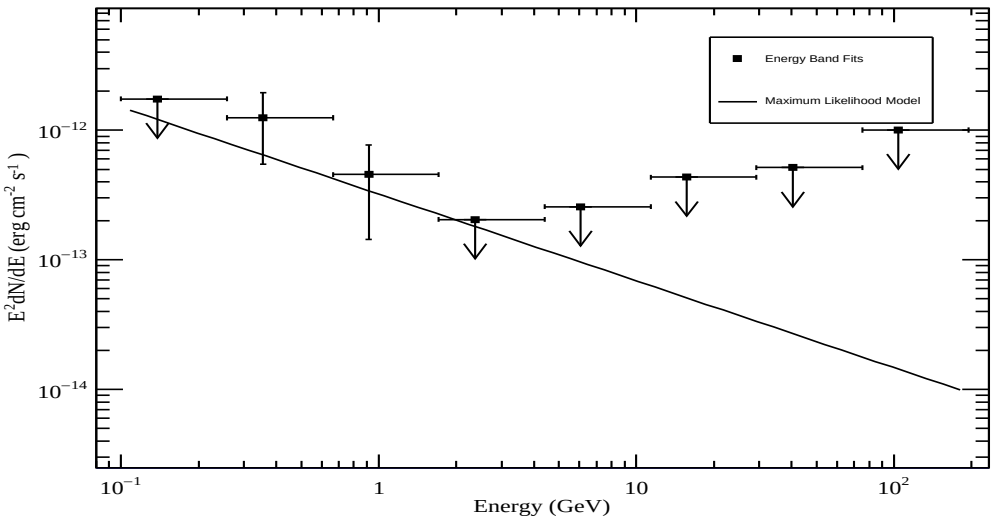

Figure 6: Energy flux SED obtained using bdlikeSED. The flux values are 2 σ upper limits.

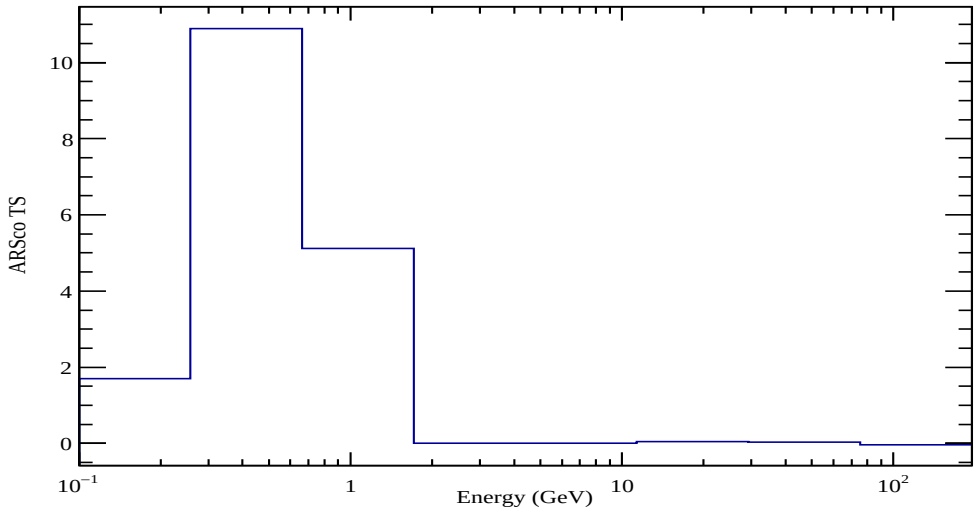

Figure 7: TS values vs energy of γ-ray photons.

From the distribution of TS vs energy results, see Fig. 7, we noticed a higher TS value from the second energy bin compared to the total TS obtained, see Table 1. Likelihood analysis has been done between the 100MeV-3GeV energy range to investigate this higher TS value. The results within this energy range shows a total TS of 11.46 at a photon flux of 0.611 ± 0.482 x 10^{-8} photons cm^{-2} s^{-1}, which corresponds to the maximum TS value obtained in Fig. 7. Due to Fermi's low spatial resolution at lower energies, it may be possible for other nearby sources to still contribute to the detected emission.

3. Conclusions

A search for possible gamma-ray emission from AR Sco was carried out by analysing the Fermi-LAT Pass 8 dataset using the Fermi Science Tools. The results from a binned-likelihood analysis on a ROI with a radius of 10° centred on the position of AR Sco, optimized with power-law, broken power law and log parabola models, revealed low-level gamma-ray flux between 100 MeV - 500 GeV at the 3.87σ level by considering the broken power law as the best fit. This is below the 5σ level heralding a possible detection. Due to the complexity of the surrounding region and the Rho Oph molecular cloud, as well as the poor spatial resolution of the Fermi-LAT telescope at lower energies, it is difficult to pinpoint the exact origin of this low level gamma-ray emission. Unbinned likelihood analysis is underway to try and maximise the probability of detection from the emitting region.

References

[1] T. R. Marsh et al. *A radio-pulsing white dwarf binary star*, *Nature* **537** (2016) 374

[2] D.A.H. Buckley, P.J. Meintjes, S.B. Potter, T.R. Marsh & B.T. Gänsicke *Polarimetric evidence of a white dwarf pulsar in the binary system AR Sco*, *Nature Astronomy* **1** (2017) 0029

[3] D.A.H. Buckley, S.B Potter, P.J. Meintjes, T.R. Marsh and b B.T. Bänsicke *Polarimetric evidence of the first white dwarf pulsar: The Binary System AR Scorpii*, *Galaxies* **6** (2018) 14

[4] S.B. Potter et al. *Polarized QPOs from the INTEGRAL polar IGRJ14536-5522 (= Swift J 1453.4 - 5524)*, *MNRAS* **402** (2010) 1161

[5] J.-J. Geng, B. Zhang, Y.-F. Huang *A model of white dwarf pulsar AR Sco*, *Astrophys. J. Lett.* **831** (2016) L1

[6] J.I. Katz *AR Sco: Presenting a white dwarf synchronar*, *Astrophys. J.* **835** (2017) 150

[7] W. Bednarek *Hadronic modelfor the non-thermal radiation from the binary system AR Scorpii*, *MNRAS* **476** (2018) L10-L14

[8] J. Takata, C. -P. Hu, L.C.C. Lin, P.H.T. Tam, P.S. Pal, C.Y. Hui, A.K.H Kong and K.S. Cheng *A non-thermal pulsed X-ray emission of AR Scorpii*, *The Astrophysical Journal* **853(2)** (2018), 106

[9] W. Becker & J. Trümper *The x-ray luminosity of rotation powered neutron stars*, *Astronomy & Astrophysics* **326** (1997) 682

[10] V.S. Paliya et al. *Detection of a Gamma-Ray Flare from the High-redshift Blazar DA 193*, *The Astrophysical Journal* **871** (2019) 211

[11] Q. Kaplan, P.J. Meintjes, K.K. Singh, H.J. van Heerden and F.A. Ramamonjisoa, *White Dwarf Pulsars as Possible Gamma-Ray Sources*, PoS(HEASA 2018)037, in Proceedings of *High Energy Astrophysics in Southern Africa-HEASA-2018*, 1-3 August 2018, Parys (South Africa)

PROCEEDINGS OF SCIENCE

White Dwarf Pulsars as Possible Gamma-Ray Sources

Q. Kaplan[1], **P.J. Meintjes**[1*], **K.K. Singh**[1,2], **H.J. van Heerden**[1], **F.A. Ramamonjisoa**[1]
1.) Department of Physics, University of the Free State, PO Box 339, Bloemfontein, 9300
2.) Astrophysical Sciences Division, Bhaba Atomic Research Centre, Mumbai, India, 400085

E-mail: MeintjPJ@ufs.ac.za

The newly discovered white dwarf binary system AR Scorpii (AR Sco) with its fascinating non-thermal dominated multi-frequency emission has sparked renewed interest in potential high energy gamma-ray emission from white dwarf pulsars. Recent studies revealed that the optical and X-ray components of the emission in AR Sco can be powered entirely by the spin-down luminosity of the white dwarf in the absence of any mass accretion in this system. The Spectral Energy Distribution (SED) below and above optical shows a clear indication of a non-thermal synchrotron component, with pulsed emission in optical and X-ray bands at the white dwarf spin period as well as a beat with the binary period. From an energy perspective the highly magnetic rotating white dwarf can accelerate particles to TeV energies. In this study, a search for high energy gamma-ray emission was conducted between 100 MeV - 500 GeV by analysing the newly available Fermi-LAT Pass 8 data with the new Fermi 1.0.1 Science Tools. From the selected Region of Interest (ROI) centred on AR Sco's position we calculated a significance of $\sqrt{TS} \leq 4.89\,\sigma$ for the integrated gamma-ray activity between 100 MeV - 500 GeV at a photon flux level of $1.076 \pm 0.318 \times 10^{-8}$photons cm^{-2}s^{-1}. However, the close-by unidentified source ($\sim 0.576^{\circ}$) $4FGLJ1623.7-2315$ may also contribute to this emission. AR Sco's location inside the Rho Ophiuchi (Rho Oph) molecular cloud complex combined with the poor spatial resolution of Fermi-LAT complicates any unambiguous identification of the source of low-level gamma-ray activity at the location that coincides with the position of AR Sco.

High Energy Astrophysics in Southern Africa - HEASA2018
1-3 August, 2018
Parys, Free State, South Africa

*Speaker.

PoS(HEASA2018)037

1. Introduction

The recent discovery ([1]) of the peculiar close binary system AR Scorpii (AR Sco) which displays non-thermal dominated multi-frequency emission (see Fig. 1) from radio to X-rays sparked enormous interest in the astronomy community. The notion that nearly the entire Spectral Energy Distribution (SED) may be dominated by non-thermal emission is of huge theoretical interest (e.g. [2, 3]). A favorite approach was to model the emission as being the result of the interaction between a highly magnetized white dwarf pulsar and an M-type secondary dwarf star. It also sparked renewed interest in white dwarf pulsars being potential high energy gamma-ray emitters (e.g. [4, 5]). This system consists of a 0.8 - 1.29 $M_{\odot}$ highly magnetic white dwarf with a surface magnetic field that can be as high as 500 MG (e.g. [4, 5]) orbiting an M5 dwarf star with mass ranging between 0.28-0.45 $M_{\odot}$ with an orbital period of $P_{\rm orb} = 3.56$ hours. Assuming the secondary star fills its Roche lobe, the distance to the system is estimated to be approximately $d \sim 116$ pc [1].

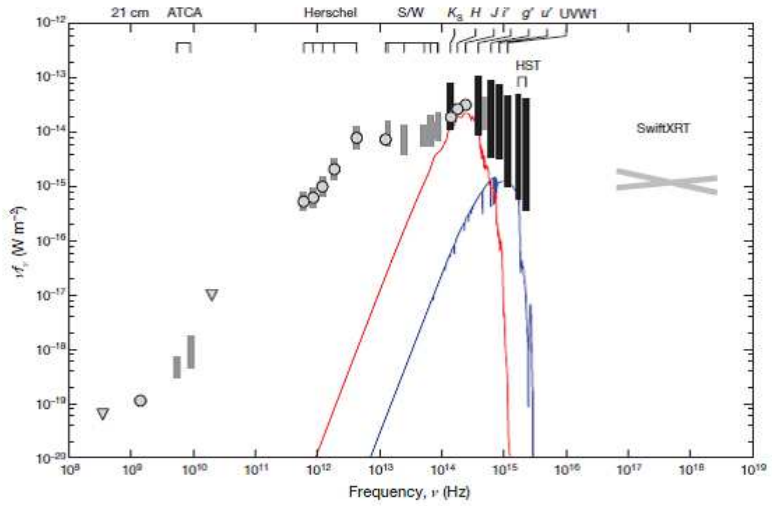

Figure 1: The multi-frequency Spectral Energy Distribution (SED) of AR Scorpii from radio to X-ray frequencies. The red and blue curves represent model atmospheres of the red M5 secondary dwarf star (T = 3100 K) and white dwarf (T = 9750 K) respectively. Adopted from [1].

In the optical band (see [1]) the system reveals pulsations at 117 s, which is the spin period of the white dwarf, superimposed on the orbital period as well as strong pulsations at 118.2 s, which is a beat period between the spin period and the binary orbital period (see Fig. 2). Both the spin and beat periods are clearly visible on a power spectrum (see Fig. 3), especially at the first harmonic where a clear differentiation can be distinguished between the spin and beat periods [1].

High-speed all-Stokes optical polarimetry utilizing the South African Astronomical Observatory (SAAO) HIPPO Polarimeter [6] on the 1.9 m telescope reveals strong a linear polarization at levels up to 40 % with significantly lower levels of circular polarization ($< 10\%$) [4, 5]. The nature of the linear polarization profile, especially the 360 degrees swing in the position angle is consistent with synchrotron emission produced in the magnetic field of a rotating magnetic dipole, strengthening the notion that the white dwarf in AR Sco is a white dwarf pulsar.

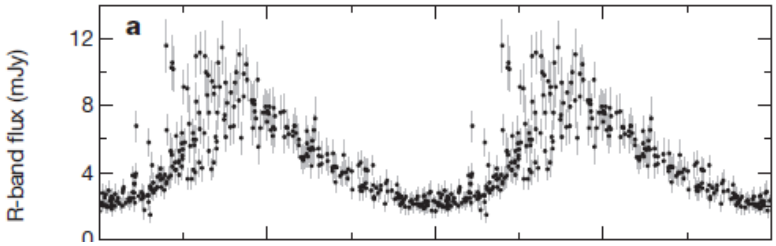

Figure 2: The orbital modulation from AR Scorpii in R-band, showing ellipsoidal variations that may be due to a Roche lobe filling (or nearly lobe filling) secondary star. Superimposed on this orbital light curve, optical pulsations can be seen at the spin period (117 s) and beat period (118.2 s) with the binary system. Adopted from [1].

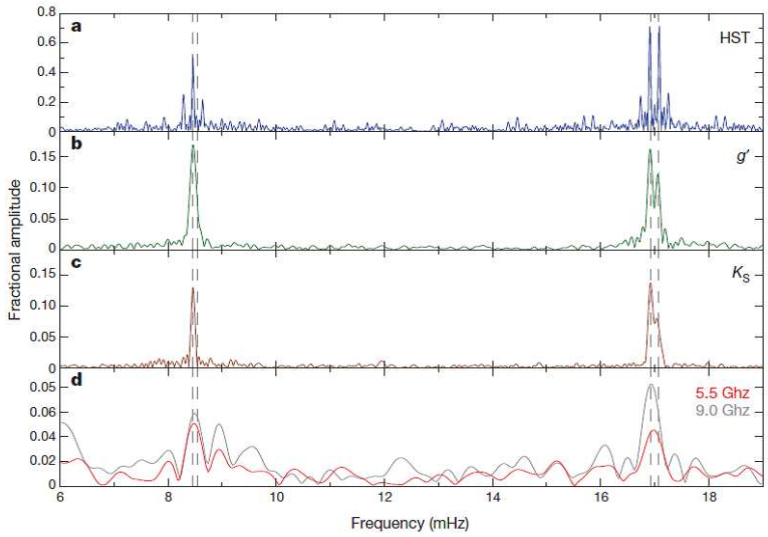

Figure 3: Periodograms from radio to optical (HST), all revealing the strong double pulse beat period between the spin and orbital periods of the system. The beat pulse and the spin frequency are most prominent at the first harmonic, close to 17 mHz. The peak on the left represents the beat while the peak on the right represents the spin frequency. Adopted from [1].

Initial pulse timing studies after its discovery, over a baseline of 7 years, suggest that the white dwarf is slowing down, resulting in a frequency derivative of - $\dot{\nu}_{\rm s,wd} = 2.86 \times 10^{-17}$ Hz s^{-1}, which for a $\sim 0.8\,M_\odot$ white dwarf ($R_{\rm wd} \approx 0.01 R_\odot$), infer a spin-down luminosity of approximately $L_{\dot{\nu}_{\rm s,wd}} \approx 1.5 \times 10^{33}$ erg s^{-1} [1]). The result of a more recent study of the spin-evolution of the white dwarf [7] is inconsistent with any reported spin-down, while another study [8] shows an evidence of a spin-down rate through a beat frequency derivative - $\dot{\nu}_{\rm s,b} = 5.14 \times 10^{-17}$ Hz s^{-1} with resultant spin-down power of $L_{\dot{\nu}_{\rm s,wd}} \approx 3 \times 10^{33}$ erg s^{-1} which is approximately twice the value reported earlier [1].

Recent studies of the pulsed nature of the emission in X-rays using XMM-Newton data [10] reveal pulsed emission consistent with the white dwarf spin period with a pulsed fraction of $\sim$

14 %. These authors suggest that the X-ray emission is produced mainly by a thermal plasma on the secondary star heated by magnetic pumping from the white dwarf field that sweeps across it during every rotation cycle. The X-ray luminosity of $L_x = 4 \times 10^{30}$ erg s^{-1} is then produced mainly by the thermalized electrons on the face of the secondary star, with the non-thermal component, peaking in IR/Optical, produced by relativistic electrons accelerated in the magnetosphere of the white dwarf [9, 10]. Further, they propose that the emission is consistent with a power-law electron spectrum with index ranging between p = 2.5 - 3.

For AR Sco the ratio of the X-ray luminosity to spin-down power, i.e. $\alpha = L_x/L_{\dot{\nu}_{s,wd}} \sim 10^{-3}$, is similar to another cataclysmic variable AE Aquarii and place both AR Sco and AE Aquarii in the same class as spin-powered pulsars [11] (see Fig. 4). The high ratio of spin-down power to thermal X-ray emission provides a reservoir for particle acceleration that makes AR Sco a possible candidate for high energy gamma-ray emission like most other spin-powered pulsars [11].

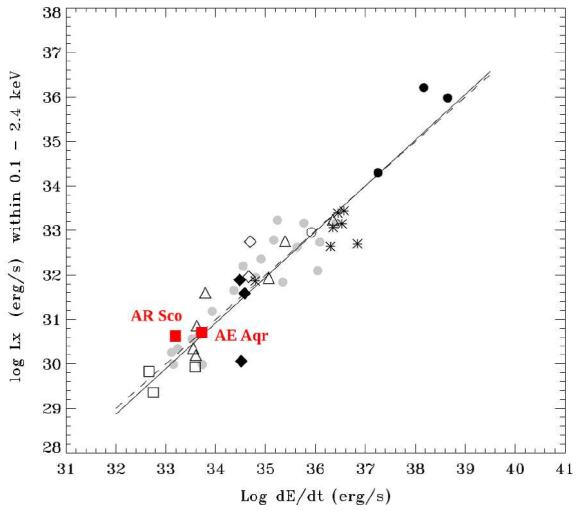

Figure 4: The X-ray luminosity versus spin-down power of spin-powered neutron stars, compared to both the white dwarfs in AR Sco and AE Aquarii. Adapted from [11].

2. The search for gamma-ray emission using 10 years of Fermi-LAT data

A Fermi-LAT dataset from the past decade (4 August 2008 - 18 March 2019) was extracted from the Fermi Science Support Center (FSSC) in the energy range of 100 MeV to 500 GeV. By using the Pass 8 data analysis pipeline, which provides a better determination of the diffuse galactic gamma-ray emission and a significant improvement in terms of energy resolution from previous Fermi-LAT pipelines, it was possible to do a standard Binned Likelihood Analysis on the Fermi-LAT dataset centred on the position of AR Sco. The analysis was performed using the recently released Fermi Tools software (Fermi 1.0.1), where a number of energy ranges were experimented with to fit and produce the likelihood statistics for AR Sco. The event files, i.e. the photon and spacecraft files that were extracted from the FSSC site, were chosen to have a Region of Interest (ROI) of 10° centred on AR Sco's position (RA:$16^h21^m47.28^s$, Dec: $-22°53'10.39''$, J2000) in order to extract the high energy photons for analysis. During reduction, only SOURCE

class events (`evclass=128`) were considered, along with the relational filter (`DATA_QUAL>0 and LAT_CONFIG==1`) to select good time intervals for the period 4 August 2008 - 18 March 2019.

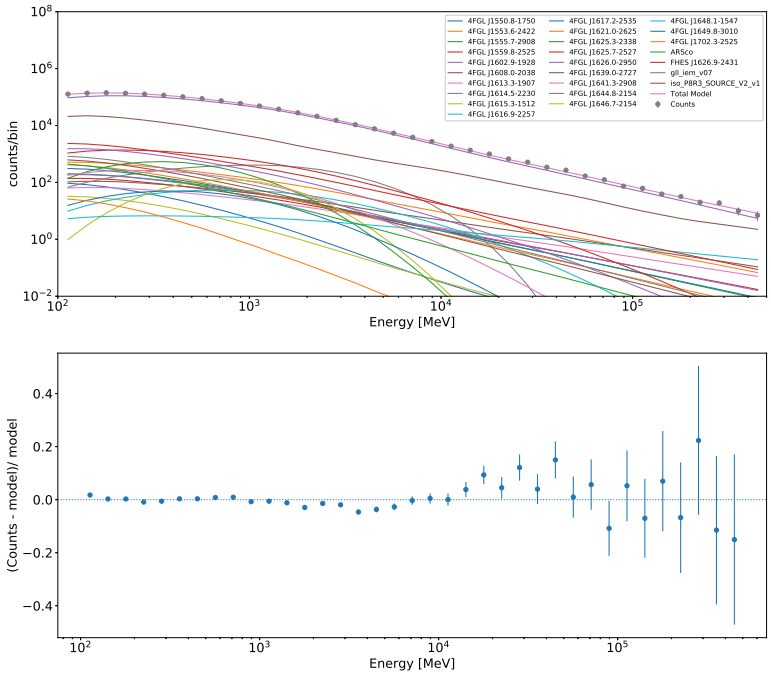

Figure 5: Counts model (top) and residual fit (bottom) from the binned likelihood analysis for AR Sco using power law spectral shape in the energy range 100 MeV to 500 GeV.

All the point sources in the fourth Fermi-LAT catalogue (4FGL) located within the ROI were used to generate the background model including the latest isotropic background and galactic diffuse emission. The spectral forms of all the point sources included in the background model file are the same as reported in the 4FGL catalogue. As AR Sco is not listed in the 4FGL catalogue, we have followed the same methodology to perform the binned likelihood analysis as ([12]) which reported the detection of a gamma-ray flare from the high redshift blazar DA 193. The target source AR Sco was added in the model file with a power law spectral shape. The associated parameters of spectral models of all the sources within the ROI were chosen to be free to vary while performing the binned likelihood fitting. The prefactor and photon index of AR Sco were also allowed to vary during the fitting. The significance of the γ-ray signal was determined from the maximum likelihood test statistic (TS) which follows a χ^2 distribution with two degrees of freedom, resulting in an upper limit significance (σ) for a large number of data points which can be approximated by $\sqrt{TS}$ ([13, 14]). All the sources, except AR Sco, with a TS value of less than 25 were removed

from the model file and the likelihood fitting was re-performed using these sources. The fitting was repeated to optimize the background model file with sources having a TS value more than or equal to 25. The results of the final binned likelihood fitting for modelling the counts and corresponding residual fit in the energy range 100 MeV to 500 GeV are shown in Fig. 5, indicating convergence up to an energy value of 10 GeV. The values of the model parameters derived from the fitting for AR Sco in different energy bands are summarized in Table 1. The model parameters reported in Table 1 indicate that the γ-ray emission from the position of AR Sco in the energy range 100 MeV-500 GeV is mainly dominated by the photons with energy in lower energy band 100 MeV-10 GeV. Above 10 GeV, the γ-ray emission from AR Sco is below the detection sensitivity of the Fermi-LAT. The residual map in the absence of a source (see Fig. 6) and TS map (see Fig. 7) seem to suggest an excess of bright pixels at the centre of the ROI. The distribution of TS values as a function of energy (see Fig. 8) also indicates that γ-ray emission from the direction of AR Sco is more significant at lower energies in the range between 100 MeV and 10 GeV. However, it is important to note here that an unidentified γ-ray source namely $4FGLJ1623.7-2315$ is also present in the background model at an angular separation of 0.576° from the position of AR Sco (or from the ROI center). Therefore, γ-ray emission from the position of AR Sco in the energy range 100 MeV-10 GeV detected by the Fermi-LAT can be contaminated by the emission from $4FGLJ1623.7-2315$ due to its poor angular resolution at low energies. A detailed analysis of the Fermi-LAT data is in progress to properly quantify possible γ-ray emission from the region containing AR Sco.

Table 1: Summary of model parameters from the power law fit for AR Sco (at the centre of ROI) using Binned Likelihood Analysis for the period 4 August 2008 - 18 March 2019.

Energy Range	Spectral Index	N_{pred}	Integral Flux (ph/cm^2/s)	TS	Significance
100 MeV-500 GeV	2.70±0.82	2041.91	$(1.076\pm0.318)\times10^{-8}$	23.93	$\leq 4.89\sigma$
100 MeV-10 GeV	2.81±0.22	1866.78	$(0.997\pm0.317)\times10^{-8}$	19.35	$\leq 4.40\sigma$
10 GeV- 500 GeV	6.03±1.04	0.00	$(5.681\pm1.160)\times10^{-16}$	0	0

The results of our present analysis in the energy range between 0.1 - 500 GeV reveals an excess at the $\sqrt{TS} \leq 4.89\sigma$ (e.g. [14]) significance level from the position of AR Sco at the centre of the ROI which also contains a nearby unclassified source $4FGLJ1623.7-2315$. After the likelihood analysis has been performed, SEDs were plotted using the Power Law model over 9 energy bins (see Fig. 9). The SED was obtained using the Fermi build-in function `bdlikeSED`. The energy flux values can be considered as 2 σ upper limits. A broadband SED (see Fig. 10) was also created with radio and optical data obtained from ([1]) and X-ray data obtained from ([10]). The flux upper limits from the AR Sco ROI between 100 MeV - 500 GeV coincides with the Fermi-LAT (10 year) [blue curve] threshold but are well below the CTA-South (50 hour) [red curve] sensitivity level in this energy interval.

3. Conclusions

A search for possible gamma-ray emission from AR Sco was carried out by analysing the Fermi-LAT Pass 8 dataset using the Fermi Science Tools. The results from a binned-likelihood

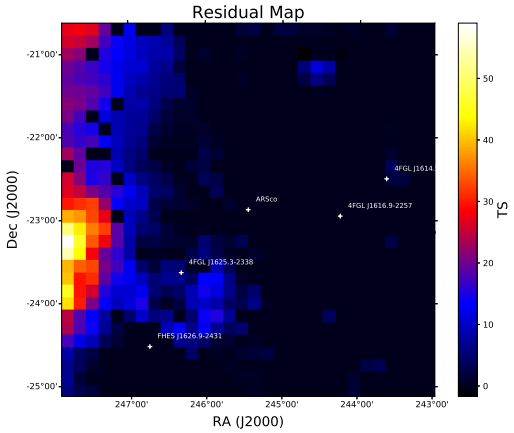

Figure 6: Residual map in the absence of target source at the centre of the ROI.

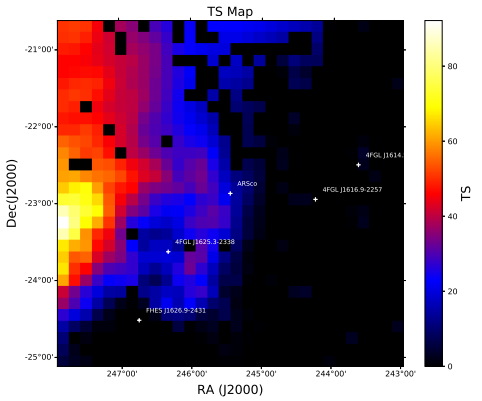

Figure 7: TS map displaying excess of bright pixels at the centre of the ROI.

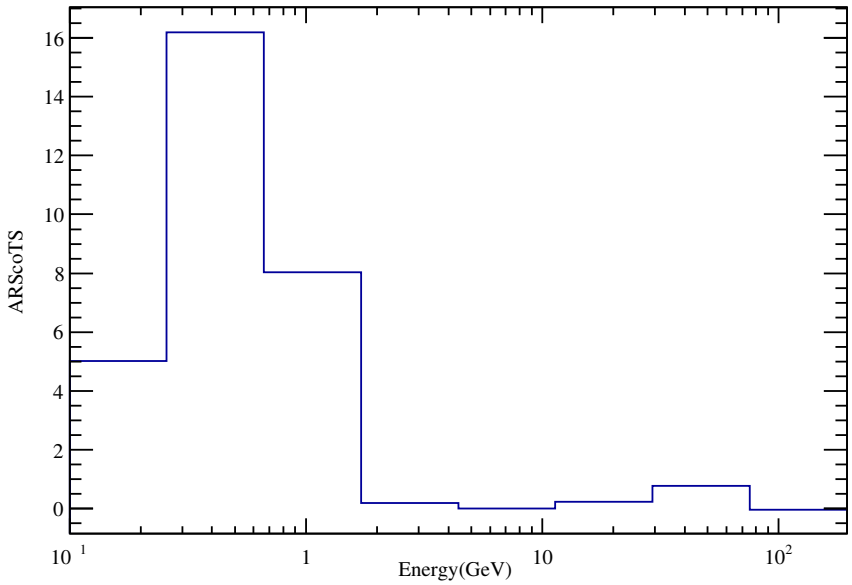

Figure 8: TS values vs energy of γ-ray photons.

analysis on a ROI with a radius of 10° centred on the position of AR Sco, optimized with a power-law model of index ($\Gamma = -2.7$), revealed a gamma-ray flux between 100 MeV - 500 GeV at the $\sqrt{TS} \leq 4.89\sigma$ level. This however may include some emission from an unclassified source $4FGLJ1623.7-2315$ which contribution to the total emission is still uncertain. The flux upper limits per energy bin correlates with the 10 year Fermi-LAT (blue) threshold but are well below the 50 hour CTA-South (red) sensitivity threshold. The location of AR Sco in the Rho Oph cloud complex combined with the presence of the nearby unclassified 4FGL source makes any unambiguous identification very difficult at this stage.

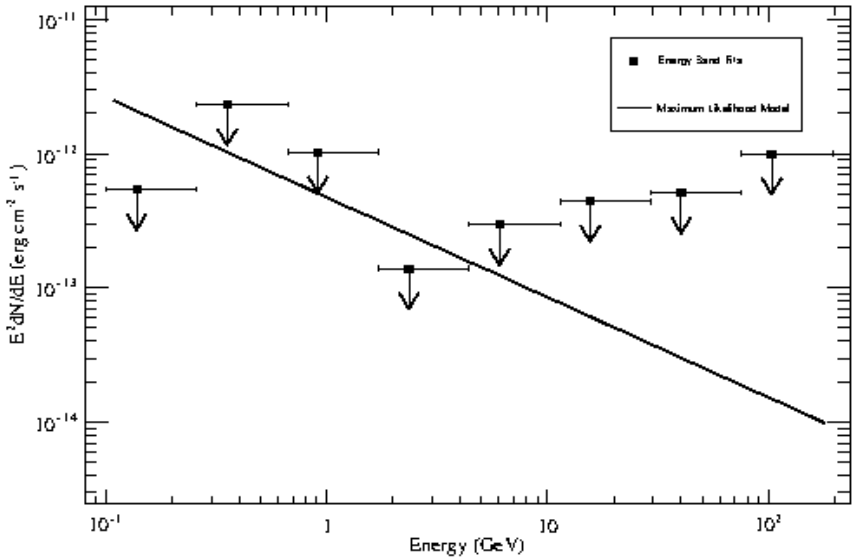

Figure 9: Energy flux SED obtained using bdlikeSED. The flux values are 2 σ upper limits.

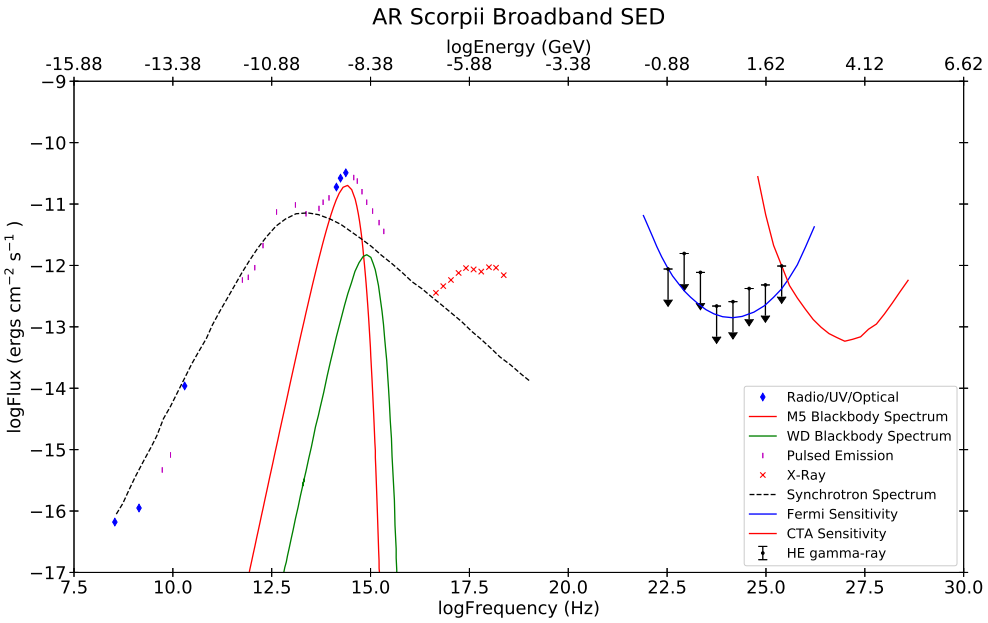

Figure 10: AR Sco broadband SED showing the gamma-ray upper limits in relation to the Fermi- LAT 10 year [1] (blue) and CTA-South 50 hour [2] (red) sensitivity curves.

[1] *http : //www.slac.stanford.edu/exp/glast/groups/canda/lat − Performance.htm*

[2] *https : //portal.cta − observatory.org/CTA − Observatory/performance/SitePages/Home*

4. Acknowledgements

The authors thank Dr R.J. Britto for his guidance with the Fermi-LAT data analysis process.

References

[1] T. R. Marsh et al. *A radio-pulsing white dwarf binary star*, *Nature* **537** (2016) 374

[2] J.-J. Geng, B. Zhang, Y.-F. Huang *A model of white dwarf pulsar AR Sco*, *Astrophys. J. Lett.* **831** (2016) L1

[3] J.I. Katz *AR Sco: Presenting a white dwarf synchronar*, *Astrophys. J.* **835** (2017) 150

[4] D.A.H. Buckley, P.J. Meintjes, S.B. Potter, T.R. Marsh & B.T. Gänsicke *Polarimetric evidence of a white dwarf pulsar in the binary system AR Sco*, *Nature Astronomy* **1** (2017) 0029

[5] D.A.H. Buckley, S.B Potter, P.J. Meintjes, T.R. Marsh and b B.T. Bänsicke *Polarimetric evidence of the first white dwarf pulsar: The Binary System AR Scorpii*, *Galaxies* **6** (2018) 14

[6] S.B. Potter et al. *Polarized QPOs from the INTEGRAL polar IGRJ14536-5522 (= Swift J 1453.4 - 5524)*, *MNRAS* **402** (2010) 1161

[7] S.B. Potter and D.A.H. Buckley *A re-evaluation of the proposed spin-down rate of the white dwarf pulsar in AR Scorpii*, *MNRAS* **478** (2018) L78

[8] R.A. Stiller, C. Littlefield, P. Garnavich, C. Wood, F-J Hambsch and G. Meyers *High-time resolution photometry of AR Scorpii: Confirmation of the white dwarf's spin-down*, *The Astronomical Journal* **156(4)** (2018) 150

[9] J. Takata, H Yang and k.S. Cheng *A model for AR Scorpii: Emission from relativistic electrons trapped by by closed magnetic field lines of magnetic white dwarfs*, *The Astrophysical Journal* **851** (2017) 143

[10] J. Takata, C. -P. Hu, L.C.C. Lin, P.H.T. Tam, P.S. Pal, C.Y. Hui, A.K.H Kong and K.S. Cheng *A non-thermal pulsed X-ray emission of AR Scorpii*, *The Astrophysical Journal* **853(2)** (2018), 106

[11] W. Becker & J. Trümper *The X-ray luminosity of rotation powered neutron stars*, *Astronomy & Astrophysics* **326** (1997) 682

[12] V.S. Paliya et al. *Detection of a Gamma-Ray Flare from the high-redshift Blazar DA 193*, *The Astrophysical Journal* **871** (2019) 211

[13] S. Wilks *The large sample distribution of the likelihood ratio for testing composite hypothesis*, *The Annals of Mathematical Statistics* **9** (1938) 60

[14] J.R. Mattox et al. *The likelihood analysis of EGRET data*, *The Astrophysical Journal* **461** (1996) 396

PROCEEDINGS OF SCIENCE

Searching for gamma-ray emission from the white dwarf pulsar system AR Sco using Pass 8 *Fermi*-LAT data

Q. Kaplan[1]*, **P.J. Meintjes**[1], **K.K. Singh**[1,2], **H.J. van Heerden**[1]
1.) Department of Physics, University of the Free State, PO Box 339, Bloemfontein, 9300
2.) Astrophysical Sciences Division, Bhabha Atomic Research Centre, Mumbai, India, 400085
E-mail: kaplanq@ufs.ac.za

AR Sco is a close compact binary system that shows non-thermal, pulsed and highly linear polarized emission. In this study, a search for high energy gamma-ray emission was conducted between 100 MeV - 500 GeV by analysing the newly available *Fermi*-LAT Pass 8 data with the newly available *Fermi* 1.0.1 Science Tools. Binned likelihood analysis was performed using power law, broken power law and log parabola models. From the selected Region of Interest (ROI) centred on AR Sco's position, we calculated a statistical significance of $\sqrt{TS} \leq 4.31\sigma$ for the integrated gamma-ray activity between 100 MeV - 500 GeV at a photon flux level of $(4.39 \pm 3.24) \times 10^{-9}$ ph cm^{-2} s^{-1} using the broken power law model. This resulted in 2σ photon flux upper-limits from the position of AR Sco. Unbinned likelihood analysis was also done to maximize the probability of detection from this faint gamma-ray emitting region, resulting in a statistical $\sqrt{TS} \leq 3.69\sigma$ value using a broken power law model with an associated photon flux level of $(3.57 \pm 1.10) \times 10^{-9}$ ph cm^{-2} s^{-1}.

7th Annual Conference on High Energy Astrophysics in Southern Africa
28 - 30 August 2019
Swakopmund, Namibia

*Speaker.

PoS(HEASA2019)049

1. Introduction

The close binary system AR Scorpii (henceforth AR Sco) [1] features non-thermal dominated multi-frequency emission from radio to X-rays. This source has been the focus of intensive multi-wavelength observational and theoretical investigation since the discovery of pulsed optical and radio emission by Marsh et al. in 2016 [1]. This binary system consists of a 0.81 - 1.29 $M_\odot$ highly magnetic white dwarf (WD) with a surface magnetic field B $\leq$ 500 MG [2, 3] orbiting a 0.28-0.45 $M_\odot$ M5 spectral-type dwarf star with an orbital period of $P_{\rm orb}$ = 3.56 hours. The WD in the system also exhibits variable pulsar-like emission at the rotational period of $P_{\rm spin}$ = 117 s, with strong supplementary pulsations at 118 s which is the beat period between the spin an orbital period [2].

Optical observations utilizing the South African Astronomical Observatory (SAAO) HIPPO Polarimeter [4] on the 1.9 m telescope reveals strong linear polarization at levels up to 40% with significantly lower levels of circular polarization (< 10%) [2, 3]. The morphology and pulse profile of the linear polarization are similar to that of the Crab pulsar, which is a young isolated neutron star pulsar that emits radiation from radio to TeV energies, e.g. [5]. The nature of the linear polarization profile is also consistent with synchrotron emission produced in the magnetic field of a rotating magnetic dipole, strengthening the notion that the WD in AR Sco may in fact be a "WD pulsar" which can produce non-thermal pulsar-like emission. Also, the possibility that nearly the entire Spectral Energy Distribution (SED) may be dominated by non-thermal emission sparked enormous interest among theorists, especially how non-thermal emission is being produced [6, 7].

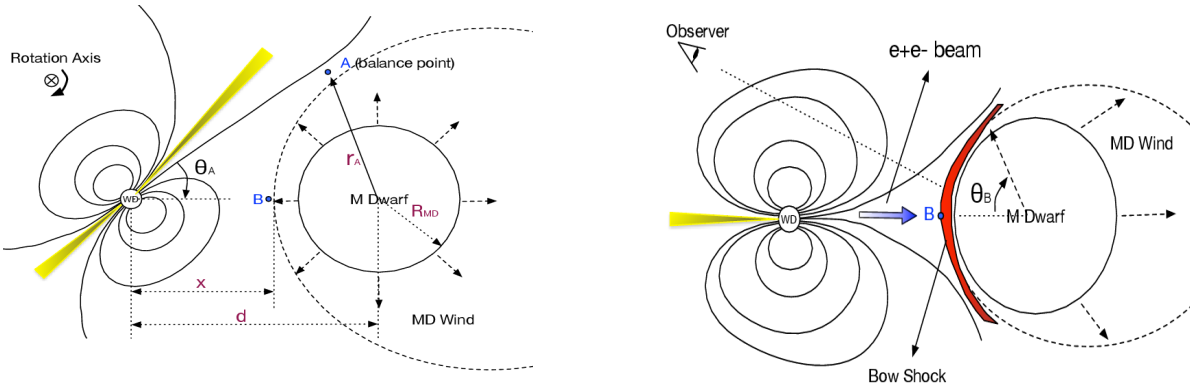

(a) (b)

Figure 1: Proposed schematic illustration of the WD/M-dwarf binary in AR Sco, where (a) shows the increase of emission from the WD as the electron/positron beam approaches the M-dwarf wind (point A), and (b) shows the episode when the open field lines of the WD interacts with the M-dwarf to form a bow shock, where electrons are accelerated to relativistic energies. Adopted from Geng et al. [6]

Geng et al. [6] modelled the emission as being the result of the interaction between the highly magnetized WD and the M5-type secondary dwarf star (see Fig. 1). In this model it is proposed that the WD is a nearly perpendicular rotator where both magnetic poles sweep across the M-type star periodically. The interaction between the particle beam streaming out from the open field line regions and the M-type wind would lead to the formation of a bow shock, where the

relativistic particles can be accelerated by e.g. magnetic pumping and shocks to produce possible synchrotron radiation from relativistic electrons in the magnetosphere of the secondary. However, other non-thermal theoretical models has also been developed postulating very high energy gamma-ray production through a hadronic channel like π^o is also possible [8], as well as inverse-Compton scattering [3, 9]. It is also suggested that the relativistic electrons are trapped within the WD's magnetic field lines due to the magnetic mirror effect and that the pulsed emission originates from the first magnetic mirror point [9]. Both the models presented by Geng et al. 2016 [6] and Takata et al. 2018 [9] suggest non-thermal emission inside the binary system.

Given the current knowledge we have on AR Sco and its non-thermal nature, an attempt is being made to search for continuum gamma-ray emission using a 10-year *Fermi*-LAT data set with *Fermi's* updated Pass 8 data analysis framework and background models. If low-level gamma-ray emission can be observed in *Fermi*-LAT data, it will definitely spark enormous interest in this source and result in highly magnetized rotating WDs in close binaries being considered as a new class of gamma-ray sources.

2. *Fermi*-LAT Analysis

Pass 8 Release 3 (P8R3) *Fermi*-LAT data from the past decade (4Aug2008-18Mar2019) were extracted from the Fermi Science Support Center (FSSC) [10] in the energy range of 100 MeV to 500 GeV. The Pass 8 data set provides a better determination of the diffuse galactic gamma-ray emission and a significant improvement in terms of energy resolution from previous *Fermi*-LAT pipelines. `SOURCE` class event files (`evclass=128, evtype=3`) corresponding to the `P8R3-SOURCE-V6` instrument response function, within a Region of Interest (ROI) of 10° centred at AR Sco (RA:$16^h21^m47.28^s$, Dec: $-22°53'10.39''$, J2000), were considered during analyses. Standard binned and un-binned likelihood analyses were performed using the recently released Fermi Tools software, *Fermi* 1.0.1. All the point sources in the fourth *Fermi*-LAT catalogue (4FGL) located within the ROI, along with recent Galactic diffuse and extragalactic isotropic background emission models[1], were used to generate a background model for subtraction, keeping their spectral shapes the same as defined in the 4FGL catalog. As AR Sco is not listed in the 4FGL catalogue, the methodology by manually adding the source to the model centred at its coordinates was used, parameterizing it with a power law spectral shape at first. The associated parameters of spectral models of all point sources within a 1° radius, including the Galactic and isotropic background models, were chosen to be free to vary while performing the likelihood fitting. After the power law model was added, both broken power law and log parabola models were also used to do a likelihood fit. Due to convergence issues, sources for the broken power law model further away than 15° with insignificant TS has been discarded to allow for a better overall convergence and fit.

3. Results and Discussion

The resulting integrated flux above 100 MeV with corresponding model parameters from the different models used during binned and un-binned likelihood analyses are presented in Table 1

[1] https://fermi.gsfc.nasa.gov/ssc/data/access/lat/BackgroundModels.html

and 2 respectively. These results of our present binned analysis in the energy range of 100 MeV - 500 GeV reveal low level emission at the $\leq 4.31\sigma$ significance level from the position of AR Sco using a broken power law model, where the statistical significance is calculated as $\sigma = \sqrt{TS}$, [11]. Using the similar model parameters as with the binned analysis, un-binned likelihood results revealed lower significant results with a $\leq 3.40\sigma$ significance level (see Table 2).

Table 1: Spectral model parameters obtained for the region centred on AR Sco in the energy interval 100 MeV - 500 GeV using binned likelihood analysis. Optimization of AR Sco was done using a power law (Γ= - (2.7 $\pm$ 0.8)), broken power law ($\Gamma_1 = -(1.00 \pm 0.31)$, $\Gamma_2 = -(3.83 \pm 1.81)$) and log parabola ($\alpha = (1.30 \pm 0.38)$, $\beta = (0.92 \pm 0.32)$) to determine the likelihood of detection of gamma-rays from the ROI centred on AR Sco. Here $N_{\rm pred}$ refers to number of predicted counts.

Binned Likelihood Analyses				
Spectral model	Flux(photons/cm^2/s)	$N_{\rm pred}$	TS	Significance
Power Law	$5.75 \pm 3.08 \times 10^{-9}$	1116.91	9.02	$\leq 3.00\sigma$
Broken Power Law	$4.39 \pm 3.24 \times 10^{-9}$	1109.37	18.54	$\leq 4.31\sigma$
Log Parabola	$2.86 \pm 2.12 \times 10^{-9}$	823.98	15.15	$\leq 3.89\sigma$

Table 2: Spectral model parameters obtained for the region centred on AR Sco in the energy interval 100 MeV - 500 GeV using un-binned likelihood analysis. Optimization of AR Sco was done using a power law (Γ= - (2.8 $\pm$ 0.29)), broken power law ($\Gamma_1 = -(1.34 \pm 0.28)$, $\Gamma_2 = -(4.99 \pm 0.43)$ and log parabola ($\alpha = (0.03 \pm 0.20)$, $\beta = (1.06 \pm 0.78)$) to determine the likelihood of detection of gamma-rays from the ROI centred on AR Sco. Here $N_{\rm pred}$ refers to number of predicted counts.

Unbinned Likelihood Analyses				
Spectral model	Flux(photons/cm^2/s)	$N_{\rm pred}$	TS	Significance
Power Law	$4.95 \pm 2.82 \times 10^{-9}$	967.93	6.52	$\leq 2.55\sigma$
Broken Power Law	$3.57 \pm 1.10 \times 10^{-9}$	941.23	13.68	$\leq 3.69\sigma$
Log Parabola	$2.70 \pm 1.96 \times 10^{-9}$	752.31	13.52	$\leq 3.67\sigma$

After the likelihood analysis had been performed, a SED was plotted using e.g. the power law model over 9 energy bins (see Fig. 2a). The SED was obtained using the *Fermi* build-in function `bdlikeSED` with the binned likelihood results. The energy flux values can be considered as 2σ upper limits based on a limiting TS < 4 value per bin due to the low overall significance of AR Sco. The distribution of TS values per energy bin (see Fig. 2b) also illustrates that the most significant emission is concentrated in the energy bins below 3 GeV. Due to *Fermi's* low spatial resolution at lower energies, it may be possible for other nearby sources to still contribute to the observed emission, resulting in larger significant values.

Residual and TS maps were also created to examine the different emission regions within the ROI and to visualize the emission excess, if any, from the coordinates centred on AR Sco (see

Fig 3). From this, some level of emission excess centred on the coordinates of AR Sco can be seen. Further investigation, however, still has to be done to verify that the upper-limit emission is observed from AR Sco itself and not from nearby sources within the ROI. Since most of the emission originate from an energy level below 10 GeV (see Fig. 2b) and the fact that AR Sco lies within the Galactic plane, it is difficult to distinguish if the detected gamma-rays come from AR Sco or from nearby sources due to *Fermi's* low spatial resolution at lower energies. It can be seen from Fig. 3 that a significant amount of residual emission is noticeable to the left of the position centred on AR Sco, which may well be attributed to the contribution from the Galactic plane. This, however, needs to be confirmed in future studies since both Galactic and isotropic background models were included during analysis.

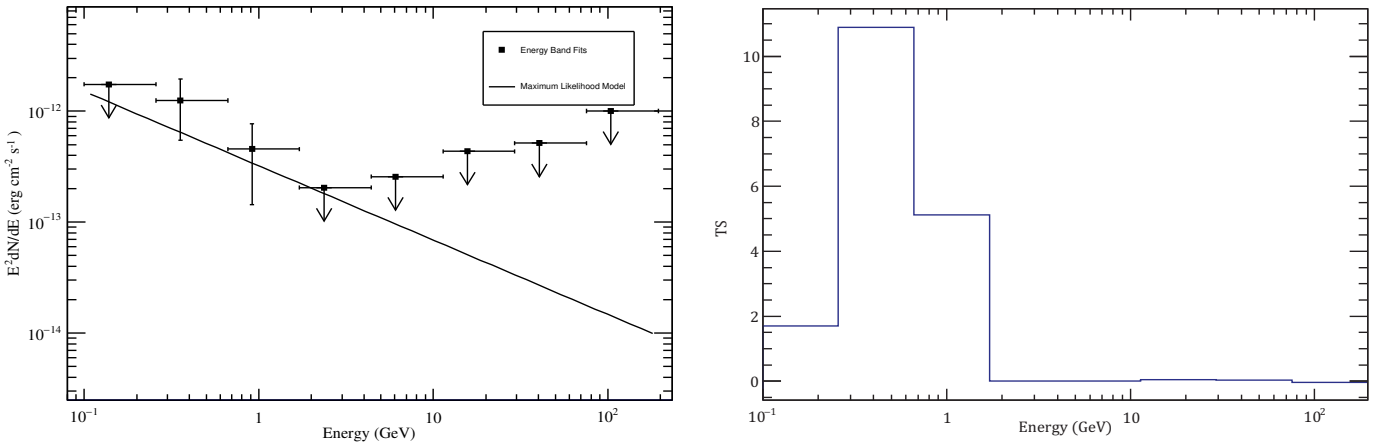

(a) Energy flux SED obtained using `bdlikeSED`.

(b) TS values vs energy of γ-ray photons.

Figure 2: The flux values are 2σ upper limits based on a limiting TS < 4 value per bin. Distribution of high energy γ-rays are more likely to be detected at lower energies.

4. Conclusion

The results from a binned likelihood analysis on a ROI with a radius of 10° centred on the position of AR Sco, optimized with power law, broken power law and log parabola models, revealed low-level gamma-ray flux between 100 MeV - 500 GeV at the $\leq 4.31\sigma$ level by considering the broken power law as the best fit. Unbinned likelihood analysis also revealed a similar $\leq 3.69\sigma$ statistical significance level, albeit at lower levels, which correlates closely with the analyses done using binned likelihood analyses. This, however, is below the 5σ *Fermi*-LAT threshold required for a definite detection. The location of AR Sco inside the Rho Ophiuchi (Rho Oph) molecular cloud complex combined with the poor spatial resolution of *Fermi*-LAT at lower energies, complicates any positive identification of low-level gamma-ray activity at the location that coincides with the position of AR Sco. With the upcoming Cherenkov Telescope Array (CTA), with a much better sensitivity and resolution than that of *Fermi*, it may be possible to detect and resolve gamma-ray emission from the region centred in AR Sco.

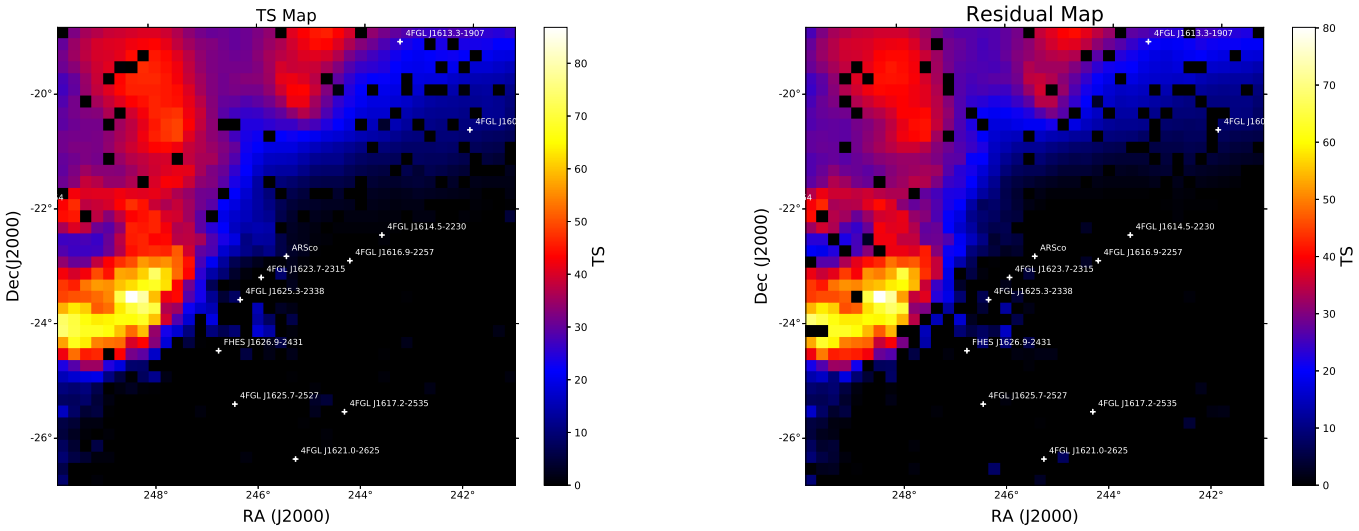

(a) TS map centred on AR Sco

(b) Residual map centred on AR Sco

Figure 3: Plots of AR Sco's TS values within its ROI where (a) shows the TS map centred on AR Sco and (b) shows the residual map centred on AR Sco. If we compare these two maps we can see some excess from the coordinates centred on AR Sco in (a) but not in (b).

5. Acknowledgements

The authors thanks the organisers for the invitation as well as the University of the Free State (UFS) Research directorates and SA GAMMA for the financial support. The *Fermi*-LAT analysis was performed using the UFS High Performance Computing (HPC) Unit.

References

[1] T. R. Marsh et al., *A radio-pulsing white dwarf binary star*, *Nature* **537** (2016) 374

[2] D.A.H. Buckley, P.J. Meintjes, S.B. Potter, T.R. Marsh & B.T. Gänsicke, *Polarimetric evidence of a white dwarf pulsar in the binary system AR Sco*, *Nature Astronomy* **1** (2017) 0029

[3] D.A.H. Buckley, S.B Potter, P.J. Meintjes, T.R. Marsh and B.T. Bänsicke , *Polarimetric evidence of the first white dwarf pulsar: The Binary System AR Scorpii*, *Galaxies* **6** (2018) 14

[4] S.B. Potter et al., *Polarized QPOs from the INTEGRAL polar IGRJ14536-5522 (= Swift J 1453.4 - 5524)*, *MNRAS* **402** (2010) 1161

[5] L. Kuiper et al., *The Crab pulsar in the 0.75-30 MeV range as seen by CGRO COMPTEL. A coherent high-energy picture from soft X-rays up to high-energy gamma-rays*, *A & A* **372** (2001) 918

[6] J.-J. Geng, B. Zhang, Y.-F. Huang *A model of white dwarf pulsar AR Sco*, *Astrophys. J. Lett.* **831** (2016) L1

[7] J.I. Katz, *AR Sco: Presenting a white dwarf synchronar*, *Astrophys. J.* **835** (2017) 150

[8] W. Bednarek, *Hadronic modelfor the non-thermal radiation from the binary system AR Scorpii*, *MNRAS* **476** (2018) L10-L14

[9] J. Takata, C. -P. Hu, L.C.C. Lin, P.H.T. Tam, P.S. Pal, C.Y. Hui, A.K.H Kong and K.S. Cheng, *A non-thermal pulsed X-ray emission of AR Scorpii*, *The Astrophysical Journal* **853(2)** (2018), 106

[10] J. McErny et al., *Fermi Science Support Centre*, *https://fermi.gsfc.nasa.gov/ssc/* , Date accessed: 18 June 2019

[11] J.R. Mattox, D.L. Bertsch, J. Chiang, *The Likelihood Analysis of Egret Data*, *The Astrophysical Journal* **461** (1996), 396-407

PROCEEDINGS OF SCIENCE

Low-power pulsed emission at the spin period of the white dwarf in AR Scorpii?

Q. Kaplan[1]*, **P.J. Meintjes**[1], **H.J. van Heerden**[1]
1.) Department of Physics, University of the Free State, PO Box 339, Bloemfontein, 9300
E-mail: kaplanq@ufs.ac.za

Previous high energy studies of AR Sco suggest that the surrounding region complicates the search for γ-ray emission from this close binary system. The fact that AR Sco lies close to the Galactic plane, Rho Oph cloud complex and strong nearby VHE *Fermi* sources, make it difficult to constrain and quantify an upper-limit of the emission from AR Sco's location in the sky. In this study, a search for high energy γ-ray emission was conducted to identify possible pulsed emission signatures within or above the noise level. Period analysis revealed low-level but consistent emission at the spin period of the white dwarf ($P_s = 117$ sec), using *Fermi*-LAT data from the past decade. Control analysis appears to show a decrease in signal strength at the spin period in regions further away from the coordinates centred on AR Sco, which may indicate the presence of low-level pulsed γ-ray emission from AR Sco.

8th High Energy Astrophysics in Southern Africa (HEASA2021)
13 - 17 September, 2021
Online

*Speaker.

PoS(HEASA2021)045

1. Introduction

AR Scorpii (henceforth AR Sco) is an enigmatic close binary system which is observable across most of the electromagnetic spectrum, [1]. The system consists of a $0.81-1.29M_{\odot}$ highly magnetic white dwarf with a surface magnetic field B $\leq$ 500 MG [2, 3] orbiting a $0.28-0.45M_{\odot}$ M5 spectral-type dwarf star with an orbital period of $P_{\rm orb}$ = 3.56 hours. Multi-wavelength emission consists of both thermal and non-thermal components, where non-thermal emission has been observed from radio to X-ray, [1, 3, 8]. This implies that AR Sco may be a source where particles are accelerated to relativistic energies, perhaps in the magnetosphere of the white dwarf with associated pulsed pulsar-like emission through, among other, synchrotron radiation.

An emphatic theoretical framework was provided by Buckley et al. (2017), [2], in an attempt to explain the multi-frequency emission from AR Sco from radio frequencies to X-ray energies. By doing optical observations utilizing the South African Astronomical Observatory (SAAO) HIPPO Polarimeter [4] on the 1.9 m telescope, strong levels of linear polarization (up to 40%) with significantly lower levels of circular polarization (< 10%) were revealed, [2, 3], which perhaps signifies a significant synchrotron component in the radio to X-ray part of the Spectral Energy Distribution (SED) of AR Sco. The morphology and pulse profile of the linear polarization are similar to that of the Crab pulsar, which is a young isolated neutron star pulsar that emits radiation from radio to TeV energies, e.g. [5]. The nature of the linear polarization profile is also consistent with synchrotron emission produced in the magnetic field of a rotating magnetic dipole, strengthening the notion that the white dwarf in AR Sco may in fact be a "white dwarf pulsar" which can produce non-thermal pulsar-like emission.

The apparent lack of accretion in the system also suggests that the highly magnetic white dwarf is primarily spin-powered, similar to pulsars, where particles can be accelerated to produce non-thermal emission. Marsh et al. (2016), [1] revealed that the white dwarf in the system is currently spinning about its own axis, at a period of $P_{\rm spin} = 117$ s, with strong supplementary pulsations at the beat period $P_b = 118$ s, which is the period between the spin and orbital period, [1]. It has been shown that it is possible for fast rotating magnetic white dwarfs to produce γ-ray emission through relativistic particle acceleration. The acceleration of particles in the magnetosphere of a rotating white dwarf is controlled by the electric field structure which is determined by the distribution of ionized gas around the star. Thus, if the white dwarf lacks a hot corona or is experiencing low/zero amounts of accretion, the surrounding area effectively acts as a vacuum. The absence of accretion in AR Sco and consequently a conducting plasma, allows for an estimated upper-limit in the electrical potential of the order

$$\Delta V \leq 10^{12} \left(\frac{P_{\rm wd}}{117\ {\rm s}}\right)^{-5/2} \left(\frac{\mu}{8\times10^{34}\ {\rm G\ cm^3}}\right) \left(\frac{R_{\rm wd}}{5.5\times10^{8}\ {\rm cm}}\right)\ {\rm V} \tag{1.1}$$

to be induced between the white dwarf and the light cylinder, [2]. In the above equation $P_{\rm wd}$ and $R_{\rm wd}$ represent the spin period and radius of the white dwarf respectively, with the magnetic moment defined by μ. Since the electric field is several orders of magnitude stronger than the force

of gravitation, charged particles such as electrons (and ions) can be pulled from the white dwarf's surface and accelerated to relativistic energies of the order of $\gamma_e \approx 10^6$, [2].

A theoretical model have also been presented by Geng et al. (2016) [6], who modelled the emission as being the result of the interaction between the highly magnetized white dwarf and the M5-type secondary dwarf star. In this model it is proposed that the white dwarf is a nearly perpendicular rotator where both magnetic poles sweep across the M-type star periodically. The interaction between the particle beam streaming out from the open field line regions and the M-type wind would lead to the formation of a 'bow shock', where the relativistic particles can be accelerated by e.g. magnetic pumping and shocks to produce possible synchrotron radiation from relativistic electrons in the magnetosphere of the secondary. However, other non-thermal theoretical models have also been developed postulating very high energy (VHE) γ-ray production through a hadronic channel like π^o, [7], as well as inverse-Compton (IC) scattering [3, 8]. It is also suggested that the relativistic electrons are trapped within the white dwarf's magnetic field lines due to the magnetic mirror effect, accelerating particle through a scattering process, [8]. The above mentioned models all serve as viable scenarios where particles can be accelerated to relativistic energies to produce the observed non-thermal emission from AR Sco. Hence, exploring the γ-ray regime of AR Sco makes it essential to constrain possible mechanisms for the observed non-thermal emission of AR Sco at higher energies.

2. *Fermi*-LAT Analysis

Previous high energy studies utilizing the *Fermi*-LAT telescope appears to show low level upper-limit detections between the energy range of 100 MeV and 500 GeV, [9]. By using a standard binned likelihood analysis, low level upper-limit emission at the $\leq 4.31\sigma$ significance level from the position of AR Sco, using a broken power-law model, was obtained. It is speculated that AR Sco's surrounding region may influence the upper-limit emission at high energies. The fact that the system lies close to the Galactic plane, the Rho Oph cloud complex and nearby high energy sources, along with *Fermi*-LAT's low spatial resolution at lower energies (0.6° at ≤ 1 GeV), [10], makes it difficult to constrain the upper-limit values. Considering these results, a search for emission at noise level was conducted by means of period analysis.

By doing a period analysis, a search for uniformity of a phase distribution at a certain predetermined period was investigated. Since the spin ($P_{spin} = 117$ s) for the rapidly rotating white dwarf is known and detectable from radio to X-ray, (e.g. [1, 2, 8]), accompanied by the argument that the white dwarf in AR Sco has similar features to that of spun-up pulsars, (e.g. [2, 3]), a search for any periodicities around this period was considered. By using Pass 8 Release 3 (P8R3) *Fermi*-LAT data from the past decade (4 August 2008- 18 March 2019)[1] a standard periodic analysis was performed in an attempt to search for pulsed emission above the *Fermi*-LAT threshold. `SOURCE` class event files within a Region of Interest (ROI) of 10° centred at AR Sco (RA:$16^h21^m47.28^s$, Dec: $-22^\circ53'10.39''$, J2000), were considered during analysis. Due to the fact that most of the

[1]Extracted from the Fermi Science Support Center (FSSC) [11]

observed emission lies below 3 GeV (see Fig. 1) an energy range of 100 MeV - 30 GeV was chosen, including the latest spacecraft file at the time of analysis, and used to obtain power spectra (periodograms) with the help of the `gtpsearch` tool.

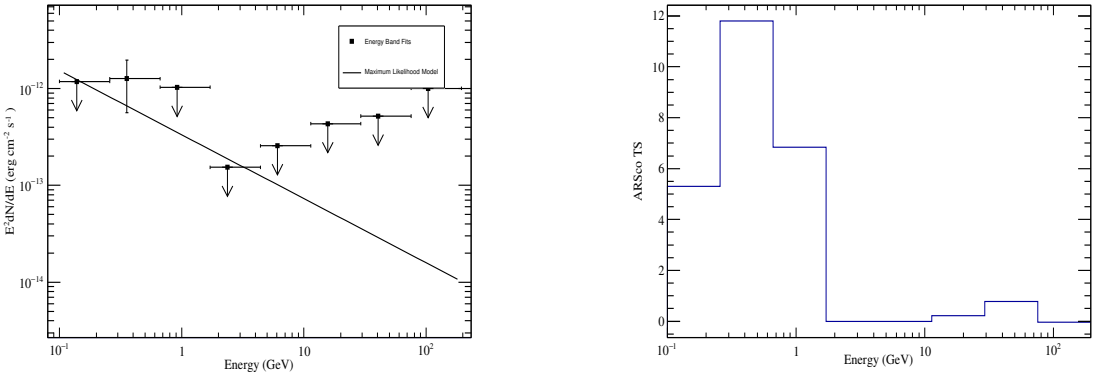

(a) Energy flux SED obtained using `bdlikeSED`.

(b) TS values vs energy of γ-ray photons.

Figure 1: AR Sco SED using the power-law model over 9 energy bins (a) shows 2σ upper-limit energy flux values (with a 3σ data point) based on a limiting TS ≤ 9 value per bin due to the low overall significance of AR Sco. The distribution of TS values per energy bin (b) also illustrates that the most significant emission is concentrated in the energy bins below 3 GeV. Distribution of high energy γ-rays are more likely to be detected at lower energies. Adopted from Kaplan et. al (2019), [9].

3. Results and Discussion

Rayleigh periodograms for AR Sco were produced by using the ephemeris from Takata et. al (2018) [8], with a reference time of $T_{s,ref} = 57641.546$ MJD and the spin frequency $\nu_{\rm spin} = 8.5390$ mHz (117.1 s). The spin-down frequency of the white dwarf in AR Sco's ($\dot{\nu} = -2.86 \pm 0.36 \times 10^{-17}$ Hz s^{-1}), was adopted from Marsh et. al (2016) [1]. A Rayleigh power spectrum centred on the coordinates of AR Sco, folded on the spin frequency of the white dwarf is shown in Fig. 2. Considering the long baseline of events in the dataset, a step size of 2.985×10^{-6} Hz at a Fourier resolution of ($\nu = 2.985 \times 10^{-9}$ Hz) was used with a number of trials as 5000, centred on the fundamental frequency of $\nu_{\rm spin} = 8.53885$ mHz (117.11 s).

A narrower Rayleigh power spectrum (Fig. 3) with step size (1.493×10^{-9} Hz) of 0.5 times the Fourier resolution of ($\nu = 2.985 \times 10^{-9}$ Hz) and number of trials 500, centred on the fundamental frequency of $\nu_{\rm spin} = 8.53885$ mHz (117.11 s) was obtained, covering frequencies from $8.5384 - 8.5393$ mHz. From this Rayleigh power an apparent signal at the fundamental spin frequency seems to be visible, albeit not at a significant level. By focusing on this fundamental frequency ($\nu_{\rm spin} = 8.53885$ mHz), we can see a more defined power spectrum, with step size (2.895×10^{-10} Hz) of 0.1 times the Fourier resolution of ($\nu = 2.985 \times 10^{-9}$ Hz) and number of trials 500.

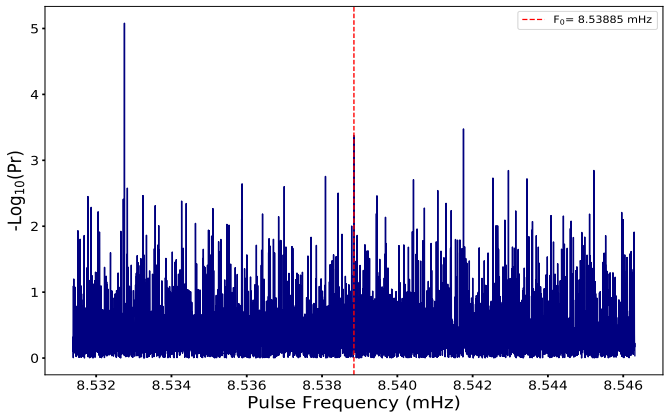

Figure 2: Rayleigh periodogram of AR Sco in the energy range of 100 MeV to 30 GeV, focusing on the spin period frequency range, covering frequencies from $8.530-8.547$ mHz. Additional line marker added showing the fundamental spin frequency ($F_0 = 8.53885$ mHz) of the white dwarf in AR Sco.

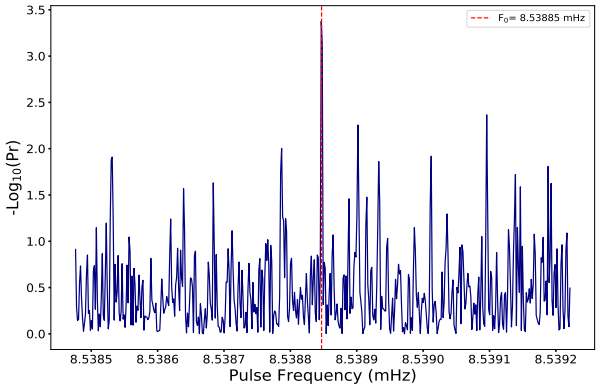

Figure 3: Rayleigh periodogram of AR Sco in the energy range of 100 MeV to 30 GeV, covering frequencies from $8.5384-8.5393$ mHz.

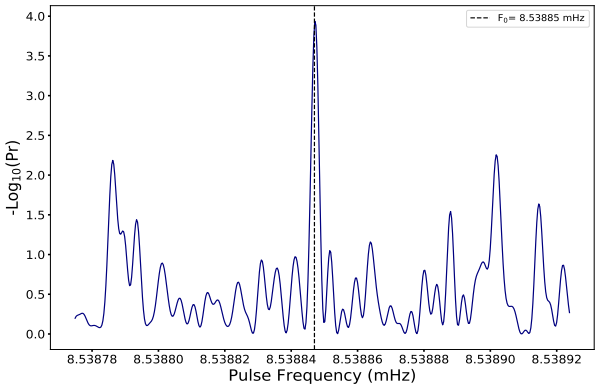

Figure 4: Rayleigh periodogram of AR Sco in the energy range of 100 MeV to 30 GeV, focusing on the spin frequency range ($8.53877-8.53893$ mHz).

3.1 Periodicity control test

To determine the validity of the power spectra, a search for a similar signal within the extracted *Fermi*-LAT dataset at locations further away from the position centred on AR Sco (within the ROI), where no γ-ray sources are detected and the γ-ray background is at a significantly low level (see Fig. 5), was conducted. If a signal is detected at any of these independent locations at the same spin frequency with the same properties as AR Sco, then the proposed signal detected in the power spectra from AR Sco could possibly be inherent to the analysis technique or data set. However, if the data reveals white noise structures, with no clear signals at locations without any

suspected γ-ray sources, it will strengthen the case that the analysis technique and results obtained are justifiable. The locations were chosen to be 2°, 3°, 5° and 8° away from the ROI centre, where low-level or no γ-ray emission is present (see Fig. 5). Rayleigh periodograms compared to each region within the ROI (centred on AR Sco) are presented in Fig. 6 and Fig. 7.

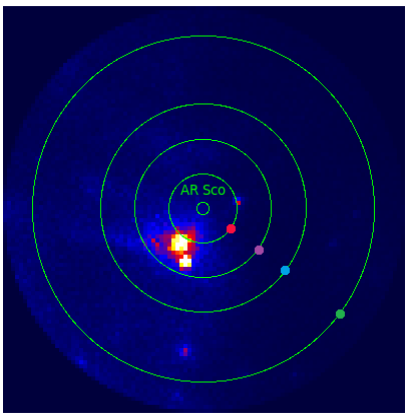

Figure 5: Counts map (100 x 100 pixels) centred on AR Sco. Green circles represents locations 2° (red), 3° (violet), 5° (blue) and 8° (green) away from the coordinates centred on AR Sco.

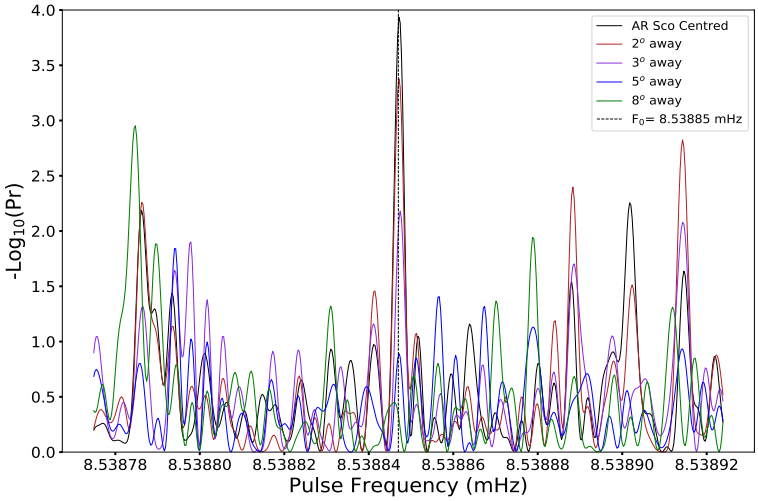

Figure 6: AR Sco power spectra (black) compared to regions 2° (red), 3° (violet), 5° (blue) and 8° (green) away from the coordinates centred on AR Sco.

4. Conclusion

From the results obtained in Fig. 4, there appears to be evidence of a power peak centred at the current ephemeris model frequency for the spin period $\nu_{\text{spin}} = 8.53885$ mHz (117.11 s). Compared to the model frequency obtained by Takata et. al (2018) [8], $\nu_{\text{spin}} = 8.5390$ mHz (117.1 s), the periodogram frequency of our current analysis is much narrower and focused on a more precise value for the white dwarf's spin frequency. This value is well within the power peaks from the periodograms obtained by Takata et. al (2018) [8].

Validity tests performed also appears to suggest a possible low-level pulsation at the spin frequency. Compared to regions further away from the ROI centre (see Fig. 6), where no known γ-ray emission is visible and only background noise is considered, it appears that the Rayleigh power at the fundamental spin frequency is decreasing in strength as one moves further away from the position centred on the coordinates of AR Sco. Even though the validity test appears to show

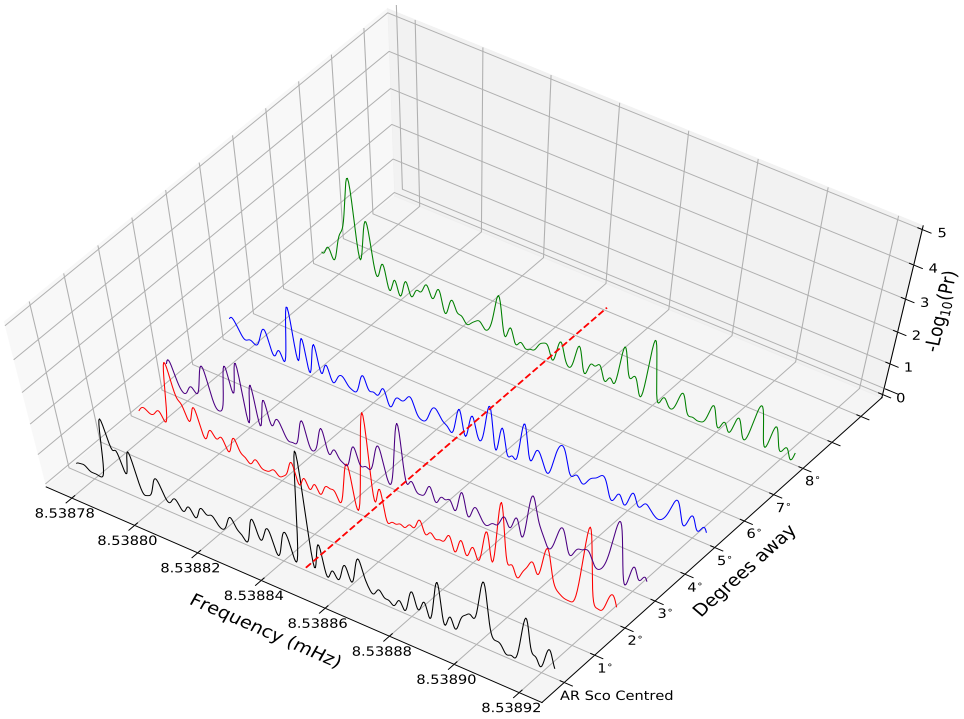

Figure 7: AR Sco power spectra (black) compared to regions 2° (red), 3° (violet), 5° (blue) and 8° (green) away from the coordinates centred on AR Sco.

a possible signal within the noise structure, confirmation of this signal can only be considered through further examination and studies. Since pulsed emission has been detected at the beat period of the white dwarf over most of the electromagnetic spectrum, [1, 2, 8], future prospects is aimed towards similar high energy period analysis for the beat period. Alternatively, period analysis of an independent source(s), using the same ephemeris of AR Sco, can be performed to serve as a second control test to confirm the validity of the technique used and results obtained for the spin period of the white dwarf.

It has been shown that AR Sco's SED can not be described by synchrotron emission alone, [12], and more comprehensive studies need to be conducted. In terms of energy, it has been shown that relativistic electrons with energies of $\gamma \sim 10^6 - 10^7$ can provide the possibility for the production of high energy γ-rays by up-scattering of soft photons from the companion star through the IC process, [13]. This is similar to the scenario proposed in nova-like variable star AE Aqr, [14]. An upper-limit for the γ-ray energies produced from these electrons is estimated to be ~ 1 TeV. The IC process in the outer gap model has also been explored by Takata et al. (2017), [15], which can produce photons with energies of > 0.1 TeV. Bednarek (2018), [7], has shown that it is possible to reach GeV-TeV energies through a hadronic model. The possibility therefore exists that high energy emission can be detected and better constrained with the increased sensitivity of CTA (Cherenkov Telescope Array). Compared to *Fermi*-LAT, CTA offers a larger collection area

and better angular resolution, which make observations of faint γ-ray sources much more efficient, [16]. Overlapping regions of energy between these two observatories also show that at an energy of about 40 GeV, *Fermi* will be doing measurements within a 10 year period that is comparable in quality to measurements of 100 hour observations with CTA, see Fig. 8. Hence, future studies using the CTA system could therefore increase the probability for detection of low-level pulsed high energy or VHE emission from AR Sco and constrain the origin and parameters of the possible high energy emission to determine the exact energy production mechanism.

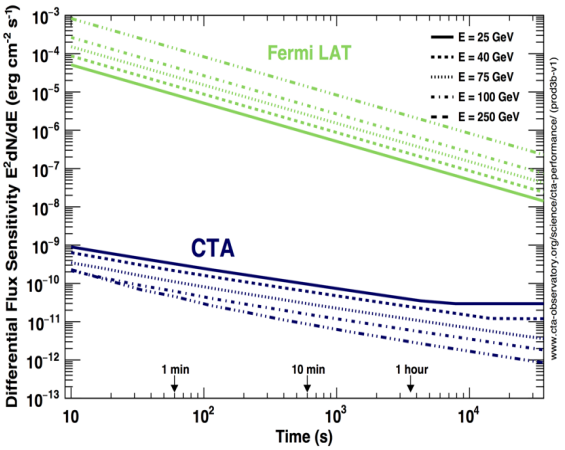

Figure 8: Differential sensitivity at selected energies as a function of observation time for CTA and *Fermi*-LAT. Adopted from CTA Consortium (2019), [17].

5. Acknowledgements

The authors thanks the organisers for the invitation as well as the University of the Free State (UFS) Research directorates and SA GAMMA for the financial support. The *Fermi*-LAT analysis was performed using the UFS High Performance Computing (HPC) Unit.

References

[1] T. R. Marsh et al., *A radio-pulsing white dwarf binary star*, *Nature* **537** (2016) 374

[2] D.A.H. Buckley, P.J. Meintjes, S.B. Potter, T.R. Marsh & B.T. Gänsicke, *Polarimetric evidence of a white dwarf pulsar in the binary system AR Sco*, *Nature Astronomy* **1** (2017) 0029

[3] D.A.H. Buckley, S.B Potter, P.J. Meintjes, T.R. Marsh and B.T. Bänsicke , *Polarimetric evidence of the first white dwarf pulsar: The Binary System AR Scorpii*, *Galaxies* **6** (2018) 14

[4] S.B. Potter et al., *Polarized QPOs from the INTEGRAL polar IGRJ14536-5522 (= Swift J 1453.4 - 5524)*, *MNRAS* **402** (2010) 1161

[5] L. Kuiper et al., *The Crab pulsar in the 0.75-30 MeV range as seen by CGRO COMPTEL. A coherent high-energy picture from soft X-rays up to high-energy gamma-rays*, *A & A* **372** (2001) 918

[6] J.-J. Geng, B. Zhang, Y.-F. Huang *A model of white dwarf pulsar AR Sco*, *Astrophys. J. Lett.* **831** (2016) L1

[7] W. Bednarek, *Hadronic modelfor the non-thermal radiation from the binary system AR Scorpii*, *MNRAS* **476** (2018) L10-L14

[8] J. Takata et al., *A non-thermal pulsed X-ray emission of AR Scorpii*, *The Astrophysical Journal* **853(2)** (2018), 106

[9] Q. Kaplan, P.J. Meintjes, K.K. Singh, H.J. van Heerden., *Searching for gamma-ray emission from the white dwarf pulsar system AR Sco using Pass 8 Fermi-LAT data*, In *7th Annual Conference on High Energy Astrophysics in South Africa,* PoS(HEASA2019) **049**, 2019.

[10] M. Ackermann, M. Ajello, A. Albert, et al., *The Fermi Large Area Telescope on Orbit: Event Classification, Instrument Response Functions, and Calibration*, *The Astrophysical Journal* **203**, (2012), 4

[11] J. McErny et al., *Fermi Science Support Centre*, *https://fermi.gsfc.nasa.gov/ssc/*, Date accessed: 18 June 2019

[12] K.K. Singh, P.J. Meintjes, Q. Kaplan, F.A. Ramamonjisoa and S. Sahayanathan, *Modelling the broadband emission from the white dwarf binary system AR Scorpii*, *Astroparticle Physics* **123**, (2020)

[13] Meintjes P.J., *On the multi-frequency emission and evolution of the white dwarf pulsar binary system AR Scorpii*, in *XII Multifrequency Behaviour of High Energy Cosmic Sources Workshop (MULTIF2017)* **044**, 2017.

[14] B. Oruru and P.J. Meintjes, *X-ray characteristics and the spectral energy distribution of AE Aquarii*, *MNRAS* **421(2)**, (2012), 1557-1568

[15] J. Takata et al., *A Model for AR Scorpii: Emission from Relativistic Electrons Trapped by Closed Magnetic Field Lines of Magnetic White Dwarfs*, *The Astrophysical Journal* **851(2)** (2017), 13

[16] S. Funk et al., *Comparison of Fermi-LAT and CTA in the region between 10-100 GeV*, *Astroparticle Physics* **43**, (2013), 348-355

[17] CTA Consortium and R. A. Ong, *The Cherenkov Telescope Array Science Goals and Current Status*. In *European Physical Journal Web of Conferences* **209**, (2019)

Astroparticle Physics 123 (2020) 102488

Contents lists available at ScienceDirect

Astroparticle Physics

journal homepage: www.elsevier.com/locate/astropartphys

Modelling the broadband emission from the white dwarf binary system AR Scorpii

K.K. Singh[a,b,*], P.J. Meintjes[a], Q. Kaplan[a], F.A. Ramamonjisoa[a], S. Sahayanathan[b]

[a] Physics Department, University of the Free State, Bloemfontein 9300, South Africa
[b] Astrophysical Sciences Division, Bhabha Atomic Research Centre, Mumbai 400 085, India

ARTICLE INFO

Article history:
Received 19 March 2020
Revised 25 May 2020
Accepted 22 June 2020
Available online 24 June 2020

Keywords:
Binaries
White dwarfs
Individual
AR Scorpii-methods
Data analysis-Gamma-rays
General-radiation mechanisms:non-thermal

ABSTRACT

AR Scorpii is a compact binary system which consists of a magnetic white dwarf and an M-type main sequence cool star. This binary system was discovered as a source of pulsating radiation in radio, infrared, optical, ultraviolet and X-ray wavebands. In this work, we have analyzed the γ-ray data in the energy range 100 MeV to 500 GeV from the *Fermi*-Large Area Telescope (LAT) observations for the period August 4, 2008 to March 31, 2019. The γ-ray emission from AR Scorpii over the last decade is not statistically significant and therefore 2σ upper limit on the integral flux above 100 MeV has been estimated. We reproduce the non-thermal broadband spectral energy distribution of AR Scorpii using an emission model having two synchrotron components due to the relativistic electrons in very high magnetic fields. The first component (Synchrotron-1) broadly describes the emissions at radio to high energy X-rays through the synchrotron radiation originating from a spherical region of radius $\sim 1.8 \times 10^{10}$ cm and a magnetic field strength of $\sim 10^3$ Gauss. The second component (Synchrotron-2) which reproduces the X-ray emission at lower energies and predicts the γ-ray emission, originates from another spherical region with radius $\sim 1.4 \times 10^{10}$ cm and a magnetic field strength of $\sim 10^6$ Gauss. The relativistic electron populations in both the emission regions are described by a smooth broken power law energy distribution. The γ-ray emission predicted by the Synchrotron-2 model is below the broadband sensitivity of the *Fermi*-LAT and is also consistent with the 95% confidence level upper limit on the integral flux above 100 MeV derived from more than 10 years of observations. According to our model, the binary system AR Scorpii could be a γ-ray source, although its emission level must be below the current detection limit of the *Fermi*-LAT.

1. Introduction

White dwarfs (WDs) are formed as the end products of the evolution of intermediate main sequence stars in the cores of red giant stars [1,2]. They are considered as compact objects (electron-degenerate stellar configurations) with an average mass of $\sim 0.6 M_\odot$ and radius of the order of 10^8 cm ($\sim$ Earth-size). WDs have therefore a very high average density of 10^6 g cm^{-3} and a large surface gravity. They are found as isolated objects or companions in various astrophysical binary systems with compact objects (black hole, neutron star, or white dwarf), main sequence stars, giant stars or ordinary stars. Isolated WDs are observed with very high surface magnetic fields in the range 10^3 - 10^9 Gauss [3]. They are referred to as *magnetic white dwarfs* (MWDs) and emit at ultraviolet and near-infrared wavelengths. The mass of MWDs ($\sim 0.8 M_\odot$) is more than the mass of non-magnetic or weakly-magnetic WDs ($\sim 0.5 M_\odot$) [3]. MWDs also exist in binary systems where they strip or accrete material from a nearby companion star. For main sequence companion stars, the accretion mainly occurs through Roche-lobe overflow whereas it is driven by the stellar wind in the case of red giant stars [4]. The resulting mass transfer from the main sequence companion stars to the MWDs produces atomic lines and X-ray emissions from the MWD binary systems [5,6]. In a typical WD binary system, the accreted matter heats up and forms a shock wave before settling down on the surface of the WD. Under the assumption of a dipole magnetic field, a MWD would behave like a radio pulsar [7]. The radio pulsars like Crab, characterized as the fast-rotating magnetized neutron stars, are assumed to be powered by the spin-down energy loss due to the rotation or spinning of neutron star [8]. The spin-down luminosity or rotational energy loss (L_{down}) of the pulsar or MWD is given by Pétri [9]

$$L_{down} = \frac{8\pi^2 M R^2 \dot{P}}{5P^3} \quad (1)$$

* Corresponding author at: Astrophysical Sciences Division, Bhabha Atomic Research Centre, 212 Nilgiri Anushakti Nagar, Mumbai, Maharashtra 400 085, India.
E-mail address: kksastro@barc.gov.in (K.K. Singh).

https://doi.org/10.1016/j.astropartphys.2020.102488
0927-6505/

where M and R are the mass and radius of the WD respectively which are used to define the moment of inertia as $I = \frac{2}{5}MR^2$. P and $\dot{P}$ are the spin period and its time derivative respectively. The magnetic spin-down luminosity (L_{mag}) for a magnetic dipole approximation of the MWD and assuming a wind outflow from the magnetosphere, can be approximated as [10]

$$L_{mag} = \frac{16\pi^4 B_s^2 R^6}{6c^3 P^4} \quad (2)$$

where B_s is the strength of the surface magnetic field at the polar cap and c is the speed of light in vacuum. If the magnetic dipole losses of the WD dominate the luminosity of a binary system, the strength of the surface magnetic field of the MWD at the polar cap is related to the different parameters of the pulsar as [10]

$$B_s = \sqrt{\frac{3Mc^3 P\dot{P}}{5\pi^2 R^4}} \quad (3)$$

and the light cylinder radius (R_{LC}) of the spinning MWD is defined by

$$R_{LC} = \frac{cP}{2\pi} \quad (4)$$

The magnetic field strength at the light cylinder (B_{LC}) is approximated as

$$B_{LC} = 4\pi^2 \sqrt{\frac{3MR^2\dot{P}}{5c^3 P^5}} \quad (5)$$

Therefore, a precise measurement of P and $\dot{P}$ is very important to derive the energetics of a pulsar or spinning MWD. B_{LC} plays a very crucial role for the γ-ray emission from these sources due to the conversion of a significant fraction of the spin-down power (L_{down}) to γ-ray luminosity.

The binary systems comprising the MWDs and main sequence stars are divided into two classes namely polar and intermediate polar depending on the strength of the surface magnetic field of the WD. For polar type, the surface magnetic field (B_s) is higher than 10^7 Gauss and accretion from the companion star is completely confined through the magnetic field of the WD [11]. In the case of intermediate polar class, B_s is in the range 10^3–10^6 Gauss and the accretion process is partially channeled through the surface magnetic field [12]. Due to the stronger surface magnetic fields, the rotation of the two stars is synchronised in the polar binary systems. Whereas, in the intermediate polar systems, the rotation of the WD is not synchronised with the companion star and the spin period of the WD is shorter than the orbital period. The formation of an accretion disk around the WD is prevented in the polar binary systems because of the synchronised rotation of the two stars and no angular momentum of the accreting matter with respect to the WD. But, an accretion disk can be formed in the intermediate polar systems and the transfer of angular momentum from the accreting matter may spin up the WD [13]. The accretion flows in polars and intermediate polars lead to the formation of funnels and curtains respectively. The differential rotation of gaseous matter leaking out from the companion star along a circular Keplerian orbit leads to a viscous rubbing of fluid elements at varying distances and causes the accretion disk to heat up. A sufficiently hot accretion disk emits radiation from optical, ultraviolet to X-rays. The surface magnetic field in the intermediate polar disrupts the inner part of the accretion disk and the accreting matter along the magnetic field lines [13]. This leads to the formation of one or more accretion columns near the magnetic poles which emit non-thermal polarized radiation from radio to X-rays. The variations in the non-thermal emissions from the intermediate polar binary systems are strongly modulated on the spin period (P) of the MWD and its harmonics [14]. However, the exact physical process involved in the non-thermal broadband emission from the WD binary systems has not been clearly understood and is being widely debated. In this work, we model the time averaged broadband spectral energy distribution (SED) of an intermediate polar AR Scorpii using observations spanned over last two decades. In Section 2, we present a brief description of the important observational features so far of AR Scorpii. The details of the broadband data set used in the present work are given in Section 3. In Section 4, we discuss the results from the multi-wavelength emission from the binary system AR Scorpii. Finally, we conclude the study in Section 5.

2. AR Scorpii

AR Scorpii is an intermediate polar type WD binary system at a distance of $d \sim 110$ pc (3.4×10^{20} cm) from the Earth and is located in the ecliptic plane near to the Galactic centre [14]. It consists of an MWD and an M-type main sequence companion star with a binary separation of $a \sim 7.6 \times 10^{10}$ cm and both move around the common centre of mass. The mass and radius of the MWD in AR Scorpii are $M = 0.8M_\odot$ and $R = 7 \times 10^8$ cm respectively and the surface magnetic field $B_s \sim 10^8$ Gauss [14]. The companion M-star has a mass of $m \sim 0.3M_\odot$ and a radius of $r \sim 2.7 \times 10^{10}$ cm. In early observations during 1970-71, AR Scorpii was classified as a periodic variable star (δ-Scuti) and recently it was discovered as a close MWD binary system with an orbital period of $P_o \sim 3.56$ hours and a spin period of the MWD $P \sim 1.95$ minutes (117 seconds) at radio and optical wavelengths [14]. The measured time derivative of the spin period of the MWD in AR Scorpii was $\dot{P} \sim 3.9 \times 10^{-13}$ seconds/second. This gives an estimate of the age of the MWD as $t = \frac{P}{2\dot{P}} \sim 4.5 \times 10^6$ years. The photometry of AR Scorpii taken over seven years suggests that the R-band optical magnitude changes from 16.9 (faintest) to 13.6 (brightest) on a time period of $\sim$ 3.56 hours. The amplitude spectra corresponding to the ultraviolet, optical, infrared and radio (9 GHz) fluxes show signals having two components, which are identified as the spin frequency ($\nu_s = P^{-1}$) and beat frequency ($\nu_b = \nu_s - \nu_o$, where $\nu_o = P_o^{-1}$ is the orbital frequency). The beat component of the signal is stronger and therefore it defines the dominant pulsation at a beat period of $P_b = 1.97$ minutes and its harmonics [14]. The observations of AR Scorpii over a wide wavelength range from radio to ultraviolet show strong double-humped pulsations with the pulse fractions between 10% to 95% [14]. The optical spectra of M-type cool main sequence star with absorption lines suggest that the radial velocity of the companion star in AR Scorpii varies sinusoidally with a time period of $\sim$ 3.56 hours and an amplitude of $\sim$ 290 km s^{-1} [14]. The MWD in AR Scorpii is not visible in the optical spectra. For a spin period $P \sim 117$ seconds, the light cylinder radius of the MWD $R_{LC} \approx 5.6 \times 10^{11}$ cm (from Eq. (4)) which is about seven times longer than the binary separation. This implies that the companion star in AR Scorpii is situated well inside the magnetosphere of the MWD. The MWD in AR Scorpii is spinning down on a characteristic timescale of $\sim 10^7$ years [14]. The X-ray emission from AR Scorpii is significantly modulated over the spin period of the MWD with a pulse fraction of $\sim$ 14% [15]. The maximum or minimum X-ray intensity is located at the superior or inferior conjunction of the M-star orbit. An evidence of a power law spectrum is found in the pulsed component of the X-ray emission [15]. The observed optical emission from AR Scorpii modulating with the beat frequency of the binary system is highly polarized with a degree of linear polarization up to 40% and a low level of circular polarization of less than 5% [16,17]. The degree of linear polarization evolves with the orbital phase and varies on both the beat frequency of the binary system and spin frequency of the MWD. The observed characteristics of the degree of linear polarization are similar to that of the well-known spin-powered Crab pulsar. The radio observations at 8.5 GHz reveal the compactness

of the emission region and confirm the identity of AR Scorpii as a point Galactic source [18]. The high resolution interferometric radio imaging of AR Scorpii indicates a strong modulation of the radio flux on the orbital and beat periods and the radio emission exhibits a weak linear polarization and very strong circular polarization [19]. High temporal resolution spectroscopy of this MWD binary system shows a complex structure of the $H\alpha$ emission lines as observed from some polars in the quiescent state [20]. The aforementioned measurements/results suggest a non-thermal origin of the broadband radiation from AR Scorpii through the synchrotron emission process.

3. Broadband data set

In this work, we use archival results from the radio, infrared, ultraviolet, optical and X-ray observations of AR Scorpii available so far in the literature [14,15]. We have also analyzed data from the *Fermi*-Large Area Telescope (LAT) observations for a period of more than 10 years to search for γ-ray emission from AR Scorpii. A brief description of the broadband archival data as well as a detailed analysis of the *Fermi*-LAT data are given below.

3.1. Archival data

We have obtained the spectral archival points at radio, infrared, ultraviolet, optical and X-ray energies from Figure 4 of Marsh et al. [14] and Figure 10 of Takata et al. [15]. These flux measurements in different wavebands include observations from a number of ground and space-based instruments during the period 2006–2016. The X-ray flux points correspond to the time averaged spectrum in the energy range 0.15-12 keV from the *XMM-Newton* observations of AR Scorpii on September 19, 2016. The *XMM-Newton* observation covers more than two orbits of AR Scorpii and the X-ray emission shows a large variation over the orbit. A detailed description of the *XMM-Newton* data can be found in Takata [15].

3.2. Fermi-*LAT data*

The Large Area Telescope (LAT) onboard the *Fermi* satellite is a pair-conversion detector to measure the energy, arrival time, and direction of the γ-ray photons in the energy range 30 MeV to more than 1 TeV [21]. It also detects the intense cosmic ray background of the charged particles and radiation trapped at the orbit of the satellite. For γ-ray photons at 1 GeV energy, the *Fermi*-LAT has an effective collection area of $\sim$ 1 m^2 at normal incidence, a wide field of view of 2.4 steradians (20% of the sky), and an angular resolution of 0.8°. At lower energies, the photon angular resolution is poor ($\sim$ 5° at 0.1 GeV) and it improves with the increase in energy ($\sim$ 0.1° above 10 GeV). Therefore, the angular resolution of the *Fermi*-LAT can be approximated as a power law function of energy ($E^{-0.8}$, where E is the energy of the γ-ray photon) in its operational energy range. The whole sky coverage is provided by the *Fermi*-LAT every three hours in survey mode of its operation.

In this work, we have extracted the Pass 8 Release 3 (P8R3) data for the position of AR Scorpii (RA: $16^h21^m47.28^s$, Dec: $-22°53'10.39''$) collected through the last decade by the *Fermi*-LAT during August 4, 2008 to March 31, 2019 (MJD 54,682–58,573) from the *Fermi* Science Support Centre.[1] The data is processed using standard *Fermi* Science Tools software version 1.0.1 (Fermi 1.0.1). We have considered only SOURCE class events ($evclass = 128$, $evtype = 3$) corresponding to the *P8R3_SOURCE_V6* instrument response function detected within a circular region of interest (ROI) of 10° radius centred on the position of AR Scorpii for the above period in the energy range 100 MeV to 500 GeV using the *gtselect* tool. In addition, a maximum zenith angle cut of 90° is applied to avoid the albedo contamination from the Earth limb γ-rays while creating the good time intervals. We have used unbinned maximum-likelihood technique implemented in the *gtlike* tool to further analyse the dataset. A background model is generated using all the sources reported in the fourth *Fermi* gamma-ray catalog (4FGL) [22] and recent Galactic diffuse and extragalactic isotropic background emission templates. All the 4FGL point sources present within the ROI are included in the model file for background subtraction keeping their spectral forms the same as defined in the 4FGL catalog [22]. Since the target source AR Scorpii is not reported in the 4FGL catalog, we have manually added this source in the model file with a spectral shape defined by a simple power law function. We use an iterative method to optimize the contribution of sources in the background model file. The associated spectral parameters of all the sources within the ROI including AR Scorpii are left free to vary during the unbinned likelihood fitting. The significance of γ-ray signal is estimated from the maximum-likelihood test statistic (TS: square-root of TS gives the statistical significance) as defined in Mattox [23]. After every fit, we remove the background sources from the model file corresponding to a value of TS $<$ 25 (statistical significance $\sim 5\sigma$) and the process is repeated until we get all the background sources with TS $\geq$ 25 within the ROI in the model file except the target source AR Scorpii. We perform the final unbinned likelihood fitting by allowing the spectral parameters of AR Scorpii and other background sources within 5° from the center of ROI to vary and the spectral parameters of all other sources lying beyond 5° are freezed to the values obtained from the optimization.

4. Results and discussion

4.1. Search for γ-ray emission from AR Scorpii

The Pass 8 dataset from the *Fermi*-LAT observations provides a better measurement of the energy of γ-ray events over a wider energy range with their improved reconstruction and a significant increase in the effective area at lower energies. From the unbinned-likelihood fitting as described above, we observe that the *Fermi*-LAT data collected in the direction of AR Scorpii for a period of more than ten years assuming a power law spectral index of -2.7 in the energy range of 100 MeV-500 GeV, exhibit a TS value of 8. This implies that the γ-ray emission from AR Scorpii integrated over a decade from the *Fermi*-LAT observations is not statistically significant ($< 3\sigma$) and the ratio of the error in the integral flux to the absolute value is more than 0.5. Therefore, we have estimated the 2σ upper limit of 2.27×10^{-12} erg cm^{-2} s^{-1} on the integral energy flux above 100 MeV for the γ-ray emission from the binary system AR Scorpii. The low statistical significance of the γ-ray observation from AR Scorpii is consistent with the fact that this source is not reported in the latest 4FGL catalog which includes more than 5000 sources above 4σ significance [22]. We have also generated the yearly light curve for AR Scorpii to observe any temporal fluctuation in the γ-ray emission from this source. The one year binned light curve of AR Scorpii in the energy range 100 MeV to 500 GeV is shown in Fig. 1. All the flux points in the light curve (Fig. 1) correspond to the 2σ upper limit on the integral flux. This indicates that AR Scorpii is not a γ-ray source above the current detection sensitivity of the *Fermi*-LAT. The Galactic diffuse emission is bright in the MeV-GeV energy regime and provides a dominant contribution to the background radiation near the Galactic plane. Due to a relatively broad angular resolution of the *Fermi*-LAT at lower energies, the emission from a faint γ-ray source like AR Scorpii may be contaminated by the diffuse background or photons from the nearby sources. This can affect the search for a pulsed

[1] https://fermi.gsfc.nasa.gov/cgi-bin/ssc/LAT/LATDataQuery.cgi

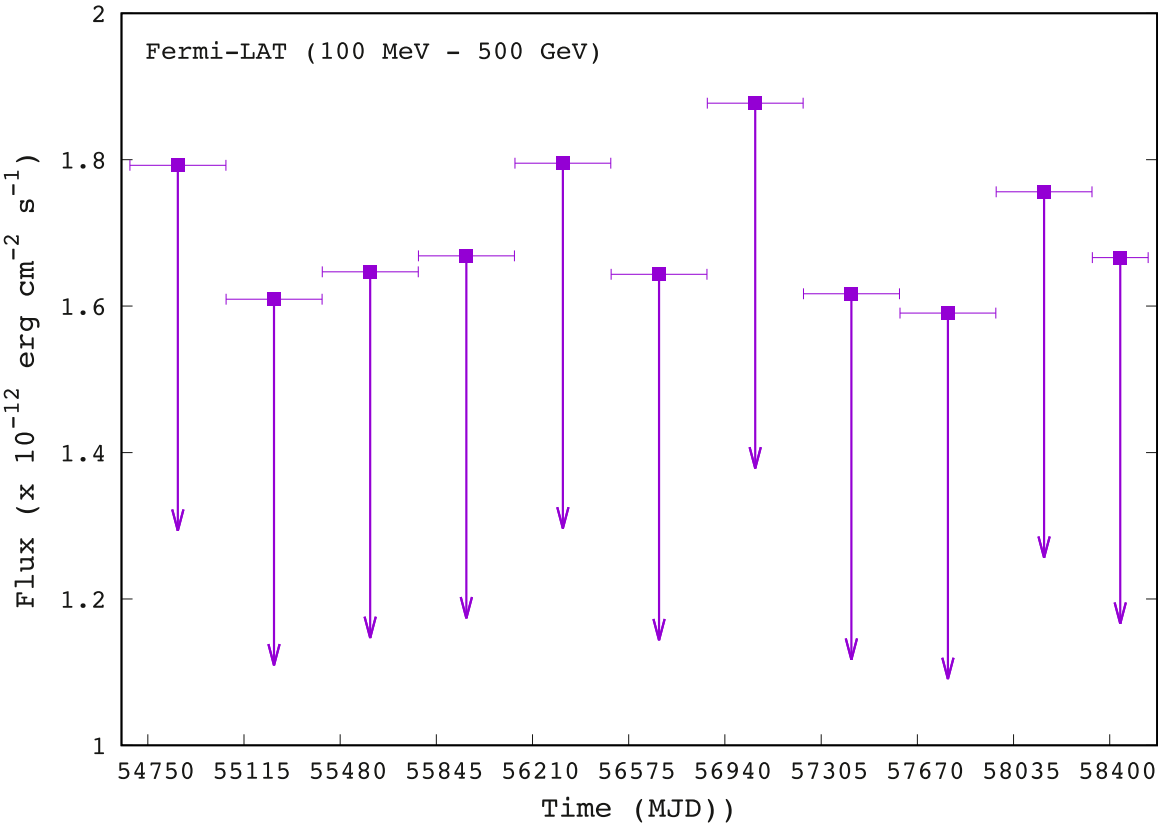

Fig. 1. One year binned (except the last data point which is averaged over about eight months) γ-ray light curve of the white dwarf binary system AR Scorpii from the *Fermi*-LAT observations between August 4, 2008 and March 31, 2019 (MJD 54,682–58,573). The downward arrows indicate 2σ upper limit on the integral energy flux above 100 MeV.

signal from the weak γ-ray sources. An event weighting technique can be used to search for a pulsation from a faint γ-ray source [24]. The search for pulsed γ-ray signal from the WD binary system AR Scorpii is beyond the scope of this work.

4.2. Broadband spectral energy distribution modelling

We have employed a leptonic synchrotron model with two emission components to reproduce the time averaged broadband SED of the binary system AR Scorpii. We assume that the non-thermal radiation from AR Scorpii is produced by the population of relativistic electrons through the synchrotron emission. The electron energy distribution is described by a smooth broken-power law of the form

$$N(\gamma) = K\left[\left(\frac{\gamma}{\gamma_b}\right)^{p} + \left(\frac{\gamma}{\gamma_b}\right)^{q}\right]^{-1} ; \quad \gamma_{\min} < \gamma < \gamma_{\max} \tag{6}$$

where $\gamma = \frac{E}{m_e c^2}$ is the typical Lorentz factor of the electron with m_e being the electron rest mass. K is the normalization coefficient, p and q are the low and high energy electron spectral indices before and after the break respectively. γ_b, $\gamma_{\min}$ and $\gamma_{\max}$ are the Lorentz factors corresponding to the break, minimum and maximum energies of the electrons respectively. The synchrotron emissivity due to an isotropic electron distribution in a tangled magnetic field (B) is calculated as

$$j_{syn}(\nu) = \frac{1}{4\pi}\int_{\gamma_{\min}}^{\gamma_{\max}} N(\gamma)P(\nu,\gamma)d\gamma \tag{7}$$

where ν is the frequency of the synchrotron photon and $P(\nu, \gamma)$ is the single electron synchrotron emissivity averaged over an isotropic distribution of pitch angles [25,26]. $P(\nu, \gamma)$ can be expressed as

$$P(\nu,\gamma) = \frac{\sqrt{3}\pi e^3 B}{4m_e c^2} F\left(\frac{\nu}{\nu_c}\right) \tag{8}$$

with the critical frequency,

$$\nu_c = \frac{3\gamma^2 eB}{16 m_e c} \tag{9}$$

where e is the charge of the electron, and $F\left(\frac{\nu}{\nu_c}\right)$ is the synchrotron power function, which can be approximately given by Sahayanathan [26]

$$F\left(\frac{\nu}{\nu_c}\right) \approx 1.8\left(\frac{\nu}{\nu_c}\right)^{1/3} e^{-\frac{\nu}{\nu_c}} \tag{10}$$

The synchrotron power function peaks at $\frac{\nu}{\nu_c} = 0.29$. This indicates that the peak frequency (ν_p) in the synchrotron spectrum is about 29% of the characteristic frequency (ν_c) defined by Eq. (9). The synchrotron flux received by the observer from the source is given by

$$F_{obs}(\nu) = \frac{V}{d^2} j_{syn}(\nu) \tag{11}$$

where d is the luminosity distance (~ distance) of the source and V is the volume of the emission region. Assuming that the emission region is a homogeneous sphere of radius R_{em} filled with the relativistic electrons defined by Eq. (6) and permeated in a tangled magnetic field of strength B, we have reproduced the time averaged broadband SED of AR Scorpii. The model curves along with the data points in different wavebands are shown in Fig. 2. We observe that the time averaged broadband emission from the binary system AR Scorpii can be broadly reproduced by two non-thermal

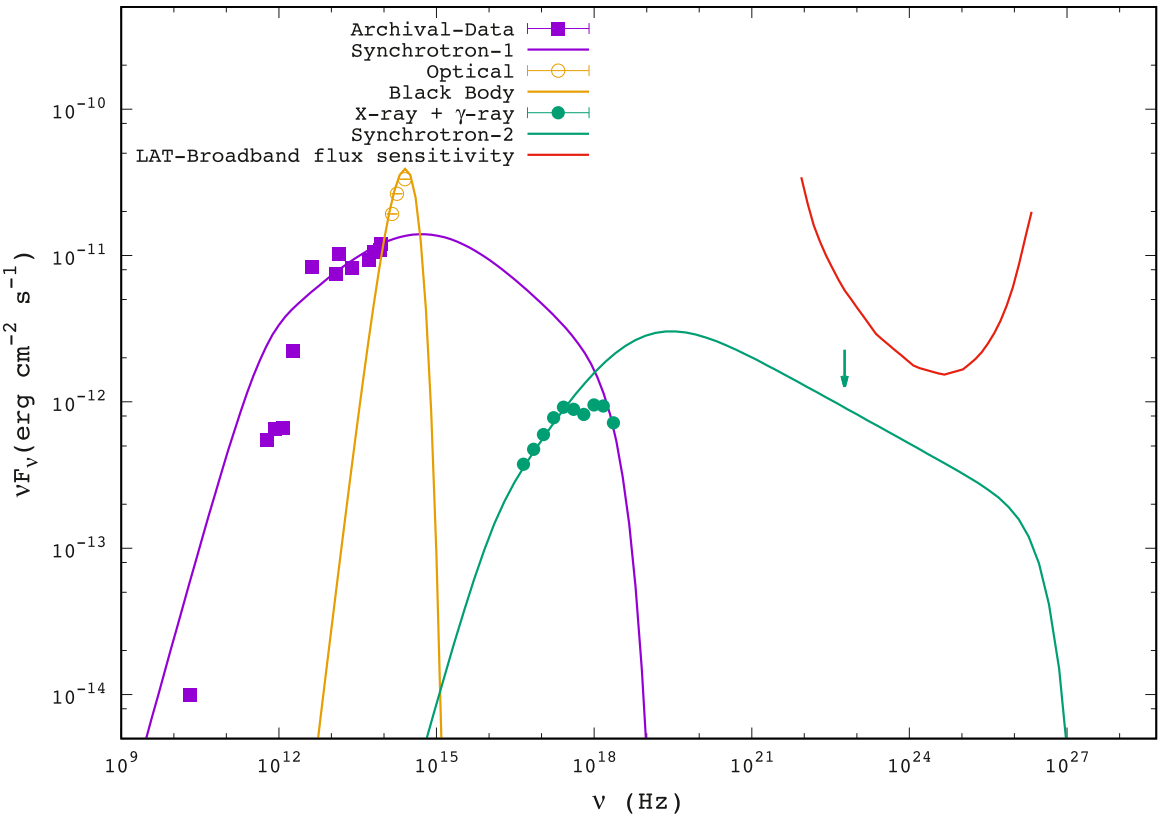

Fig. 2. Broadband spectral energy distribution of AR Scorpii with the time averaged observed data points without measurement errors and model curves. The curves with purple and green colours correspond to the Synchrotron-1 and Synchrotron-2 components of the model for a time averaged non-thermal emission from the binary system AR Scorpii respectively. The yellow curve is associated with the black body emission at a temperature of $T_b \sim$ 3100 K from the companion M-type star of radius $r = R_b \sim 3 \times 10^{10}$ cm in the binary system. The data point with downward arrow represent 2σ upper limit on the integral flux above 100 MeV from the *Fermi*-LAT observations over a decade. The measured 2σ upper limit and non-thermal emission predicted by the Synchrotron-2 component of the model indicate that the γ-ray emission from the source is very weak and below the current flux sensitivity of the *Fermi*-LAT, depicted by the red curve (taken from the *Fermi*-LAT Performance at the *Fermi* Science Support Center).

components referred to as *Synchrotron-1* and *Synchrotron-2*. The multi-wavelength data points in Fig. 2 have been used without taking into account the measurement errors from different instruments and are reprocduced through the χ-by-eye fitting process. It is evident from Fig. 2 that the Synchrotron-1 component of the model describes the emission in the low energy band (radio-IR-Optical-UV), whereas the Synchrotron-2 component predicts soft X-ray and γ-ray emissions from the binary system AR Scorpii. The high energy end of the X-ray emission (hard X-rays) in the energy range 0.15–12 keV is reproduced by the tail of the synchrotron spectrum from the Synchrotron-1 component of the model. A comparison of the γ-ray emission level predicted by the Synchrotron-2 model with the broadband flux sensitivity of the *Fermi*-LAT in Fig. 2 suggests that the γ-ray flux above 100 MeV expected from AR Scorpii is below the current detection sensitivity of the LAT as well as the 2σ upper limit on the integral flux derived from more than 10 years of observations. The best fit model parameters derived from the non-thermal broadband SED modelling of AR Scorpii are given in Table 1. We note that the size of the emission region (R_{em}) for the Synchrotron-1 and Synchrotron-2 components is much smaller than the light cylinder radius (R_{LC}) of the MWD and/or the binary separation (a) in AR Scorpii. This implies that the non-thermal emission zones are situated well inside the light cylinder. The magnetic field strength in the X-ray and γ-ray emission regions (Synchrotron-2) is much higher than that in the low energy emission zone (Synchrotron-1). However, the strength of the magnetic field in both the emission regions is significantly less than the surface magnetic field (B_s) of the MWD in AR Scorpii. The dipole magnetic field of the MWD at a radial distance x is given by

$$B_x = B_s\left(\frac{R}{x}\right)^3 \tag{12}$$

Using this relation, we get an estimate of the locations of the emission regions from the MWD as $x_1 = 3.1 \times 10^{10}$ cm and $x_2 = 3.1 \times 10^9$ cm corresponding to the Synchrotron-1 and Synchrotron-2 components respectively. This implies that the low energy emission zone (Synchrotron-1) is near to the M-type companion star ($x_1 \sim a \sim 10^{10}$ cm), whereas the high energy emission zone (Synchrotron-2) is located between the MWD and M-type companion star ($x_2 < a$) in the binary system.

The particle spectral indices p and q describing the smooth broken-power law energy distribution (Table 1) indicate an efficient acceleration of electrons to relativistic energies and synchrotron cooling in the binary system AR Scorpii. The energy density of relativistic electrons (U_e) in the emission region is given by

$$U_e = m_e c^2 \int_{\gamma_{\min}}^{\gamma_{\max}} N(\gamma) d\gamma. \tag{13}$$

From Table 1, we find that the energy density of the electrons in the high energy emission zone (Synchrotron-2) is about 5 times higher than that in the low energy emission region (Synchrotron-1). This indicates that the electrons associated with the Synchrotron-2 component are accelerated to higher relativistic energies ($\gamma_{\max} \sim 10^6$) than those involved in the Synchrotron-1 component. Therefore, electrons near to the MWD experience relatively more acceleration as compared to the far away electrons. The values of p and q for both the emission components are very

Table 1
Best fit model parameters from the non-thermal spectral energy distribution modelling of the binary system AR Scorpii.

Parameter	Symbol	Synchrotron-1	Synchrotron-2
Size of emission region	R_{em}	1.8×10^{10} cm	1.4×10^{10} cm
Magnetic field strength	B	1.1×10^{3} G	1.1×10^{6} G
Low energy index of particle ditribution	p	2.3	1.8
High energy index of particle ditribution	q	3.7	3.4
Break energy of particle distribution	$\gamma_b m_e c^2$	200 MeV	715 MeV
Minimum Lorentz factor of particle distribution	$\gamma_{\rm min}$	10	50
Maximum Lorentz factor of particle distribution	$\gamma_{\rm max}$	2×10^{4}	8×10^{6}
Particle energy density	U_e	0.46 erg cm^{-3}	2.40 erg cm^{-3}

close to the condition of radiative cooling break $q = p + 1$. The synchrotron cooling time scale for an electron is defined as [27]

$$t_{sync} = \frac{9}{4}\frac{m_e^3 c^5}{e^4 B^2 \gamma} = 7.7 \times 10^4 \left(\frac{10G}{B}\right)^2 \left(\frac{10^2}{\gamma}\right) \text{ second.} \quad (14)$$

If the maximum energy of an electron in the emission region is determined by the synchrotron cooling, the acceleration timescale should be the same as t_{sync}. Therefore, assuming $\gamma = \gamma_{\rm max}$, the acceleration timescale of an electron in AR Scorpii can be expressed as

$$t_{acc} = 7.7 \times 10^4 \left(\frac{10G}{B}\right)^2 \left(\frac{10^2}{\gamma_{\rm max}}\right) \text{ second.} \quad (15)$$

Using the values of B and $\gamma_{\rm max}$ from Table 1, we find that t_{acc} is very small and therefore, suggests a very fast and efficient acceleration of electrons in AR Scorpii. The exact acceleration process for the electrons in the WD binary systems remains unclear. However, several plausible scenarios have been proposed for AR Scorpii. In the first scenario [28], a magnetized plasma ejected from the polar cap of the MWD sweeps the stellar wind from the M-type companion star and interaction between the plasma and stellar wind leads to the formation of a bow shock. This bow shock propagates in the stellar wind and accelerates the electrons to relativistic energies in the wind to produce synchrotron radiation. In the second scenario [29], the magnetic interaction on the surface of the M-type companion star has three dissipation effects namely heating of the surface of M-star, an overflow from the M-star and acceleration of electrons to the relativistic energies with $\gamma = 50$–100. The accelerated electrons move from the companion star to the surface of the MWD along the magnetic field lines and are trapped in the closed magnetic field lines region due to the magnetic mirror effect. The synchrotron radiation is produced by the trapped electrons at the magnetic mirror point. In the third scenario [30], the particles are accelerated through the magnetic reconnection or *Fermi* acceleration process in a turbulent collision region produced by the interaction of the MWD magnetic field with a dense atmosphere of the M-type star. In a relatively different hybrid scenario [31], electrons and protons are accelerated to the relativistic energies close to the surface of the companion M-star as postulated in the third scenario and the broadband non-thermal emission is produced by the relativistic electrons and/or by the electron-positron pairs from the pion decay created by the interaction of relativistic protons with the matter in the atmosphere of the M-star. Under the framework of the bow shock acceleration, the electron energy distribution has been reasonably described by a broken-power law with $p \sim 2.4$ and $q = p + 1$ constrained by the X-ray observations [28]. The measurements of the optical linear polarization from AR Scorpii support the bow shock acceleration of electrons [16]. Therefore, the electron energy distribution described by a smooth broken-power law in the present study can be attributed to the bow shock acceleration scenario.

However, from Fig. 2, we observe that a hump at the optical frequencies cannot be reproduced by the non-thermal synchrotron emission predicted by the Synchrotron-1 model. Therefore, we use a simple black body emission to model this optical emission from AR Scorpii. The spectral energy distribution for a thermal emission from a black body is estimated as

$$\nu F_\nu = 8\pi h \left(\frac{R_b}{d}\right)^2 \frac{\nu^4}{c^2} \left(e^{h\nu/kT_b} - 1\right)^{-1} \quad (16)$$

where R_b and T_b are the radius and temperature of the black body respectively. h and k are the Planck and Boltzmann constants respectively. From the best fit of the optical hump in Fig. 2, we get $R_b = 3.2 \times 10^{10}$ cm and $T_b = 3100$ K. These parameters are in good agreement with the values reported in the literature [14,15,28]. Hence, the black body can be associated with the companion M-type star in AR Scorpii. This supports the above finding that the Synchrotron-1 emission zone is near to the M-star in the binary system. Therefore, the thermal emission from the M-type star dominates over the synchrotron radiation at the optical frequencies. The dominant thermal emission from the M-type star can play a major role in the depolarization of the synchrotron radition at the optical wavelengths. Therefore, the thermal contribution of the M-type star should be taken into account while modelling the synchrotron polarization of the source. The intrinsic synchrotron polarization modelling will help to better understand the acceleration process in AR Scorpii.

5. Conclusions

We have used the broadband archival data from radio to X-ray observations to reproduce the time averaged spectral energy distribution of the binary system AR Scorpii under the framework of a leptonic emission model. We have also derived a 2σ upper limit on the γ-ray integral flux above 100 MeV by analysing the *Fermi*-LAT data for a period of more than a dacade. The important findings of this study are as follows:

- The synchrotron emission produced by the relativistic electrons described by a smooth broken-power law energy distribution from two independent components located well inside the light cylinder of the MWD contributes to the observed broadband SED of AR Scorpii.
- Low energy observations in the radio, infrared, optical and ultraviolet frequency bands are broadly reproduced by the non-thermal emission which originates from a spherical region near the M-type companion star. In this region, we find that the strength of the magnetic field is $\sim 10^3$ G and the electron energy distribution is decribed by the spectral indices 2.3 and 3.7 before and after the break respectively with a break energy of $\sim$ 200 MeV.
- Most of the X-ray flux points in the energy range 0.15–12 keV are reproduced by the synchrotron emission from a spherical zone with a magnetic field strength of $\sim 10^6$ G and located at a distance of $\sim 10^9$ cm from the MWD. The relativistic electrons in this region also follow an energy distribution with

spectral indices 1.8 and 3.4 before and after the break respectively and having a break at ~ 715 MeV. The flux points at the high energy end of the X-ray spectra are described by the tail of the synchrotron radiation which is dominant at the low energy component of the broadband SED of AR Scorpii.

- The measured optical emission from AR Scorpii indicates a hump in the broadband SED and cannot be modelled by any of the non-thermal emission components. Instead, the optical hump is well reproduced by a black body spectrum associated with the M-type companion star in the binary system.
- The high energy γ-ray emission level predicted by the SED modelling of the source is below the 2σ upper limit on the integral energy flux above 100 MeV as well as the current broadband flux sensitivity of the *Fermi*-LAT. This suggests that if the binary system AR Scorpii emits gamma rays, it would be a weak Galactic source, but we cannot make an implicit assumption that it is. However, it can be a potential target for the upcoming ground-based γ-ray observatory namely the Cherenkov Telescope Array (CTA) with a low energy threshold and better sensitivity.

Declaration of Competing Interest

The authors declare that they have no known competing financial interests or personal relationships that could have appeared to influence the work reported in this paper.

Acknowledgements

Authors thank the anonymous reviewer for the important and valuable suggestions to improve the manuscript. We acknowledge the use of public data obtained through the Fermi Science Support Center (FSSC) provided by NASA, and other archival data from various observations in this study.

References

[1] P.E. Tremblay, et al., MNRAS 461 (2016) 2100.
[2] J.D. Cummings, et al., ApJ 866 (2018) 21.
[3] L. Ferrario, et al., SSRv 191 (2015) 111.
[4] M.J. Darnley, et al., ApJ 746 (2012) 61.
[5] P. Szkody, et al., AJ 142 (2011) 181.
[6] M. Revnivtsev, et al., A&A 489 (2008) 1121.
[7] B. Zhang, J. Gil, ApJL 631 (2005) L143.
[8] T. Gold, Nature 218 (1968) 731.
[9] J. Pétri, MNRAS 484 (2019) 5669.
[10] I. Contopoulos, A. Spitkovsky, ApJ 643 (2006) 1139.
[11] L. Ferrario, R. Wehrse, MNRAS 310 (1999) 189.
[12] L. Ferrario, et al., MNRAS 260 (1993) 149.
[13] S.H. Lubow, F.H. Shu, ApJ 198 (1975) 383.
[14] T.R. Marsh, et al., Nature 537 (2016) 374.
[15] J. Takata, et al., ApJ 853 (2018) 106.
[16] D.A.H. Buckley, et al., NatAs 1 (2017) 0029.
[17] J. Takata, K.S. Cheng, ApJ 875 (2019) 119.
[18] B. Marcote, et al., A&A 601 (2017) L7.
[19] E.R. Stanway, et al., A&A 611 (2018) A66.
[20] P. Garnavich, et al., ApJ 872 (2019) 67.
[21] W.B. Atwood, et al., ApJ 697 (2009) 1071.
[22] S. Abdollahi, et al., The fermi-LAT collaboration, ApJS 247 (2020) 33.
[23] R.J. Mattox, et al., ApJ 461 (1996) 396.
[24] P. Bruel, A&A 622 (2019) A108.
[25] G. Ghisellini, et al., ApJL 334 (1988) L5.
[26] S. Sahayanathan, et al., RAA 18 (2018) 035.
[27] Y. Inoue, et al., ApJ 880 (2019) 40.
[28] J.J. Geng, et al., ApJL 831 (2016) L10.
[29] J. Takata, et al., ApJ 851 (2017) 143.
[30] J.I. Katz, ApJ 835 (2017) 150.
[31] W. Bednarek, MNRAS 476 (2018) L10.